2011-06-06

Electronic Unsaturation of Organometallic Complexes Imparted by Sterically Demanding Ligands

Derek M. Isrow
University of Miami, disrow@med.miami.edu

UNIVERSITY OF MIAMI

ELECTRONIC UNSATURATION OF ORGANOMETALLIC COMPLEXES IMPARTED BY STERICALLY DEMANDING LIGANDS

By

Derek Isrow

A DISSERTATION

Submitted to the Faculty
of the University of Miami
in partial fulfillment of the requirements for
the degree of Doctor of Philosophy

Coral Gables, Florida

June 2011

UNIVERSITY OF MIAMI

A dissertation submitted in partial fulfillment of
the requirements for the degree of
Doctor of Philosophy

ELECTRONIC UNSATURATION OF ORGANOMETALLIC COMPLEXES IMPARTED BY STERICALLY DEMANDING LIGANDS

Derek Isrow

Approved:

_____ Burjor Captain, Ph.D. Professor of Chemistry	_____ Terri A. Scandura, Ph.D. Dean of the Graduate School
_____ Françisco M. Raymo, Ph.D. Professor of Chemistry	_____ Roger M. LeBlanc, Ph.D. Professor of Chemistry

_____
Barbara Nozière, Ph.D.
Professor of Chemistry
Institut de Recherches sur la Catalyse
et l'Environnement de Lyon

ISROW, DEREK (Ph.D., Chemistry)

Electronic Unsaturation of Organometallic Complexes Imparted by Sterically Demanding Ligands. (June 2011)

Abstract of a dissertation at the University of Miami.

Dissertation supervised by Professor Burjor Captain.
No. of pages in text. (217)

The reactivity of bulky ligands with various transition metal complexes was studied to better understand the nature of organometallic electronic unsaturation and the role this plays in small molecule activation. A bulky stannyl hydride, $^{t}Bu_3SnH$, was synthesized by a revised procedure that is far more facile and reproducible. This sterically encumbered ligand was shown to oxidatively add to a broad range of transition metal complexes, particularly those displaying carbonyl ligands, in greatly differing manners. Reaction of $^{t}Bu_3SnH$ with $Ni(COD)_2$ and $^{t}BuNC$ was found to yield the mononuclear complex $Ni(Sn^{t}Bu_3)_2(^{t}BuNC)_3$. This compound possesses photochemical reactivity, most likely attributable to the massive steric bulk surrounding the Ni center, and generates electronically unsaturated metal centered radicals upon photolysis. This complex and its photochemical products were studied from both experimental and spectroscopic aspects. The stable organic radical TEMPO was also reacted with $Ni(COD)_2$ to afford the unsaturated square planar complex $Ni(\eta^2\text{-N,O-TEMPO})_2$ which was studied both experimentally and spectroscopically. This deceivingly simple compound displays a wide spectrum of complicated reactivity and small molecule activation which may be utilized in future catalysis.

ACKNOWLEDGEMENTS

It is with great honor that I am able to dedicate this work to my family. Without the loving support of my mother Karen, father Allen, and brother Jordan there is simply no way I would be the person I am today. Equally as important, I give tremendous thanks to my boss and friend, Dr. Burjor Captain. To have known this man is a true privilege, and I owe more to him than can be counted. I am infinitely fortunate to have been in his tutelage, and the expanse of chemical knowledge that he has bestowed upon me will echo in my heart and mind forever. I am undoubtedly certain that his burgeoning career will be long and esteemed, and I am lucky to bear his chemical brand.

I must thank the exceptional people I have shared the lab with during my time at UM: Dr. Lei Zhu, Veeranna Yempally, Sumit Saha, and Anjaneyulu Koppaka. It is because of these fine men that I am able to write this work. Much appreciation goes to Stefania Impellizzeri, Dr. Dave Hudson, and Ed Torres for their many hours of effort and assistance with my spectroscopic measurements. I am deeply grateful to my committee members Dr. Françisco Raymo, Dr. Roger LeBlanc, and Dr. Barbara Nozière for their assistance and guidance throughout my time in the chemistry department.

Lastly, I would like to thank the University of Miami for many years of wonderful experiences as well as financial support. I am proud to wear the U, **GO CANES!**

For my Dad, the greatest man I will ever know. Keep it in the fairway.

TABLE OF CONTENTS

LIST OF FIGURES

CHAPTER 1

CHAPTER 2

CHAPTER 3

CHAPTER 4

APPENDIX A

APPENDIX B

APPENDIX C

LIST OF SCHEMES

CHAPTER 1

CHAPTER 2

CHAPTER 3

LIST OF TABLES

APPENDIX A

APPENDIX B

APPENDIX C

Chapter 1: Electronic Unsaturation of Organometallic Complexes Imparted By Sterically Encumbered Ligand Systems.

1.1 Introduction

Perhaps the most basic definition of an organometallic complex is a metal center possessing covalent bonds to carbon or hydrogen atoms. One of the first organometallic complexes ever reported was Zeise's salt, $K[PtCl_3(\eta^2\text{-}C_2H_4)]\cdot H_2O$, and this platinum-olefin compound changed the world of chemistry forever.[1] Formed while studying the reaction of K_2PtCl_4 in boiling ethanol, Zeise proposed that the product contained "side-on" bound ethylene gas, an interesting suggestion considering it was a previously unknown coordinative possibility. This hypothesis was criticized by some of the more influential chemists of the 1800's, and was not even proven to be completely true until the advent of X-ray crystallography in the 20th century.[2] Zeise's revolutionary product helped give rise to the new field of organometallics, as well as exciting chemical concepts such as hapticity, η, used in the chemical equation $K[PtCl_3(\eta^2\text{-}C_2H_4)]\cdot H_2O$. This term denotes the coordination of both carbon atoms in ethylene to the metal center seen in Figure 1.1, a binding mode that was previously unknown.

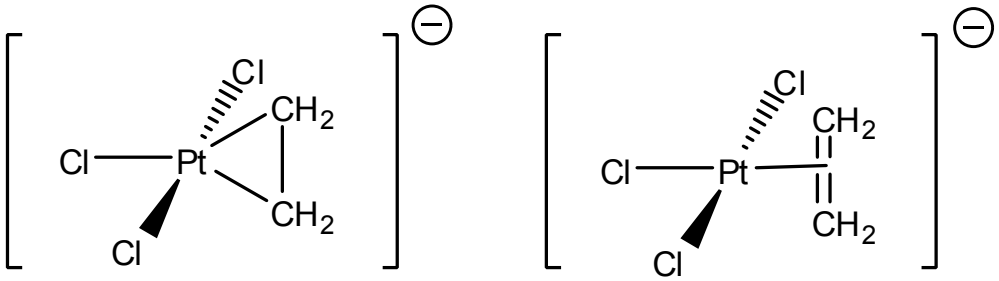

Figure 1.1 Line drawings of Ziese's salt, $K[PtCl_3(\eta^2\text{-}C_2H_4)]\cdot H_2O$ in two different styles.

Since that initial discovery, a vast library of organometallic complexes have been synthesized and characterized. Many of these metal-organic compounds were found to inexplicably increase the rate of certain chemical reactions, and thus they were grouped under the term "catalyst" which was born of the Greek καταλύειν. A catalyst is technically any substance that will lower the rate-limiting energy of activation for a specific chemical reaction, thereby speeding up the rate while not being consumed in the reaction itself. A very generic image showing the thermodynamic changes in a catalyzed reaction profile is shown in Figure 1.2. Catalyzed reactions will typically have higher kinetic rates than the uncatalyzed reactions at a given temperature.

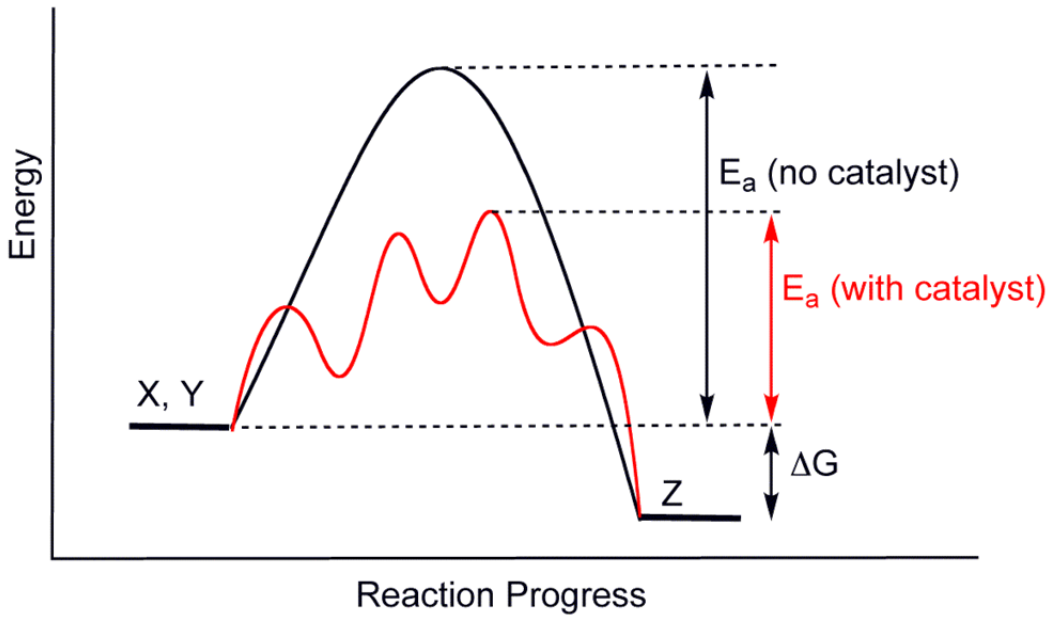

Figure 1.2 Potential energy diagram of a hypothetical catalyzed reaction vs the hypothetical uncatalyzed reaction.

The field of chemistry would not be the same without catalysts. Likewise, nearly all important biochemical reactions necessary for life to exist require catalytic enzymes.[3] Catalysis is incorporated into almost every aspect of our daily lives, from combustion exhaust converters to meat tenderizers. The fertilizers we use are made from ammonia, produced annually in megaton amounts by the Haber-Bosch process which fixes atmospheric N_2 utilizing an iron based catalyst.[4,5] This reaction, first discovered in 1909, converts N_2 and $3H_2$ to $3NH_3$ under heterogeneous conditions but requires extreme temperatures and pressures seen in equation 1.1.

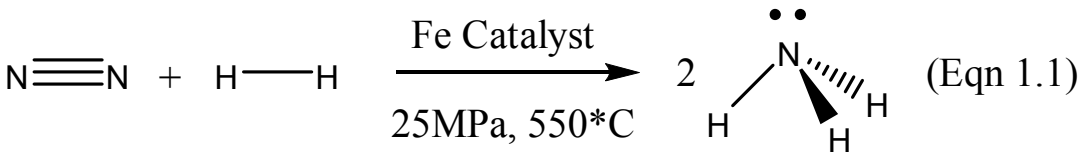

Even today after over a century, there is much research interest in finding a new nitrogen fixation catalyst for this reaction that is sufficiently active at more mild conditions, perhaps operating in solution under homogeneous conditions saving vast amounts of energy.[6] In fact, over 90% of all commercially synthesized chemical products require catalysts at some stage in their manufacturing, and many of the catalysts are active only under extreme conditions.[7] These chemical products generate nearly 1$ trillion worldwide annually combined.[8] Surely novel catalysts capable of high efficiency at more mild conditions could help reduce costs and preserve precious resources as we face ever increasing global demand.

Scientific understanding of catalysts has improved in recent times, and there are numerous laboratories across the globe currently performing excellent experimental

searches for active compounds. When attempting to create an organometallic homogeneous catalyst, possibly the most necessary requirement is a metal center with a vacant electronic orbital.[9] An empty electronic orbital on the metal should ideally allow coordination of compatible small molecules which may then be "activated" to chemically react by some alteration of their electronic configuration. There are now numerous examples of organometallic complexes in the literature capable of small molecule activation and transformation, some of which are employed as industrial catalysts, and almost all of these compounds share one important common characteristic--*electronic unsaturation*.

1.2 Electronic Unsaturation of Metal Centers

One of the best, and coincidentally earliest, examples of a highly active organometallic complex capable of small molecule activation is Vaska's complex $Ir(Cl)(CO)(PPh_3)_2$.[10] Studies of this compound laid the groundwork for understanding homogeneous catalysis as we know it today. This square planar iridium complex contains 16 electrons around the metal center, not the ideally preferred count of 18 which provides "nobility", and is therefore electronically unsaturated by $2e^-$.[11] This can be attributed to the *trans* triphenyl phosphine ligands which provide immense steric protection of the metal center, seen in Figure 1.3. Steric protection by bulky phosphines was extensively studied later by Tolman who coined the term "ligand cone angle", and he showed that PPh_3 provides a relatively large cone angle of nearly 145 °.[12] This structural characteristic is measured as the angle formed with the central metal at the vertex and the

hydrogen atoms of the phosphine substituents at the perimeter of the cone, and it was found to be a concept of significant importance in homogeneous catalysis.

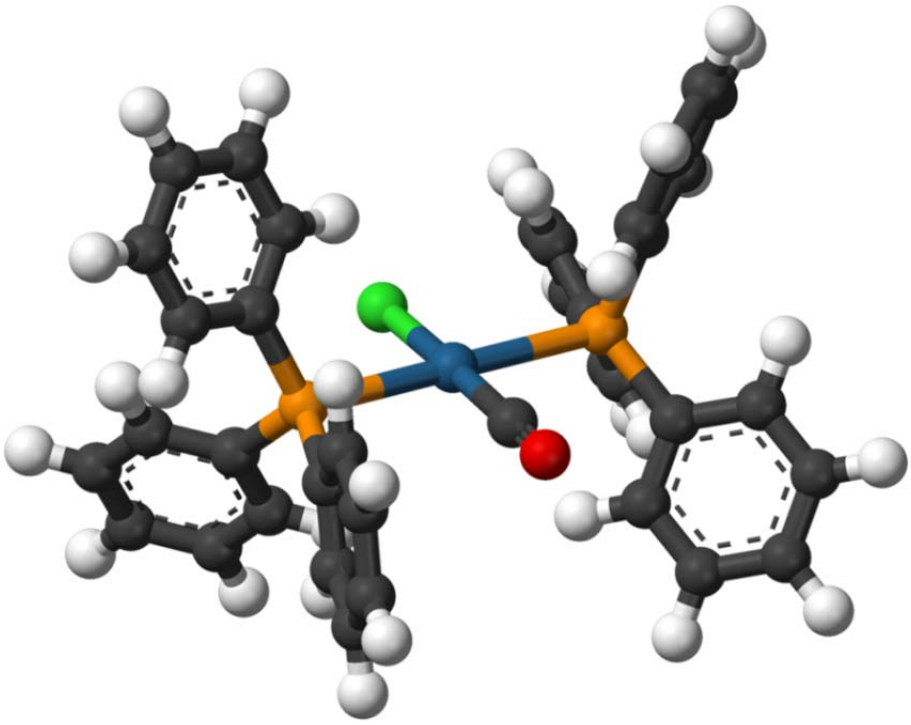

Figure 1.3 Ball and stick figure showing Vaska's complex, $Ir(Cl)(CO)(PPh_3)_2$. Carbon shown in black, hydrogen in white, phosphorus in gold, iridium in blue, chlorine in green, and oxygen in red.

The large cone angle of triphenyl phosphine seems to prevent the Ir center in Vaska's complex from binding inappropriately sized molecules or potentially dimerizing, and thus they maintain both coordinative and electronic unsaturation of the iridium metal center. This electronic unsaturation was shown to be quenched by addition of an appropriately sized ligand to furnish $18e^-$ Ir. This small molecule could be a single $2e^-$ donor like CO or two $1e^-$ donors such as in Cl_2, I_2, HCl, CH_3I, H_2, etc. This gain of two $1e^-$ donors from a single ligand is termed *oxidative addition,* and the Ir^I center is indeed

oxidized to Ir ^{III} by reaction with any of the previously mentioned reagents. Coordination of small molecules via oxidative addition to Vaska's complex forces a geometric transformation from four coordinate square planar to six coordinate octahedral, seen in Scheme 1.1. The phosphines are still located *trans* to one another while CO and Cl become *cis*, most likely due to steric repulsion.

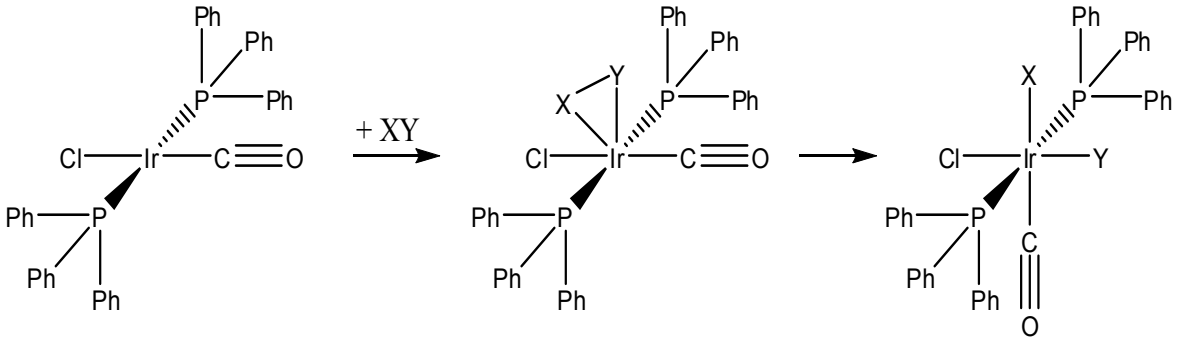

Scheme 1.1 Line drawing showing the oxidative addition of small molecule X-Y to Vaska's complex to afford an octahedral product.

Surprisingly, this complex was found to *reversibly* add and eliminate many small molecules, including O_2 and H_2, by respective oxidative addition and *reductive elimination* at the metal center. The oxidative addition of small molecules to a metal center is known to be the important rate-limiting initial activation step in many catalytic reactions, and reductive elimination of the transformed product is usually the final step. This will be shown below in Scheme 1.2.

It was clear at the time that the chemical abilities of electronically unsaturated organometallic complexes were very powerful tools, undoubtedly useful in synthetic chemistry. Having shown that sterically encumbered triphenyl phosphine ligands possessed the power to prevent electronic saturation of organometallic complexes like

Vaska's, there was a sudden outpouring of new unsaturated compounds capable of remarkable chemistry almost all with one common characteristic: *bulky ligands*.

1.3 The Role of Sterically Encumbered Ligands

Enzymes are nature's catalysts. Nearly all contain a metal center embedded in a ligand system, similar to man-made organometallic complexes. These enzymes are reactive due to a similar electronic unsaturation of the metal atom, and this deficiency of electrons is typically maintained by ligand systems that force a particular electronic conformation either by rigid structure or sheer size. Without the appropriate ligand environment provided by protein scaffolding around the metal atom, enzymes simply would not function properly. Similarly, organometallic chemists have at their disposal restrictively rigid ligands like porphyrins and extremely bulky ligands like phosphines, and these can be used to alter the ligand environment around a metal center in desired ways. These rigid metal-porphyrin systems are analogous to biochemical heme groups of hemoglobin found in our red blood cells. These heme groups are made from precursors like Fe-protoporphyrin IX, amongst many other examples, and the central metal atom is forced into a planar arrangement by the rigid ligand system with vacant axial sites for reaction seen in Figure 1.4.[13,14,15]

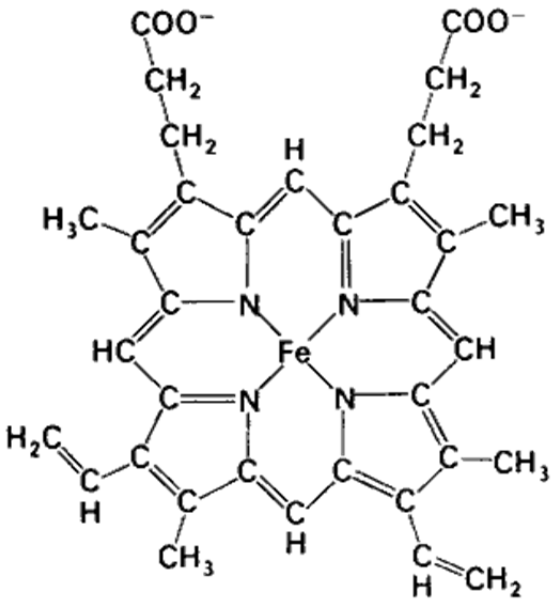

Figure 1.4 Line drawing of the heme group in hemoglobin, Fe-protoporphyrin IX.

Geometric restriction by rigid ligands like porphyrins has proven to be very useful in generating electronically unsaturated compounds capable of performing chemical reactions, though maybe not as useful as sheer volume occupancy by bulky ligands. The steric bulk of tri-phenyl phosphine groups was previously shown by Vaska to prevent electronic saturation of his Ir complex, and Wilkinson quickly followed with his structurally similar rhodium compound $Rh(PPh_3)_3(Cl)$. Wilkinson's complex contains a third bulky phosphine and was found to be an extremely active catalyst for a wide variety of chemical reactions including alkene hydrogenation shown in Scheme 1.2.[16] This catalytic process requires oxidative addition of H_2, π-orbital complexation of an alkene, hydrogen transfer, and reductive elimination of the newly formed alkane product. These amazingly intricate processes are conducted harmoniously by the precious rhodium center which can vary from 18 all the way down to 14 valence electrons at will.

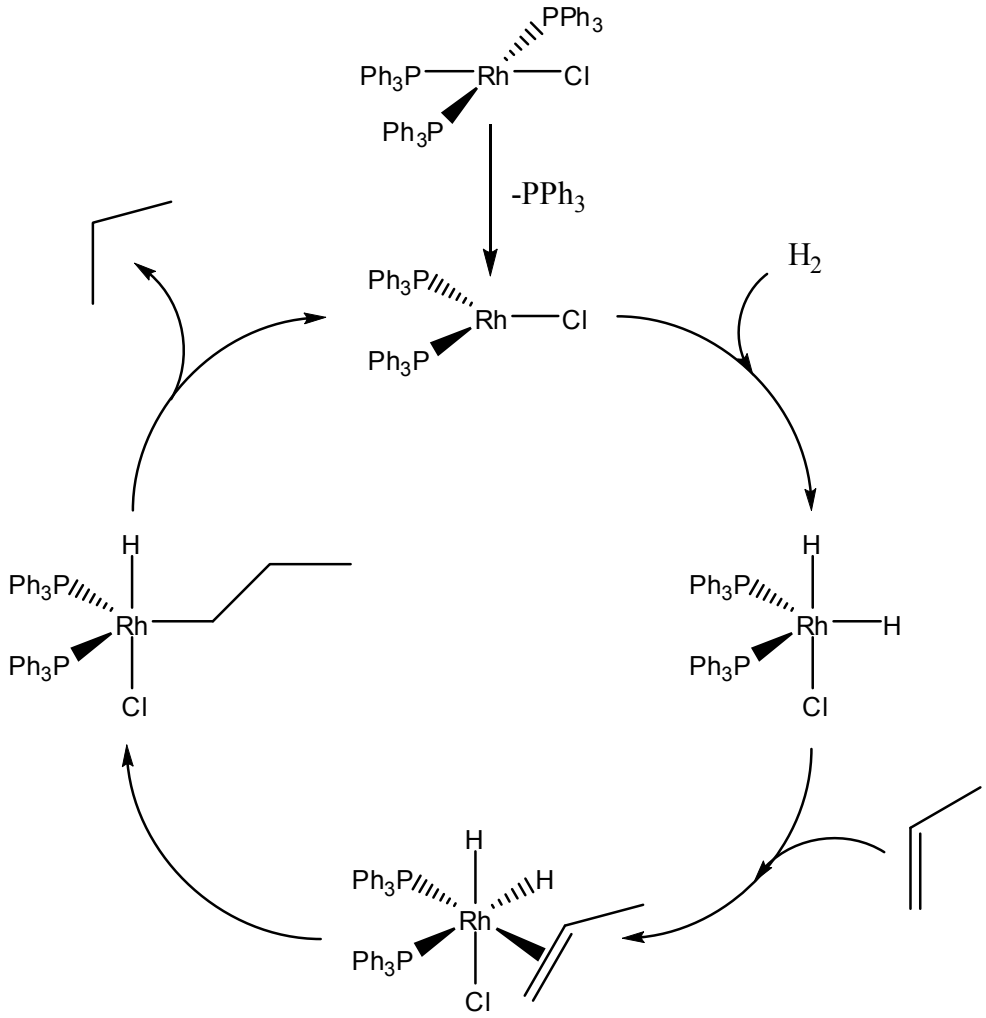

Scheme 1.2 Line drawing of the catalytic alkene hydrogenation cycle performed by Wilkinson's Catalyst.

The search began for differing types of bulky ligands, especially those containing no phosphorus which was shown to irreversibly poison many catalysts as well as scientists.[17,18] One of the most promising new classes of ligand to emerge from this search was the carbene.[19,20,21] A carbene is any molecule containing a neutrally charged carbon atom with two single covalent bonds and two unshared valence electrons, similar to the lone pair of electrons on a phosphine, shown in Figure 1.5.

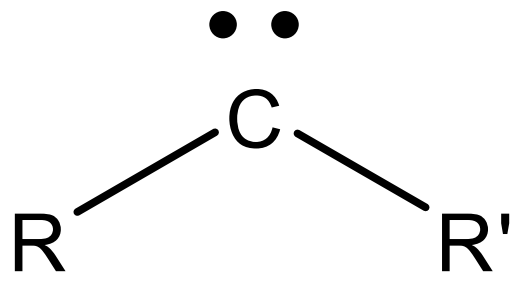

Figure 1.5 Line drawing of a generic carbene.

Free carbenes typically exist in either singlet or triplet electronic states, and will quickly dimerize to form double bonds if the R groups are not sufficiently bulky to prevent approach of a second equivalent according to the Wanzlick equilibrium.[22] The early carbenes were generated in situ by deprotonation of imidazolinium salts or photolysis of diazoalkanes, and they found immediate use in organometallic chemistry. Later, stable and free non-heterocyclic carbenes (NHCs) displaying substituents with massive bulk were synthesized by Arduengo et al. and their ease of handling and use quickly had many organometallic researchers studying their coordination to metal centers.[23,24]

The 1st generation Grubb's complex $Ru(PCy_3)_2(Cl)_2(=CHPh)$ contains bulky tricyclohexyl phosphines and is a highly active catalyst for olefin-metathesis, an extremely important process in hydrocarbon reforming and other industrial applications.[25] The second generation Grubb's catalyst, replacing phosphine with the new non-heterocyclic carbene, was found to be even more active and this catalytic advantage sparked massive interest in these NHC ligands.[26] A large number of metal-carbene complexes have since been produced and many possess profound electronic unsaturation.

A suitable generic example of existing 14e$^-$ platinum-carbene complexes is shown below in Figure 1.6 where R can be many different options.[27]

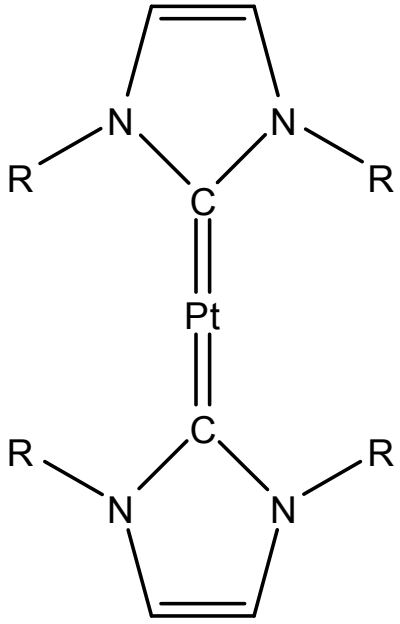

Figure 1.6 A generic14e$^-$ platinum complex, generated with bulky non-heterocyclic carbenes.

Some of these metal-NHC compounds are capable of small molecule activation and subsequent catalytic conversion of these small molecules to useful products. Synthetic knowledge of stable carbenes has led to the formation of stable silicon, germanium, and tin centered "carbenes" known as silylenes, germylenes, and stannylenes, respectively.[28,29,30] All of these "-ene" compounds have shown to be excellent ligands for providing protective steric bulk to a metal center, however they are 2e$^-$ neutral donors like triphenyl phosphine and CO, unable to change the oxidative state of the central metal. Most of the well-known industrial homogeneous catalysts make use of metal centers with varying oxidation states, seen above.

Mentioned earlier, the Haber-Bosch process converts dinitrogen and dihydrogen into ammonia, a product vital to modern society. Work by both the Schrock and Cummins groups has provided several low valence group 6 organometallic complexes capable of binding and activating the nearly inert N_2 molecule under homogeneous conditions.[31,32] Schrock's $Mo(HIPTN_3N)_3(N\equiv N)$ is shown in Figure 1.7.

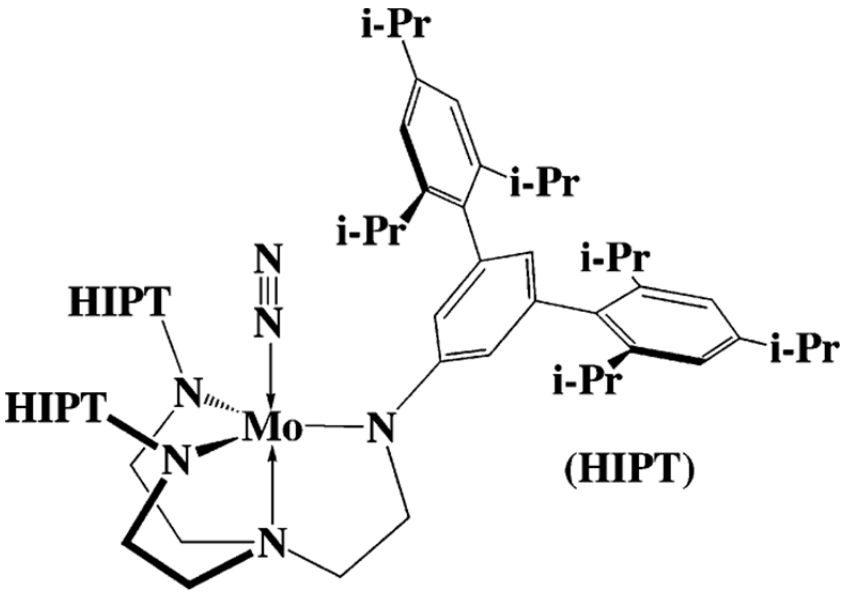

Figure 1.7 Line drawing of Schrock's $Mo(HIPTN_3N)(N\equiv N)$ complex.

In fact, several of these compounds have been able to subsequently cleave the N_2 triple bond into 2 M≡N nitrido complexes by various mechanisms, rare and exciting steps towards homogeneous nitrogen fixation.[33] Work still persists with these promising compounds in hopes of increasing our understanding of homogeneous catalysis and nitrogen fixation. The reactive group 6 complexes are highly unsaturated according to the $18e^-$ rule, and the electronic configuration is supported by sterically encumbering amide ligands bearing branched aryl and alkyl groups seen in Figure 1.7. These amides

are examples of $1e^-$ donating anionic ligands that are capable of providing steric bulk as well as altering the oxidation state of metal centers. Clearly ligands which possess ample steric bulk and are capable of altering the oxidation sates of metal centers are powerful tools for an organometallic chemist seeking to generate new catalysts.

1.4 Statement of Purpose

The following will detail our attempts at generating novel electronically unsaturated organometallic complexes by utilizing sterically demanding ligands. We will strive to exclude phosphine and carbene ligands from these compounds, and instead search for suitable replacements that will not only provide protective steric bulk but also alter the oxidation state of the central metal while increasing the overall reactivity of the molecule in general. We will revise the synthesis of a tin-hydride reagent that was previously too difficult to reproduce, tri-*tert*-butyl tin hydride. Tin is a well-known modifier/enhancer of chemical activity, and possesses its own reactivity and abilities as well. This ^{t}Bu derivative possesses superior steric bulk to any commercially available tin hydride and we will seek to react it with various transition metal complexes, especially nonprecious nickel. We will also investigate the coordination properties of the deceptively bulky TEMPO radical which has been shown to conduct numerous chemical reactions. TEMPO is capable of unusual binding mode transitions and these facile changes in coordination may impart reactivity to metal-TEMPO complexes. All synthesized products will be structurally and spectroscopically characterized and any possible reactivity will be investigated. The primary goal of this work is to better

understand the role electronic unsaturation plays in small molecule activation by organometallic complexes, and how said unsaturation can be induced by sterically encumbered ligands other than phosphines and carbenes. A secondary goal is to synthesize nonprecious organometallic complexes capable of small molecule activation in hopes of replacing expensive metals such as platinum, palladium, rhodium etc. The information contained hereafter will be of use in any future attempts at designing active homogeneous catalysts for a wide variety of applications.

Chapter 2: Tri-*Tert*-Butyl Tin Hydride: An Extremely Bulky Tool for the Production of Bimetallic Complexes.

2.1 Background

Tin is a rather versatile element. It resides in group 14 below carbon and silicon, sandwiched between germanium and lead, all of which show similar reactivity to this main group metal, Sn. Tin has 10 stable isotopes (the largest amount on the periodic table), as well as two possible oxidation states of +2 and +4. It has been used for thousands of years, primarily alloyed with copper in bronze, because of its resistance to oxidation and subsequent corrosion. Some of the more globally important tin compounds are Sn^{II} and Sn^{IV}, stannous and stannic, chlorides which have found uses as reducing agents in synthetic chemistry, mordants in industrial printing processes, and even as catalysts in chemical reactions.[34,35] These simple tin-halides have been shown to modify the platinum group metals and alter their catalytic activity in beneficial ways such as enhanced selectivity and efficiency.[36] These group 10 heterobimetallic tin compounds, as well as many other group metal-tin mixtures, have been shown to act as heterogeneous alloy catalysts for a wide variety of important industrial reactions.[37] However, these basic tin chlorides can be chemically altered to play a completely different role, particularly in the organometallic chemistry of homogeneous catalysis.

Organotin compounds, or stannanes, are tin centers surrounded by mostly hydrocarbon substituents, usually alkyl or aryl. They are normally formed by reaction of the previously mentioned tin halides with either organo-lithium or organo-magnesium halide compounds like methyl lithium and phenyl magnesium bromide, etc. Mentioned

in the last chapter, tin metal was recently used in place of carbon in the very reactive and bulky "carbene" analogues, stannylenes.[38] There are even stable organotin centered radicals with wide application.[39] These are two excellent examples of organotin products, and they possess great chemical potential.

Most important to this chapter of work and the next is the ability of organotin compounds to be bound to hydrogen yielding organotin hydrides, extremely reactive and useful products.[40,41] It is these stannyl hydrides that we seek to use as a replacement for phosphine ligands in our attempt to generate electronically unsaturated organometallic complexes capable of homogeneous small molecule activation. Phosphines have been the mainstay for steric encumberment of a metal center for many years, but they are being phased out of use due to their less than desirable properties and toxicities.

Tin hydrides have been known for some time, and perhaps the most notable is tri-*n*-butyl tin hydride, $^{n}Bu_3SnH$.[42] This organotin hydride is a versatile reagent in organic synthesis and can be combined with azobisisobutyronitrile (AIBN) or irradiated with light to cleave the Sn-H bond, yielding the tri-*n*-butyl tin radical which can react with organic substrates by substituting a halogen atom for a hydrogen atom, thus initiating a radical chain reaction. This is used to perform many types of chemistry including polymer synthesis and dehalogenation of organic molecules.[43] The field of organometallics has a very different use for these hydride compounds.

The Sn-H bond has been shown to readily react with transition metal complexes via oxidative addition, especially those possessing carbonyl ligands, to afford heterobimetallic compounds displaying both stannyl and hydride ligands, shown in

equation 2.1.[44] In fact, these stannyl ligands show great promise for the replacement of bulky phosphines which have been found to poison both humans and catalysts.

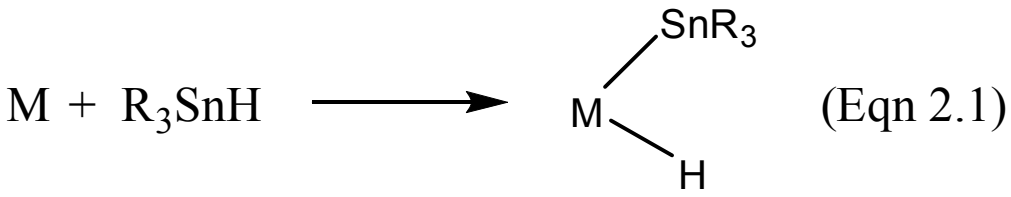

As stated in the first chapter, it has long been known that ligands with excessive steric bulk may be used to generate electronically unsaturated organometallic complexes, and oxidative addition changes the oxidation state of the central metal in potentially beneficial ways. While *n*-butyl groups are not particularly bulky, there are a number of organotin hydrides which possess severely encumbered substituents such as cyclohexyl and phenyl rings. However, the work presented here is based on an organotin hydride with superior bulk to any of those currently available commercially, tri-*tert*-butyl tin hydride ($^{t}Bu_3SnH$), shown below in Figure 2.1. The Tolman cone angle for $P^{t}Bu_3$ was found to be 182 °, much larger than that of PPh_3 at 145 °. It is fair to assume the tin analogues would follow suit.

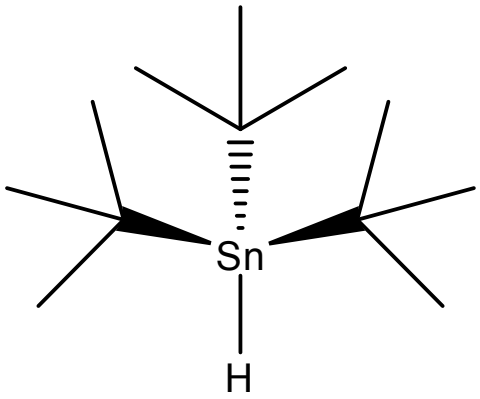

Figure 2.1 Line drawing of tri-*tert*-butyl tin hydride.

This compound was reported by Schneider and Wilhelm in 1967, but the synthesis was extremely lengthy and difficult to follow, as well as being published in German.[45] Most tertiary butyl derivatives of tin have not been well studied or characterized due to discouragingly difficult syntheses, and spectroscopic data for many of the already known compounds are in odd solvents and questionable at best.[46,47]

Reported in this chapter of work is a revised, easy to follow synthesis of $^{t}Bu_3SnH$ along with complete spectroscopic characterization of all intermediates, as well as some of our early experimental results exemplifying how this poorly studied organotin hydride reacts with various transition metal complexes to afford bi and trimetallic compounds possessing this bulky stannyl group. It is interesting to note that this tin hydride can react in various ways based on the transition metal complex studied, discussed later. Also contained here is a brief look at how the mixed-metal organometallic compounds generated by reaction with tin hydride contain consistent stoichiometric metal/metal ratios and how these bi- and tri-metallic complexes may be converted to uniform nanoparticle heterogeneous catalysts with great industrial potential.

2.2 Results and Discussion

A Revised Synthesis for Tri-*Tert*-Butyl Tin Hydride ($^{t}Bu_3SnH$). As stated earlier, $^{t}Bu_3SnH$ was reported by Schneider and Wilhelm in 1967, albeit completely in German. The synthetic process is extremely confusing even after translation and requires much time and energy to provide low yields with many undesirable side products that are exceedingly difficult to separate. Here we provide a revised synthesis which is easily

followed and reproduced, and results in a very reasonable yield of spectroscopically pure product.

The precursor for most organotin hydrides is tri-alky or tri-aryl tin chloride, R_3SnCl, which can be synthesized readily according to literature procedures.[48,49] This entails the initial formation of the Grignard reagent, RMgCl, and the subsequent dropwise addition of this Grignard to a solution of $SnCl_4$. However, the *tert*-butyl derivative does not behave in such a predictable manner, and addition of 3 equivalents of ^tBuMgCl to $SnCl_4$ will afford only the di-substituted $^tBu_2SnCl_2$. The published procedure for the synthesis of $^tBu_3SnCl$ requires an extra step which is the addition of ^tBuLi to a solution of $^tBu_2SnCl_2$, and this will give relatively clean reaction to the desired tri-*tert*-butyl tin chloride product.[50] Both the di and tri-*tert*-butyl tin chlorides can be vacuum distilled at mild temperatures as an excellent purification step, and this is highly recommended before further synthetic reactions.

It is from this point that the synthesis of the corresponding hydride became difficult. Nearly all organotin hydrides are formed by the facile reaction of R_3SnCl with one of the following: NaH, LiH, $LiAlH_3$, or $NaBH_4$. However, this is not so with $^tBu_3SnCl$ and reaction with these metal-hydride reagents yields almost no detectable tin-hydride product. This was unexpected and we performed many elaborate experiments with a lengthy list of other hydrogenating reagents, none were successful.

The answer to our tri-*tert*-butyl tin hydride synthesis dilemma came in the form of two short steps resulting in the desired clean formation of $^tBu_3SnH$ shown in equation

2.2.[51] These facile reactions provided a mechanistic detour around the use of dangerous alkali metal hydride reagents which require extreme caution when being handled.

$$^{t}Bu_3SnCl \xrightarrow[-NaCl]{NaOH/H_2O} {}^{t}Bu_3SnOH \xrightarrow[-H_2O]{BH_3/THF} {}^{t}Bu_3SnH \quad \text{(Eqn 2.2)}$$

When $^{t}Bu_3SnCl$ is dissolved in diethyl ether and stirred over a concentrated $NaOH/H_2O$ solution, the hydroxide product $^{t}Bu_3SnOH$ is afforded in nearly quantitative yield as a white crystalline solid (heating this solution to reflux will generate the distannoxane product $(^{t}Bu_3Sn)_2O$, seen in the next chapter). A simple reduction of this hydroxide with borane in tetrahydrofuran solution (BH_3/THF) followed by refluxing for one hour will produce the desired product $^{t}Bu_3SnH$ in nearly quantitative yield as a clear viscous liquid. The limiting factor in the entire process is the efficient production of pure $^{t}Bu_2SnCl_2$, and thus subsequent $^{t}Bu_3SnCl$, which is far more difficult than it would first appear according to the published literature yields. $SnCl_4$ will react violently with even the smallest amounts of oxygen and moisture to give white precipitate and HCl gas.

Our best attempts at revising this initial $^{t}Bu_2SnCl_2$ synthesis were mostly unsuccessful and its generation is still in mediocre yield and often problematic when it comes to separation and purification. The dichloride $^{t}Bu_2SnCl_2$ is commercially available at a reasonable price and this can be used to avoid a laborious synthesis.[52] However, the final product $^{t}Bu_3SnH$ can be typically isolated in acceptable yields of approximately 15 % (as high as 33 %) based on $SnCl_4$ as an extremely pure colorless liquid, and this provides a more than sufficient amount for our milligram scale reactions. This entire

process could undoubtedly be scaled up for large scale production, most likely increasing all reported yields significantly.

The complete synthesis of $^{t}Bu_3SnH$, starting from $SnCl_4$, is listed in the experimental section later in this chapter and is shown below in Scheme 2.1. The ^{1}H NMR spectra of pure $^{t}Bu_3SnH$ is shown in Figure 2.2. The one bond tin coupling to the hydride gives a large $^{1}J_{Sn\text{-}H}$= 1354 Hz and peak integration gives an appropriate ^{t}Bu to hydride ratio of 27**:**1.

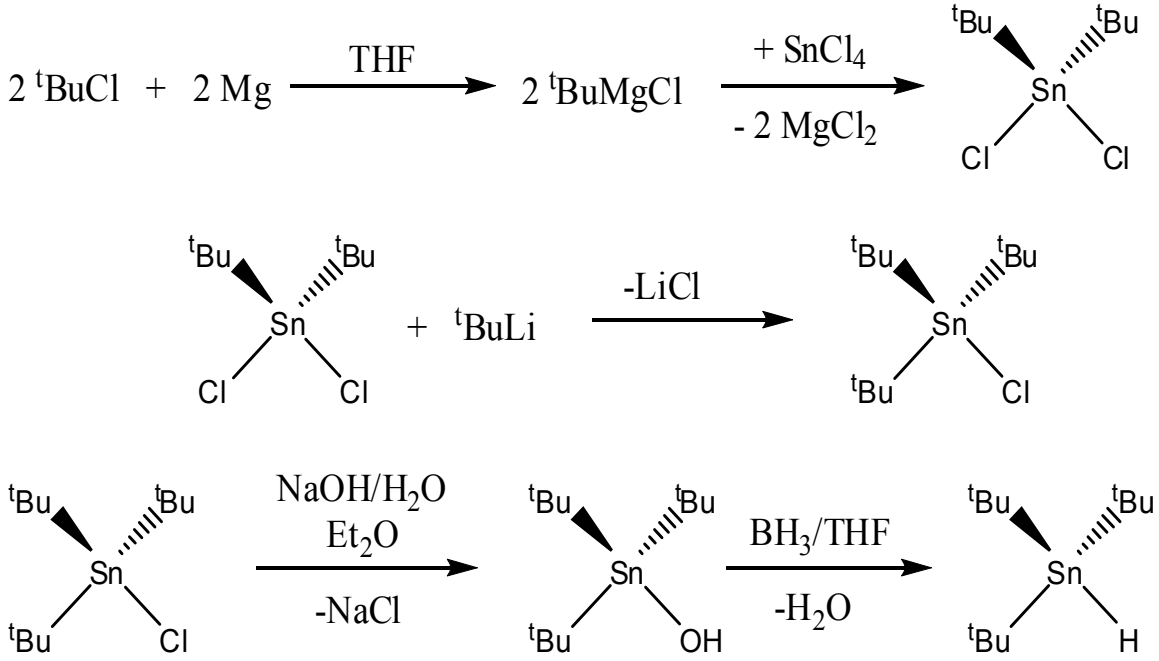

Scheme 2.1 Line drawings for the synthesis of $^{t}Bu_3SnH$.

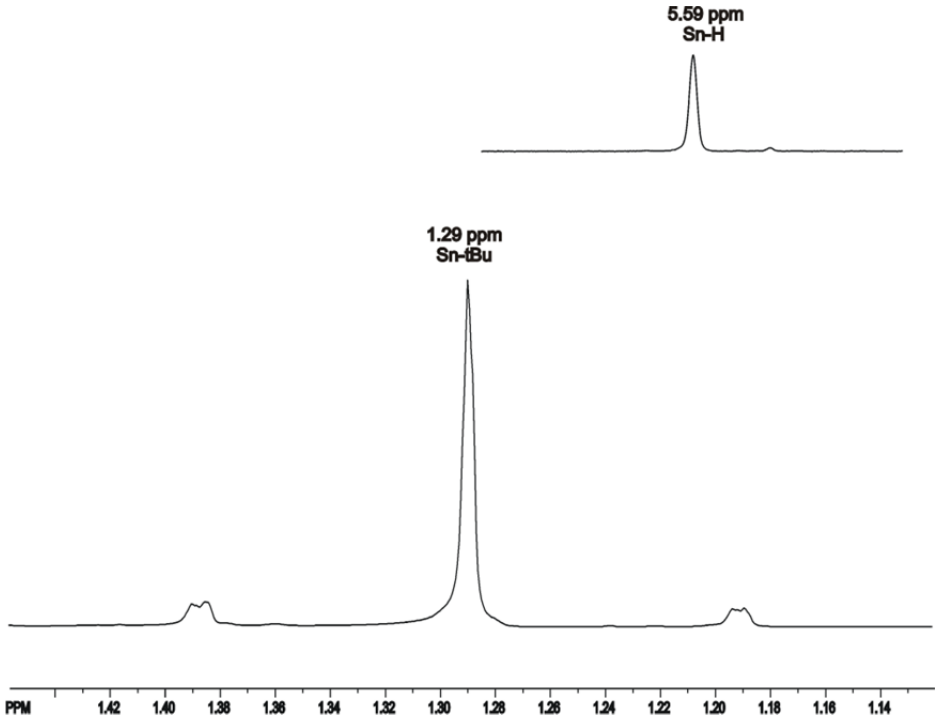

Figure 2.2 ^{1}H NMR spectra of $^{t}Bu_3SnH$ in C_6D_6 showing ^{t}Bu and Hydride regions.

Reaction of $^{t}Bu_3SnH$ with Di- and Tetracobalt Carbonyls. One of our first successes at synthesizing organometallic complexes containing the bulky $^{t}Bu_3Sn$ ligand was with cobalt carbonyl compounds. Cobalt based inorganic pigments have long been used in inks and dyes due to their lustrous blue color.[53] Organometallic cobalt complexes do not typically possess this blue color but they can play many diverse chemical roles, for example in Vitamin B_{12} which is the only vitamin to contain an active metal atom.[54] The organometallic complex dicobalt octacarbonyl, $Co_2(CO)_8$, exists in equilibrium between two isomers in solution with the bridging-carbonyl species predominating, shown in equation 2.3.[55] This relatively simple complex is well known catalyst in carbonylation and hydroformylation reactions.[56]

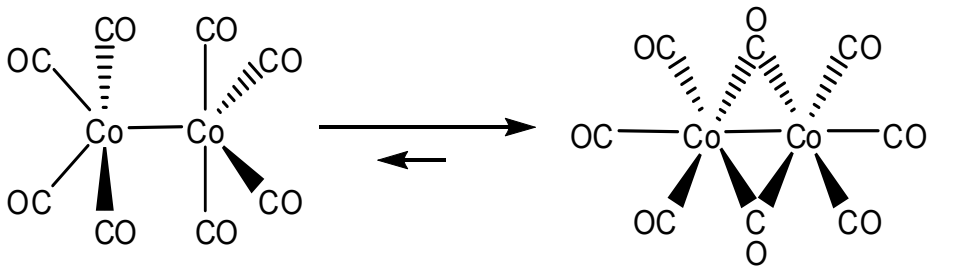

(Eqn 2.3)

Addition of 2eq of $^{t}Bu_3SnH$ to a an ethereal solution of $Co_2(CO)_8$ at 35 °C afforded the novel bimetallic compound $Co(Sn^{t}Bu_3)(CO)_4$ in 80 % yield. This reaction was accompanied by a color change from orange to very light yellow. FTIR spectroscopy showed clean reaction in terms of carbonyl containing compounds. This bimetallic complex was characterized by a combination of ^{1}H NMR, FTIR, elemental and single crystal X-ray diffraction analyses. An ORTEP of its molecular structure is shown in Figure 2.3 and further crystallographic data is provided in Appendix A Table A.1. The Co atom is in a trigonal bipyramidal arrangement containing axial $^{t}Bu_3Sn$ and CO ligands, and would appear to be the product of reaction with the minor isomer shown in equation 2.3.

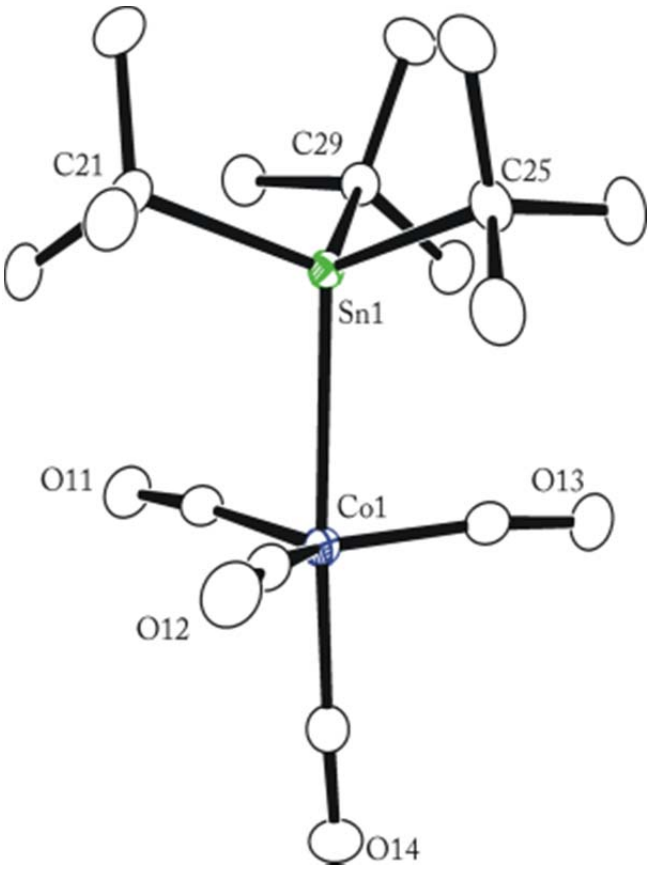

Figure 2.3 An ORTEP showing the molecular structure of $Co(Sn^tBu_3)(CO)_4$ at 100 K and 40 % thermal ellipsoid probability.

The previously published compound $Co(SnPh_3)(CO)_4$ is very similar to $Co(Sn^tBu_3)(CO)_4$, however the Co-Sn bond distance of 2.6696(2) Å is slightly longer than the Co-Sn bond in $Co(SnPh_3)(CO)_4$ which is 2.5953(7) Å.[57] This increase in bond length is to be expected from the greater steric repulsion of the *tert*-butyl groups compared to phenyl groups. It is apparent from the crystal structure of $Co(Sn^tBu_3)(CO)_4$ that there is a minor symmetry distortion of the equatorial carbonyl groups as they are bent slightly towards the $^tBu_3Sn$ ligand and away from the axial CO. This is also the case for $Co(SnPh_3)(CO)_4$, as well as the recently published rhodium-germanium compound $Rh(GePh_3)(CO)_4$, both of which show equatorial CO symmetry distortion toward the

$SnPh_3$ and $GePh_3$ ligands, respectively.[58] This phenomenon has been previously studied,[59] and a possible rationalization was determined that is proposed as follows: the Sn^tBu_3 group is very electropositive and can be thought of as the weakly coordinated anion $^tBu_3Sn^+$ bound to the $18e^-$ d^{10} $[Co(CO)_4]^-$ fragment which would ideally prefer a tetrahedral arrangement, thus forming the capped tetrahedral structure seen in $Co(Sn^tBu_3)(CO)_4$.

The complex $Co(Sn^tBu_3)(CO)_4$ has approximate C_{3v} symmetry and should thus display three FTIR active stretches, and appropriately the FTIR spectrum does indeed show these and they are assigned to the $2A_1$ and E modes.[60] The *n*-butyl analogue of $Co(Sn^tBu_3)(CO)_4$, $Co(Sn^nBu_3)(CO)_4$, was synthesized by Heiber and Breu, however their reaction proceeded through a different mechanistic pathway and utilized salt-elimination from $NaCo(CO)_4$ and $^nBu_3SnCl$.[61] No crystal structure of this *n*-butyl analogue was reported.

The proposed formation of $Co(Sn^tBu_3)(CO)_4$ is shown in equation 2.4. A similar reaction was first described by Chalk and Harrod and later by others.[62]

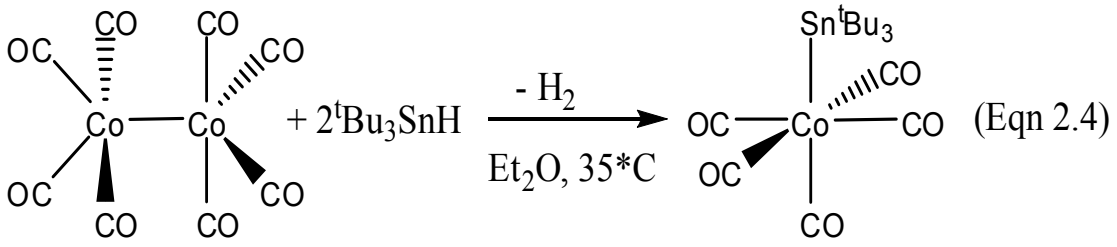

When the reaction was carried out in a sealed NMR tube, elimination of H_2 gas was indicated by ^{1}H NMR as a singlet at 4.47 ppm in C_6D_6, appropriately. If the reaction is carried out at elevated temperatures (> 70 °C), $Co(Sn^tBu_3)(CO)_4$ is formed only in minor amounts and FTIR spectroscopy confirms the presence of tetracobalt dodecacarbonyl, $Co_4(CO)_{12}$. Similarly, $Co(Sn^tBu_3)(CO)_4$ can be formed by reaction of $^tBu_3SnH$ and $Co_4(CO)_{12}$ at 110 °C for 3 hours, however in a much lower yield of 35 %. Addition of excess tin does not result in higher yields or formation of other products with either di or tetracobalt carbonyls. $Co(Sn^tBu_3)(CO)_4$ is slightly air sensitive and X-ray crystallographic analysis required low temperature data collection at 100 K underflow of N_2 atmosphere to avoid crystal decomposition.

Reaction of $^tBu_3SnH$ and $Ni(CO)_4$. As stated in the next chapter, one of the main goals of our work with $^tBu_3SnH$ was to generate bimetallic nickel-tin compounds that exhibit chemical reactivity and usefulness, in hopes of replacing very expensive precious metal catalysts such as platinum, palladium, and rhodium. Ni-Sn compounds are known to possess favorable chemical activity, and these two metals are both abundant and inexpensive.[63] The bimetallic Ni-Sn compound $Ni(Sn^tBu_3)_2(CO)_3$ was obtained in 50 % yield from the reaction of nickel tetracarbonyl, $Ni(CO)_4$, and $^tBu_3SnH$ in heptane at 97 °C for 30 minutes. This compound may also be formed in comparable yield (44 %) after 18 hours of room temperature reaction. The heterobimetallic complex $Ni(Sn^tBu_3)_2(CO)_3$ was characterized by a combination of FTIR, ^{1}H NMR, mass spectrometry, and single crystal X-ray diffraction analysis. An ORTEP of its molecular structure is shown in Figure 2.4 and relevant crystallographic data is listed in Appendix A Table A.1.

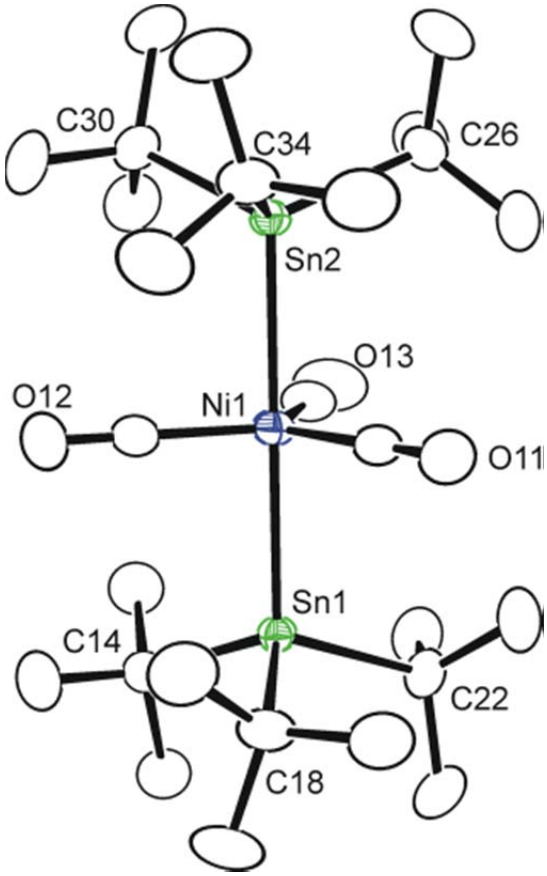

Figure 2.4 An ORTEP showing the molecular structure of $Ni(Sn^tBu_3)_2(CO)_3$ at 30 % thermal ellipsoid probability.

The geometry of this complex is trigonal bipyramidal much like $Co(Sn^tBu_3)(CO)_4$, however there are now two axial Sn^tBu_3 groups with the 3 CO ligands in the equatorial plane. The Sn(1)-Ni(1)-Sn(2) angle is nearly an ideal 180° at 177.847(14)° and the C-Ni-Sn angles for the CO ligands are all close to 90°, within the range of 89.13(8)-91.62(9)°. Not considering the ^{t}Bu groups on the tin ligands, $Ni(Sn^tBu_3)_2(CO)_3$ exhibits D_{3h} symmetry and should thus display only one CO stretching frequency in the FTIR spectrum for the three carbonyl ligands, and appropriately this is seen in hexane at 1991 cm^{-1}. As far as determining which ligands are axial and which are equatorial, it has been shown using molecular orbital theory and calculations that the

axial sites of trigonal bipyramidal complexes will be preferred by good sigma (σ) donor ligands, like Sn^tBu_3, while the equatorial positions are preferred by good pi (π) acceptor ligands, such as CO, when the metal has a d^8 electronic configuration.[64] Since CO ligands are known to be excellent pi orbital acceptors, it is reasonable to assume they are equatorial in the complex $Ni(Sn^tBu_3)_2(CO)_3$. It is also possible that the tin groups have taken *trans* axial positions due to steric repulsion between the two extremely bulky tin centers, similar to Vaska's octahedral complexes with *trans* PPh_3 groups. The proposed reaction is shown in equation 2.5. Similar to reaction of $^tBu_3SnH$ with cobalt carbonyls, ^1H NMR indicates the presence of H_2 gas.

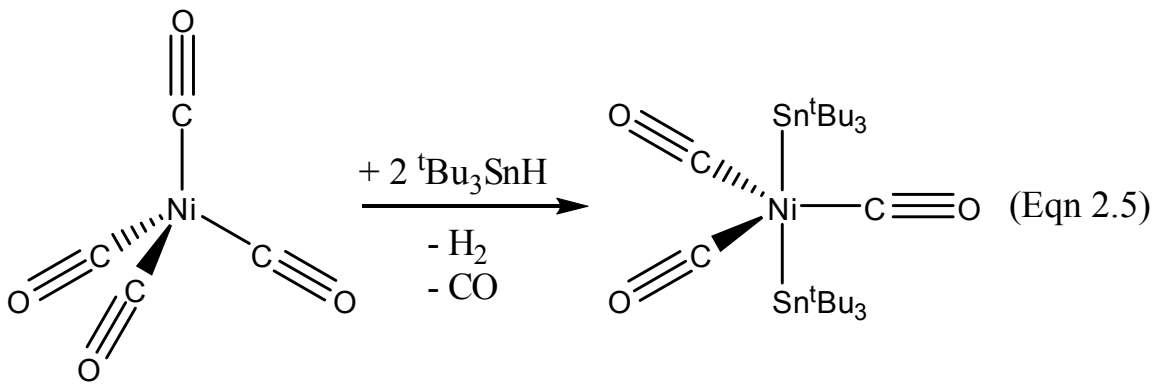

(Eqn 2.5)

There are quite a few tetrahedral and trigonal bipyramidal nickel-carbonyl complexes with bulky phosphine and carbene ligands found in the literature. However, to our knowledge this is one of the first structurally characterized examples of a Ni^{II} complex with the general formula $Ni(CO)_3(L)_2$ where the L groups are in axial positions for trigonal bipyramidal geometry.[65] Years ago Klabunde et al. prepared the complexes $Ni(SiR_3)_2(CO)_3$ (R= F, Cl) and reported the crystal structure of $Ni(SiCl_3)_2(CO)_3$, which is very similar to $Ni(Sn^tBu_3)_2(CO)_3$, both possessing D_{3h} symmetry.[66]

Due to the steric bulk of the axial Sn^tBu_3 groups, it was assumed that the CO ligands would be quite labile. However, reaction with many chemical reagents including phosphines (which are known to easily replace CO ligands in various organometallic complexes) showed no change in FTIR spectrum, even at temperatures of 110 °C in toluene solvent. This may be due to the extremely large steric cone angle of protection provided by $^tBu_3Sn$ which prevents access to the Ni center. The next chapter will revisit this complex and examine its unexpected photochemical reactivity.

Reaction of $^tBu_3SnH$ with $Fe_2(CO)_9$. Activation and functionalization of the carbon-hydrogen bonds in organic molecules by transition metal complexes has always been a major area of research in both industry and academia.[67] Useful catalysts for this purpose must clearly be selective, as many organic molecules will contain a variety of C-H bonds, such as alky and aryl. Both tin and iron have been shown to possess the ability to activate benzylic C-H bonds.[68,69] By combining the two metals, a synergistic effect may be found that enables a Fe-Sn bimetallic complex to activate benzylic C-H bonds more efficiently and selectively than either metal alone. This would be of great intellectual value to both industrial and academic fields.

The heterobimetallic Fe-Sn complex $Fe_2(\mu\text{-}Sn^tBu_2)_2(CO)_8$ was produced by reaction of $^tBu_3SnH$ and $Fe_2(CO)_9$ in heptane at 97 °C in 47 % yield, and shows apparent elimination of isobutane (H^tBu) from each tin to form $\mu\text{-}Sn^tBu_2$ ligands. This compound was first reported several years ago by the mechanistically different salt-forming reaction of $Na_2Fe(CO)_4$ and $Sn^tBu_2Cl_2$ in 50 % yield and its structure was correctly postulated based on FTIR spectroscopy and molecular weight measurements.[70] We have obtained the molecular structure of $Fe_2(\mu\text{-}Sn^tBu_2)_2(CO)_8$ by single crystal X-ray diffraction

analysis, and an ORTEP of the molecular structure is shown in Figure 2.5. Further crystallographic information is provided in Appendix A Table A.2.

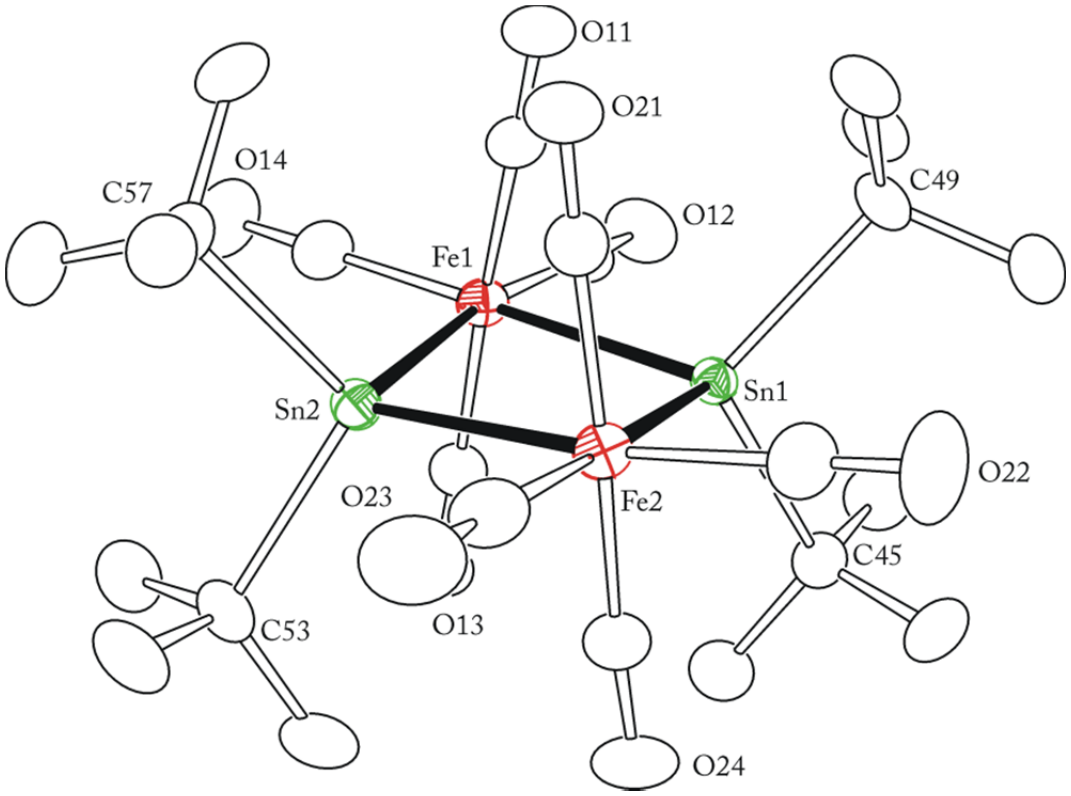

Figure 2.5 An ORTEP showing the molecular structure of $Fe_2(\mu\text{-}Sn^tBu_2)_2(CO)_8$ at 30 % thermal ellipsoid probabilities.

This structure is very similar to the known dimethyl tin analogue complex $Fe_2(\mu\text{-}SnMe_2)_2(CO)_8$.[71] The two iron atoms in $Fe_2(\mu\text{-}Sn^tBu_2)_2(CO)_8$, which are separated by 4.225(1) Å *{4.153(1) Å in molecule 2, as there are two molecules in the asymmetric unit}*, are non-bonding and similar to the iron-iron non-bonding distance in $Fe_2(\mu\text{-}SnMe_2)_2(CO)_8$ of 4.139(15) Å. Each iron atom possesses the ideal $18e^-$ count. It is worth noting that the novel spiro-tin complex $Fe_4(\mu_4\text{-}Sn)(\mu\text{-}Sn^tBu_2)_2(CO)_{16}$ is also formed in small amounts when the reaction is carried out in refluxing octane, seen in Figure 2.6

with methyl groups excluded for clarity. Further crystallographic data is provided in Appendix A Table A.3. Spiro tin ligands are not particularly common and their formation often requires thermolysis.[72] This example was generated here by complete elimination of hydride and *tert*-butyl groups presumably in the form of isobutane and isobutene, covered below.

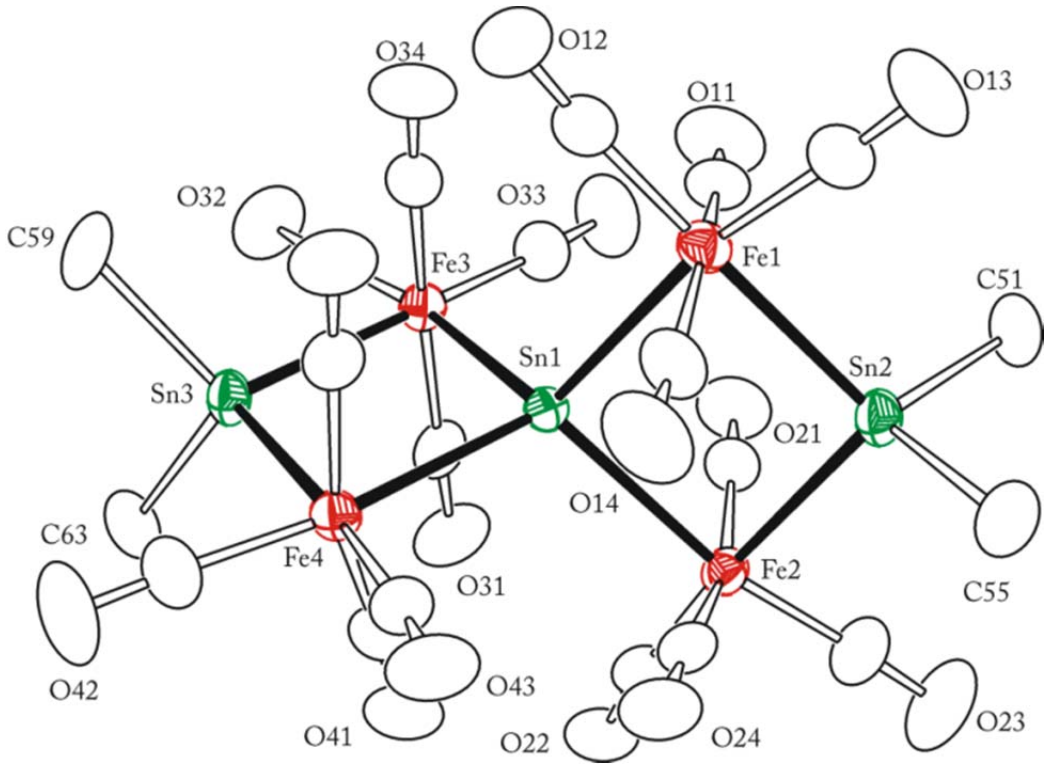

Figure 2.6 An ORTEP showing the molecular structure of $Fe_4(\mu_4\text{-}Sn)(\mu\text{-}Sn^tBu_2)_2(CO)_{16}$ at 30 % thermal ellipsoid probability. Methyl groups excluded for clarity.

When the reaction of $^tBu_3SnH$ and $Fe_2(CO)_9$ was carried out in refluxing toluene solvent (110 °C), $Fe_2(\mu\text{-}Sn^tBu_2)_2(CO)_8$ was not formed, but rather the new complex $Fe_2[\mu\text{-}Sn^tBu(CH_2Ph)]_2(CO)_8$ was obtained in very low 4 % yield. This new compound was characterized by FTIR, ^1H NMR, and single crystal X-ray diffraction analyses. An

ORTEP showing the molecular structure of $Fe_2[\mu\text{-}Sn^tBu(CH_2Ph)]_2(CO)_8$ is shown in Figure 2.7 and further crystallographic data is found in Appendix A Table A.2.

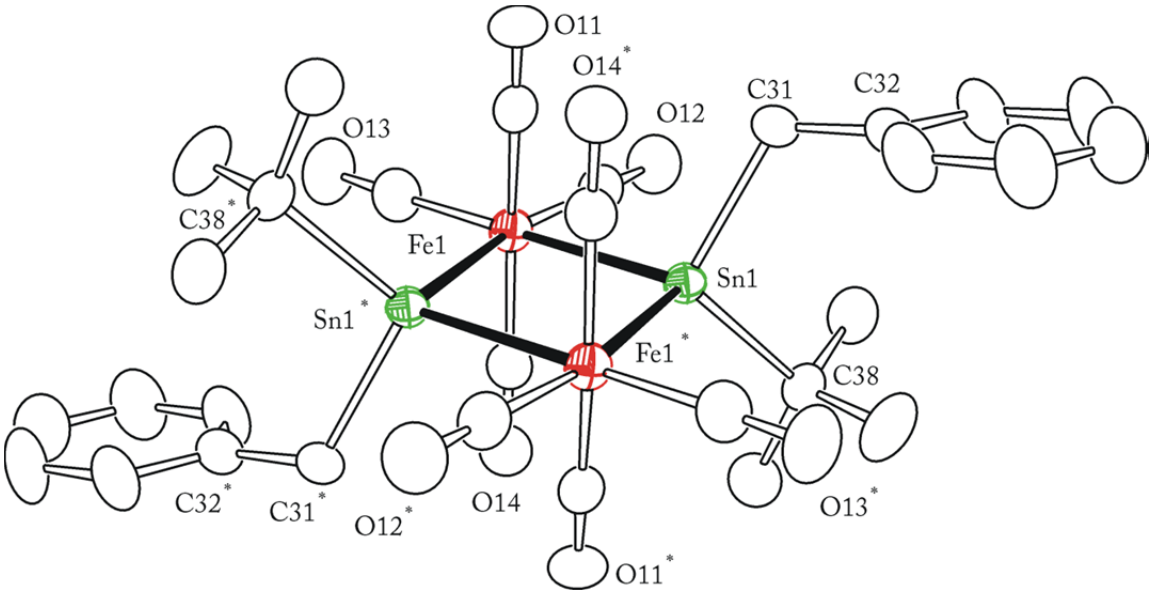

Figure 2.7 An ORTEP showing the molecular structure of $Fe_2[\mu\text{-}Sn^tBu(CH_2Ph)]_2(CO)_8$ at 30 % thermal ellipsoid probability.

It is clear from the structure of $Fe_2[\mu\text{-}Sn^tBu(CH_2Ph)]_2(CO)_8$ that two of the ^{t}Bu groups have been replaced by benzyl groups from the solvent toluene, an example of selective benzylic C-H activation. This form of bond activation and cleavage is extensively studied for its potential use in petroleum reforming and organic synthesis, and eloquent examples can be found in the literature.[73] Indeed when pure $Fe_2(\mu\text{-}Sn^tBu_2)_2(CO)_8$ is dissolved in toluene and heated to reflux, $Fe_2[\mu\text{-}Sn^tBu(CH_2Ph)]_2(CO)_8$ was obtained in a higher 21 % yield. As seen in Figure 2.7, the benzyl groups are located *trans* to one another, however ^{1}H NMR spectroscopy after TLC workup indicated the presence of another compound, believed to be the *cis* isomer complex. These 2 isomers are not able to be separated by TLC chromatography, and as

of yet we have not successfully crystalized this *cis* isomer. ^{1}H NMR spectroscopy showed the relative proportion of the two isomers to be approximately 50:50, however the *trans* isomer can be obtained in a pure form by fractional crystallization at -25 °C from methylene chloride/hexane solution mixtures.

To further study the ability of $Fe_2(\mu\text{-}Sn^tBu_2)_2(CO)_8$ to activate the benzylic C-H bond in alkylaromatic compounds, we investigated the reaction of $Fe_2(\mu\text{-}Sn^tBu_2)_2(CO)_8$ with *ortho, meta,* and *para*-xylenes. Refluxing $Fe_2(\mu\text{-}Sn^tBu_2)_2(CO)_8$ in any of these 3 solvents will afford benzylically substituted compounds similar to $Fe_2[\mu\text{-}Sn^tBu(CH_2Ph)]_2(CO)_8$, shown in Appendix A Figures A.1, A.2, and A.3. A proposed mechanism for the initial reaction of $Fe_2(\mu\text{-}Sn^tBu_2)_2(CO)_8$ in refluxing toluene with generation of isobutane is shown in Scheme 2.2, and we believe the reactions in *o, m,* and *p*-xylene proceed through nearly identical mechanisms.

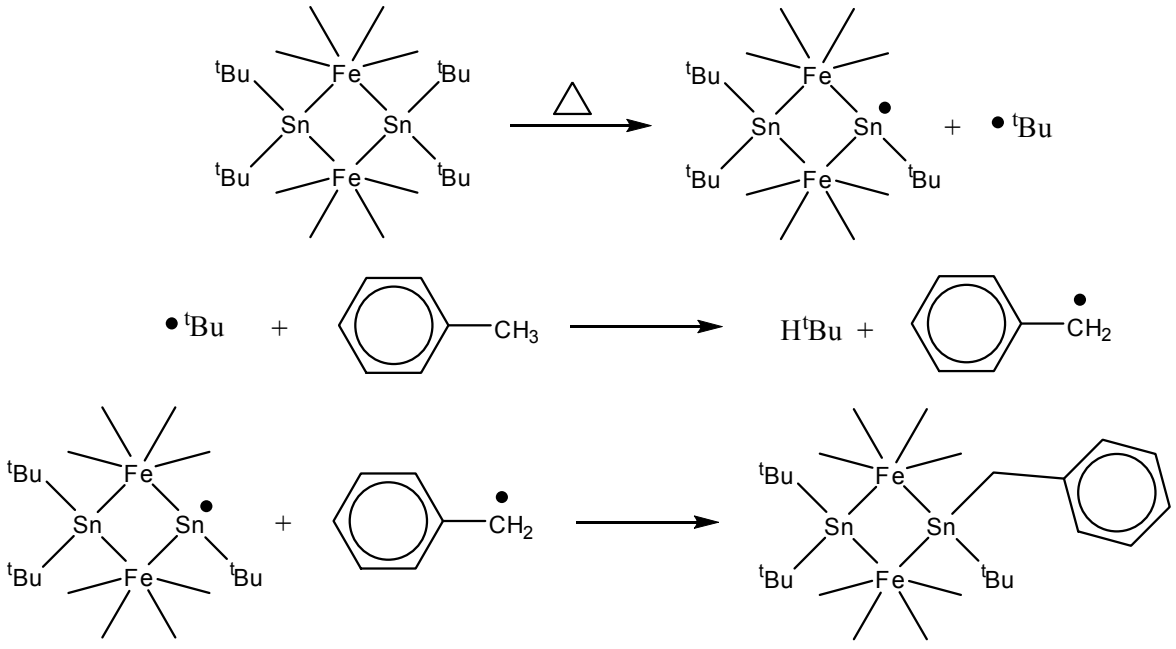

Scheme 2.2 Proposed mechanism for the initial reaction of $Fe_2(\mu\text{-}Sn^tBu_2)_2(CO)_8$ in refluxing toluene. CO ligands on Fe atoms are shown as sticks for clarity.

In fact a portion of the *ortho*, *meta,* and *para*-xylene derivatives are driven to the point of total loss of ^{t}Bu groups from tin with complete replacement by xylene ligands resulting in tetra-substituted complexes, exemplified by $Fe_2[\mu\text{-}Sn(m\text{-}CH_2PhMe)_2]_2(CO)_8$ shown in Figure 2.8. Further crystallographic information is provided in Appendix A Table A.3.

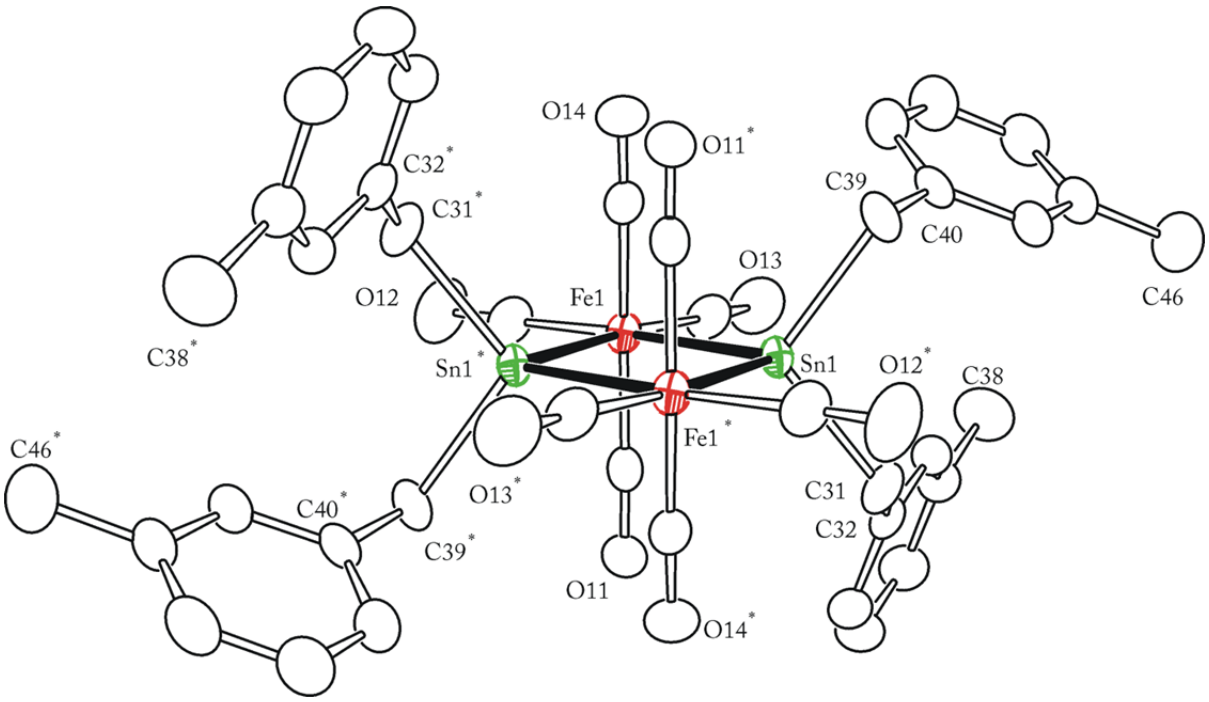

Figure 2.8 An ORTEP showing the molecular structure of $Fe_2[\mu\text{-}Sn(m\text{-}CH_2PhMe)_2]_2(CO)_8$ at 30 % thermal ellipsoid probability.

To test the proposed reaction mechanism, we sought to detect deuterated isobutane, D^{t}Bu, in reaction mixture. When reaction was carried out inside a sealed NMR tube with toluene-d_8 solvent, ^{2}H NMR showed a singlet at 1.63 ppm, appropriate for isobutane-d_1 (D^{t}Bu), as well as detectable amounts of isobutylene. It is necessary to

mention that ^{1}H NMR spectra showed large amounts of non-deuterated isobutane and isobutene as well, and this is possibly attributed to the reaction shown in equation 4.6.

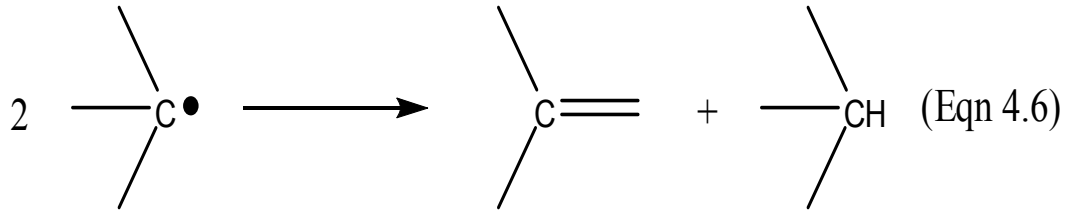

(Eqn 4.6)

Pryor and Tang also observed this disproportionation of ^{t}Bu radicals to isobutene and isobutane.[74] Furthermore, with a yield maximum of 21 %, there must be large amounts of chemical decomposition with subsequent formation of isobutane and other various products. This series of Fe-Sn complexes are some of the rare examples in the literature for C-H activation by a tin center.

These compounds were also intriguing due to the apparent initial elimination of both a ^{t}Bu and a hydride group from $^{t}Bu_3SnH$, presumably also in the form of isobutane ($H^{t}Bu$), resulting in a μ-$^{t}Bu_2Sn$ ligand somewhat resembling carbenes and stannylenes. This ability of tin hydrides to eliminate hydrogenated ligands is well known[75,76] (for instance, as benzene from Ph_3SnH), and some beautiful examples of (μ-Ph_2Sn)M compounds are available in the literature.[77,78] We were not certain at the onset of our research if the bulky $^{t}Bu_3SnH$ would behave in a similar manner (eliminating isobutane to form bridging tins), but these Fe-Sn compounds are experimental evidence in favor of similar reactivity to Ph_3SnH and other organotin hydrides.

Reaction of $^{t}Bu_3SnH$ with $Pt_2Ru_4(CO)_{18}$. Multimetallic platinum complexes have attracted a great deal of interest for decades, especially as heterogeneous alloy catalysts for the process of petroleum reforming and other organic molecule transformations.[79] Bimetallic complexes of platinum containing Fe, Co, and Os are well known and their reactions with alkynes, dihydrogen, 1,5-cyclo-octadiene and even other transition metal complexes have been extensively studied.[80]

Previous work by Adams et al. resulted in the generation of the electronically unsaturated multimetallic platinum-ruthenium cluster complex $Pt_2Ru_4(CO)_{14}$.[81] This bright violet compound has been shown to react with many ligands in interesting ways,[82] and so we sought to react it with our bulky $^{t}Bu_3SnH$. When two equivalents of tri-*tert*-butyl tin hydride was added to a solution of $Pt_2Ru_4(CO)_{18}$, the cluster was broken yielding the two new isolatable products $Pt_2Ru_2(Sn^{t}Bu_3)_2(CO)_9(\mu\text{-}H)_2$ and $Pt(Sn^{t}Bu_3)_2(CO)_2$, shown in Figures 2.9 and 2.10. Detailed crystallographic information for these two compounds is provided in Appendix A Table A.4.

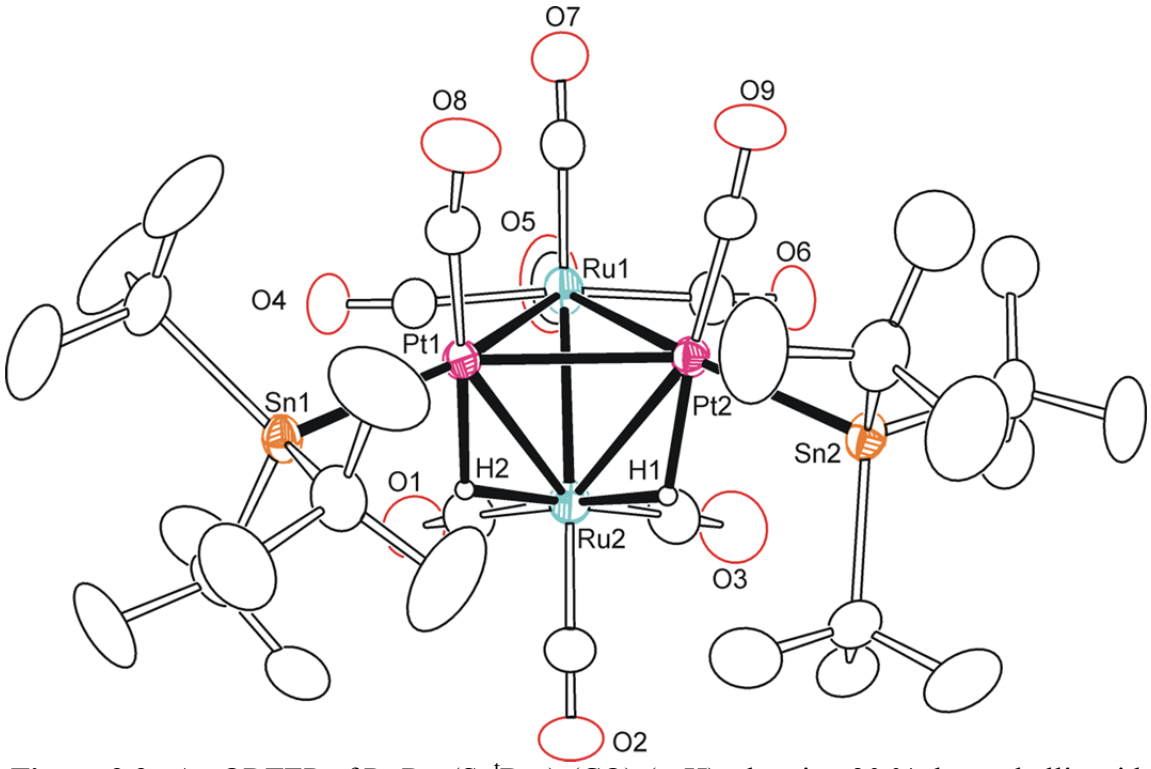

Figure 2.9 An ORTEP of $Pt_2Ru_2(Sn^tBu_3)_2(CO)_9(\mu\text{-}H)_2$ showing 30 % thermal ellipsoid probability.

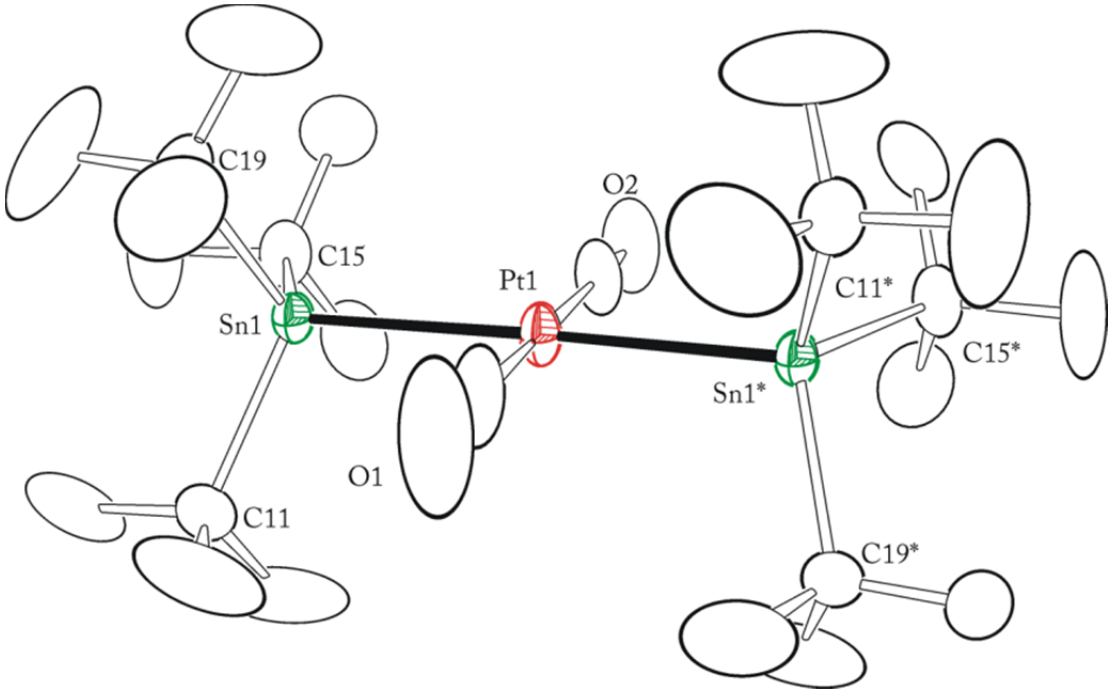

Figure 2.10 An ORTEP of $Pt(Sn^tBu_3)_2(CO)_2$ showing 30 % thermal ellipsoid probability.

The trimetallic $Pt_2Ru_2(Sn^tBu_3)_2(CO)_9(\mu\text{-}H)_2$ was our first success at transferring both tin and hydride ligands to a transition metal complex by oxidative addition, and appears to be the only characterized example of a PtRuSn compound possessing an unreduced 2:2:2 metal ratio as well as the first with a 1:1:1 ratio containing no phosphines.[83] Some of our recent collaborative work takes advantage of this specific stoichiometric ratio and will be discussed below.

There is a constant interest in reducing waste and improving yields of commodity chemicals in industrial synthesis. Without better understanding the nature of catalytic active sites and the role played by precise metal/metal stoichiometries, the development of new more effective catalysts will become increasingly difficult. It was recently reported that a series of Ru-Sn organometallic complexes with varying Ru:Sn ratios were converted to silica-supported heterogeneous nanoparticle catalysts capable of efficiently hydrogenating 1,5,9-cyclododecatriene (CDT) to cyclododecene (CDE), a very important reagent used in the production of synthetic fibers like nylon and polyester.[84] In fact, the Ru-Sn catalysts were shown to grow increasingly selective as a function of tin content.

Silica and alumina supported mixed metal heterogeneous catalysts based on platinum have long been studied for their application in petroleum reforming and other major chemical industries.[85] Much work has been done with Pt-Sn compounds, many of which are extremely active for a wide range of reactions. If the previously mentioned series of bimetallic Ru-Sn compounds are capable of useful chemistry, then the addition of platinum should afford trimetallic Pt-Ru-Sn complexes with even greater chemical potential.

Gianotti and Manzoli have studied a series of organometallic-cluster-derived silica-supported $Ru_xPt_ySn_z$ nanoparticles, including ones made from our $Pt_2Ru_2(Sn^tBu_3)_2(CO)_9(\mu\text{-}H)_2$, for their use in the hydrogenation of nitrobenzene to aniline under relatively mild conditions, shown in equation 2.7.[86]

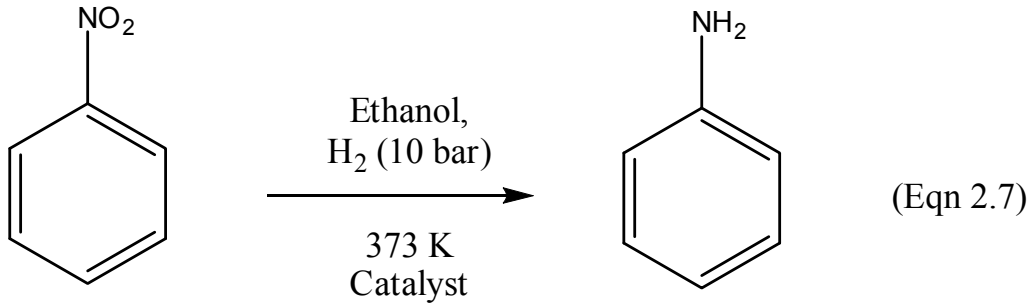

(Eqn 2.7)

Aniline is commonly used in the preparation of methylene diphenyl diisocyanates, precursors to polyurethane plastics; millions of tons of nitrobenzene are hydrogenated to aniline per year for this sole purpose.[87] The amount of resources that could be saved by a catalyst that is highly active under mild conditions is immense, totaling billions of US dollars annually.

By using organometallic compounds with proven mixed metal/metal ratios, these nanoparticle catalysts can be synthesized with very precise metal stoichiometries, as opposed to the older method of mixing single metal compounds together in desired ratios, for example 1eq $PtCl_2(PPh_3)_2$ and 2eq $SnCl_2$ to synthesize an approximated $PtSn_2$ alloy.[88] These "in-situ" generated mixed metal alloys do not produce uniform nanoparticle catalysts, and this is why utilizing organometallic complexes with precise metal stoichiometries is quickly becoming the preferred method of manufacture.

To study the role of metal synergy in mixed metal nanoparticle catalysts, 5 separate compounds were utilized with varying metal ratios of Ru:Pt:Sn and supported on mesoporous silica according to standard sintering procedure: Ph_3SnH (Sn/SiO_2), $Ru_5(\mu_5\text{-}C)(CO)_{15}$ (Ru_5/SiO_2), $PtRu_5(\mu_6\text{-}C)(CO)_{16}$ (Ru_5Pt/SiO_2), and our $Pt_2Ru_2(Sn^tBu_3)_2(CO)_9(\mu\text{-}H)_2$ ($Ru_2Pt_2Sn_2/SiO_2$). The conversion and selectivity of nitrobenzene to aniline achieved by the various metal combinations under heterogeneous conditions is shown in Figure 2.11.

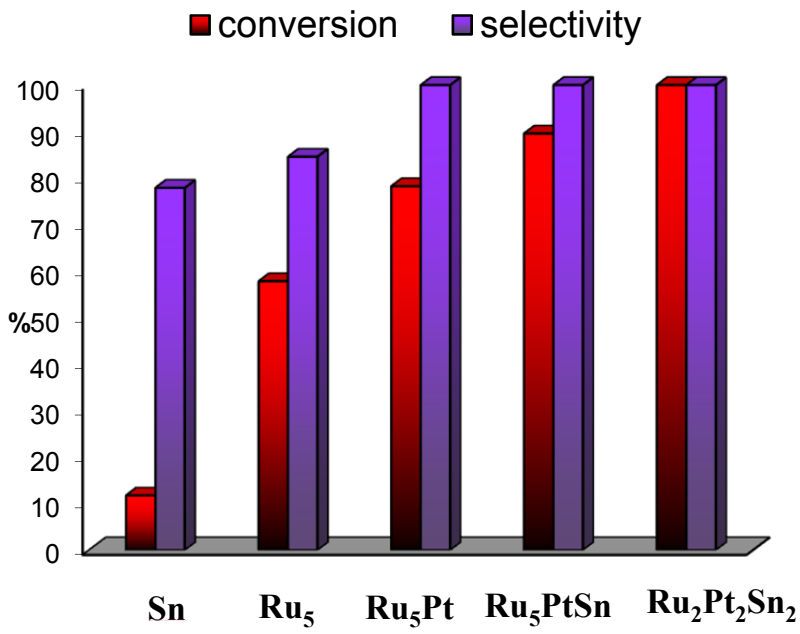

Figure 2.11 Conversions and selectivities in the hydrogenation of nitrobenzene to aniline using $Ru_xPt_ySn_z$ cluster-derived nanoparticles supported on mesoporous silica.

It is apparent from Figure 2.11 that tin by itself is virtually inactive, portraying both low conversion and poor selectivity. Clearly efficiency and selectivity increase as a function of overall mixed metal content. In fact, both conversion and selectivity were found to be optimized, nearly 100 %, for our $Ru_2Pt_2Sn_2$ complex.

Noble metals such as rhodium and platinum have long been known to improve catalytic activity of hydrogenation reactions, while tin has been used as a "promoter" in heterogeneous catalysis to increase selectivity of ruthenium-based catalysts in a variety of chemical reactions. This work highlights the future applications of multimetallic complexes containing tin and their use as heterogeneous nanoparticle catalysts for any number of possible industrial procedures.

Reaction of $^{t}Bu_3SnH$ with $Pt(COD)_2$ and CO gas. The presence of $Pt(Sn^{t}Bu_3)_2(CO)_2$ in the previous reaction mixture suggested a fracture of the $Pt_2Ru_4(CO)_{18}$ cluster, though no other metal fragments, either platinum or ruthenium, have been isolated from the reaction of $Pt_2Ru_4(CO)_{18}$ with $^{t}Bu_3SnH$. The dark green, square planar $Pt(Sn^{t}Bu_3)_2(CO)_2$ is a $16e^{-}$ Pt^{II} complex and was characterized by FTIR, NMR, elemental and X-ray crystallographic analyses. It is one of the first *electronically unsaturated* compound we generated exemplifying the use of bulky tri-*tert*-butyl tin ligands. This group 10 carbonyl complex is nothing like the $Ni(Sn^{t}Bu_3)_2(CO)_3$ product described earlier produced by reaction of $Ni(CO)_4$ with $^{t}Bu_3SnH$, and that is due to platinum's preference for a $16e^{-}$ d^8 square planar configuration as opposed to nickel's ideal 18 or 20 electron count seen in $Ni(Sn^{t}Bu_3)_2(CO)_3$.[105] Since the corresponding $Pt(CO)_4$ compound is not able to be synthesized for comparable reaction to the Ni analogue, we attempted to react $^{t}Bu_3SnH$ with 1,5-bis-cylco-octa-diene platinum, $Pt(COD_2)$, in the presence of CO gas. Indeed, there is almost instantaneous room temperature reaction of these three reagents, and the green $Pt(Sn^{t}Bu_3)_2(CO)_2$ is produced in greater than 90 % yield.

The proposed reaction of this bulky tin hydride with $Pt(COD)_2$ and CO is shown in equation 2.8. It should be noted that there is no reaction of $Ni(COD)_2$ with $^tBu_3SnH$ in a wide variety of solvents at extremes of temperature, while $Pt(COD)_2$ will react with this tin hydride rapidly at room temperature in any solvent. This exemplary difference of reactivity between Ni and Pt and will be reviewed in more detail in the next chapters.

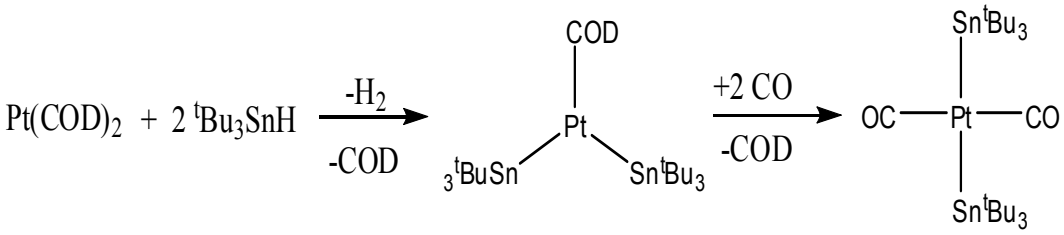

(Eqn 2.8)

2.3 Conclusions

The previously unclear synthesis of $^tBu_3SnH$ was revised and presented in a fully characterized manner. This extremely bulky organotin hydride is now able to be produced in reasonable yield with much less difficulty and its reactivity and properties will hopefully be further studied by other interested laboratories. Tri-*tert*-butyl tin hydride shows great promise as a future replacement for poisonous phosphines in organometallic chemistry, utilizing sheer steric volume to impart electronic unsaturation of metal centers by oxidative addition. This tin hydride was shown to react with transition metal complexes in manners differing from sole stannyl addition to both tin and hydride transfer at the metal center.

Cobalt carbonyl clusters were broken to give $Co(Sn^tBu_3)(CO)_4$ in good yield and the crystal structure demonstrated a capped tetrahedral structure with distorted equatorial CO ligands bent towards the axial Sn^tBu_3 group, suggesting a weakly coordinated $^tBu_3Sn^+$ cation. Nickel tetracarbonyl allowed substitution of one CO ligand for 2 *trans* $^tBu_3Sn$ groups affording the trigonal bipyramidal $Ni(Sn^tBu_3)_2(CO)_3$ which is quite different from the *cis* $Ni(SnPh_3)_2(CO)_3$ due to the superior steric bulk. Both $Co(Sn^tBu_3)(CO)_4$ and $Ni(Sn^tBu_3)_2(CO)_3$ were shown to be formed with concurrent elimination of hydrides as H_2. The complex $Ni(Sn^tBu_3)_2(CO)_3$ will be revisited in the next chapter for its unexpected photochemical reactivity.

Reaction of tri-*tert*-butyl tin hydride with $Fe_2(CO)_9$ produced the previously known $Fe_2(\mu\text{-}Sn^tBu_2)_2(CO)_8$, although in a different mechanistic fashion not making use of salt-elimination metathesis. When this Fe-Sn complex was dissolved in toluene and heated to reflux, two ^{t}Bu groups were lost and substituted with solvent toluene to give $Fe_2[\mu\text{-}Sn^tBu(CH_2Ph)]_2(CO)_8$. This compound exemplifies selective benzylic C-H activation, a property highly valued in industry and petroleum reforming. Similar reactions were found to proceed in refluxing *o, m,* and *p*-xylene. The *meta*-xylene reaction was shown to produce complete loss of ^{t}Bu ligands and substitution with four *solvent* molecules bound by benzylic C-H activation. These are among the few literature examples of C-H activation by a tin center. The reaction of tin hydride with $Fe_2(CO)_9$ also produces the novel spiral tin complex $Fe_4(\mu_4\text{-}Sn)(\mu\text{-}Sn^tBu_2)_2(CO)_{16}$ in small amounts. Importantly, this reaction showed that $^tBu_3SnH$ was able to eliminate both hydride and ^{t}Bu ligands in the form of isobutane to form bridging $\mu\text{-}Sn^tBu_2$, an ability

similar to other known tin hydrides such as benzene elimination from Ph_3SnH to form μ-$SnPh_2$.

Addition of $^tBu_3SnH$ to $Pt_2Ru_4(CO)_{18}$ gave two major products, $Pt_2Ru_2(Sn^tBu_3)_2(CO)_9(\mu\text{-}H)_2$ and $Pt(Sn^tBu_3)_2(CO)_2$. The trimetallic $Pt_2Ru_2(Sn^tBu_3)_2(CO)_9(\mu\text{-}H)_2$ was our first example of both stannyl and hydride transfer to metal complexes by oxidative addition of $^tBu_3SnH$, and it was shown to be a highly efficient and selective heterogeneous nanoparticle catalyst for hydrogenation of nitrobenzene to aniline. The square planar $Pt(Sn^tBu_3)_2(CO)_2$ was also found to be formed in good yield by reaction of $Pt(COD)_2$ with tin hydride and carbon monoxide gas at room temperature. This compound as well as the reaction of $^tBu_3SnH$ with $Pt(COD)_2$ will be briefly revisited in the next chapter.

These early experimental results indeed show that the previously unavailable $^tBu_3SnH$ is similar to other tin hydrides in reactivity, yet possesses superior bulk to any commercially available. Tri-*tert*-butyl tin hydride is apparently a bit more difficult to add to transition metal centers than other tin derivatives such as Ph_3SnH, and this is evidenced by lack of reaction with several compounds that Ph_3SnH is known to readily react with like $Ru_3(CO)_{12}$, $Os_4(CO)_{12}$, etc. Our lab continues work with $^tBu_3SnH$ and its reaction with other transition group metal complexes in hopes of generating electronically unsaturated organometallic complexes that possess useful catalytic abilities. The next chapter is focused on this tin hydride as well, specifically its reaction with $Ni(^tBuNC)_4$ and the photochemically active compound $Ni(Sn^tBu_3)_2(^tBuNC)_3$ that is produced.

2.4 Experimental

General Data. Unless otherwise stated, all reactions and crystallizations were performed under an atmosphere or Argon. Reagent grade solvents were dried by the standard procedures, freshly distilled prior to use, and degassed with argon. Infrared spectra were recorded on a Nicolet 380 FT-IR spectrophotometer. ^{1}H NMR spectra were recorded on a Bruker 400 spectrometer operating at 399.993 MHz. ^{2}H NMR were recorded on a Varian Mercury/VX 400 operating at 61.395 MHz. Elemental analyses were performed by Columbia Analytical Services (Tucson, AZ). Mass spectrometry measurements performed by direct-exposure probe using electron impact ionization (EI) were made on a VG 70S instrument at the University of South Carolina, Columbia, SC. Bis(1,5-cyclooctadiene)nickel(0), $Ni(COD)_2$, dicobalt octacarbonyl, $Co_2(CO)_8$, tetracobalt dodecacarbonyl, $Co_4(CO)_{12}$, and magnesium turnings were purchased from Strem Chemicals, used without further purification, and stored/handled in a MBraun Unilab inert atmosphere glovebox. Di-iron nonacarbonyl, $Fe_2(CO)_9$, toluene-d_8, magnesium sulfate ($MgSO_4$), sodium hydroxide (NaOH), borane (BH_3 1.7 M in THF), and concentrated aqueous hydrochloric acid (HCl/H_2O) were purchased from Sigma-Aldrich and were used without further purification. *Tert*-butyl lithium (^{t}BuLi, 1.7 M in pentane), *tert*-butyl chloride (^{t}BuCl), xylene solvents, and tin tetrachloride ($SnCl_4$) were purchased from Alfa Aesar and used without further purification. Product separations were performed by TLC in air on Analtech preparative silica gel GF 250 or 500 μm glass plates. Silica gel (60-200μm, 70-230 mesh) used for column chromatography separations was purchased from Silicycle. $Pt(COD)_2$ was synthesized according to literature procedure.[89]

Synthesis of $^{t}Bu_3SnH$. The individual synthetic details presented below were modified appropriately by making use of several combined literature procedures mentioned earlier. At times, $^{t}Bu_3SnCl_2$ was purchased from Strem Chemicals to avoid initial synthesis of di-*tert*-butyl tin dichloride.

Conversion of $SnCl_4$ to $^{t}Bu_2SnCl_2$

30 g of magnesium turnings (1.25 mol) and 600 mL of distilled tetrahydrofuran were added to a 1000 mL 3-neck flask equipped with a stir bar, gas inlet, water cooled condenser, and 250 mL dropping funnel. The system was evacuated and filled with argon three times and 92 g of *tert*-butyl chloride (1 mol) was added to the dropping funnel. A very small amount of Iodine crystals were added to the THF/Mg solution to act as indicator/initiator. When the brown color was no longer present, the *tert*-butyl chloride was added drop-wise over a period of 2 hours to prevent overheating. The reaction provided 1 mol of *tert*-butyl magnesium chloride Grignard.

600 mL of distilled hexane was added to a 2000 mL 3-neck flask equipped with a stir bar, gas inlet, water cooled condenser, and a 1000 mL dropping funnel. The system was evacuated and filled with argon three times, and then 120 g of $SnCl_4$ (0.464 mol, d= 2.26 g/mL) was added to the hexane solution by syringe. NOTE: Care must be taken to prevent oxygen and water contamination as these will decompose the tin chloride very readily, leaving white solid and HCl gas in the reaction flask. The previously synthesized Grignard was then transferred via cannula to the dropping funnel and added dropwise, during which time the reaction mixture became chalky white as magnesium chloride precipitated. The mixture was then heated to reflux for 2 hours. After cooling, the

contents of the flask were added to a 2000 mL separatory funnel along with 400 mL of dilute HCl/H_2O. The aqueous layer was then removed and the organic layer washed twice more with 400 mL of deionized water. Evaporation of the organic layer provided a yellow oil that was then vacuum distilled with mild heating to afford 44 g of white, solid $^t Bu_2SnCl_2$ (0.145 mol). ^{1}H NMR (C_6D_6 in ppm): δ = 1.17 (s, 18H, ^{t}Bu, $^3J_{117Sn-H}$ = 111 Hz, $^3J_{119Sn-H}$ = 116 Hz).

Conversion of $^t Bu_2SnCl_2$ to $^t Bu_3SnCl$

A 44 g amount of $Bu^t{}_2SnCl_2$ (0.145 mol) and 600 mL of distilled hexane were added to a 1000 mL sidearm Schlenk flask equipped with a 100 mL dropping funnel. The system was evacuated and filled with argon three times and cooled in ice bath. 85 mL of 1.7 M *tert*-butyl lithium/pentane solution was added to the dropping funnel by cannula and added dropwise very slowly (~ 1h). The reaction was allowed to warm to room temperature while stirring for another hour after all of the *tert*-butyl lithium was added. The solution was placed in a 1000 mL separatory funnel and washed with 400 mL of dilute HCl/H_2O. The aqueous layer was removed and the organic layer was washed two more times with 400 mL of deionized water. Evaporation of the organic layer resulted in a yellow oil which was then vacuum distilled to give 24 g of clear, liquid $^t Bu_3SnCl$ (0.074 mol). ^{1}H NMR (C_6D_6 in ppm): δ = 1.26 (s, 27H, ^{t}Bu, $^3J_{117Sn-H}$ = 70 Hz, $^3J_{119Sn-H}$ = 74 Hz).

Conversion of $^{t}Bu_3SnCl$ to $^{t}Bu_3SnOH$

A 24 g amount of Bu^{t}_3SnCl (0.074 mol) and 500 mL of diethyl ether were added to a 1000 mL round bottom flask equipped with a stir bar. 10 g of NaOH and 100 mL of deionized water were mixed together and allowed to cool before adding the $NaOH/H_2O$ mixture to the tin/ether solution. The mixture was vigorously stirred for three hours. The mixture was then transferred to a 1000 mL separatory funnel and the aqueous layer was removed. The organic layer was washed two times with 300 mL of deionized water, dried over magnesium sulfate, and evaporated to give 20 g of white, solid $^{t}Bu_3SnOH$ (0.065 mol). ^{1}H NMR (C_6D_6, in ppm): δ = 1.24 (s, 27H, ^{t}Bu, $^{3}J_{117Sn\text{-}H}$ = 64 Hz, $^{3}J_{119Sn\text{-}H}$ = 67 Hz).

Conversion of $^{t}Bu_3SnOH$ to $^{t}Bu_3SnH$

A 20 g amount of $^{t}Bu_3SnOH$ and 500 mL of distilled tetrahydrofuran were added to a 1000 ml three-neck flask equipped with a stir bar, 100 mL dropping funnel, reflux condenser and gas inlet. The system was evacuated and filled with argon three times. 65 mL of 1 M borane solution (BH_3 in THF) were syringed into the dropping funnel and added dropwise. After all of the borane was added, the reaction mixture was heated to reflux for 1 hour. The volatiles were then removed in *vacuo* and the residual contents of the flask were re-dissolved in 500 mL of diethyl ether and transferred to a separatory funnel. The ether solution was then washed two times with 100 mL of deionized water, dried over magnesium sulfate, and evaporated to give 18 g of clear, liquid $^{t}Bu_3SnH$ (0.062 mol). A percent yield of 13 % was obtained based on moles of tin. ^{1}H NMR

(C_6D_6 in ppm): δ = 1.29 (s, 27H, ^{t}Bu, $^3J_{117Sn-H}$= 57 Hz, $^3J_{119Sn-H}$= 60 Hz), 5.59 (s, 1H, hydride, $^1J_{117Sn-H}$= 1324 Hz, $^1J_{119Sn-H}$= 1387 Hz).

Synthesis of $Co(Sn^tBu_3)(CO)_4$. In a Schlenk flask, 35 mg (0.102 mmol) of $Co_2(CO)_8$ and 65 mg (0.22 mmol) of $^tBu_3SnH$ were dissolved in 25 mL of diethyl ether by stirring and heated to reflux for 40 minutes resulting in a color change from orange to light yellow. The volatiles were removed in vacuo and the solid residue was redissolved in methylene chloride and filtered through a plug of silica gel. A 75 mg amount of light-yellow crystalline solid $Co(Sn^tBu_3)(CO)_4$ (80 % yield) can be obtained by fast evaporation of solvent under argon flow at room temperature. This complex can also be formed in 35 % yield by the reaction of $Co_4(CO)_{12}$ with $^tBu_3SnH$ in refluxing toluene after 3 hours followed by similar workup. Spectral data for $Co(Sn^tBu_3)(CO)_4$: FTIR ν_{CO} (cm^{-1} in hexane): 2077 (m), 2015 (m), 1985 (s). ^{1}H NMR (C_6D_6 in ppm): δ= 1.35 (s, 27H, ^{t}Bu, $^3J_{Sn-H}$= 67 Hz). Elemental Analysis: Calculated- C 41.56 %, H 5.89 %. Found- C 41.67 %, H 5.76 %.

Synthesis of $Ni(Sn^tBu_3)_2(CO)_3$. In a Schlenk flask, 50 mg (0.18 mmol) of $Ni(COD)_2$ and 105 mg (0.36 mmol) were dissolved in 20 mL of heptane by stirring. The solution was purged with carbon monoxide (CO) gas while being heated to reflux for 30 min resulting in a color change from colorless to light pink to dark yellow. The volatiles were removed in vacuo and the solid residue was redissolved in methylene chloride and filtered through a plug of silica gel. A 65 mg amount (50 % yield) of light-yellow

crystalline $Ni(Sn^tBu_3)_2(CO)_3$ can be obtained by fast evaporation of solvent under argon flow at room temperature. This complex can also be formed in 46 % yield at room temperature after 18 hours. Spectral data for $Ni(Sn^tBu_3)_2(CO)_3$: FTIR ν_{CO} (cm^{-1} in hexane): 1991. ^1H NMR ($CDCl_3$ in ppm): δ= 1.41 (s, 54H, ^{t}Bu, $^3J_{Sn-H}$= 62 Hz). EI/MS: m/z 722 (M^+), 665 ($M^+ - C_4H_9$), 609 ($M^+ - C_4H_9$ -2CO). The isotope pattern is consistent with the presence of one nickel atom and two tin atoms.

Synthesis of $Fe_2(\mu\text{-}Sn^tBu_2)_2(CO)_8$. In a Schlenk flask, 280 mg (0.77 mmol) of $Fe_2(CO)_9$ and 460 mg (1.58 mmol) were dissolved in 50 mL of heptane by stirring and heated to reflux for 20 minutes. The volatiles were removed in *vacuo* and the solid residue was redissolved in methylene chloride and filtered through a plug of silica gel. A 258 mg amount (41 % yield) of light-yellow crystalline $Fe_2(\mu\text{-}Sn^tBu_2)_2(CO)_8$ can be obtained by fast evaporation of solvent under argon flow at room temperature. Spectral data for $Fe_2(\mu\text{-}Sn^tBu_2)_2(CO)_8$: FTIR ν_{CO} (cm^{-1} in hexane): 2038 (s), 1990 (m), 1970 (s). ^1H NMR (C_6D_6 in ppm): δ= 1.54 (s, 36H, ^{t}Bu, $^3J_{Sn-H}$= 79 Hz). Complete spectroscopic data for all associated compounds made from *o, m,* and *p*-xylenes is provided elsewhere.[90]

Synthesis of $Fe_2(\mu\text{-}Sn^tBu[CH_2Ph])_2(CO)_8$. In a Schlenk flask, 30 mg (0.082 mmol) of $Fe_2(CO)_9$ and 50 mg (0.17 mmol) of $Bu^t{}_3SnH$ were dissolved in 10 mL of toluene by stirring and then heated to reflux for 3 hours. After 3 hours, FTIR spectroscopy showed complete consumption of the starting material. The volatiles were

removed *in vacuo* and the solid residue product was separated by TLC using hexane solvent to afford 3.1 mg (4 % yield) of colorless product. ^{1}H NMR indicates the presence of another resonance which is attributed to the *cis* isomer, which we are not able to separate by chromatography. Spectral data for $Fe_2(\mu\text{-}Sn^tBu[CH_2Ph])_2(CO)_8$: FTIR ν_{CO} (cm^{-1} in hexane): 2044 (vs), 1997 (m), 1992 (w), 1980 (s). ^{1}H NMR (toluene-d_8 in ppm): δ = 7.27-6.98 (m, 10H, Ph), 3.44 (s, 4H, CH_2, $^{2}J_{Sn\text{-}H}$ = 34 Hz), 1.31(s, 18H, ^{t}Bu, $^{3}J_{117Sn\text{-}H}$ = 94 Hz, $^{3}J_{119Sn\text{-}H}$= 97 Hz). Elemental Analysis: Calculated- C 41.43 %, H 3.71 %. Found- C 41.12 %, H 3.97 %. Complete syntheses and spectroscopic data for all associated compounds made from *o, m,* and *p*-xylenes are provided elsewhere.[91]

Synthesis of $Pt_2Ru_2(Sn^tBu_3)_2(CO)_9(\mu\text{-}H)_2$. In a Schlenk flask, 50 mg (0.038 mmol) of $Pt_2Ru_4(CO)_{18}$ and 50 mg (0.17 mmol) were dissolved in 25 mL of hexane by stirring and heated to reflux for 45 minutes. The volatiles were removed in vacuo and the solid residues were separated by TCL in air using hexane solvent to afford 24 mg (44 % yield) of brown $Pt_2Ru_2(Sn^tBu_3)_2(CO)_9(\mu\text{-}H)_2$ and 22 mg of starting $Pt_2Ru_4(CO)_{18}$. The dark green $Pt(Sn^tBu_3)_2(CO)_2$ was also formed in small yield, and its alternate synthesis is reported next. NOTE: increasing the reaction time leads to considerable decomposition and decreased yield of final product. Spectral data for $Pt_2Ru_2(Sn^tBu_3)_2(CO)_9(\mu\text{-}H)_2$: FTIR ν_{CO} (cm^{-1} in hexane): 2087 (m), 2060 (vs), 2037 (s), 2029 (w, sh), 2019 (m), 1999 (w), 1959 (w). ^{1}H NMR (C_6D_6 in ppm): δ= 1.38 (s, 54H, ^{t}Bu, $^{3}J_{Sn\text{-}H}$ = 63 Hz), -10.48 (s, 2H, hydride, $^{1}J_{Pt\text{-}H}$= 745 Hz, $^{2}J_{Pt\text{-}H}$= 32 Hz, $^{2}J_{Sn\text{-}H}$= 11 Hz). ELEMENTAL ANALYSIS: Found- C 28.23 %, H 4.47 %. Calculated- C 27.78 %, H 3.95 %.

Synthesis of $Pt(Sn^tBu_3)_2(CO)_2$. In a Schlenk flask, 53 mg (0.128 mmol) of $Pt(COD)_2$ and 80 mg (0.274 mmol) of $^tBu_3SnH$ were dissolved in 10 mL of hexane by stirring, at which time CO gas was purged through the solution for 30 minutes. A color change to dark green occurred, and the volatiles were removed in *vacuo*. The solid residues were redissolved in methylene chloride, filtered through a plug of silica gel, and evaporated under flow of argon to yield 98 mg (91 % yield) of $Pt(Sn^tBu_3)_2(CO)_2$. Spectral data for $Pt(Sn^tBu_3)_2(CO)_2$: ^{1}H NMR ($CDCl_3$ in ppm): δ = 1.38 (s, 54 H, ^{t}Bu, $^3J_{Sn\text{-}H}$ = 59 Hz. ^{1}H NMR (C_6D_6 in ppm): δ = 1.44 (s, 54 H, ^{t}Bu$_3$, $^3J_{Sn\text{-}H}$ = 59 Hz. FTIR ν_{CO} (cm^{-1} in hexane): 2007 (vs). Elemental Analysis: Calculated- C 37.56 %, H 6.54 %. Found- C 37.77 %, H 6.42 %.

Crystallographic Analyses. All single crystals in this chapter were grown by slow evaporation of methylene chloride/hexane solutions at -25 °C and glued to a thing glass fiber for data collection at room temperature in air. The only exception is $Co(Sn^tBu_3)(CO)_4$ which was grown by slow evaporation of a diethyl ether solution at -25 °C and mounted on a thing glass fiber with Paratone-N for data collection at 100 K under flow of nitrogen. X-ray intensity data were measured by using a Bruker SMART APEX2 CCD-based diffractometer using Mo Kα radiation (λ = 0.71073 Å).[92] The raw data frames were integrated with the SAINT+ program by using a narrow-frame integration algorithm.[93] Corrections for Lorentz and polarization effects were also applied with SAINT+. An empirical absorption correction based on the multiple measurement of equivalent reflections was applied using the program SADABS. All structures were solved by a combination of direct methods and difference Fourier syntheses, and refined

by full-matrix least-squares on F^2 by using the SHELXTL software package.[93] All non-hydrogen atoms were refined with anisotropic displacement parameters. Hydrogen atoms were placed in geometrically idealized positions and included as standard riding atoms during the least-squares refinements. Crystal data, data collection parameters, and results of the analyses are listed in Appendix A Tables A.1-A.4.

Single crystals of $Co(Sn^tBu_3)(CO)_4$ crystallized in the monoclinic crystal system. The systematic absences in the intensity data were consistent with the unique space group $P2_1/n$. The data was collected at 100 K under nitrogen as these crystals slowly decompose at room temperature in air.

Single crystals of $Ni(Sn^tBu_3)_2(CO)_3$ crystallized in the monoclinic crystal system. The systematic absences in the intensity data were consistent with the unique space group $P2_1/c$.

Single crystals of $Fe_2(\mu\text{-}Sn^tBu_2)_2(CO)_8$ crystallized in the triclinic crystal system. The space group $P\ \bar{1}$ was assumed and confirmed by the successful refinement and solution of the structure.

Single crystals of $Fe_2[(\mu\text{-}Sn^tBu)(CH_2Ph)](CO)_8$ crystallized in the triclinic crystal system. The space group $P\ \bar{1}$ was assumed and confirmed by the successful refinement and solution of the structure.

Single crystals of $Fe_2[\mu\text{-}Sn(m\text{-}CH_2PhMe)_2]_2(CO)_8$ crystallized in the triclinic crystal system. The space group $P\ \bar{1}$ was assumed and confirmed by the successful refinement and solution of the structure.

Single crystals of $Fe_4(\mu_4\text{-}Sn)(\mu\text{-}Sn^tBu_2)_2(CO)_{16}$ crystallized in the triclinic crystal system. The space group $P\bar{1}$ was assumed and confirmed by the successful refinement and solution of the structure.

Single crystals of $Pt_2Ru_2(Sn^tBu_3)_2(CO)_9(\mu\text{-}H)_2$ crystallized in the triclinic crystal system. The space group $P\bar{1}$ was assumed and confirmed by the successful refinement and solution of the structure. All non-hydrogen atoms were refined successfully with isotropic thermal parameters. The hydrido ligands were located and refined successfully with isotropic thermal parameters.

Single crystals of $Pt(Sn^tBu_3)_2(CO)_2$ crystallized in the monoclinic crystal system. The systematic absences in the intensity data were consistent with the unique space group $C2/c$.

Chapter 3: Photochemical Synthesis, Characterization, and Reactivity study of the Nickel-Tin Dimer $[Ni(Sn^tBu_3)(^tBuNC)_2(CO)]_2$: Radical Generation and Small Molecule Activation.

3.1 Background

The world's dependence on precious metals for a wide variety of catalytic applications is quickly becoming a problem of both supply and demand.[94,95] The need for effective, less expensive and more easily attainable alternatives grows every day. Major industrial stock chemicals such as cyclododecene (CDE) are typically produced by selective hydrogenation of a corresponding starting substrate, 1,5,9-cyclododecatriene (CDT) in this case. Platinum and palladium are the catalysts of choice for many of these important hydrogenation reactions, as well as performing countless other types of chemical transformations, though their selectivity is normally less than ideal.[96] Clearly a suitable alternative to these precious metal catalysts will be required in the near future as global growth begins to accelerate exponentially.

Bimetallic complexes have been shown to be effective catalysts for many processes such as preferential oxidation of carbon monoxide;[97] however many of these compounds still contain the aforementioned precious metals, platinum and palladium. Adams et al. recently showed that bimetallic ruthenium-tin complexes were not only efficient nanocluster catalysts for the hydrogenation of CDT, but also grow increasingly more selective as a function of overall tin content.[96] In fact, tin is known to be an excellent modifier of heterometal catalytic properties, as well as possessing certain catalytic abilities itself.[98] The last chapter portrayed how nitrobenzene can be efficiently

and selectively converted to aniline by heterogeneous nanoparticles created from our trimetallic $Pt_2Ru_2Sn_2$ hydride cluster complex, an ode to tin's ability to modify and improve heterometal chemical reactivity. It is with these results in mind that we have set our goals on discovering bimetallic compounds containing tin and "cheaper" transition metals with known catalytic potential for future use in any of the major fields of industrial catalysis.

Nickel, found above platinum and palladium, is known for its own ability to conduct many important chemical reactions including hydrogenation.[99] Raney nickel is a solid catalyst consisting of nickel-aluminum alloy and finds use in many industrial hydrogenation processes.[100] More recently it is used as a heterogeneous catalyst in a variety of organic syntheses, most notably hydrogenation by H_2 activation and transfer.[101] In nature, organometallic nickel plays a vital role in the essential enzymes CO-dehydrogenase, acetyl-CoA synthase, [NiFe] hydrogenase, methyl-CoM reductase, urease, and Ni SOD.[102] Nickel-tin compounds have been shown to catalyze both the oxidation of CO as well as the dehydrogenation of cyclohexene.[103,104] Nickel is abundantly found in the Earth's crust primarily in ores and minerals such as limonite, garnierite, and pentlandite. Nickel metal is available at almost $1/1000^{th}$ the price of platinum and palladium.

A select few organometallic nickel compounds have even shown the ability to react with light.[105] The very interesting cluster complex $Ni_3(\mu_3\text{-}I)_2(dppm)_3$, synthesized by Kubiak et al., was shown to undergo oxidative photochemical transformation to its corresponding radical cation shown in equation 3.1.

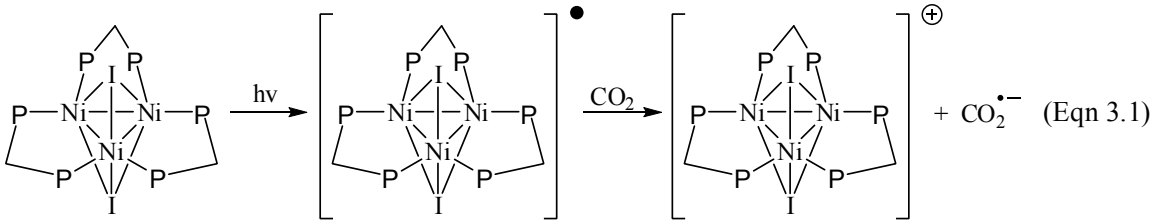

This energetic species was then able to transfer its lone electron to effectively reduce CO_2, yielding the radical anion $CO_2^{\bullet -}$, followed by addition to cyclohexene. This reaction selectively produces the industrial feedstock chemical 1,2-cyclohexanedicarboxylic acid which is an important plasticizer for the manufacture of flexible plastic articles, most notably in the medical and food packaging fields. Photochemical activation and transformation of abundant atmospheric gasses like CO_2, O_2, and N_2 into useful chemical products may play a large role in future technologies.

This chapter will highlight our efforts at generating reactive Ni-Sn organometallic compounds that contain our bulky $^tBu_3Sn$ ligands. By focusing on these two abundant metals, we hope to learn more about the synergistic effects produced within heterobimetallic complexes. If we can synthesize complexes with varying metal to metal ratios, future research may be able to put such compounds to use as heterogeneous nanoparticles in experiments that check for unexpected catalytic ability. Reported herein is our work with a series of Ni-Sn complexes possessing the general formula $Ni(Sn^tBu_3)_2(^tBuNC)_x(CO)_{3-x}$ where x can equal 3, 2, 1, and 0. These compounds are all structurally similar and photoactive, yet behave in very different manners at varying temperatures.

3.2 Results and Discussion

In the last chapter, we showed that $Ni(CO)_4$ will react with two equivalents of $^tBu_3SnH$ to afford the complex $Ni(Sn^tBu_3)_2(CO)_3$. The nickel tetracarbonyl was generated in situ by reaction of 1,5-bis-cyclo-octadiene nickel, $Ni(COD)_2$, with carbon monoxide gas in hexane solvent. However in the absence of CO gas, $Ni(COD)_2$ will simply not react with $^tBu_3SnH$. Attempted reaction of these two chemicals in all manners of solvents and at a wide range of temperatures was carried out to no avail. Clearly, the nickel metal requires initial activation by reaction with another reagent such as CO to become more susceptible to oxidative addition of $^tBu_3SnH$.

Also stated in the previous chapter, the complex $Pt(Sn^tBu_3)_2(CO)_2$ was prepared by reaction of $Pt(COD)_2$ and 2eq $^tBu_3SnH$ under and atmosphere of CO. However, the reaction of $Pt(COD)_2$ and $^tBu_3SnH$ will proceed without the addition of carbon monoxide, evidenced by a rapid color change. This is a good example portraying the vast difference in chemical reactivity of Pt and Ni, the primary reason metals such as platinum and palladium are found in so many industrial catalysts. One equivalent of $Pt(COD)_2$ and tri-*tert*-butyl tin hydride will react almost instantaneously even at low temperatures to give the unsaturated hydride complex $Pt(COD)(Sn^tBu_3)(H)$, seen in Figure 3.1.

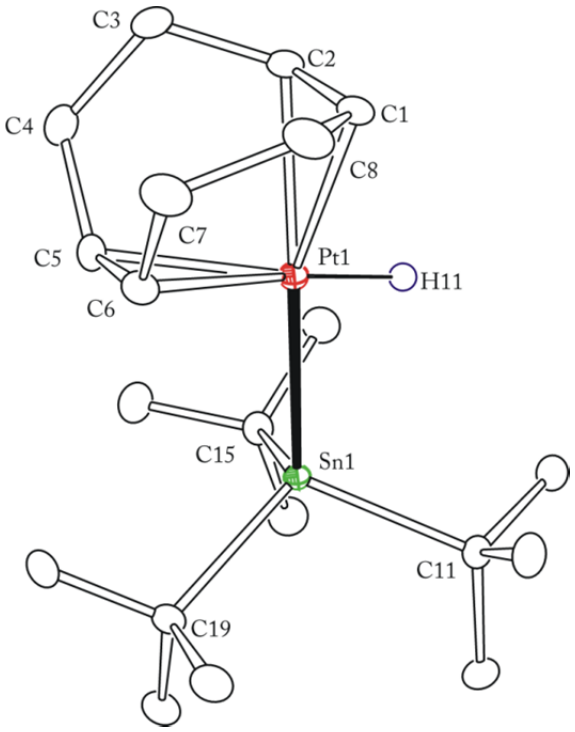

Figure 3.1 An ORTEP showing the molecular structure of Pt(COD)(Sn^{t}Bu$_3$)(H) at 30 % thermal ellipsoid probability.

Simple unsaturated Pt-Sn complexes like Pt(COD)(Sn^{t}Bu$_3$)(H) that contain only tin, hydrocarbons, and hydride ligands are exactly what our lab desired from this reaction. However, the nickel analogue of this beautiful platinum-tin-hydride compound does not exist. Pt(COD)(Sn^{t}Bu$_3$)(H) appears to even add a second equivalent of tin-hydride while eliminating a molecule of dihydrogen, seen in Scheme 3.1, to give Pt(COD)(Sn^{t}Bu$_3$)$_2$.

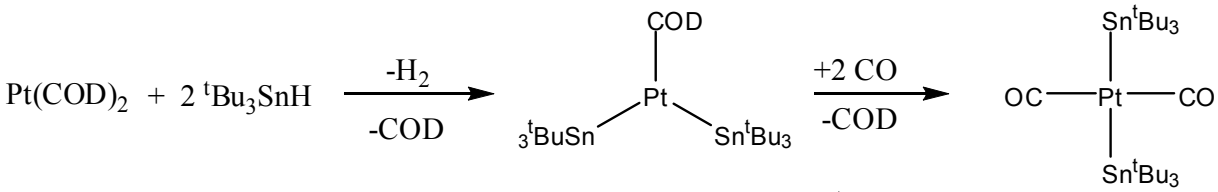

Scheme 3.1 Line drawing for the reaction of Pt(COD)$_2$ with ^{t}Bu$_3$SnH and CO gas.

We believe it is this intermediate complex $Pt(COD)(Sn^tBu_3)_2$ that exists in solution and reacts with CO to yield the dark green $Pt(Sn^tBu_3)_2(CO)_2$, also shown in equation 3.2, and there is literature evidence to support this non-isolated compound.[96] However, reacting 2eq of tin and 1eq of platinum under an argon atmosphere will ultimately yield only crystals of the Pt-Sn dimer $Pt_2(\mu\text{-}Sn^tBu_2)_2(Sn^tBu_3)_2(\mu\text{-}H)_2$, seen in Figure 3.2. This Pt-Sn dimer has eliminated ^{t}Bu groups from tin similar to last chapter's $Fe(\mu\text{-}Sn^tBu_2)_2(CO)_8$ and thus can no longer react with CO to give $Pt(Sn^tBu_3)_2(CO)_2$, but will rather yield the dimeric $Pt_2(\mu\text{-}Sn^tBu_2)_2(Sn^tBu_3)_2(CO)_2$, shown in Appendix B Figure B.1 which possesses a single CO per platinum and maintains the Pt-Pt bond.

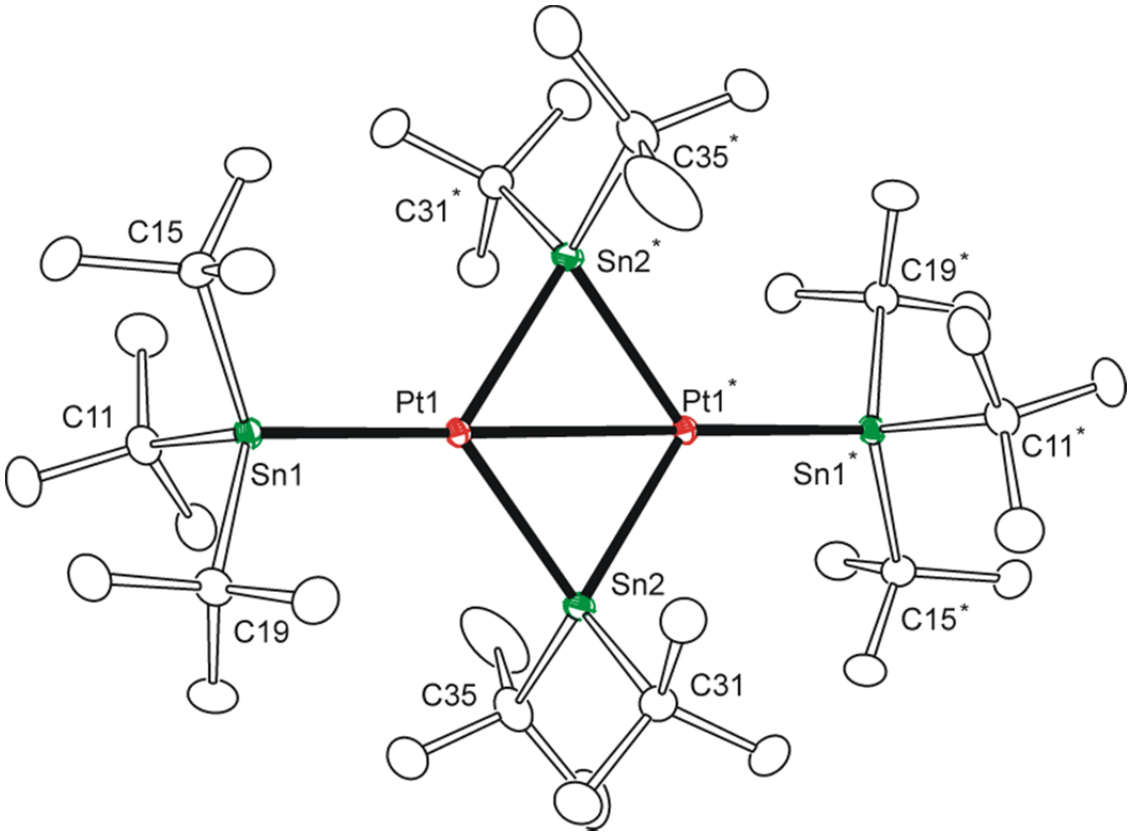

Figure 3.2 An ORTEP showing the molecular structure of $Pt_2(\mu\text{-}Sn^tBu_2)_2(Sn^tBu_3)_2(\mu\text{-}H)_2$ at 30 % thermal ellipsoid probability. Hydrides are not shown.

When 2eq of the bulky *tert*-butyl isocyanide, ^{t}BuNC, was substituted for CO in the reaction mixture, the magenta Pt-Sn complex $Pt(Sn^{t}Bu_3)_2(^{t}BuNC)_2$ was formed. This remarkable compound, discovered and studied in our lab by Veeranna Yempally and Dr. Lei Zhu, was then found to reversibly add and eliminate H_2 in a facile manner at room temperature, even in the solid state, shown in Figure 3.3.[106] In fact, an assortment of reactive platinum-tin complexes have been generated and studied by Veeranna and Lei possessing the bulky $^{t}Bu_3Sn$ ligand, including those above, and several of these also exhibit reversible hydrogen activation which is a more than rare chemical ability.

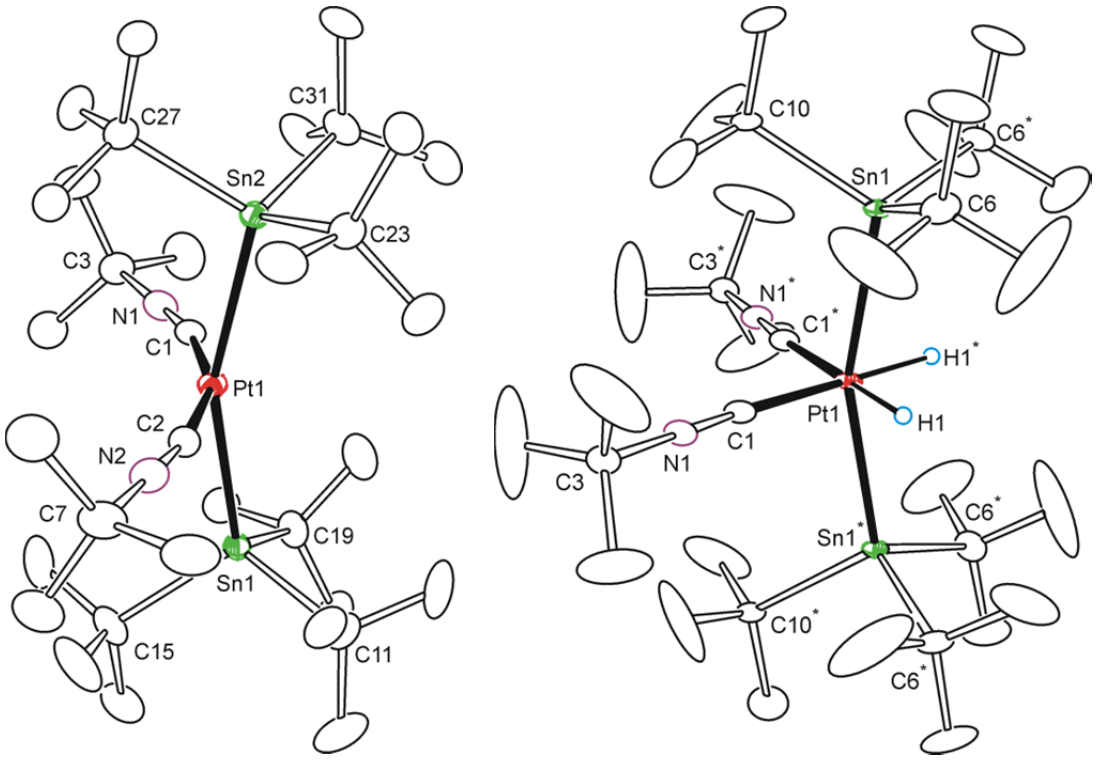

Figure 3.3 ORTEPs showing the reversible molecular structures of $Pt(Sn^{t}Bu_3)_2(^{t}BuNC)_2$ (left) and $Pt(Sn^{t}Bu_3)_2(^{t}BuNC)_2(H)_2$ (right) at 30 % thermal ellipsoid probability.

The non-hydride complex $Pt(Sn^tBu_3)_2(^tBuNC)_2$ is electronically similar to $Pt(Sn^tBu_3)_2(CO)_2$ though the bulky isocyanides force geometrical distortion from square planarity as evidenced by the "X" shape seen around platinum in Figure 3.3. The sterically induced symmetry distortion is possibly responsible for this Pt-Sn complex's remarkable properties. $Pt(Sn^tBu_3)_2(CO)_2$ has not shown similar reactivity to $Pt(Sn^tBu_3)_2(^tBuNC)_2$ as far as hydrogen activation, most likely attributable to the non-bulky CO ligands which allow a perfectly planar arrangement that is stable and preferred for $16e^-$ Pt. Having seen these very promising Pt-Sn results portrayed in Figure 3.3 we sought to react $Ni(COD)_2$ and $^tBu_3SnH$ in the presence of ^{t}BuNC with hopes of generating an unsaturated Ni-Sn compound similar to $Pt(Sn^tBu_3)_2(^tBuNC)_2$ capable of small molecule activation.

Reaction of $Ni(COD)_2$ with $^tBu_3SnH$ and ^{t}BuNC. Assuming the nickel analogue of $Pt(Sn^tBu_3)_2(^tBuNC)_2$ was able to be synthesized, one equivalent of $Ni(COD)_2$ was mixed with two equivalents of $^tBu_3SnH$ and two equivalents of ^{t}BuNC in hexane resulting in a dark red solution. The FTIR spectra of this solution showed new broad stretches in the isocyanide region with no appreciable decrease in the amount of free tin hydride but complete consumption of free ^{t}BuNC, and thus the reaction mixture was brought to 68 °C. Approaching reflux temperature, the solution quickly changed color from dark red to gold, and the volatiles were removed in *vacuo*. The residues were redissolved in a methylene chloride/hexane mixture and filtered through silica gel. Slow evaporation of solvent yielded orange block crystals which were determined by X-ray crystallographic analysis to be $Ni(Sn^tBu_3)_2(^tBuNC)_3$ shown in Figure 3.4. Further crystallographic data is listed in Appendix B Table B.1. The compound

$Ni(Sn^tBu_3)_2(^tBuNC)_3$ was characterized by a combination of ^1H NMR, FTIR, UV-Vis, elemental analysis, mass spectrometry, and single crystal X-ray diffraction. For reasons that will be discussed later, mass spectrometry of this compound did not result in parent peak M = 888 m/z detection, but rather always yielded the M - Sn^tBu_3 = 598 m/z peak.

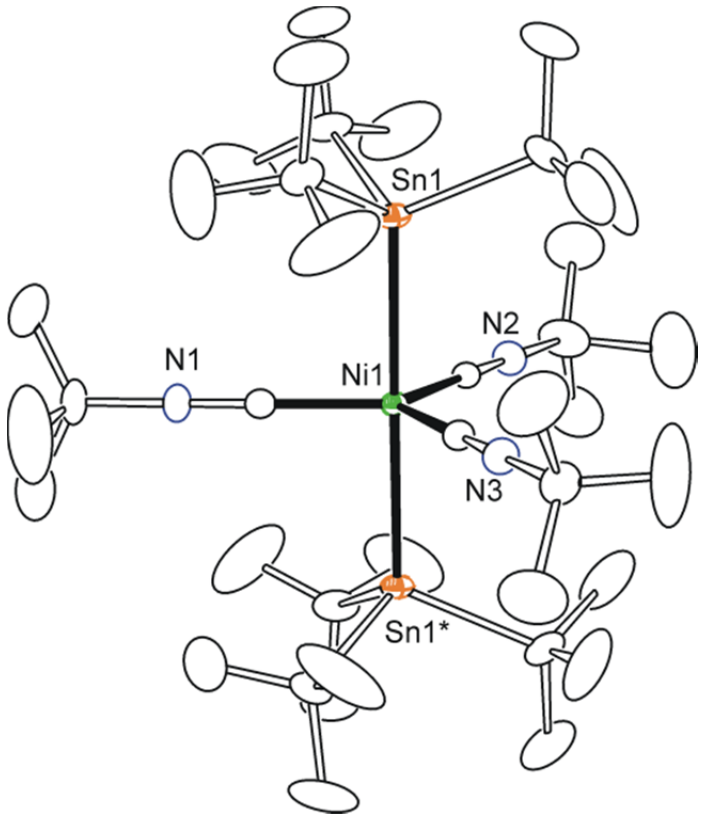

Figure 3.4 An ORTEP showing the molecular structure of $Ni(Sn^tBu_3)_2(^tBuNC)_3$ at 30 % thermal ellipsoid probability.

It is apparent from the Figure 3.4 that this $18e^-$ complex is more structurally analogous to last chapter's $Ni(Sn^tBu_3)_2(CO)_3$ than $Pt(Sn^tBu_3)_2(^tBuNC)_2$ seen in Figure 3.3, and it similarly displays approximate D_{3h} symmetry. However, the FTIR spectrum of $Ni(Sn^tBu_3)_2(^tBuNC)_3$ shows 2 distinct isocyanide stretches, shown in Appendix B Figure B.2 as opposed to the theoretical 1 ν_{CN} for trigonal bipyramidal $M(L)_2(CO)_3$ with axial L.

It is still unknown why there is an extra FTIR active stretch, but evidence for sterically induced symmetry distortion in solution is provided below. The FTIR disagreement with normal symmetry theory is the first of many unusual pieces of information found in this work. It is worth mentioning that the platinum analogue $Pt(Sn^tBu_3)_2(^tBuNC)_3$ is unable to be synthesized even in the presence excess isocyanide, yet the palladium analogue $Pd(Sn^tBu_3)_2(^tBuNC)_3$ is easily afforded and under study by Veeranna Yempally. This palladium compound will be mentioned again in a later conclusion.

Determining the crystal structure of $Ni(Sn^tBu_3)_2(^tBuNC)_3$ allowed us to make an educated guess as to its formation mechanism. Having previously shown that $Ni(CO)_4$ will release one CO ligand to react with two $^tBu_3SnH$, it was fair to assume that very similar tetrahedral $Ni(^tBuNC)_4$ may be the reactive species in this case. Indeed, later experiments showed that $Ni(Sn^tBu_3)_2(^tBuNC)_3$ is readily formed by reaction of $Ni(^tBuNC)_4$ and 2eq $^tBu_3SnH$ in refluxing hexane, shown in equation 3.3, with release of H_2 gas and ^tBuNC. The reaction proceeds at room temperature, but much more slowly.

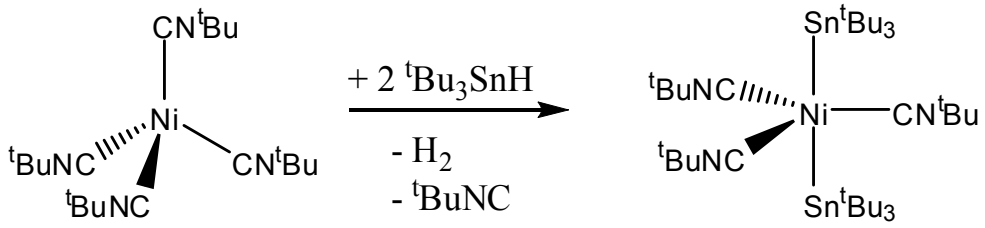

(Eqn 3.3)

However, there is precedence for the reactivity of tetrahedral $Ni(CO)_4$ and $Ni(RNC)_4$ to proceed via ligand dissociation yielding reactive trigonal planar $Ni(CO)_3$ and $Ni(RNC)_3$ intermediates.[107] Both $Ni(Sn^tBu_3)_2(CO)_3$ and $Ni(Sn^tBu_3)_2(^tBuNC)_3$ may be thought of as the respective oxidatively trapped intermediates. Our proposed mechanism

proceeds via two distinct tin additions, seen in Scheme 3.2, because a concerted mechanism with release of H_2 is unlikely due to steric restraints.

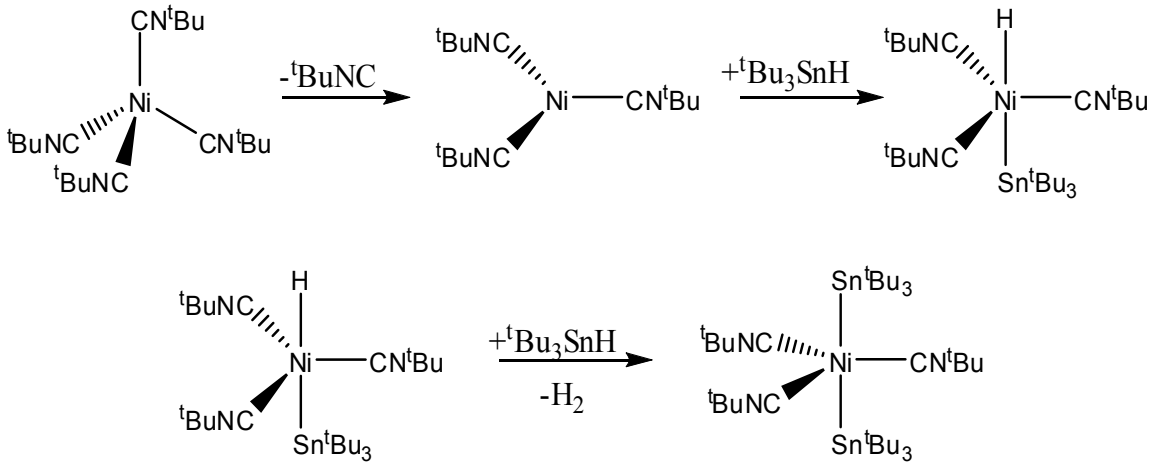

Scheme 3.2 Line drawing of proposed formation mechanism for $Ni(Sn^tBu_3)_2(^tBuNC)_3$.

Slowly adding one diluted equivalent of $^tBu_3SnH$ dropwise to a solution of $Ni(^tBuNC)_4$ at any temperature will afford only a mixture of $Ni(Sn^tBu_3)_2(^tBuNC)_3$ and $Ni(^tBuNC)_4$. Detection of any hydride intermediates at NMR time scales is so far unsuccessful, and this suggests a rapid rate of reaction completion once initiated by the first tin binding. The proposed hydride species $Ni(Sn^tBu_3)(^tBuNC)_3(H)$ will be mentioned later.

The initial reaction conditions described earlier used only 2eq of ^{t}BuNC and formed a dark red intermediate. A literature search determined that this afforded the nickel cluster $Ni_4(^tBuNC)_7$ which also apparently reacts with $^tBu_3SnH$ to give the same product $Ni(Sn^tBu_3)_2(^tBuNC)_3$ but in understandably lower yield due to deficiency of isocyanide.[108]

Reaction of $Ni(Sn^tBu_3)_2(^tBuNC)_3$ with Carbon Monoxide, CO. When a gold colored hexane solution of $Ni(Sn^tBu_3)_2(^tBuNC)_3$ was exposed to an atmosphere of carbon monoxide, a color change to light-yellow occurred. FTIR spectroscopy showed release of free isocyanide and clean formation of a new compound displaying both CN and CO stretches. X-ray crystallographic analysis of this new product provided the molecular structure of $Ni(Sn^tBu_3)_2(^tBuNC)_2(CO)$, shown in Figure 3.5. Further crystallographic data is found in Appendix B Table B.1. The complex $Ni(Sn^tBu_3)_2(^tBuNC)_2(CO)$ was characterized by a combination of ^1H NMR, ^{13}C-CO NMR, FTIR, UV-Vis, mass spectrometry, and single crystal X-ray diffraction. The symmetry distortion due to steric repulsion is clearly exemplified by the crystal structure seen in Figure 3.5.

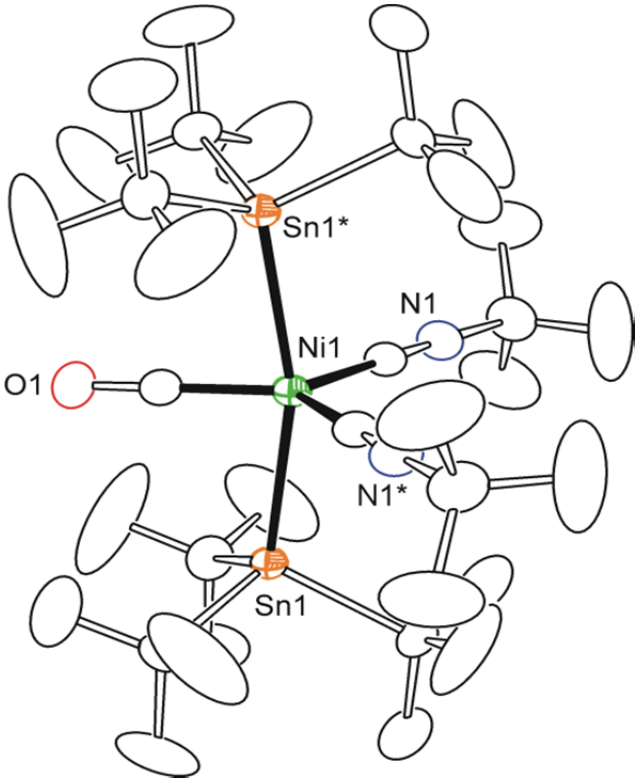

Figure 3.5 An ORTEP showing the molecular structure of $Ni(Sn^tBu_3)_2(^tBuNC)_2(CO)$ at 30 % thermal ellipsoid probability.

The structure of $Ni(Sn^tBu_3)_2(^tBuNC)_2(CO)$ is very similar to the dihydride and zero-hydride platinum complexes shown earlier in Figure 3.3, and it displays approximate C_{2v} symmetry. It is also nearly identical to Veeranna's platinum analogue $Pt(Sn^tBu_3)_2(^tBuNC)_2(CO)$ shown in Appendix B Figure B.3 which easily eliminates CO to regenerate $Pt(Sn^tBu_3)_2(^tBuNC)_2$. This compound will also be mentioned in a later conclusion. The axial tin groups seen in Figure 3.5 bend away from the bulky equatorial isocyanides in attempt to relieve steric strain. The *tert*-butyl groups even arrange themselves appropriately *anti* to further reduce any molecular tension. Both $Ni(Sn^tBu_3)_2(^tBuNC)_3$ and $Ni(Sn^tBu_3)_2(^tBuNC)_2(CO)$ are stable to wet air as solids and in solution for extended periods of time. The only substance we have found capable of reaction with either of these Ni-Sn complexes is iodine, I_2 *{$Ni(Sn^tBu_3)_2(^tBuNC)_3$ will also react with $(Ph_3C)^+(PF_6^-)$}*, and this will be discussed later.

If $Ni(Sn^tBu_3)_2(^tBuNC)_3$ or $Ni(Sn^tBu_3)_2(^tBuNC)_2(CO)$ is exposed to CO in refluxing hexane or THF, an almost 50:50 mixture of $Ni(Sn^tBu_3)_2(^tBuNC)_2(CO)$ and $Ni(Sn^tBu_3)_2(^tBuNC)(CO)_2$ is produced. These two compounds are extremely similar, and their separation requires large amounts of time and resources. We have characterized $Ni(Sn^tBu_3)_2(^tBuNC)(CO)_2$ by FTIR, ^1H NMR, and X-ray crystallographic analysis but did not further pursue its reactivity or photochemical properties due to its difficult isolation in purity. The crystal structure of $Ni(Sn^tBu_3)_2(^tBuNC)(CO)_2$ is provided in Appendix B Figure B.4 and further crystallographic information is provided in Appendix B Table B.1. Complete spectral data for $Ni(Sn^tBu_3)_2(^tBuNC)_3$, $Ni(Sn^tBu_3)_2(^tBuNC)_2(CO)$, and $Ni(Sn^tBu_3)_2(^tBuNC)(CO)_2$ is provided in this chapter's experimental section.

Photochemical Reaction of $Ni(Sn^tBu_3)_2(^tBuNC)_2(CO)$. When an oxygen-free yellow hexane solution of $Ni(Sn^tBu_3)_2(^tBuNC)_2(CO)$ was exposed to incandescent light, a rapid color change to metallic purple occurred, and is shown in Figure 3.6.

Figure 3.6 Photographs showing the color change of $Ni(Sn^tBu_3)_2(^tBuNC)_2(CO)$ (left) following photolysis (right).

The photochemical reaction was initially assumed to induce elimination of CO producing $Ni(Sn^tBu_3)_2(^tBuNC)_2$, the Ni analogue of the previously mentioned (Figure 3.3) unsaturated platinum-tin complex $Pt(Sn^tBu_3)_2(^tBuNC)_2$, shown in Equation 3.4.

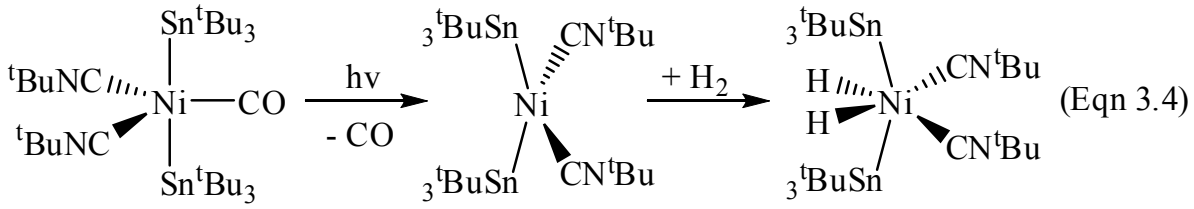

(Eqn 3.4)

The purple color of this photochemically generated product is nearly identical, though slightly darker, to that of $Pt(Sn^tBu_3)_2(^tBuNC)_2$. CO dissociation is a very common

mechanism in metal-carbonyl photochemical reactions, and we quickly purged carbon monoxide gas through the solution to check for reformation of starting material with subsequent decolorization. However, the purple solution was relatively stable to CO, as well as hydrogen gas (Equation 3.4).

Repeated attempts under varying reaction conditions consistently failed to afford dark crystals from purple solutions, but rather ample amounts of starting material yellow crystals which FTIR spectroscopy showed to be nearly consumed in purple photolytic reaction mixtures. It was found that lower temperatures aided both this reaction and product, signified by a visual increase in apparent reaction rate and intensity of purple color. Eventually dichroic purple/green crystals were formed by slow evaporation of concentrated diethyl ether solutions at -20 °C under argon atmosphere. Crystallographic analysis of this photochemical product yielded the dimeric structure of $[Ni(Sn^tBu_3)(^tBuNC)_2(CO)]_2$ shown in Figure 3.7. Further crystallographic data is provided in Appendix B Table B.2. The compound $[Ni(Sn^tBu_3)(^tBuNC)_2(CO)]_2$ was characterized by a combination of ^1H NMR, ^{13}C-CO NMR, FTIR, UV-Vis, ESR, elemental and single crystal X-ray diffraction analyses. This Ni-Sn dimer is a stable solid in air for an extended period of time, but will quickly decolorize to yellow in both oxygenated and oxygen free room temperature solutions.

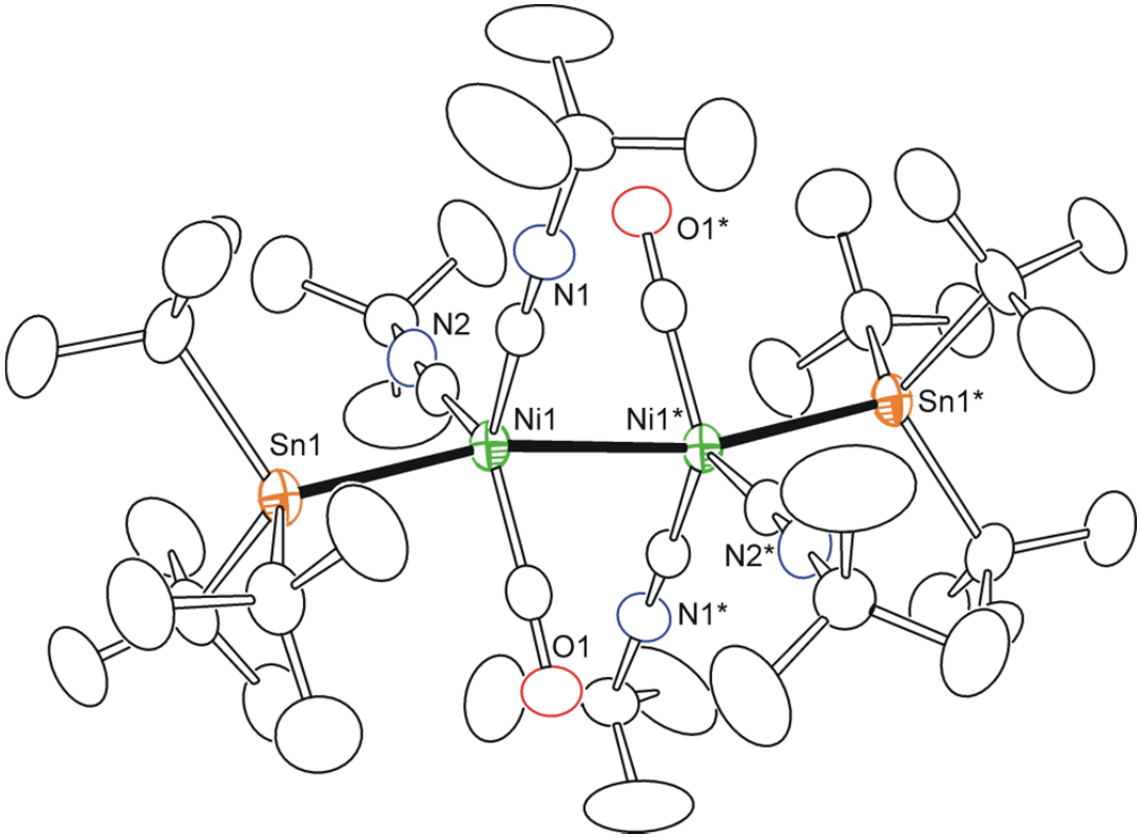

Figure 3.7 An ORTEP showing the molecular structure of $[Ni(Sn^tBu_3)(^tBuNC)_2(CO)]_2$ at 30 % thermal ellipsoid probability.

It is apparent from the crystal structure that CO ligands were not lost, but rather Ni-Sn bonds were cleaved and a Ni-Ni bond was formed. We propose a radical mechanism for this reaction with photogeneration of the tetrahedral Ni^I species $\bullet Ni(Sn^tBu_3)(^tBuNC)_2(CO)$ and the planar $\bullet Sn^tBu_3$, both radicals (Scheme 3.3). Such tetrahedral Ni^I species are very elusive and known to be paramagnetic.[109] This zig-zagging Sn-Ni-Ni-Sn structure with approximate C_{2h} symmetry can be thought of as the combined product of two such $\bullet Ni(Sn^tBu_3)(^tBuNC)_2(CO)$ radical monomers, and adopts an *anti* configuration presumably to relieve equatorial strain.

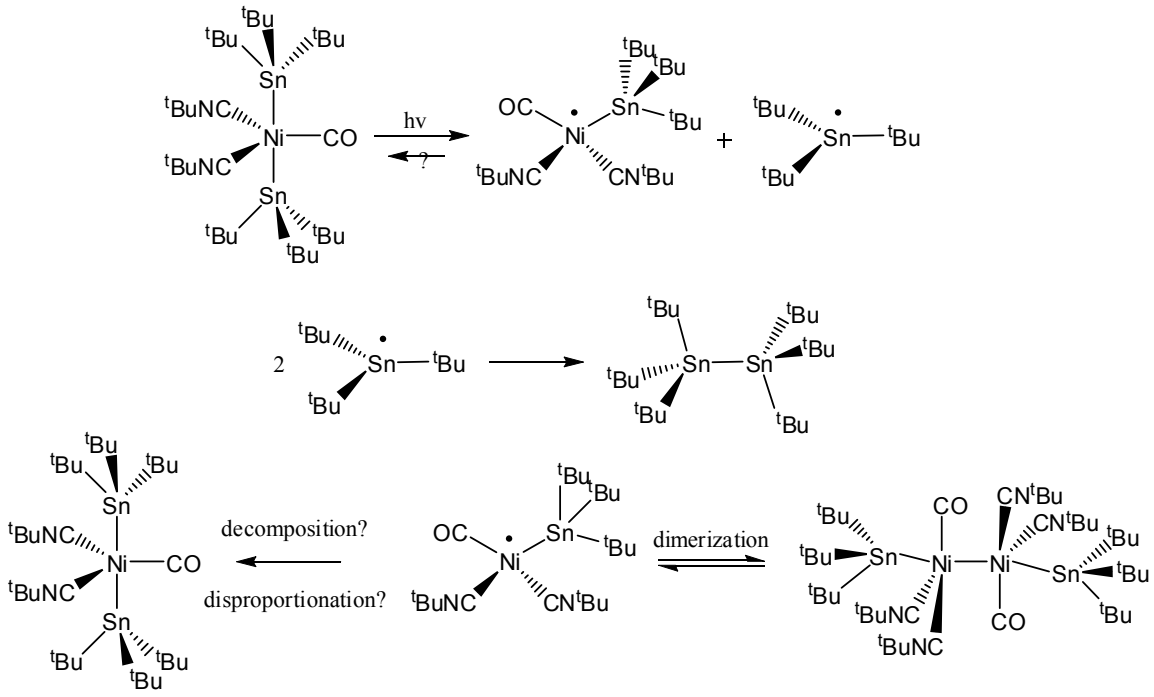

Scheme 3.3 Proposed mechanism for photolysis of $Ni(Sn^tBu_3)_2(^tBuNC)_2(CO)$ to $[Ni(Sn^tBu_3)(^tBuNC)_2(CO)]_2$ with generation of $^tBu_6Sn_2$.

Tri-alkyl tin radicals are known to be generated by thermolysis of the corresponding di-stannane at elevated temperatures.[110] Based on this logic we should be able to detect and isolate the room temperature side-product of two combined tin fragments which is hexa-*tert*-butyl-di-stannane, $^tBu_6Sn_2$, and indeed this is seen in reaction mixture NMR spectra and can be isolated.[111] If extreme care is not taken to eliminate as much oxygen from the reaction mixture as possible, $(^tBu_3Sn)_2O$ is detected and isolated as colorless plates.[112] Both of these previously known di-tin structures were re-solved in our lab and are shown in Figure 3.8.

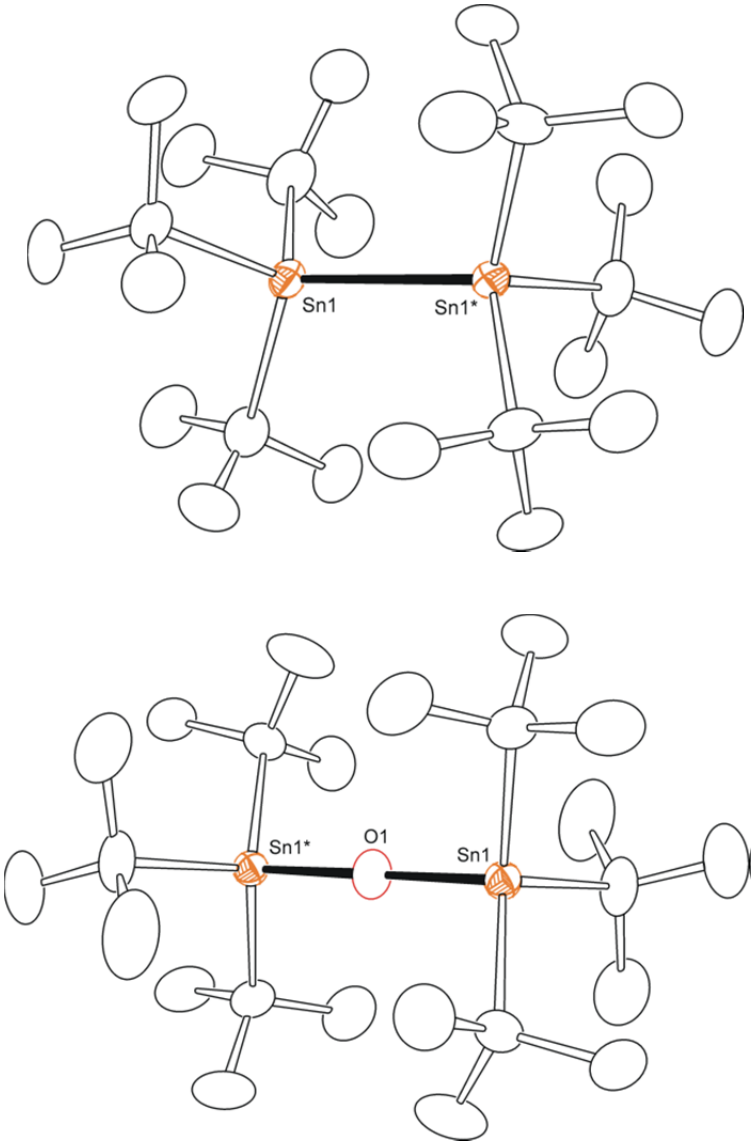

Figure 3.8 ORTEPs showing the molecular structures of $^{t}Bu_6Sn_2$ (top) and $(^{t}Bu_3Sn)_2O$ (bottom) at 30 % thermal ellipsoid probability.

It is worth noting that if $Ni(Sn^{t}Bu_3)_2(^{t}BuNC)_2(CO)$ is photolyzed in an environment containing both of O_2 as well as carbon dioxide, CO_2, the $^{t}Bu_3Sn$ fragment is readily converted to the tin-carbonate product $[Sn(O)(^{t}Bu)_2(CO_3Sn^{t}Bu_3)]_2$ with ^{1}H NMR (C_6D_6) at 1.26ppm (s, 36H, ^{t}Bu, $^{3}J_{Sn-H}$= 72 Hz) and 1.24ppm (s, 54H, ^{t}Bu, $^{3}J_{Sn-H}$ = 65 Hz). A few tin-carbonate compounds similar to $[Sn(O)(^{t}Bu)_2(CO_3Sn^{t}Bu_3)]_2$ are known,

normally produced by the reaction of tin-alkoxides, Sn-OR, with CO_2.[113-116] Several of these metallated carbonate complexes show some catalytic activity in methanol to produce dimethyl carbonate, DMC, which has many applications ranging from sustainable fuel sources to environmentally safe methylating agents.[117,118] This is apparently the first example of such a tin-carbonate compound containing additional terminal tin ligands, thus making the molecule a tetra-nuclear tin-carbonate compound, shown in Figure 3.9. Further crystallographic information is provided in Appendix B Table B.2.

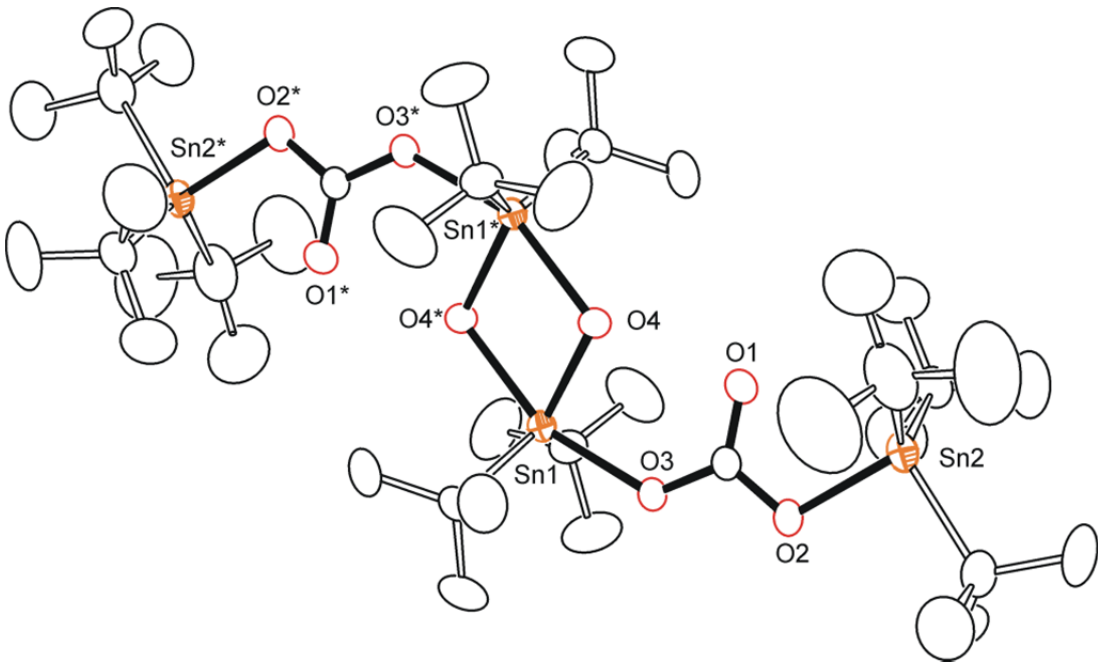

Figure 3.9 An ORTEP showing the molecular structure of $[Sn(O)(^tBu)_2(CO_3Sn^tBu_3)]_2$ at 30 % thermal ellipsoid probability.

Today's society is rightfully becoming more concerned with attaining an eco-friendly "Green" future, and photochemical activation and utilization of CO_2 is certainly one such

technology that would lead the way. Further study of this complex is currently underway in our lab.

The proposed tetrahedral Ni^{I} species $\bullet Ni(Sn^{t}Bu_3)(^{t}BuNC)_2(CO)$ is unsaturated by one electron and apparently dimerizes forming the solid state compound $[Ni(Sn^{t}Bu_3)(^{t}BuNC)_2(CO)]_2$, though its existence and stability in solution is still mostly unclear to us presently. The crystal structure is similar to that of $Co(Sn^{t}Bu_3)(CO)_4$ presented in the last chapter, both displaying equatorial bending of ligands as if existing as a capped tetrahedral structure, shown more clearly from a different perspective in Figure 3.10 with methyl groups excluded for clarity.

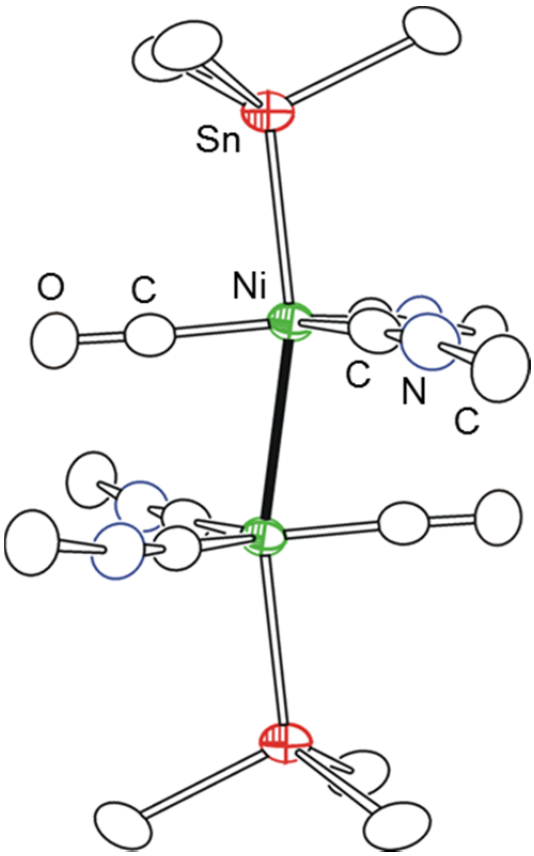

Figure 3.10 An ORTEP showing the molecular structure of $[Ni(Sn^{t}Bu_3)(^{t}BuNC)_2(CO)]_2$ from a different perspective to better portray the bending of equatorial ligands away from axial tins and towards the center of the Ni-Ni bond. Methyl groups excluded for clarity.

Solid state FTIR spectroscopy confirms the crystal structure, showing a spectrum very similar to $Ni(Sn^tBu_3)_2(^tBuNC)_2(CO)$ but shifted slightly, seen in Figure 3.11. It is interesting to note that the shape of the isocyanide stretches changed from having the less intense minor peak on the left to the right side of the major peak, a lower energy stretch suggesting an increased pi back donation from Ni into the C≡N bond. Room temperature solution FTIR spectra of this Ni-Sn dimer show many peaks including starting material and are never fully reproducible, suggesting a secondary process in solution. Pure crystalline $[Ni(Sn^tBu_3)(^tBuNC)_2(CO)]_2$ dissolved in room-temperature solvents will decolorize with time to yield a light yellow solution exhibiting major spectral characteristics of $Ni(Sn^tBu_3)_2(^tBuNC)_2(CO)$, yet will remain a deep purple solution nearly indefinitely under argon in a -80 °C freezer.

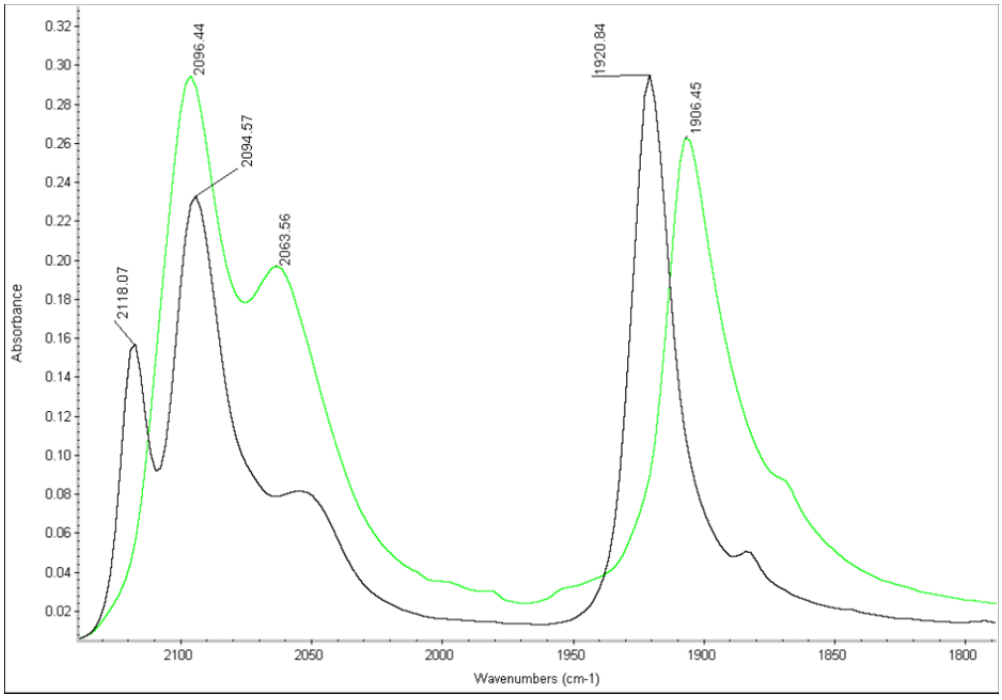

Figure 3.11 Solid FTIR spectra comparing $Ni(Sn^tBu_3)_2(^tBuNC)_2(CO)$ (black) to $[Ni(Sn^tBu_3)(^tBuNC)_2(CO)]_2$ (green).

In fact, visibly purple solutions of pure crystalline $[Ni(Sn^tBu_3)(^tBuNC)_2(CO)]_2$ in C_6D_6 show the room-temperature ^1H NMR spectra of $Ni(Sn^tBu_3)_2(^tBuNC)_2(CO)$ with other minor unidentified peaks in the ^{t}Bu region, shown in Figure 3.12.

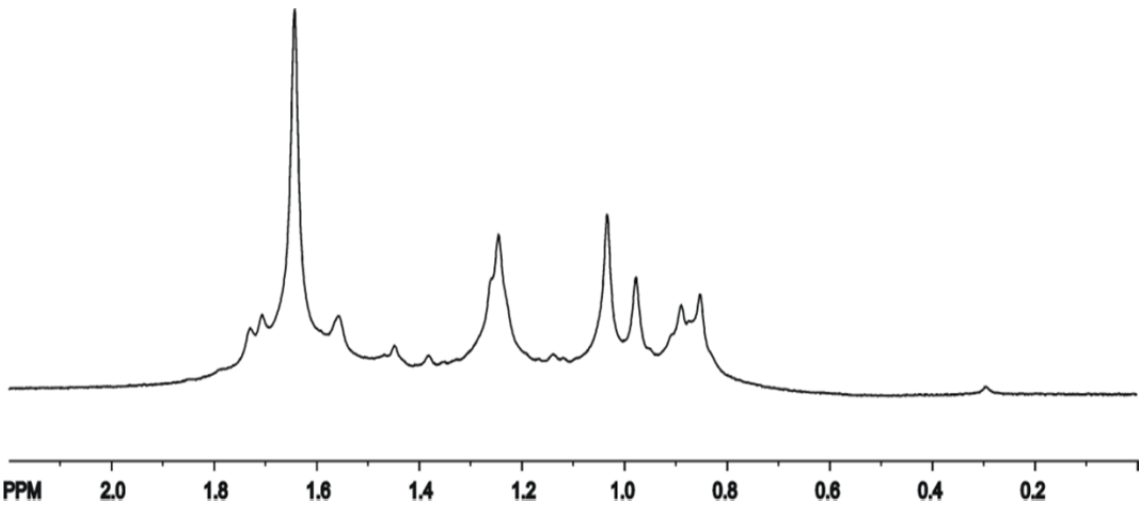

Figure 3.12 ^1H NMR spectra of $[Ni(Sn^tBu_3)(^tBuNC)_2(CO)]_2$ at room temperature.

Integration of the major Sn-^{t}Bu peak at 1.64 ppm versus the CN-^{t}Bu peak at 1.03 ppm gives a ratio of 54(3):18(1), consistent with $Ni(Sn^tBu_3)_2(^tBuNC)_2(CO)$, opposed to the expected 54(3):36(2) for $[Ni(Sn^tBu_3)(^tBuNC)_2(CO)]_2$. The lack of any major product peaks easily assignable to $[Ni(Sn^tBu_3)(^tBuNC)_2(CO)]_2$ leads us to believe there is dissociation equilibrium in solution, most likely consisting of the monomer-dimer complexes of $[Ni(Sn^tBu_3)(^tBuNC)_2(CO)]_2$**.** The monomeric, tetrahedral Ni^I radical $\bullet Ni(Sn^tBu_3)(^tBuNC)_2(CO)$ appears to not be stable with respect to itself at room temperature and may disproportionate, decompose, or react with another monomer to regenerate $Ni(Sn^tBu_3)_2(^tBuNC)_2(CO)$ by unknown mechanisms shown in Scheme 3.3. Whether or not the $\bullet$Ni-Sn and $\bullet$Sn radical fragments that are photogenerated can recombine is still unclear.

Spectral Characterization of $[Ni(Sn^tBu_3)(^tBuNC)_2(CO)]_2$ in Solution. A variable temperature ^1H NMR experiment was performed to check for low temperature stabilization of any possible dimeric or monomeric species other than $Ni(Sn^tBu_3)_2(^tBuNC)_2(CO)$ in solutions of $[Ni(Sn^tBu_3)(^tBuNC)_2(CO)]_2$, and indeed there was evidence of major change in the Sn-^{t}Bu region. $Ni(Sn^tBu_3)_2(^tBuNC)_2(CO)$ shows only one Sn-^{t}Bu peak at both 298 and 193 K, though it is no surprise solubility is a problem at such cold temperatures. The spectrum of pure $[Ni(Sn^tBu_3)(^tBuNC)_2(CO)]_2$ in toluene-d_8 begins as single, very broad Sn-^{t}Bu and CN-^{t}Bu peaks at 193 K that start to split as the temperature increases, shown in Figure 3.13. At 233 K there are two clear Sn-^{t}Bu peaks, both somewhat broadened -- the left peak gradually decreases to 0 with increasing temperatures giving way to the second peak, that of the starting complex $Ni(Sn^tBu_3)_2(^tBuNC)_2(CO)$. The area of CN-^{t}Bu around 1 ppm is inherently too unclean for solutions of $[Ni(Sn^tBu_3)(^tBuNC)_2(CO)]_2$ to make justifiable conclusions about the decrease or increase of any peaks in this region.

In an attempt to "clean up" these spectra, a sample of ^{13}CO-$Ni(Sn^tBu_3)_2(^tBuNC)_2(CO)$ was prepared and photolytically converted to ^{13}CO-$[Ni(Sn^tBu_3)(^tBuNC)_2(CO)]_2$. Spectral data for these are shown in Appendix B Figures B.5 and B.6 and listed in this chapter's experimental section. Single crystal FTIR spectroscopy of these ^{13}C-CO products confirmed that the complexes were successfully labeled with a satisfactory isotopic content of > 90 %.

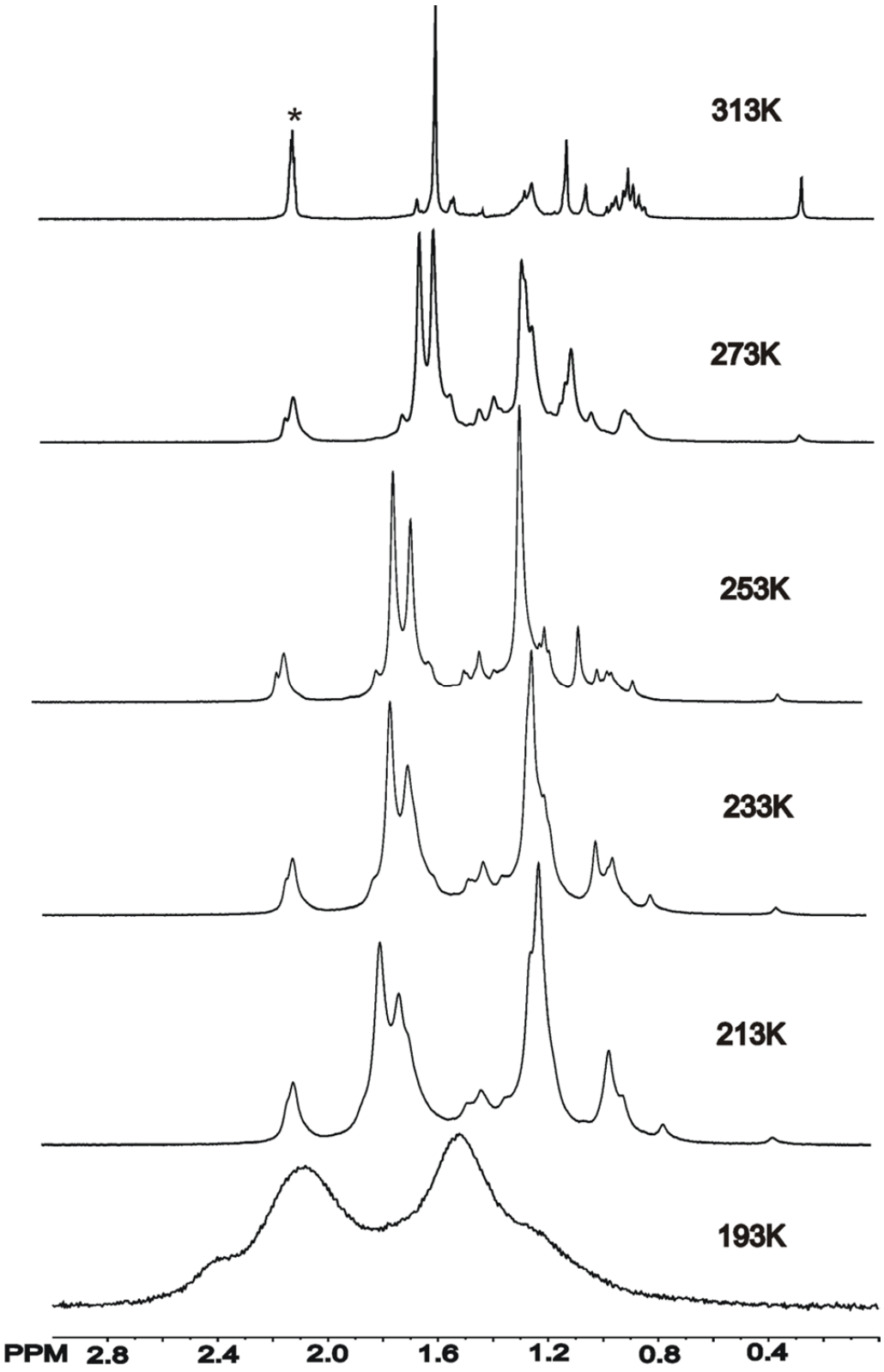

Figure 3.13 Variable temperature ^{1}H NMR of $[Ni(Sn^{t}Bu_3)(^{t}BuNC)_2(CO)]_2$. * denotes toluene-$d_8$.

The ^{13}C NMR spectra of ^{13}CO- $Ni(Sn^tBu_3)_2(^tBuNC)_2(CO)$ shows only one resonance in toluene-d_8 of 197 ppm at 193 and 296 K now with two bond tin coupling of $^2J_{Sn-C}$= 127 Hz. A 10 mg sample of pure ^{13}CO-$[Ni(Sn^tBu_3)(^tBuNC)_2(CO)]_2$ was prepared and loaded into a screw-cap NMR tube along with 0.6 mL of touene-d_8. The NMR tube was quickly brought out of the glovebox and kept in ice while being transferred to the instrument room. The sample tube was inserted into the NMR chamber which was already cooled to 193 K and collected for 2.5 hours. The time spent above 193 K between dissolution and data collection may have resulted in some disproportionation/decomposition products, though we assume these to be minimal. The ^{13}C-CO area showed several new peaks, the major peak (205 ppm) being very large and broad compared to the smaller peak of ^{13}CO- $Ni(Sn^tBu_3)_2(^tBuNC)_2(CO)$ (197 ppm) upfield, shown in Figure 3.14.

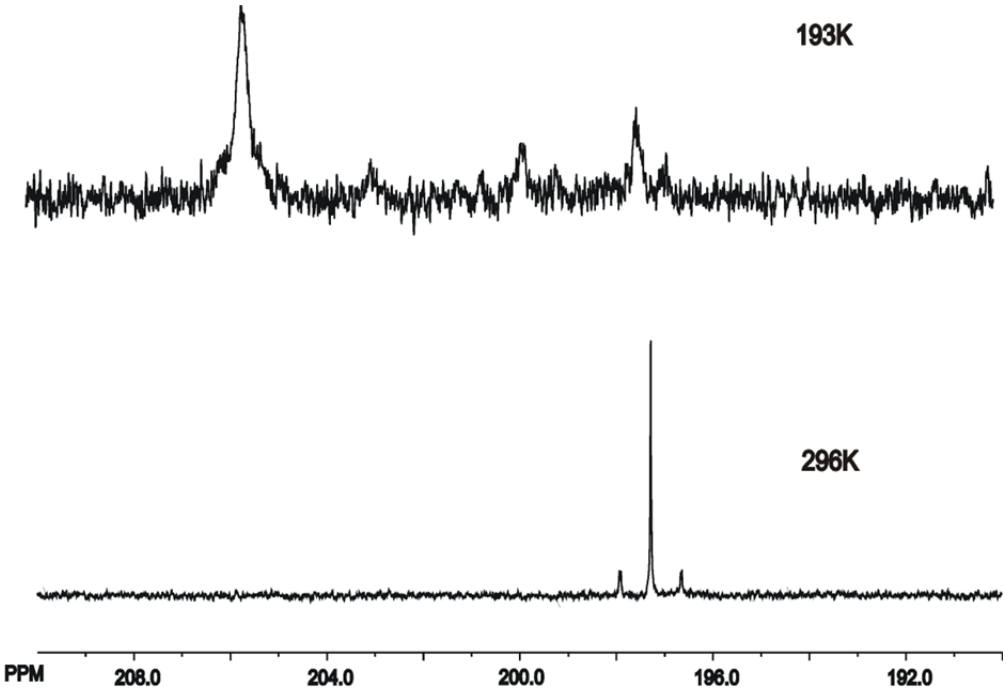

Figure 3.14 ^{13}C NMR of ^{13}CO-$Ni(Sn^tBu_3)_2(^tBuNC)_2(CO)$ at 296 K (bottom) and ^{13}CO-$[Ni(Sn^tBu_3)(^tBuNC)_2(CO)]_2$ at 193 K (top). Note: ^{13}CO-$Ni(Sn^tBu_3)_2(^tBuNC)_2(CO)$ spectrum is identical at 193 K, only less intense.

In agreement with the crystal structure this new major peak seems to show three as well as two bond couplings for Sn to ^{13}C of approximately $^{3}J_{Sn\text{-}13C}$= 80 Hz and $^{2}J_{Sn\text{-}13C}$= 132 Hz, respectively. This was the first clear NMR evidence of any major Ni products in solutions of pure $[Ni(Sn^tBu_3)(^tBuNC)_2(CO)]_2$ that was not attributable to $Ni(Sn^tBu_3)_2(^tBuNC)_2(CO)$**.** The other ^{13}CO peaks are similar in size to that of $Ni(Sn^tBu_3)_2(^tBuNC)_2(CO)$ and are as of yet unidentified. It is possible that one of these peaks is the monomeric radical which would explain the spectral noise and broadening, though we cannot say so with any kind of certainty.

Detection of Paramagnetic Species in Solutions of $[Ni(Sn^tBu_3)(^tBuNC)_2(CO)]_2$. Having confirmed the presence of a major product in solutions of $[Ni(Sn^tBu_3)(^tBuNC)_2(CO)]_2$ that was not starting material $Ni(Sn^tBu_3)_2(^tBuNC)_2(CO)$, the inherent low temperature line broadening in the NMR spectra led us to attempt ESR spectroscopy of $[Ni(Sn^tBu_3)(^tBuNC)_2(CO)]_2$ at depressed temperatures. Samples of pure $[Ni(Sn^tBu_3)(^tBuNC)_2(CO)]_2$ and ^{13}CO-$[Ni(Sn^tBu_3)(^tBuNC)_2(CO)]_2$ were dissolved in toluene, loaded into quartz ESR tubes, and frozen with liquid N_2 on their way to the instrument room. Surprisingly, the royal purple color of $[Ni(Sn^tBu_3)(^tBuNC)_2(CO)]_2$ is transformed to a vibrant fluorescent pink at 77 K, seen in Figure 3.15, and may be due to extremely low temperature stabilization of monomeric radical species.

Indeed, there was ESR signal present at 134 K. The ^{13}CO-$[Ni(Sn^tBu_3)(^tBuNC)_2(CO)]_2$ spectrum is shown below in Figure 3.16 and the ^{12}CO spectrum is shown in Appendix B Figure B.7. The g factor for these paramagnetic species is approximately g = 2.059 and is in good agreement with other Ni^I centered

radicals found in the literature.[119] In the future we would like to attempt ESR spectroscopy at even lower temperatures.

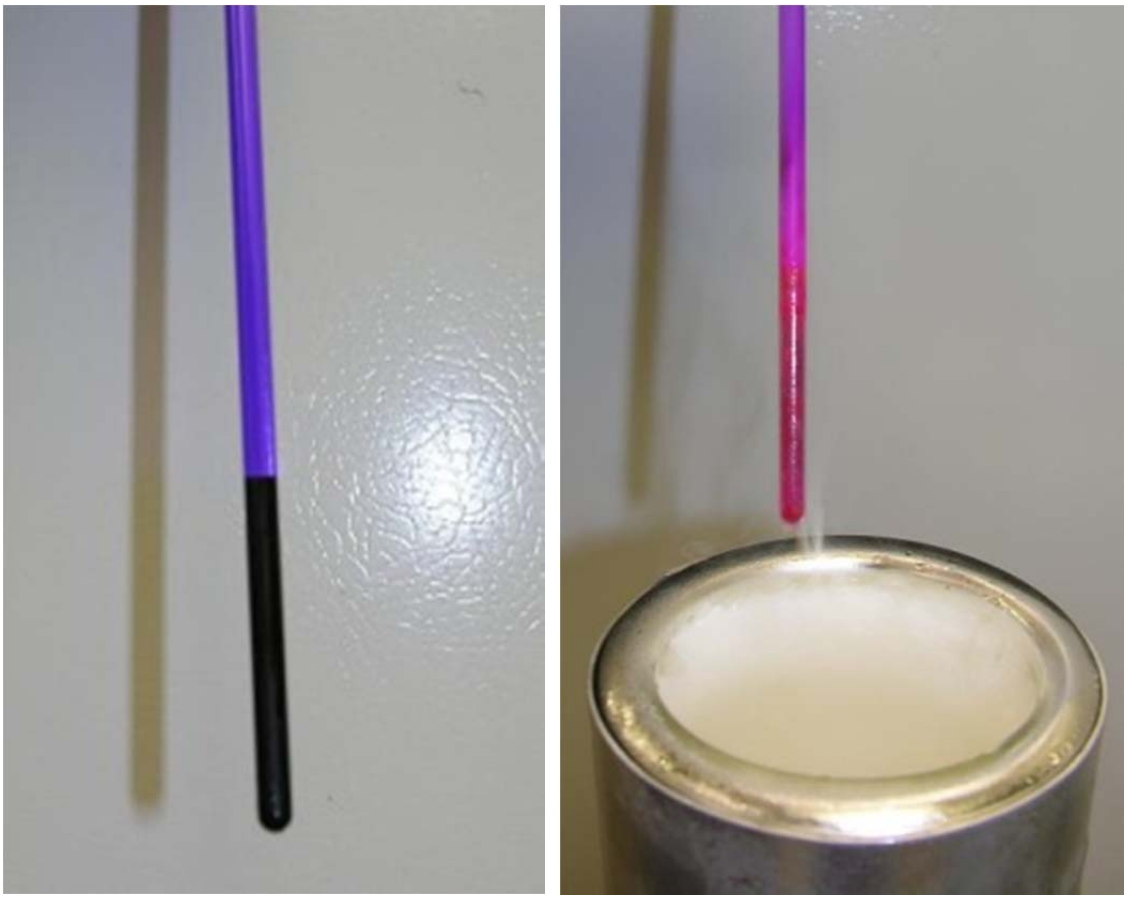

Figure 3.15 Photographs displaying the room temperature deep purple color of $[Ni(Sn^tBu_3)(^tBuNC)_2(CO)]_2$ and the corresponding fluorescent pink color at 77 K.

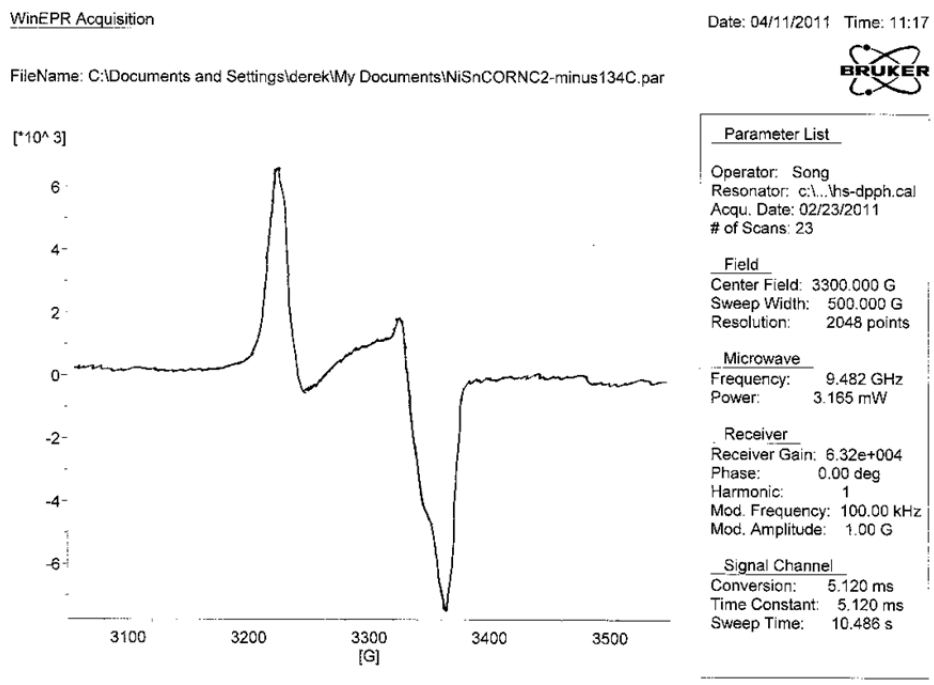

Figure 3.16 ESR spectra ^{13}CO-[Ni(Sn^{t}Bu$_3$)(^{t}BuNC)$_2$(CO)]$_2$ at 134 K. g = 2.059.

It is clear from Figure 3.16 compared to Figure B.7 that the ^{13}CO dimer compound shows some hyperfine coupling to this magnetically active nucleus. This is strong evidence in favor of our nickel centered radical •Ni(Sn^{t}Bu$_3$)(^{t}BuNC)$_2$(CO) assuming that only Ni species possess ^{13}CO ligands. It is also evident that the paramagnetism of the ^{13}CO sample is significantly more intense than the ^{12}CO sample, and we are still unsure as to the nature of this possible isotope effect.

Photochemical Reaction of Ni(Sn^{t}Bu$_3$)$_2$(^{t}BuNC)$_3$. After having gathered a slightly better understanding regarding the photochemical generation of [Ni(Sn^{t}Bu$_3$)(^{t}BuNC)$_2$(CO)]$_2$ from Ni(Sn^{t}Bu$_3$)$_2$(^{t}BuNC)$_2$(CO) , we questioned whether or not the original Ni(Sn^{t}Bu$_3$)$_2$(^{t}BuNC)$_3$ possessed the same photolytic capability. When a

room temperature solution of $Ni(Sn^tBu_3)_2(^tBuNC)_3$ was exposed to light very little change occurred as far as color goes, and if anything the solution instantly became a lighter shade of yellow. FTIR spectroscopy showed this solution to contain a single broad isocyanide stretch that was oddly familiar, and X-ray diffraction analysis of the crystallized product confirmed the presence of $Ni(^tBuNC)_4$, the starting material used to synthesize $Ni(Sn^tBu_3)_2(^tBuNC)_3$. This previously unknown structure is shown in Figure 3.17 and further crystallographic information is provided in Appendix B Table B.2. Literature references for this compound and its synthesis do not provide useful spectroscopic data for our needs, and so we characterized $Ni(^tBuNC)_4$ by FTIR spectroscopy in hexane and ^1H NMR spectroscopy in C_6D_6, provided in the experimental section of this chapter.

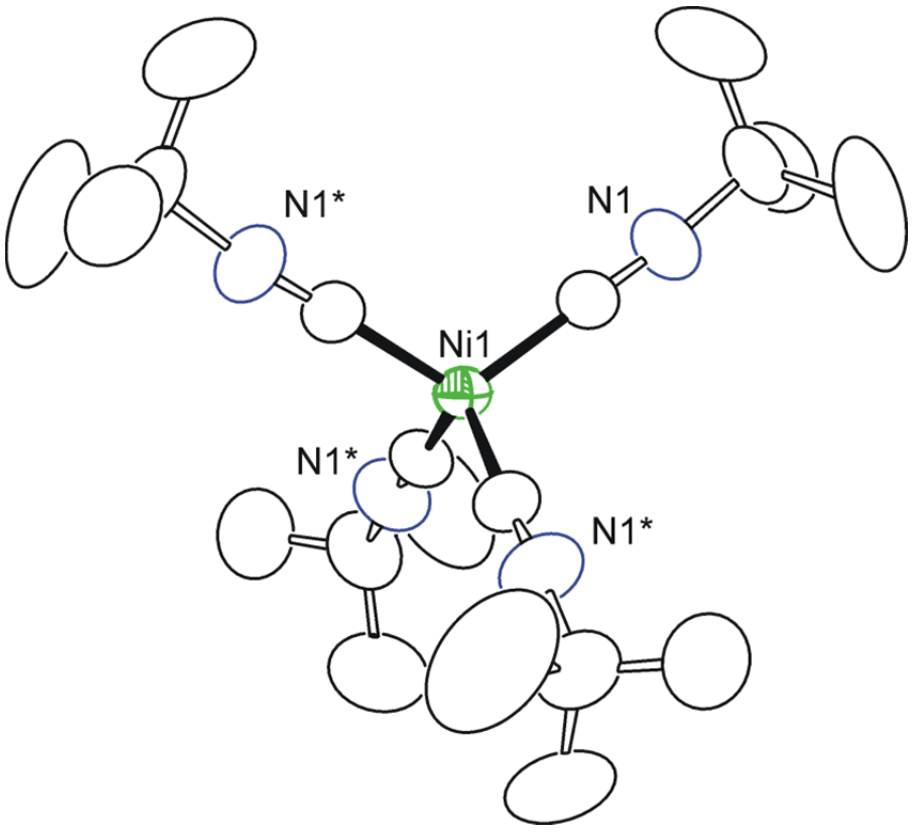

Figure 3.17 An ORTEP showing the molecular structure of $Ni(^tBuNC)_4$ at 30 % thermal ellipsoid probability.

The isolation of $Ni(^tBuNC)_4$ was very interesting, and may possibly shed some light on the decomposition/disproportionation of $\bullet Ni(Sn^tBu_3)(^tBuNC)_2(CO)$ to partially regenerate $Ni(Sn^tBu_3)_2(^tBuNC)_2(CO)$. This result was rationalized as follows: we expected to isolate the similar dimeric product $[Ni(Sn^tBu_3)(^tBuNC)_3]_2$ in this photochemical reaction, however the tris-isocyanide complex $Ni(Sn^tBu_3)_2(^tBuNC)_3$ possesses even more extreme equatorial bulk compared to the CO substituted $Ni(Sn^tBu_3)_2(^tBuNC)_2(CO)$. Examination of the crystal structure for $[Ni(Sn^tBu_3)(^tBuNC)_2(CO)]_2$ in Figure 3.10 shows approximately 7 ° of bend for equatorial ligands towards the center of the Ni-Ni bond. This is most likely possible due to the presence of CO ligands providing space for the isocyanide ligands to bend away from the bulky axial tins. This is not so for the tris-isocyanide derivative, and its symmetrically bulky equatorial ligands should provide almost no room for steric relief, thus forcing the dimerization equilibrium towards the proposed monomeric $\bullet Ni(Sn^tBu_3)(^tBuNC)_3$ shown below in Figure 3.18.

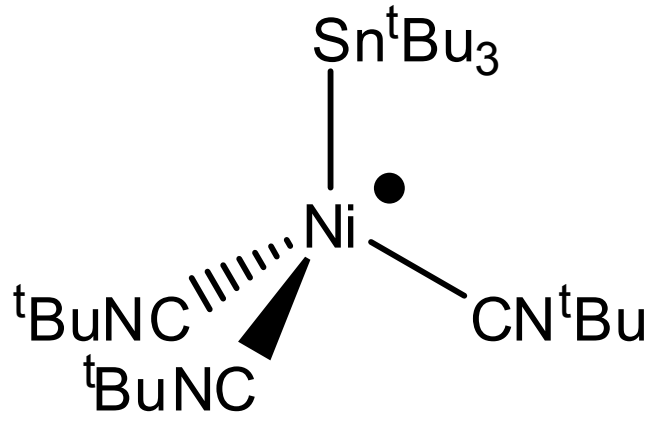

Figure 3.18 Lines structure of the proposed $\bullet Ni(Sn^tBu_3)(^tBuNC)_3$.

This equates to more time spent as the above monomer in solution which is prone to undergo temperature dependent decomposition/disproportionation to regenerate $Ni(Sn^tBu_3)_2(^tBuNC)_3$ and $Ni(^tBuNC)_4$ by an unknown mechanism. According to this logic, there may be $Ni(^tBuNC)_3(CO)$ or $Ni(^tBuNC)_2(CO)_2$ in solutions of $[Ni(Sn^tBu_3)(^tBuNC)_2(CO)]_2$, however we have not detected these as of yet.

When the photolysis of $Ni(Sn^tBu_3)_2(^tBuNC)_3$ was performed at -78 °C, the solution quickly became a deep peacock blue. It is assumed that low temperature has stabilized the photochemical product shown in Figure 3.18, evidenced by a color change similar to the generation of $[Ni(Sn^tBu_3)(^tBuNC)_2(CO)]_2$. Photographic examples for this low temperature photolysis are provided in Figure 3.19. Analogous to the royal purple color of $[Ni(Sn^tBu_3)(^tBuNC)_2(CO)]_2$, the deep peacock blue color becomes a lighter fluorescent sky blue at when frozen in liquid nitrogen. Both of these colors are somewhat visible in Figure 3.19 but much more apparent in-person. The ESR spectrum of this blue solution at 170 K in toluene is shown in Appendix B Figure B.13.

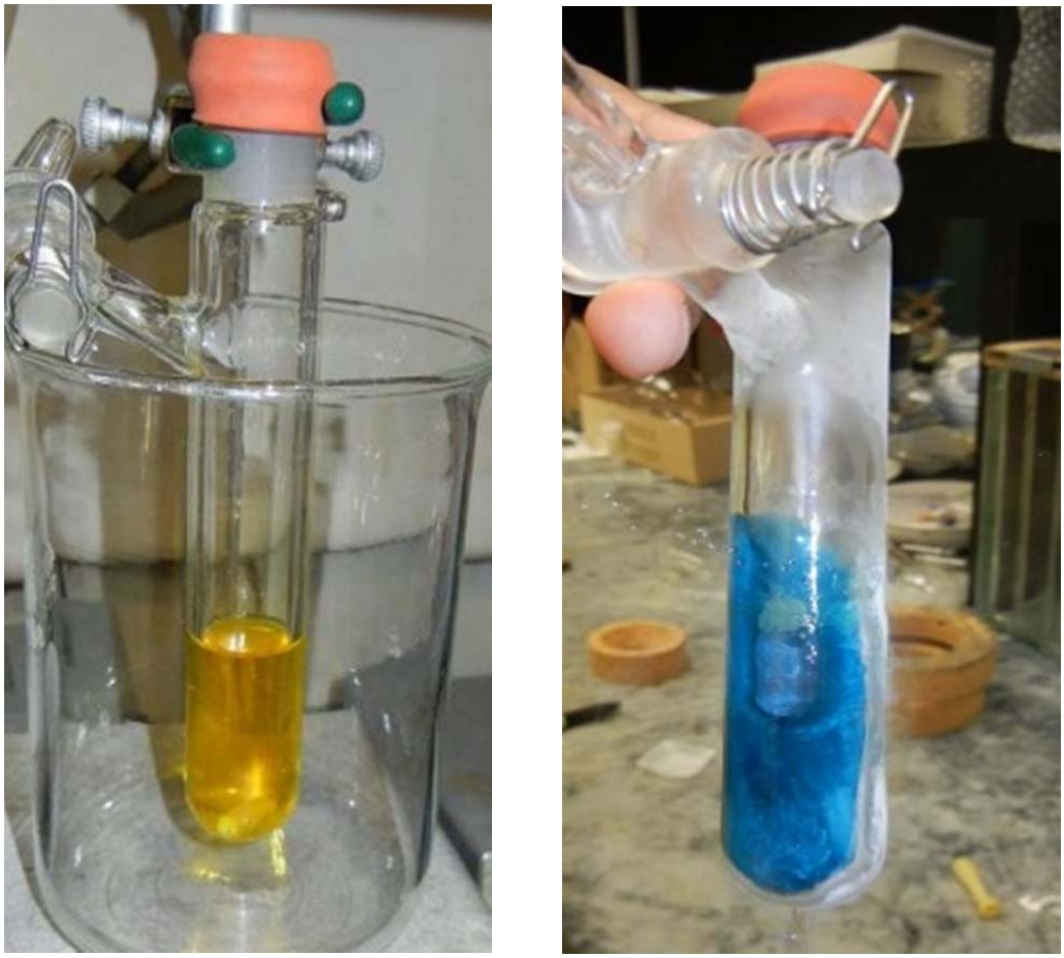

Figure 3.19 Photographs showing $Ni(Sn^tBu_3)_2(^tBuNC)_3$ (left) and photolysis to the hypothesized $[Ni(Sn^tBu_3)(^tBuNC)_3]_2$ and $\bullet Ni(Sn^tBu_3)(^tBuNC)_3$ at -78 °C.

This new deep peacock blue solution is extremely temperature sensitive, and will quickly decolorize to yellow even at -20 °C, thus making isolation and characterization of any new products nearly impossible for us. However, we isolate the products $Ni(Sn^tBu_3)_2(^tBuNC)_3$, $Ni(^tBuNC)_4$, $^tBu_6Sn_2$ and $^tBu_6Sn_2O$ from reaction mixtures, and therefore we believe the mechanism to be identical for the photolysis of $Ni(Sn^tBu_3)_2(^tBuNC)_3$ and $Ni(Sn^tBu_3)_2(^tBuNC)_2(CO)$. Indeed, the experiments described below give nearly identical results when using either $Ni(Sn^tBu_3)_2(^tBuNC)_3$ or $Ni(Sn^tBu_3)_2(^tBuNC)_2(CO)$.

Attempted Trapping of Radical Species. With ESR spectroscopy showing paramagnetic species in solutions of $[Ni(Sn^tBu_3)(^tBuNC)_2(CO)]_2$, we set out to trap any odd electron compounds generated in the photolysis of $Ni(Sn^tBu_3)_2(^tBuNC)_3$ and $Ni(Sn^tBu_3)_2(^tBuNC)_2(CO)$. The first substance we employed for this purpose was (2,2,6,6-Tetramethylpiperidin-1-yl)oxyl, TEMPO.[120] This stable radical, shown in Figure 3.20, enjoys a wide variety of uses from polymerization initiation to catalytic oxidation, and is known for its ability to trap radical intermediates.[121] The next chapter will revisit this TEMPO radical and present its exciting reaction with $Ni(COD)_2$.

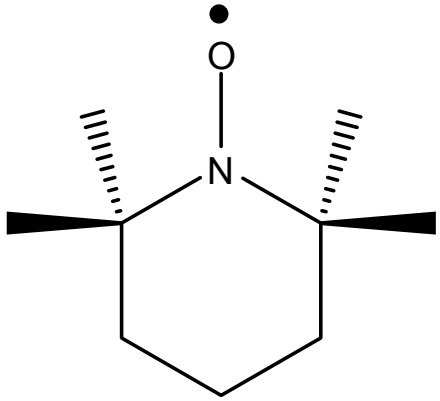

Figure 3.20 Line structure of (2,2,6,6-Tetramethylpiperidin-1-yl)oxyl, TEMPO, radical.

When three equivalents of TEMPO radical were added to a solution of $Ni(Sn^tBu_3)_2(^tBuNC)_2(CO)$ and subsequently photolyzed, the mixture did not take on the characteristic purple color of the dimer, but rather darkened slightly to a brownish yellow. Similar color change occurred when using $Ni(Sn^tBu_3)_2(^tBuNC)_3$. Evacuation of volatiles and recrystallization of the solid residue from diethyl ether at -25 °C yielded brown yellow crystalline blocks of $Ni(\eta^2\text{-N,O-TEMPO})(Sn^tBu_3)(^tBuNC)$ in 54 % yield.

Seen in Figure 3.21, Ni(η^2-N,O-TEMPO)(Sn^{t}Bu$_3$)(^{t}BuNC) was characterized by a combination of ^{1}H NMR, FTIR, and single crystal X-ray diffraction. Further crystallographic data is found in Appendix B Table B.3.

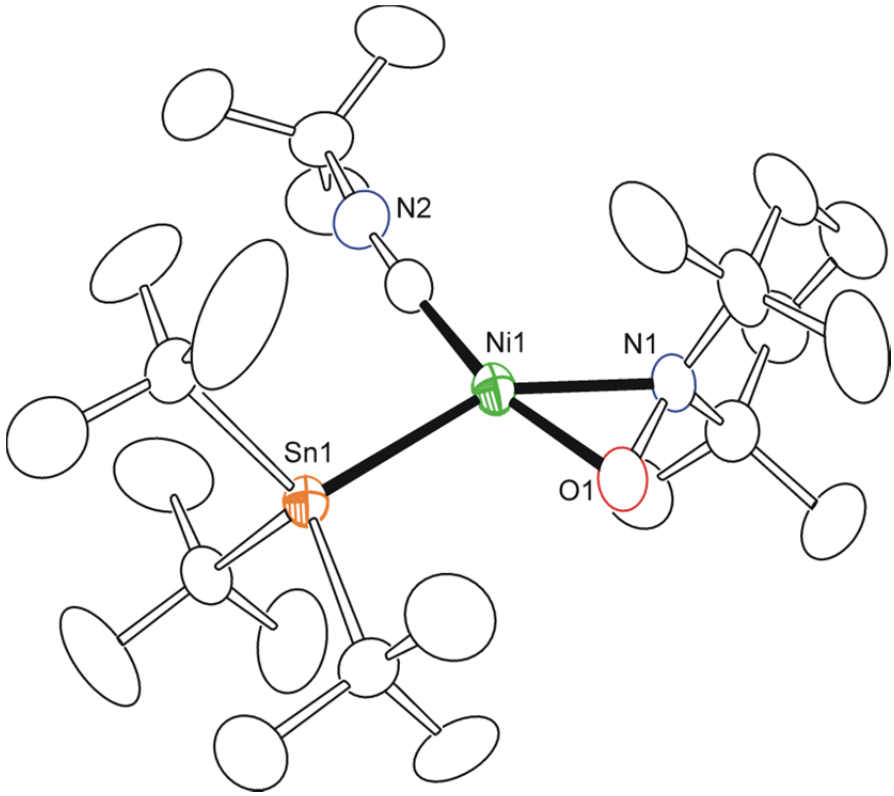

Figure 3.21 An ORTEP showing the molecular structure of Ni(η^2-N,O-TEMPO)(Sn^{t}Bu$_3$)(^{t}BuNC) at 30% thermal ellipsoid probability.

This is a good example of a captured •Ni-Sn fragment from the photolyzed reaction mixture, but it is clearly missing both isocyanide and carbon monoxide ligands (only isocyanide ligands for •Ni(Sn^{t}Bu$_3$)(^{t}BuNC)$_3$). It is proposed in Scheme 3.4 that TEMPO initially binds η^1-O to the Ni^I center followed by 1e$^-$ reduction of TEMPO to its monoanion, oxidizing the metal center back to Ni^{II}. Repulsive elimination of isocyanide gives the tetrahedral 16e$^-$ intermediate Ni(η^1-O-TEMPO)(Sn^{t}Bu$_3$)(^{t}BuNC)(CO). The

TEMPO then transitions to its 3e$^-$ η^2-N,O binding mode, displacing a CO ligand (or a second isocyanide for •Ni(Sn^{t}Bu$_3$)(^{t}BuNC)$_3$) due to steric interactions and favorable heats of formation, forcing a 16e$^-$ distorted square planar final product. The N1-O1 bond distance of 1.409(1) Å is longer than that found in free TEMPO which is 1.283(9) Å. The geometry around the N1 atom is pyramidal [O1-N1-C22 = 117.75(4) °, O1-N1-C26 = 111.16(7) °, C26-N1-C22 = 119.25(1) °] and the Ni1-N1 and Ni1-O1 bond distances are short [Ni1-N1 = 1.958(2) Å, Ni1-O1 = 1.825(4) Å]. All of these structural parameters are consistent with a bidentate η^2-N,O-TEMPO coordination mode and formulation of a reduced TEMPO radical as a monoanionic TEMPO ligand according to the literature.[122]

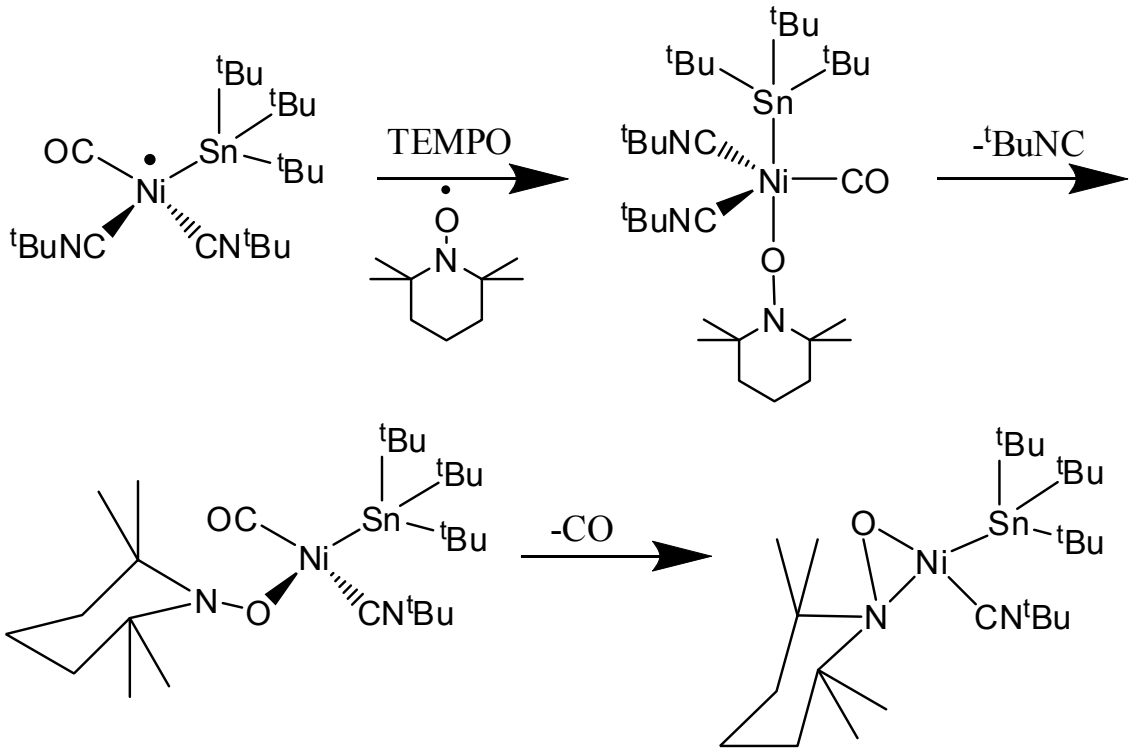

Scheme 3.4 Proposed mechanism for the formation of Ni(η^2-N,O-TEMPO)(Sn^{t}Bu$_3$)(^{t}BuNC).

^{1}H NMR of Ni(η^2-N,O-TEMPO)(Sn^{t}Bu$_3$)(^{t}BuNC) confirms the 3e$^-$ η^2-N,O binding mode of TEMPO, displaying magnetically inequivalent methyl group substituents. The loss of two 2e$^-$ donors and addition of one 3e$^-$ donor suggests that TEMPO initially interacted with a •Ni-Sn complex possessing an odd number 17e$^-$ to yield the 16e$^-$ final product, supporting Scheme 3.4 and providing further evidence for the proposed •Ni(Sn^{t}Bu$_3$)(^{t}BuNC)$_2$(CO). Why we do not isolate the 18e$^-$ trigonal bipyramidal intermediate Ni(η^1-O-TEMPO)(Sn^{t}Bu$_3$)(^{t}BuNC)$_2$(CO) in Scheme 3.3 is still unclear, and the next chapter will revisit this apparent requirement for η^2-N,O coordination of TEMPO to Ni. Despite our hopes of isolating ^{t}Bu$_3$Sn-(η^1-O-TEMPO), ^{t}Bu$_6$Sn$_2$ and ^{t}Bu$_6$Sn$_2$O are isolated as per usual.

To test the proposed dimer dissociation of [Ni(Sn^{t}Bu$_3$)(^{t}BuNC)$_2$(CO)]$_2$ into two •Ni(Sn^{t}Bu$_3$)(^{t}BuNC)$_2$(CO) radicals, pure crystalline [Ni(Sn^{t}Bu$_3$)(^{t}BuNC)$_2$(CO)]$_2$ was dissolved in C_6D_6 with two equivalents of TEMPO radical and the solution quickly decolorized to the characteristic brownish yellow of Ni(η^2-N,O-TEMPO)(Sn^{t}Bu$_3$)(^{t}BuNC) in ambient light. ^{1}H NMR spectroscopy confirmed the solution to contain a nearly pure mixture of Ni(η^2-N,O-TEMPO)(Sn^{t}Bu$_3$)(^{t}BuNC) and free isocyanide**.** This seems to imply the dissociation of [Ni(Sn^{t}Bu$_3$)(^{t}BuNC)$_2$(CO)]$_2$ into the radical monomers, which then reacts with the TEMPO radical.

There are few metal-η^2-N,O -TEMPO compounds reported,[123-125] and Ni-TEMPO is exceptionally uncommon with apparently two published examples.[126] Several of these metal-TEMPO complexes exhibit unusual catalytic abilities, especially in the way of alcohol oxidation to the corresponding aldehydes. Further study of Ni(η^2-N,O-TEMPO)-(Sn^{t}Bu$_3$)(^{t}BuNC) is currently under way in our lab. The successful trapping of a •Ni-Sn

fragment with TEMPO led us to attempt the capture of the complete monomeric species $\bullet Ni(Sn^tBu_3)(^tBuNC)_2(CO)$ by one electron oxidation to its non-coordinated cationic counterpart, similar to that seen in equation 3.1.

The first characterized example of a stable tin radical was reported by Sekiguchi et al. and it possessed an almost perfectly planar structure, as predicted.[39] Addition of triphenylcarbenium(Ph_3C^+, trityl) $[BAr^F{}_4]^-$ to a solution of this stable radical resulted in one electron oxidation of the radical to the planar cationic tin compound with a non-coordinating anion, shown in Figure 3.22.

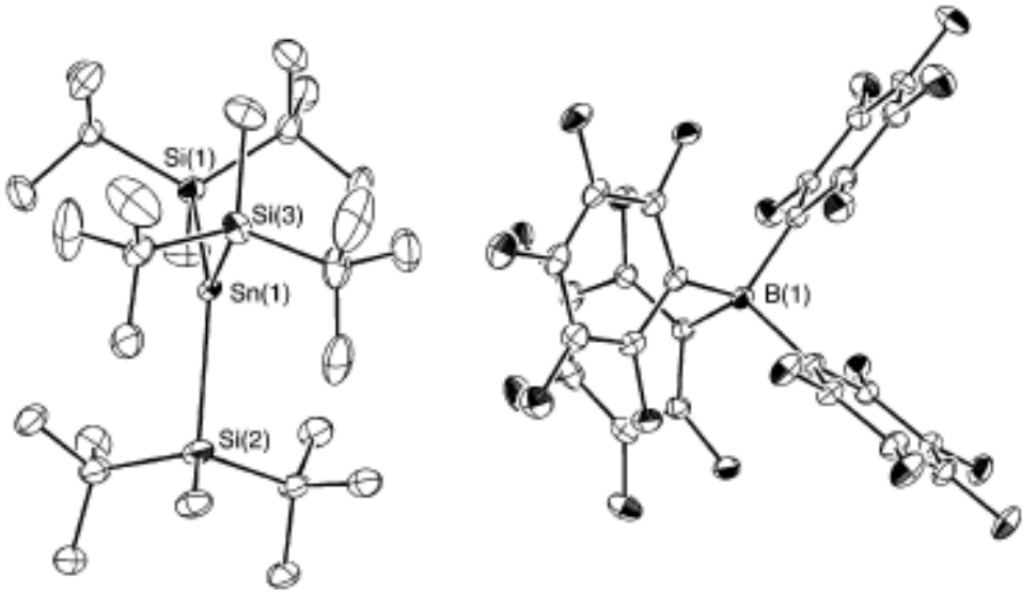

Figure 3.22 An ORTEP of the non-coordinated planar tin cation $(^tBu_2MeSi)_3Sn^+$ $BAr^F{}_4^-$

Desiring a similar result with the hypothesized $\bullet Ni(Sn^tBu_3)(^tBuNC)_2(CO)$ and $\bullet Sn^tBu_3$, starting material $Ni(Sn^tBu_3)_2(^tBuNC)_2(CO)$ was dissolved in THF with three equivalents of the similar triphenylcarbenium(trityl) hexafluorophosphate, $(Ph_3C)^+(PF_6)^-$,

and subsequently photolyzed. The reaction mixture initially becomes characteristically deep purple, but quickly decolorizes to the characteristic orange color of trityl-PF_6 after extinguishing the light source. As of yet, all we have isolated from this reaction is the quizzically trapped tin radical, $[(^tBu_3Sn)(PF_4)]_\infty$. We expected to capture $\bullet Sn^tBu_3$ as the non-coordinated cationic tin monomer similar to that seen in Figure 3.22, but X-ray diffraction analysis of $[(^tBu_3Sn)(PF_4)]_\infty$ (^{1}H NMR in toluene-d_8 at 1.264ppm, $^3J_{Sn\text{-}H}$= 73 Hz) instead yielded the linear polymeric salt structure of alternating planar tri-*tert*-butyl tin cations and bridging tetrahedral tetra-fluoro*phosphite* anions, PF_4^-, shown in Figure 3.23. Further crystallographic information is provided in Appendix B Table B.3.

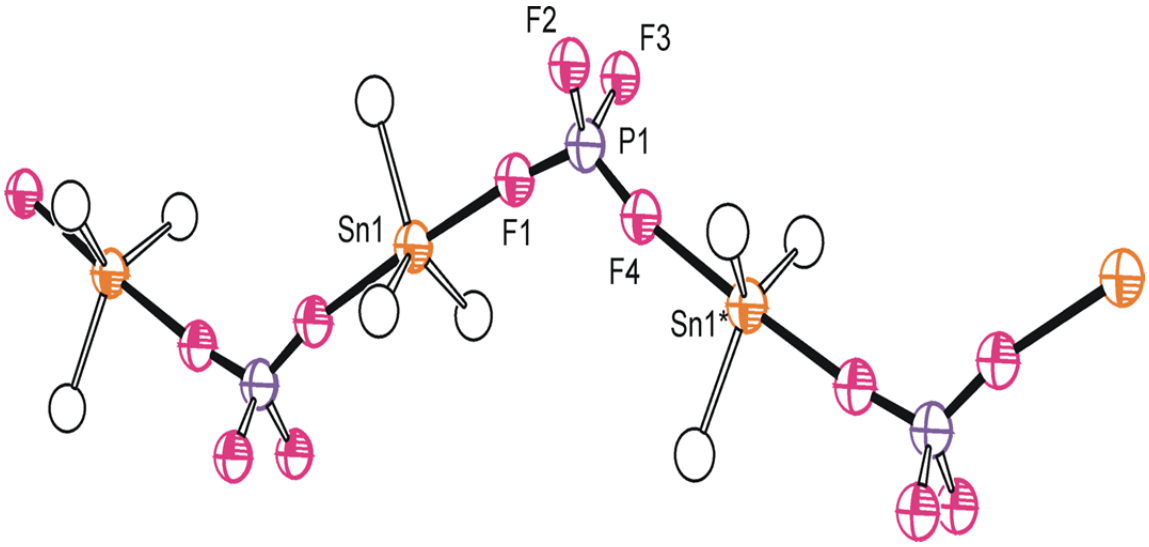

Figure 3.23 An ORTEP showing the partial molecular structure of $[(^tBu_3Sn)(PF_4)]_\infty$ at 30 % thermal ellipsoid probability. Methyl groups excluded for clarity.

Careful comparison of Figures 3.22 and 3.23 reveals structural similarity and the planar arrangement of $^tBu_3Sn$ in $[(^tBu_3Sn)(PF_4)]_\infty$ is clear. However, the non-coordinating PF_6^- anion has been activated and bound unlike the vastly superior $BAr^F{}_4^-$.

X-ray crystallographic and ^{31}P NMR analysis of trityl-PF_6 was done to assure we were not supplied with BF_4 and these shown in Appendix B Figures B.8 and B.9. The structure of trityl-PF_6 was previously unknown and further crystallographic data is provided in Appendix B Table B.3.

This extraordinarily rare four-coordinate anion of phosphorus, PF_4^-, has been shown to exist in recent years and its synthesis was more than difficult.[127] There is only one structurally characterized metal complex in the literature containing this linking decomposition product of PF_6^- as a bridging tetrahedral PF_4^-, and it is a dinuclear gold-carbene complex.[128] In $[(^tBu_3Sn)(PF_4)]_\infty$ the PF_4^- and $^tBu_3Sn^+$ form crystallographically infinite Sn-F-P linear chains which may prove to function as molecular wires, possibly possessing favorable properties for use in nanotechnology.[129] Any electronic properties of $[(^tBu_3Sn)(PF_4)]_\infty$ are beyond the scope of our research and were not pursued. Phosphorus-fluorine bond activation and PF_4^- formation is infamously difficult, and yet was accomplished at room temperature by the facile photo generation of our tin radical.

It is necessary to mention that when trityl-PF_6 is added (even in a dark room) to a solution of $Ni(Sn^tBu_3)_2(^tBuNC)_3$ there is immediate color change to the blue/green of the low temperature photolysis product seen in Figure 3.19, which then quickly decolorizes at room temperature. The compounds $[(^tBu_3Sn)(PF_4)]_\infty$ and $Ni(^tBuNC)_4$ are isolated from this reaction mixture. This was very unexpected, as the non-photochemical cleavage of the Ni-Sn bond does not occur with $Ni(Sn^tBu_3)_2(^tBuNC)_2(CO)$. This is another possible piece of evidence for symmetry distortion in solutions of $Ni(Sn^tBu_3)_2(^tBuNC)_3$ resulting in two FTIR active stretches. Perhaps $Ni(Sn^tBu_3)_2(^tBuNC)_3$ is so sterically strained that the Ni-Sn bonds are in state of flux leaving them extremely vulnerable to reaction.

It is interesting to note that all attempts at different types of mass spectroscopy for $Ni(Sn^tBu_3)_2(^tBuNC)_3$ resulted in one major peak at 598.2668 m/z. This is almost the exact predicted molecular weight of the of the proposed monomeric radical $\bullet Ni(Sn^tBu_3)(^tBuNC)_3$ to within a few ten thousandths of an amu, and it indeed shows identical isotope distribution to the theoretically generated plot shown in Figure 3.24.

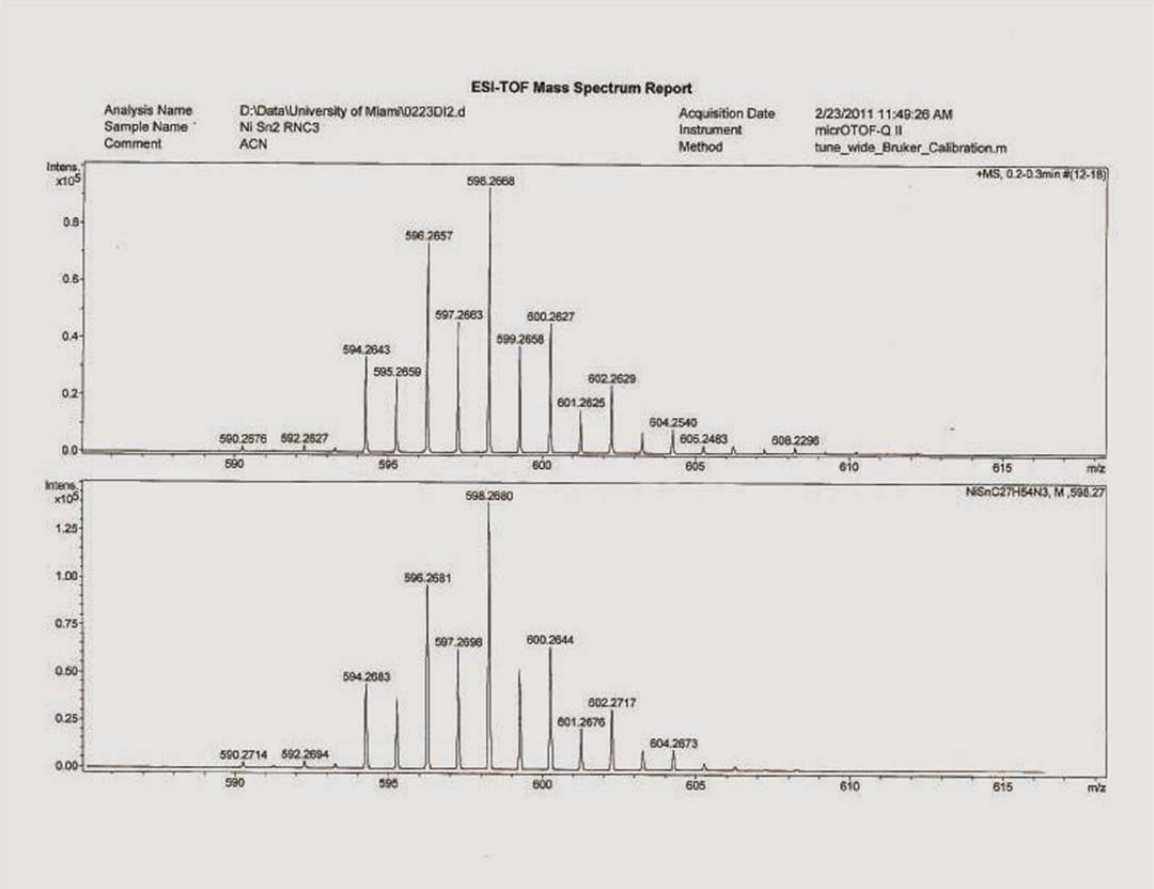

Figure 3.24 ESI-TOF mass spectrum report for $Ni(Sn^tBu_3)_2(^tBuNC)_3$ (top) and the predicted spectrum of $\bullet Ni(Sn^tBu_3)(^tBuNC)_3$ (bottom).

This provides convincing data for the extreme lability of the Ni-Sn bond in $Ni(Sn^tBu_3)_2(^tBuNC)_3$ and evidence for the existence of the proposed radicals $\bullet Ni(Sn^tBu_3)(^tBuNC)_3$ and $\bullet Ni(Sn^tBu_3)(^tBuNC)_2(CO)$. A space filling model of $Ni(Sn^tBu_3)_2(^tBuNC)_3$ was generated to display the immense equatorial bulk responsible

for this bond instability and it is provided in Appendix B Figure B.10. Examination of this space filling model reveals an extremely encumbered situation around the Ni center which likely imparts extra reactivity to $Ni(Sn^tBu_3)_2(^tBuNC)_3$ vs $Ni(Sn^tBu_3)_2(^tBuNC)_2(CO)$. Accordingly, mass spectra of $Ni(Sn^tBu_3)_2(^tBuNC)_2(CO)$ do not give the predicted spectrum of $\bullet Ni(Sn^tBu_3)(^tBuNC)_2(CO)$ but rather fragmentation patterns like [M – CO] and [M – ^{t}Bu].

Mentioned earlier, both $Ni(Sn^tBu_3)_2(^tBuNC)_3$ and $Ni(Sn^tBu_3)_2(^tBuNC)_2(CO)$ will react with iodine, I_2. This was discovered when we attempted to trap radical intermediates as iodide salts. Before photolysis could even be initiated, these Ni-Sn compounds reacted with I_2 to yield the dark red $16e^-$ square planar $Ni(I)_2(^tBuNC)_2$ shown in Figure 3.25, as well as $^tBu_6Sn_2$ and free CO/isocyanide. The structure of $Ni(I)_2(^tBuNC)_2$ was not previously known, so it is presented here and further crystallographic information is provided in Appendix B Table B.4.[130]

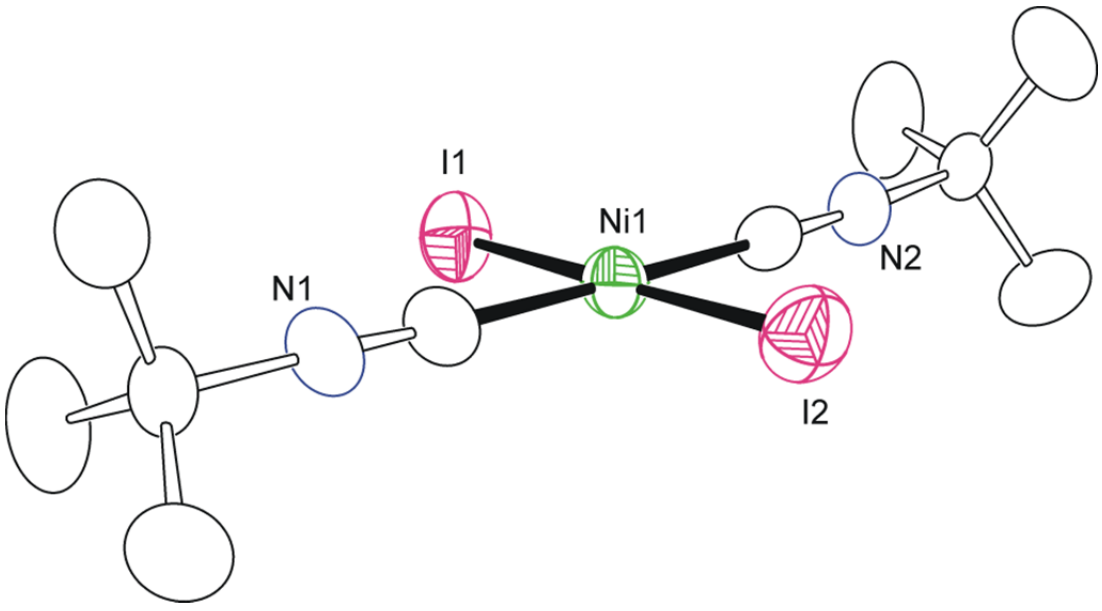

Figure 3.25 An ORTEP showing the molecular structure of $Ni(I)_2(^tBuNC)_2$ at 30 % thermal ellipsoid probability.

Presently we have not successfully trapped the entire monomeric radical species $\bullet Ni(Sn^tBu_3)(^tBuNC)_2(CO)$ or $\bullet Ni(Sn^tBu_3)(^tBuNC)_3$, though we consider the dimeric $[Ni(Sn^tBu_3)(^tBuNC)_2(CO)]_2$ to technically be two trapped radicals available for reaction. Effort persists in our lab to isolate a complete monomeric species.

UV-Vis Spectroscopy of $Ni(Sn^tBu_3)_2(^tBuNC)_3$, $Ni(Sn^tBu_3)_2(^tBuNC)_2(CO)$, and $Ni(Sn^tBu_3)_2(CO)_3$ and Their Room Temperature Photolysis Products. When working with photochemically active compounds, UV-Vis spectroscopic characterization can be enlightening and is clearly required. Presented in the previous chapter, the complex $Ni(Sn^tBu_3)_2(CO)_3$ was made in an analogous manner to $Ni(Sn^tBu_3)_2(^tBuNC)_3$, utilizing $Ni(CO)_4$ in place of $Ni(^tBuNC)_4$. It was unknown if this tris-carbonyl compound would possess photochemical properties similar to $Ni(Sn^tBu_3)_2(^tBuNC)_3$ and $Ni(Sn^tBu_3)_2(^tBuNC)_2(CO)$, and *qualitative* UV-Vis spectroscopic measurements provided an excellent means of answering this question as well as several others. The first experiment we conducted was the serial dilution of $Ni(Sn^tBu_3)_2(^tBuNC)_2(CO)$ in hexane to afford the appropriately low concentration of approximately 10^{-5} M. The UV-Vis spectrum showed a strong absorbance peak in the near UV at 375 nm. We were unsure if photolysis was possible at such low concentrations, but subsequent exposure to light resulted in a faint color change to purple as well as the presence of a new absorbance peak in the visible spectrum at 564 nm, shown in Figure 3.26. To confirm these results, pure crystalline $[Ni(Sn^tBu_3)(^tBuNC)_2(CO)]_2$ was diluted to appropriate concentrations as quickly as possible, and rapidly brought to the instrument room for spectroscopy. The spectrum indeed shows strong absorbance at 564 nm which we attribute to $[Ni(Sn^tBu_3)(^tBuNC)_2(CO)]_2$ as well as strong absorbance at 375 nm, attributed to

$Ni(Sn^tBu_3)_2(^tBuNC)_2(CO)$. When the absorbance of this cuvette at 564 nm was followed over time at room temperature, it was seen to decrease to nearly 0 with smooth kinetics while the peak at 375 nm grew considerably, seen in Figures 3.27 and 3.28. We consider this to be reliable proof for the room temperature dissociation/decomposition/ disproportionation of $[Ni(Sn^tBu_3)(^tBuNC)_2(CO)]_2$ to partially regenerate the starting complex $Ni(Sn^tBu_3)_2(^tBuNC)_2(CO)$.

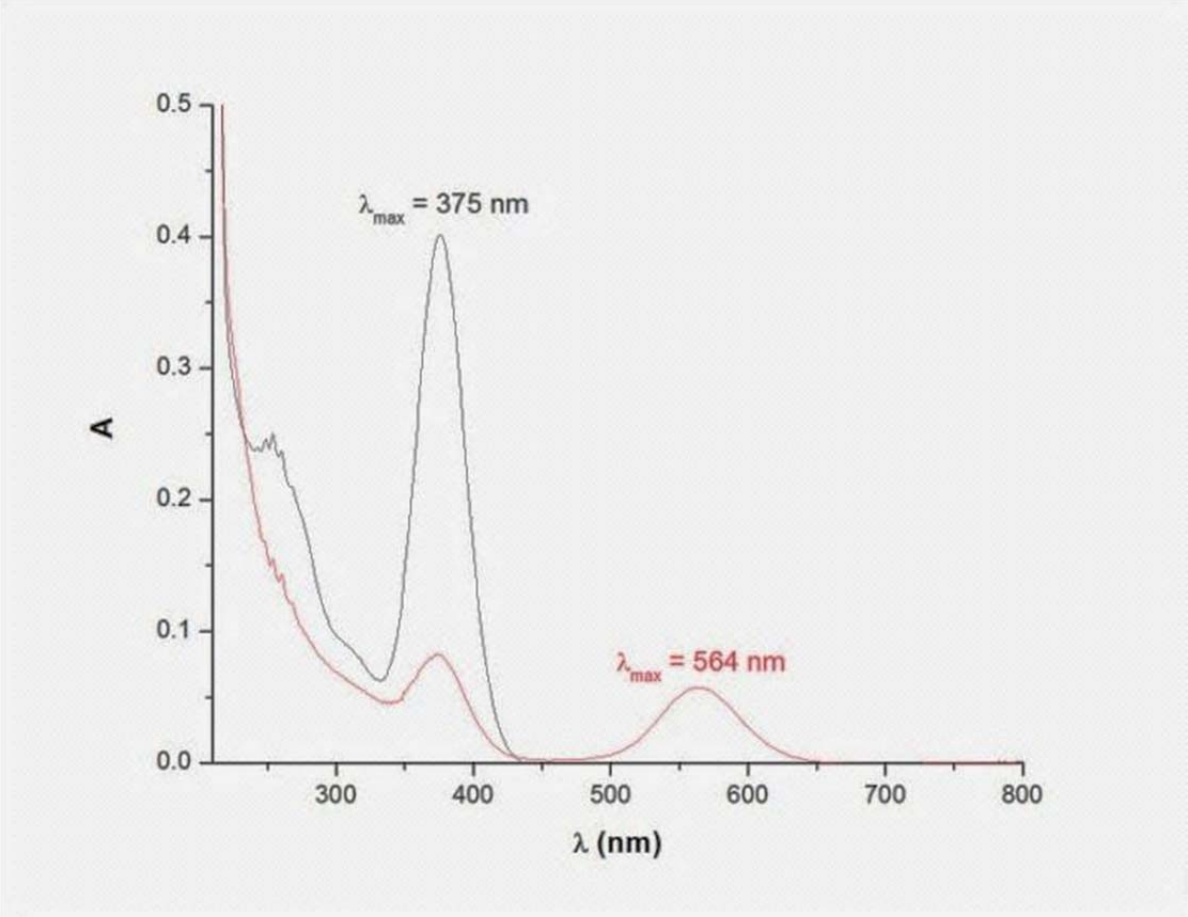

Figure 3.26 UV-Vis spectra showing $Ni(Sn^tBu_3)_2(^tBuNC)_2(CO)$ (black) and subsequent photolysis to $[Ni(Sn^tBu_3)(^tBuNC)_2(CO)]_2$ with remaining starting material (red).

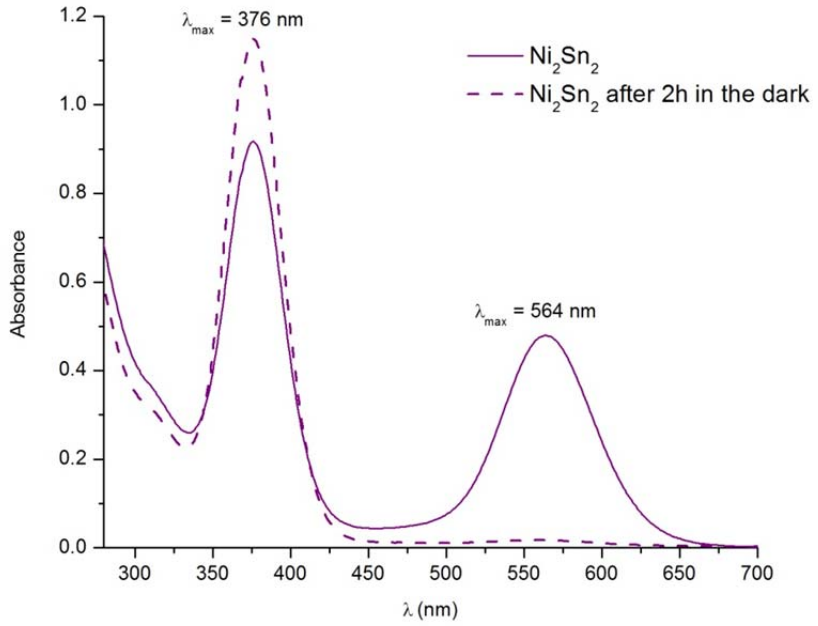

Figure 3.27. UV-Vis spectra showing pure $[Ni(Sn^tBu_3)(^tBuNC)_2(CO)]_2$ dissolved in room temperature hexane (solid line) and its partial regeneration of $Ni(Sn^tBu_3)_2(^tBuNC)_2(CO)$ after 2 hours (dashed line).

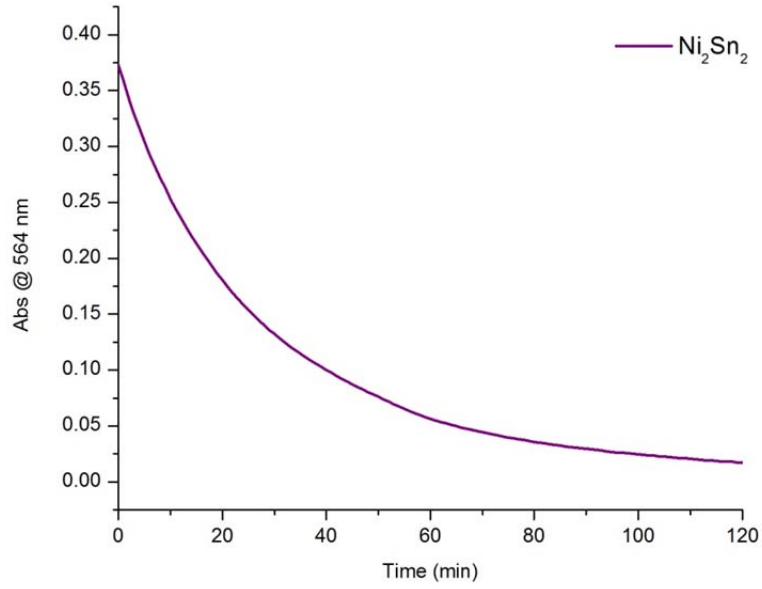

Figure 3.28. Plot of UV-Vis absorption at 564 nm for $[Ni(Sn^tBu_3)(^tBuNC)_2(CO)]_2$ vs time over two hours.

When $Ni(Sn^tBu_3)_2(^tBuNC)_3$ was diluted to appropriate concentrations and scanned, a similar absorbance was seen at a lower energy of 392 nm. This was expected since we had previously shown that the Ni-Sn bonds in $Ni(Sn^tBu_3)_2(^tBuNC)_3$ were more labile than $Ni(Sn^tBu_3)_2(^tBuNC)_2(CO)$, attributed to steric repulsion. When the cuvette was photolyzed, the lack of major color change suggested the expected conversion to $Ni(^tBuNC)_4$. Appropriately, the UV-Vis spectrum showed complete consumption of $Ni(Sn^tBu_3)_2(^tBuNC)_3$ with no appearance of any new absorbances, shown in Appendix B Figure B.11. To check this finding, a sample of pure $Ni(^tBuNC)_4$ was synthesized and diluted for UV-Vis measurement which showed no appreciable absorbance above baseline even at extremely high concentrations. Unfortunately we were not able to attempt a low temperature UV-Vis for this measurement, but it is safe to assume that the cold blue solution seen in Figure 3.19 would display a new absorbance similar to $[Ni(Sn^tBu_3)(^tBuNC)_2(CO)]_2$ around 500-600 nm.

Before any spectroscopic experiments with $Ni(Sn^tBu_3)_2(CO)_3$ were performed, we hypothesized that it would have similar absorbance to $Ni(Sn^tBu_3)_2(^tBuNC)_3$ and $Ni(Sn^tBu_3)_2(^tBuNC)_2(CO)$, though at a shorter wavelength. This was assumed because the tris-carbonyl equatorial ligands provide little steric repulsion, and the Ni-Sn bond should be more difficult to cleave which requires higher energy photons. Indeed, diluted solutions of $Ni(Sn^tBu_3)_2(CO)_3$ show strong absorbance at 352 nm, higher energy than 375 and 392 nm shown in Appendix B Figure B.12. Photolysis of these dilute $Ni(Sn^tBu_3)_2(CO)_3$ solutions produce a slight amount of detectable photolysis product, seen at 511 nm, but intentional over concentration of cuvettes to absorbance > 1 will

produce excellent photolysis to give a dark pink solution with strong absorbance at 511 nm, seen in Figure 3.29

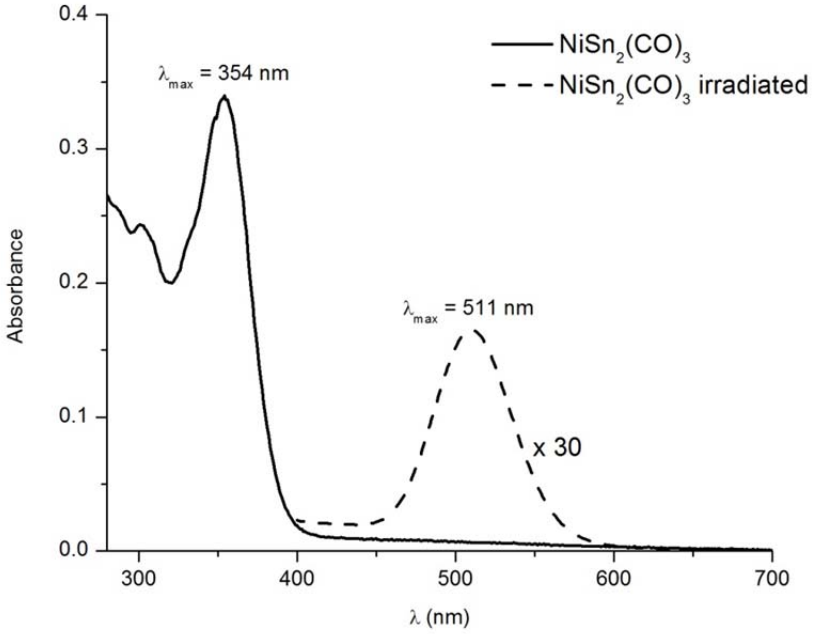

Figure 3.29 UV-Vis spectra of $Ni(Sn^tBu_3)_2(CO)_3$ (solid line) and subsequent photolysis product from a 30 times more concentrated solution (dashed line).

Photolyzing an even more concentrated sample of $Ni(Sn^tBu_3)_2(CO)_3$ at – 78 °C in a Schlenk flask results in a dark brown purple solution, a similar color to the blue and purple of $Ni(Sn^tBu_3)_2(^tBuNC)_3$ and $Ni(Sn^tBu_3)_2(^tBuNC)_2(CO)$ photolysis products, respectively. These UV-Vis spectroscopy experiments have shown that the photolysis reaction of $Ni(Sn^tBu_3)_2(CO)_3$ is nearly identical to that of $Ni(Sn^tBu_3)_2(^tBuNC)_3$ or $Ni(Sn^tBu_3)_2(^tBuNC)_2(CO)$, and we assume the same for $Ni(Sn^tBu_3)_2(^tBuNC)(CO)_2$. X-ray quality crystals of the proposed dimer $[Ni(Sn^tBu_3)(CO)_3]_2$ have as of yet not been grown, though work continues in our lab.

The photolytic reaction of $Ni(Sn^tBu_3)_2(CO)_3$ in the presence of TEMPO ligand does not produce the expected $Ni(\eta^2\text{-N,O-TEMPO})(Sn^tBu_3)(CO)$ and this may be due to the less bulky CO ligands having stronger bonds to the Ni center. $Ni(Sn^tBu_3)_2(CO)_3$ will not react with I_2 to give $Ni(I)_2(CO)_2$, nor is it vulnerable to trityl-PF_6. All of these differences in reactivity seem to be attributed to the bulkier nature of ^{t}BuNC vs CO.

Photocatalytic Cycle of $Ni(Sn^tBu_3)_2(^tBuNC)_3$. Having gathered all the previously presented experimental data and observations, a relation between the reactants and products in equation 3.3 became evident. This permitted the formation of a proposed photocatalytic cycle shown in Scheme 3.5.

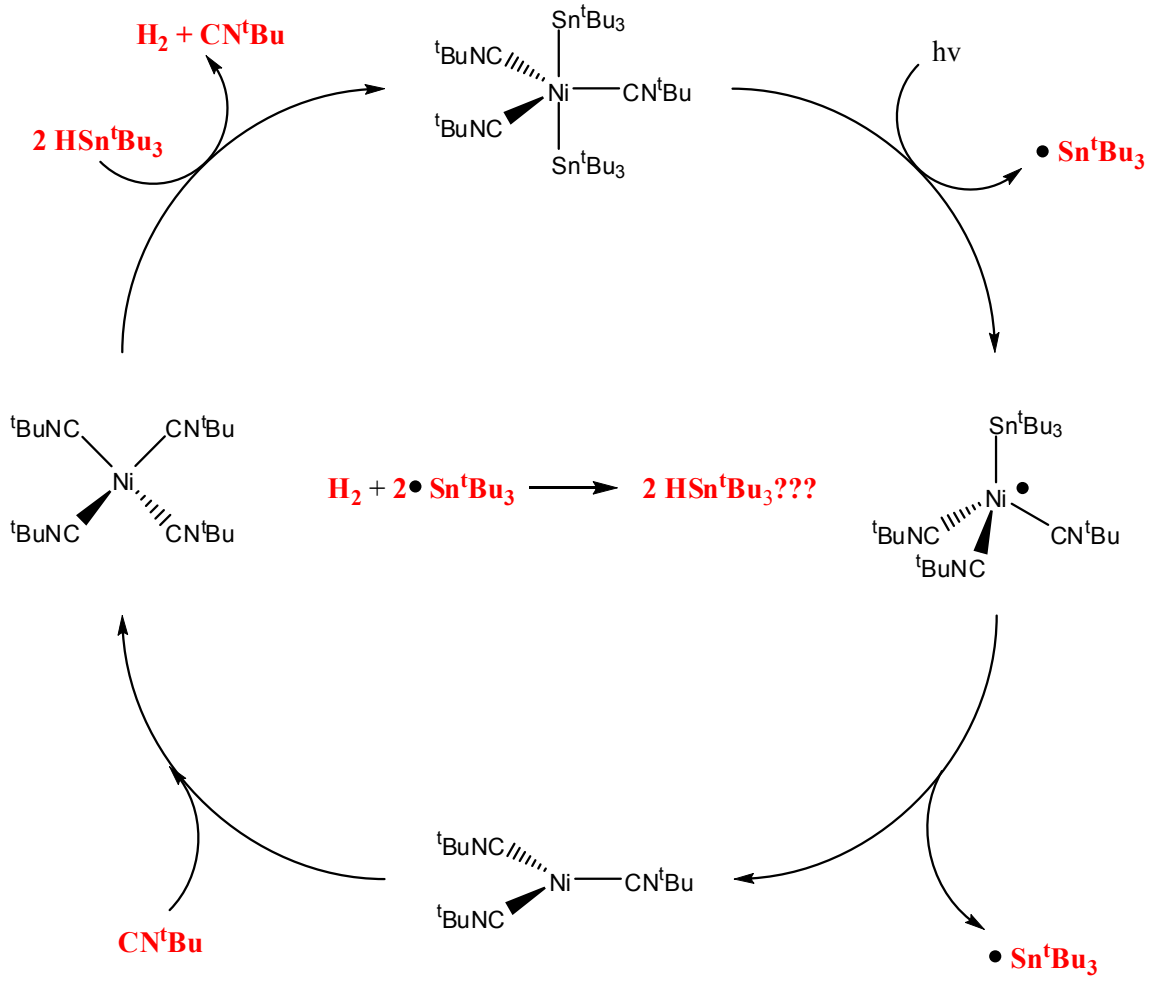

Scheme 3.5 Proposed photocatalytic cycle of Ni(^{t}BuNC)$_4$ with ^{t}Bu$_3$SnH.

This cycle takes advantage of the fact that the starting material, Ni(^{t}BuNC)$_4$, is converted to Ni(Sn^{t}Bu$_3$)$_2$(^{t}BuNC)$_3$ by adding two ^{t}Bu$_3$Sn fragments while eliminating H$_2$ and ^{t}BuNC. Photolysis of Ni(Sn^{t}Bu$_3$)$_2$(^{t}BuNC)$_3$ results in the regeneration of Ni(^{t}BuNC)$_4$ by picking up free isocyanide either added in excess or from decomposition/ disproportionation of another molecule, and formation of ^{t}Bu$_6$Sn$_2$ and H$_2$. Literature

reference supports the intermediate in this cycle, providing evidence for the existence of $Ni(^tBuNC)_3$.[131]

^1H NMR experiments showed that room temperature photolysis of $Ni(Sn^tBu_3)_2(^tBuNC)_3$ in the presence of excess $^tBu_3SnH$ and ^tBuNC will convert $Ni(Sn^tBu_3)_2(^tBuNC)_3$ to $Ni(^tBuNC)_4$ and completely catalyze the conversion of tin hydride into $^tBu_6Sn_2$ and H_2 with little to no decomposition of Ni products. The ^1H NMR spectra exemplifying this is shown in Figure 3.30.

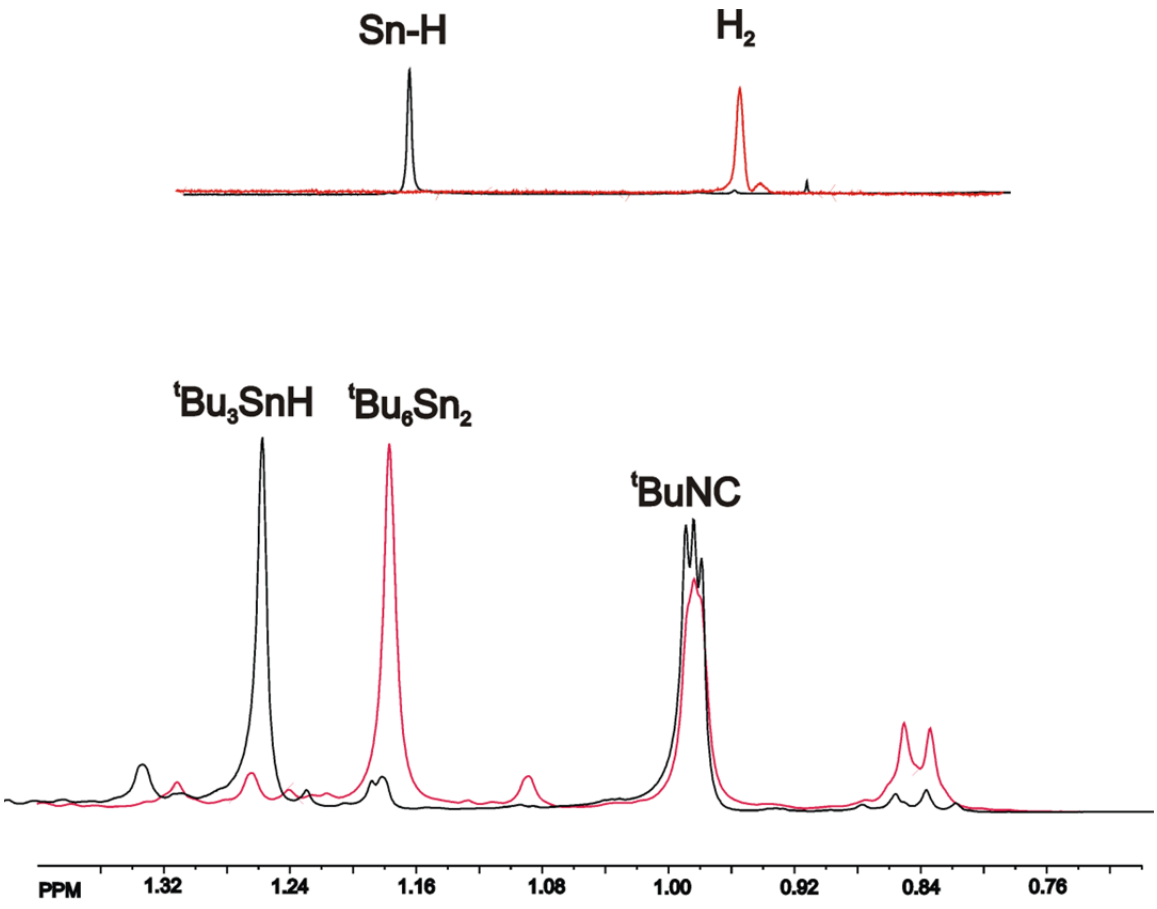

Figure 3.30 ^1H NMR in toluene-d_8 of 1eq $Ni(Sn^tBu_3)_2$, 10eq $^tBu_3SnH$, and 10eq ^tBuNC before photolysis (black) and after photolysis (red).
Top insert is the hydride and H_2 region.

A very interesting question is whether or not the tin radical $\bullet Sn^tBu_3$ is capable of activating and splitting H_2 gas to regenerate $^tBu_3SnH$, seen in Scheme 3.5 as red text. If this were possible, the previous catalytic cycle becomes a completely closed system under H_2 atmosphere with only the input of light energy to do chemistry. Such a closed system could be compared to natural photosynthesis with the uptake of light energy to perform useful chemical reactions.[132] However the cycle shown above would afford no new chemicals, bur would rather generate thermal heat as the reaction proceeds to completion only to be reversed by "free" light energy.

A separate ^1H NMR experiment was performed identical to the one stated above with a catalytic amount of $Ni(Sn^tBu_3)_2(^tBuNC)_3$ and excess $^tBu_3SnH$ and ^tBuNC, but this NMR tube was placed under an atmosphere of D_2 as opposed to the usual argon. Based on the proposed hydrogenating mechanism in red, the repeated reaction would consume and produce tin-hydride, but under an atmosphere of D_2 there should be a scrambling of H_2 and D_2 to afford H-D which would display a triplet in NMR spectra. However H-D scrambling has not yet been detected. The resulting ^1H NMR spectra was nearly identical to that seen in 3.30. There was no evidence for $Ni(Sn^tBu_3)(^tBuNC)_3H$ or D in any of these experiments. Further fine-tuning of this reaction is in progress and may yet be successful in the future.

Determining the Photochemical Role of Bulky ^{t}Bu Substituents. To better understand the photochemical nature of these compounds, we sought to synthesize the triphenyl tin analogue $Ni(SnPh_3)_2(^tBuNC)_3$ to check for similar photolytic activity. This novel compound is indeed afforded in good yield by the reaction of $Ni(^tBuNC)_4$ and the commercially available Ph_3SnH in refluxing hexane. The molecular structure of

$Ni(SnPh_3)_2(^tBuNC)_3$, seen in Figure 3.31, is very similar to $Ni(Sn^tBu_3)_2(^tBuNC)_3$, both possessing approximate D_{3h} symmetry. FTIR spectral data is provided in Appendix B Figure B.2 and further crystallographic data is provided in Appendix B Table B.4.

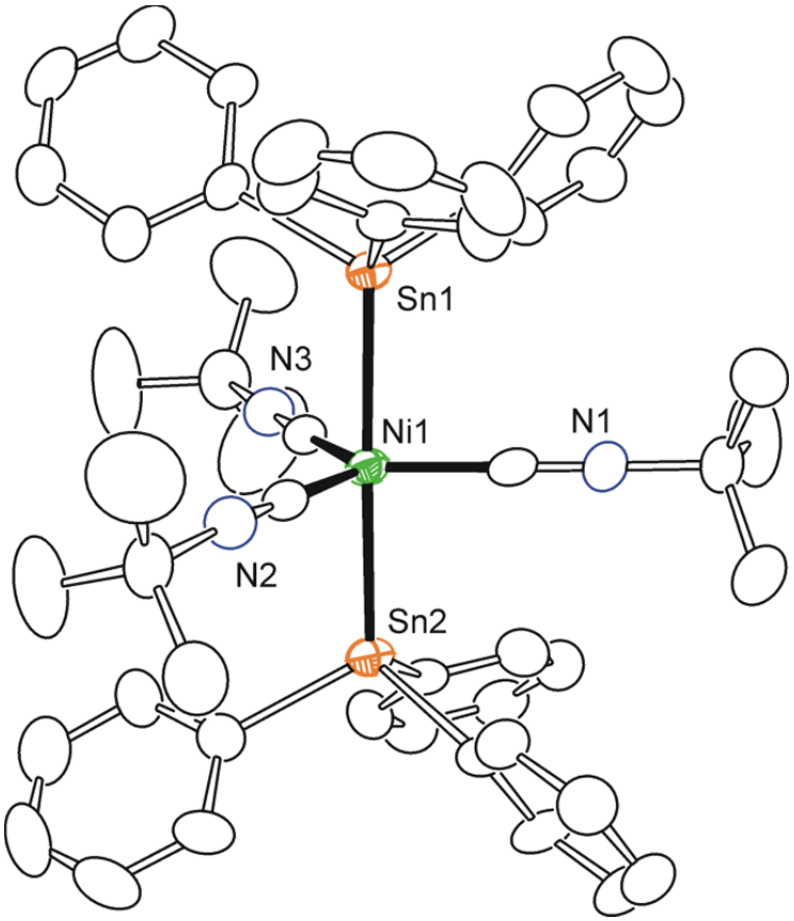

Figure 3.31 An ORTEP showing the molecular structure of $Ni(SnPh_3)_2(^tBuNC)_3$ at 30 % thermal ellipsoid probability.

Based on the structural and spectroscopic similarity to $Ni(Sn^tBu_3)_2(^tBuNC)_3$ we fully expected successful photolysis, perhaps even aided by the electron withdrawing resonance of the phenyl rings. However, photolysis at both room and low temperature yielded no reaction. FTIR spectroscopic analysis showed virtually no change in solution spectra even after several minutes of photolysis with a 300 W mercury halide lamp.

While it is unclear as to why $Ni(SnPh_3)_2(^tBuNC)_3$ exhibits no photochemical reactivity, we are lead to believe it is the superior bulk of the *tert*-butyl tin ligands that allow cleavage of the sterically strained Ni-Sn bond by light. Infact, the Sn-Ni bonds in $Ni(SnPh_3)_2(^tBuNC)_3$ are 2.49 Å vs 2.61 Å in $Ni(Sn^tBu_3)_2(^tBuNC)_3$. The significantly longer Ni-Sn distance of the ^{t}Bu derivative can be attributed to its superior bulk vs the phenyl analogue, and thus the Ni-Sn bonds in $Ni(Sn^tBu_3)_2(^tBuNC)_3$ should be much more labile than those in $Ni(SnPh_3)_2(^tBuNC)_3$. $Ni(SnPh_3)_2(^tBuNC)_3$ is also stable to trityl-PF_6. This is an excellent example of chemical and photochemical reactivity imparted solely by more sterically demanding ligands, $^tBu_3Sn$ vs Ph_3Sn in this case.

Transference of $\bullet Sn^tBu_3$ to Metal Carbonyls. After many unsuccessful attempts at capturing the monomeric radicals $\bullet Ni(Sn^tBu_3)(^tBuNC)_2(CO)$ and $\bullet Ni(Sn^tBu_3)(^tBuNC)_3$, we chose to put that project on hold and move forward to explore the possible chemistry of the photochemically generated tin radical, $\bullet Sn^tBu_3$. It has already been shown to dimerize yielding $^tBu_6Sn_2$ and $(^tBu_3Sn)_2O$ in Figure 3.8. It also possesses the ability to activate and bind both CO_2 and PF_6^-, the products of which are shown in Figures 3.9 and 3.23, respectively. It stands to reason that this reactive tin species should be able to coordinate with other transition metal compounds, particularly metal carbonyl complexes.

In the last chapter, we showed that $Fe_2(CO)_9$ will react with $^tBu_3SnH$ to give $Fe_2(\mu\text{-}Sn^tBu_2)_2(CO)_8$ and that this complex was capable of selective benzylic C-H activation. However, this compound was only formed at very high temperatures near 100 °C. In fact, tri-*tert*-butyl tin hydride has also been mixed with $Fe(CO)_5$ and $Fe_3(CO)_{12}$ at extreme temperatures, yielding little to no isolatable products. This tendency for Fe

carbonyls to not react with $^{t}Bu_3SnH$ was unforeseen as Ru analogues react nicely.[133] The idea arose that perhaps the photochemically generated tin radical would be capable of reaction with iron carbonyls, and indeed we were successful at synthesizing a new Fe-Sn compound, *trans*-$Fe(Sn^{t}Bu_3)_2(CO)_4$, shown in Figure 3.32. Photolysis in the presence of $Fe_3(CO)_{12}$ yielded a characteristically dark purple solution of $[Ni(Sn^{t}Bu_3)(^{t}BuNC)_2(CO)]_2$ indicating no reaction with Ni-Sn species, but workup and crystallization of the reaction mixture also yielded colorless crystals of $Fe(Sn^{t}Bu_3)_2(CO)_4$. Further crystallographic data is provided in Appendix B Table B.5.

This *trans* di-tin iron complex was characterized by FTIR spectroscopy (1976 cm^{-1} in hexane) and X-ray crystallographic analysis. Possessing an octahedral geometry, $Fe(Sn^{t}Bu_3)_2(CO)_4$ can be considered the oxidative product of planar $Fe(CO)_4$ and two $\bullet Sn^{t}Bu_3$ radicals, and was formed in a facile manner by room temperature photolysis of $Ni(Sn^{t}Bu_3)_2(^{t}BuNC)_3$ or $Ni(Sn^{t}Bu_3)_2(^{t}BuNC)_2(CO)$ in the presence of $Fe_3(CO)_{12}$. The $SnPh_3$ analogue of this Fe-Sn_2 complex was synthesized in 1977 by combining $Na_2Fe(CO)_4$ with Ph_3SnCl, a salt elimination metathesis reaction.[134] However, this phenyl derivative exists in the *cis* form and seems to be a capped version of a tetrahedral $Fe(CO)_4$. The geometric preference of $Fe(CO)_4$ with the differing tin ligands is interesting. The *trans* state assumed by $Fe(Sn^{t}Bu_3)_2(CO)_4$ is yet another testament to the superior bulk of ^{t}Bu vs Ph groups.

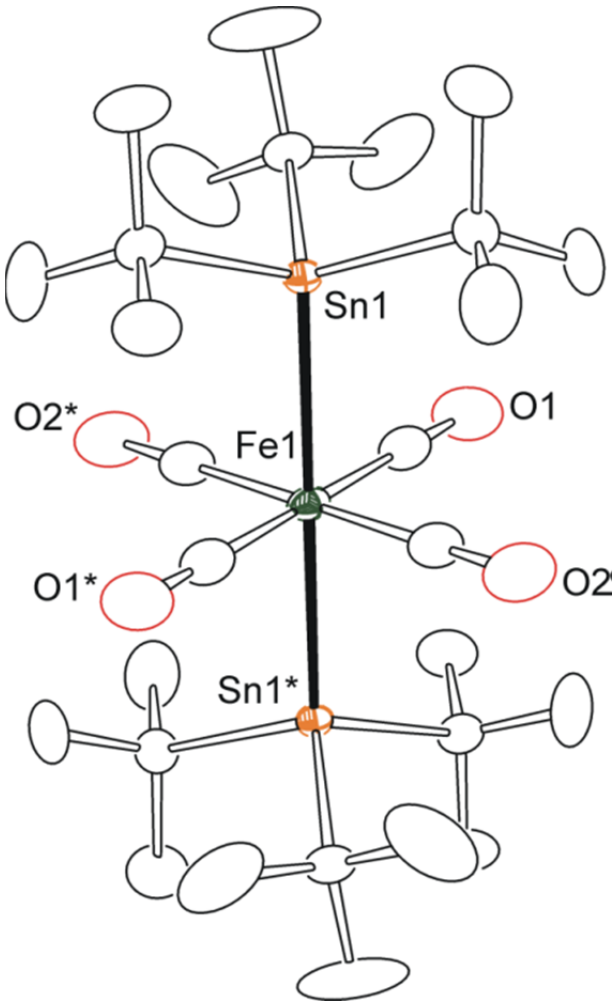

Figure 3.32 An ORTEP showing the molecular structure of $Fe(Sn^tBu_3)_2(CO)_4$ at 30 % thermal ellipsoid probability.

Another example of tin transference to a metal carbonyl complex was found when $Ni(Sn^tBu_3)_2(^tBuNC)_3$ or $Ni(Sn^tBu_3)_2(^tBuNC)_2(CO)$ was photolyzed in the presence of the molybdenum-hydride "piano stool" complex, $HMo(CO)_3Cp$ (HMp).[135] Photolysis yielded a characteristically dark purple solution of $[Ni(Sn^tBu_3)(^tBuNC)_2(CO)]_2$ indicating no reaction with Ni-Sn species, but workup and crystallization of the reaction mixture also yielded light orange crystals. X-ray diffraction analysis of these crystals gave the structure of $Mo(CO)_3(Cp)(Sn^tBu_3)$ shown in Figure 3.33. FTIR spectroscopy shows two

stretches appropriately at 1994 and 1904 cm^{-1} in hexane. Our hope of hydrogen atom transfer to $\bullet Ni(Sn^tBu_3)(^tBuNC)_2(CO)$ and $\bullet Ni(Sn^tBu_3)(^tBuNC)_3$ was not successful and hydrogen was most likely eliminated as H_2 gas. However, the tin radical was efficiently trapped by the $\bullet Mp$ fragment. Similar compounds to this have also been generated, again utilizing thermodynamically favorable salt formation reactions.[136]

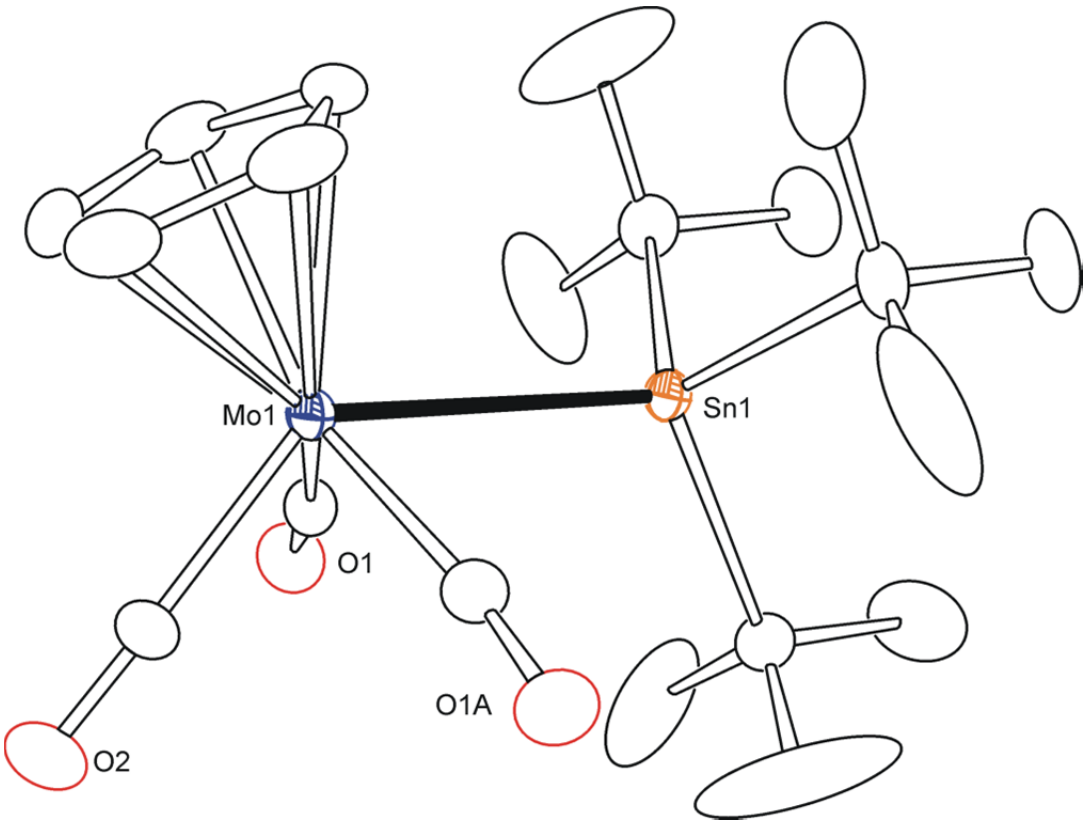

Figure 3.33 An ORTEP showing the molecular structure of $Mo(Sn^tBu_3)(CO)_3Cp$ at 30% thermal ellipsoid probability.

Evidently the tin radical $\bullet Sn^tBu_3$ is highly reactive and can proceed through mechanistic pathways inaccessible to the tin hydride $^tBu_3SnH$ which is presumably forced to react and bind via oxidative addition. This new synthetic route should provide many metal-Sn^tBu_3 complexes that were previously unable to be generated with $^tBu_3SnH$.

Further attempts at transferring the $\bullet Sn^tBu_3$ fragment to other metal complexes are in progress.

3.3 Conclusions

We have reported the successful synthesis of heterobimetallic Ni-Sn compounds containing the sterically encumbered Sn^tBu_3 ligand: $Ni(Sn^tBu_3)_2(^tBuNC)_3$, $Ni(Sn^tBu_3)_2(^tBuNC)_2(CO)$, $Ni(Sn^tBu_3)_2(^tBuNC)(CO)_2$, $[Ni(Sn^tBu_3)(^tBuNC)_2(CO)]_2$, and $Ni(\eta^2\text{-N,O-TEMPO})(Sn^tBu_3)(^tBuNC)$. The previous chapter presented $Ni(Sn^tBu_3)_2(CO)_3$ which is structurally analogous to $Ni(Sn^tBu_3)_2(^tBuNC)_3$. The unexpected reaction of $Ni(Sn^tBu_3)_2(^tBuNC)_3$ and $Ni(Sn^tBu_3)_2(^tBuNC)_2(CO)$ with light was found to cleave Ni-Sn bonds, but only the dimeric product $[Ni(Sn^tBu_3)(^tBuNC)_2(CO)]_2$ has been isolated from these photolysis reactions. Evidence has been presented for the existence of both nickel and tin centered radicals due to initial bond photolysis generating $\bullet Ni(Sn^tBu_3)(^tBuNC)_2(CO)$ and $\bullet Sn^tBu_3$ as well as dissociation of the Ni-Ni bond in $[Ni(Sn^tBu_3)(^tBuNC)_2(CO)]_2$ yielding two $\bullet Ni(Sn^tBu_3)(^tBuNC)_2(CO)$. The room-temperature photolysis of $Ni(Sn^tBu_3)_2(^tBuNC)_3$ was found to regenerate the starting material $Ni(^tBuNC)_4$, while low-temperature photolysis produced a peacock blue solution which we believe contains $[Ni(Sn^tBu_3)(^tBuNC)_3]_2$ and $\bullet Ni(Sn^tBu_3)(^tBuNC)_3$. Characterization of $[Ni(Sn^tBu_3)(^tBuNC)_2(CO)]_2$ in solution was difficult and we utilized low temperature ^1H and ^{13}C NMR. ^{13}CO-$[Ni(Sn^tBu_3)(^tBuNC)_2(CO)]_2$ showed a major resonance at 205 ppm, completely new and unattributed to $Ni(Sn^tBu_3)(^tBuNC)_2(CO)$. Low temperature NMR studies showed line broadening and excess noise to signal.

Low temperature ESR of $[Ni(Sn^tBu_3)(^tBuNC)_2(CO)]_2$ showed paramagnetic species in solution. The spectrum of ^{13}CO-$[Ni(Sn^tBu_3)(^tBuNC)_2(CO)]_2$ shows hyperfine coupling of the radical and ^{13}C nucleus. The ^{12}C spectrum does not, and this is evidence in favor of $\bullet Ni(Sn^tBu_3)(^tBuNC)_2(CO)$. Attempted trapping of $\bullet Ni(Sn^tBu_3)(^tBuNC)_2(CO)$ or $\bullet Ni(Sn^tBu_3)(^tBuNC)_3$ with the stable TEMPO radical afforded the $16e^-$ square planar $Ni(\eta^2\text{-N,O-TEMPO})(Sn^tBu_3)(^tBuNC)$. This Ni-TEMPO compound provides additional evidence for the $17e^-$ intermediate complexes $\bullet Ni(Sn^tBu_3)(^tBuNC)_2(CO)$ and $\bullet Ni(Sn^tBu_3)(^tBuNC)_3$. A photocatalytic cycle was derived and performed based on these results which utilizes $Ni(^tBuNC)_4$ to convert 2 $^tBu_3SnH$ into $^tBu_6Sn_2 + H_2$. This cycle has not been fully optimized as of yet, but it would become a closed system if the tin radical can be made to split H_2 regenerating $^tBu_3SnH$. The reaction under D_2 shows no H-D scrambling. These photolytic reactions and products were spectroscopically characterized in many ways, some utilizing low temperatures to stabilize previously unstable products.

Qualitative UV-Vis spectroscopy was used to answer several experimental questions. Last chapter's $Ni(Sn^tBu_3)_2(CO)_3$ was shown to possess similar photoreactivity, though requiring higher energy photons than $Ni(Sn^tBu_3)_2(^tBuNC)_3$ or $Ni(Sn^tBu_3)_2(^tBuNC)_2(CO)$ due to less steric hindrance of the equatorial ligands. Concentration of the nickel-tin dimer $[Ni(Sn^tBu_3)(^tBuNC)_2(CO)]_2$ was shown to decrease over time at room temperature while the concentration of $Ni(Sn^tBu_3)_2(^tBuNC)_2(CO)$ increased and this is evidence for our proposed disproportionation/decomposition of the dimer to partially regenerate monomeric starting material.

Various tin side products have been isolated from our experiments and characterized. The previously known $^{t}Bu_6Sn_2$ and $(^{t}Bu_3Sn_2)O$ were isolated as predicted photolytic side products. The compounds $[Sn(O)(^{t}Bu)_2(CO_3Sn^{t}Bu_3)]_2$ and $[(^{t}Bu_3Sn)(PF_4)]_\infty$ demonstrate photochemical activation of CO_2 and PF_6^- by generation of reactive tin radicals, respectively. The tin-carbonate compound may possess the ability to produce dimethylcarbonate, and this will be studied in the future. Activating either CO_2 or PF_6^- is known to be rather challenging yet was accomplished in a facile manner at room temperature by photolysis. The tin radical was successfully transferred to other metal centers, exemplified by $Fe(Sn^{t}Bu_3)_2(CO)_4$ and $Mo(CO)_3(Cp)(Sn^{t}Bu_3)$. These were afforded by Ni-Sn photolysis in the presence of $Fe_3(CO)_{12}$ and MpH, respectively. Similar compounds to these are known, yet they were synthesized using different metathesis mechanisms such as salt elimination. The addition of $\bullet Sn^{t}Bu_3$ to other transition metal complexes is underway. We were also successful in synthesizing Ni-Sn compounds with varying Ni:Sn ratios of 1:1, 1:2, and 2:2 that may play a part in future heterogeneous catalysis experiments.[137]

Mentioned earlier in this chapter, the compounds $Pd(Sn^{t}Bu_3)_2(^{t}BuNC)_3$ and $Pt(Sn^{t}Bu_3)_2(^{t}BuNC)_2CO$ have also been synthesized in our laboratory, however neither of these precious metal analogues seem to possess similar photoreactivity even with intense irradiation. This is an extremely unusual case where Ni shows increased chemical reactivity compared to Pt and Pd, precisely what we had set out to accomplish. The next chapter will again show enhanced chemical reactivity of Ni vs Pt/Pd. Indeed, Ni-Sn bimetallic compounds do exhibit useful functionality and may yield future complexes

which reduce the need for platinum, palladium and other precious metals. Further study of all reported compounds is under way.

3.4 Experimental

General Data. Unless otherwise stated, all reactions were carried out under an argon atmosphere in Schlenk flasks or an MBraun Unilab inert atmosphere glovebox. Reagent grade solvents were dried according to standard procedures and freshly distilled before use. Infrared spectra were recorded on a Nicolet 380 FT-IR spectrophotometer. Single crystal FTIR spectra were recorded on a Perkin Elmer Spectrum 400 using a Perkin Elmer Universal ATR Sampling Accessory. ^{1}H and ^{13}C NMR spectra were recorded on a Bruker 400 spectrometer operating at 399.993 MHz. UV-Vis spectra were recorded on a Varian Cary 100 Bio Spectrophotometer using screw-cap quartz cuvettes with 1 cm path lengths. Mass spectrometric measurements performed by direct–exposure probe using electron impact ionization (EI) were made on a VG 70S instrument at the University of South Carolina, Columbia, SC, and electrospray mass spectrometric measurements were obtained on a Bruker microTOF-Q II at the University of Miami. ESR spectra were recorded on a Bruker EMX ESR Spectrometer. Elemental analyses were performed by Columbia Analytical Services (Tucson, AZ). Photolysis was accomplished with a 150 W Sylvania flood lamp. Bis(1,5-cyclo-octadiene) nickel, $Ni(COD)_2$, was purchased from Strem Chemicals and used without further purification. Tri-iron dodecacarbonyl, $Fe_3(CO)_{12}$, was purchased from Aldrich and used without further purification. *Tert*-butyl isocyanide, ^{t}BuNC, trityl hexafluorophosphate, Ph_3C^+

PF_6^-, and TEMPO radical were purchased from Alfa Aesar and used without further purification. Argon, carbon monoxide, hydrogen, and carbon dioxide gasses were purchased from AirGas Supplies. $HMo(CO)_3Cp$, HMp, and ^{13}CO were kindly provided to us by Dr. Carl Hoff and his group. Tri-*tert*-butyl tin hydride, $^tBu_3SnH$, was synthesized according to our previous procedure in Chapter 2.

Synthesis of Ni(^{t}BuNC)$_4$. A 100 mg (0.36 mmol) sample of $Ni(COD)_2$ was loaded into a sidearm Schlenk flask. 30 mL of hexane was added by cannula under flow of argon and the mixture was stirred to dissolve all solids. To this solution, 132 mg (1.6 mmol) of ^{t}BuNC was added resulting in immediate color change to pale yellow with solid precipitation. The solution was stirred for 30 minutes and then the volatiles were removed in *vacuo*. The solid residues were redissolved in 4 mL of diethyl ether, filtered into a glass vial, and placed in a -25 °C freezer in the drybox. Slow evaporation of solvent afforded 124 mg (88 % yield) of light yellow blocks Ni(^{t}BuNC)$_4$. Spectral data for Ni(^{t}BuNC)$_4$: ^{1}H NMR (C_6D_6 in ppm): δ= 1.08 (s, 36 H, ^{t}Bu). FTIR in hexane- ν_{CN} cm^{-1}: 2012 (s).

Synthesis of Ni(Sn^{t}Bu$_3$)$_2$(^{t}BuNC)$_3$. A 100 mg (0.36 mmol) sample of $Ni(COD)_2$ and 215 mg (0.74 mmol) of $^tBu_3SnH$ were loaded into a sidearm Schlenk flask equipped with a water cooled condenser. Under flow of argon, 50 mL of hexane was added by cannula and the mixture was stirred to dissolve all solids. 100 mg (1.25 mmol) of ^{t}BuNC was added resulting in an immediate color change to pale yellow. The solution was

stirred for 10 minutes and heated to a brief reflux, resulting in a color change to gold, before removing the volatiles in *vacuo*. The solid residue was redissolved in methylene chloride and passed down a column of silica gel. The solution was evacuated to dryness, redissolved in 4ml of a 1:1 methylene chloride/hexane solution, filtered into a glass vial, and placed in a -25 °C freezer in the drybox. Slow evaporation of solvent resulted in 239 mg (74% yield) of orange blocks of $Ni(Sn^tBu_3)_2(^tBuNC)_3$**.** A similar yield can be obtained by room temperature reaction after approximately 12 hours. Spectral data for $Ni(Sn^tBu_3)_2(^tBuNC)_3$**:** ^{1}H NMR (C_6D_6 in ppm): δ= 1.676 (s, $^3J_{Sn\text{-}H}$ = 47 Hz, 54 H, Sn-^{t}Bu), 1.191 (s, 27 H, CN-^{t}Bu). FTIR in hexane- ν_{CN} cm^{-1}: 2034 (s), 2062 (w). UV-Vis= 392 nm. Elemental analysis: Found = C 51.98 %, H 9.12 %, N 4.46 %; Calculated = C 52.75 %, H 9.19 %, N 4.73 %. EI Mass Spec shows major peak at 598 m/z which is $Ni(Sn^tBu_3)_2(^tBuNC)_3$ **-** (Sn^tBu_3)= 888 - 290= 598. Spectral pattern is consistent with the presence of 1 Ni and 1 Sn atom.

The phenyl analogue, $Ni(SnPh_3)_2(^tBuNC)_3$, can be made in an identical manner with similar yield utilizing commercially available Ph_3SnH. Crystals were produced by slow evaporation of a methylene chloride/hexane solution at -20 °C. FTIR in hexane- ν_{CN} cm^{-1}: 2077 (s), 2105 (w). This compound is not photoactive and was not further studied.

Synthesis of $Ni(Sn^tBu_3)_2(^tBuNC)_2(CO)$. A 50 mg (0.0056 mmol) sample of $Ni(Sn^tBu_3)_2(^tBuNC)_3$ was loaded into a sidearm Schlenk flask. Under flow of argon, 30 mL of hexane was added by cannula and the mixture was stirred to dissolve all solids.

The argon atmosphere was evacuated and replaced by carbon monoxide, CO. The stirred solution changed color from dark gold to light yellow over a period of several minutes. The solution was evacuated to dryness and the solid residue was redissolved in 2ml of a 1:1 methylene chloride/hexane solution, filtered into a glass vial, and placed in a -25 °C freezer in a drybox. Slow evaporation of solvent resulted in 38 mg (82% yield) of yellow blocks of $Ni(Sn^tBu_3)_2(^tBuNC)_2(CO)$. A sample of ^{13}CO- $Ni(Sn^tBu_3)_2(^tBuNC)_2(CO)$ was prepared for ^{13}C NMR by using ^{13}CO in the same procedure. Spectral data for $Ni(Sn^tBu_3)_2(^tBuNC)_2(CO)$**:** ^{1}H NMR ($C_6D_6$ in ppm): δ= 1.642 (s, 54H, Sn-^{t}Bu, $^3J_{Sn-H}$= 52 Hz), 1.037 (s, 18H, CN-^{t}Bu). ^{13}C-CO NMR (toluene-d_8)= 197.27 ppm (s, 1C, $^2J_{Sn-C}$= 127 Hz at 25°C) and 197.40 ppm (s, 1C, $^2J_{Sn-H}$= 127 Hz at -80°C). FTIR in hexane- ν_{CN} cm^{-1} : 2092 (s), 2114 (m). ν_{CO} cm^{-1} : 1935 (s). Single Crystal FTIR- ν_{CN} cm^{-1}: 2094 (s), 2118 (m). ν_{CO} cm^{-1}: 1920 (s). UV-Vis= 375 nm. EI Mass Spec shows major peaks at 832, 775 and 747 m/z which are $Ni(Sn^tBu_3)_2(^tBuNC)_2(CO)$, $Ni(Sn^tBu_3)_2(^tBuNC)_2(CO)$ – ^{t}Bu = 832 – 57 = 775 and $Ni(Sn^tBu_3)_2(^tBuNC)_2(CO)$ – ^{t}Bu – CO = 832 – 57 – 28 = 747, respectively. Spectral pattern is consistent with the presence of 1 Ni and 2 Sn atoms.

Synthesis of $Ni(Sn^tBu_3)_2(^tBuNC)(CO)_2$. A 50 mg (0.0056 mmol) sample of $Ni(Sn^tBu_3)_2(^tBuNC)_3$ was loaded into a sidearm Schlenk flask equipped with a water cooled condenser. Under flow of argon, 30 mL of hexane was added by cannula and the mixture was stirred to dissolve all solids while being heated to reflux. The argon atmosphere was replaced by purging carbon monoxide, CO, through the solution. The stirred solution quickly changed color from dark gold to light yellow. FTIR spectroscopy showed the presence of $Ni(Sn^tBu_3)_2(^tBuNC)_2(CO)$ and a new species in an approximate

50:50 ratio. The solution was evacuated to dryness and the solid residue was separated into 2 yellow bands by TLC in air using pure hexane. The yellow band not attributed to $Ni(Sn^tBu_3)_2(^tBuNC)_2(CO)$ was redissolved in a methylene chloride/hexane mixture. Slow evaporation of solvent at -20 °C resulted in yellow blocks of $Ni(Sn^tBu_3)_2(^tBuNC)(CO)_2$ in an approximate 40 % yield. Spectral data for $Ni(Sn^tBu_3)_2(^tBuNC)_2(CO)_2$: ^1H NMR (C_6D_6 in ppm): δ = 1.566 (s, 54H, Sn-^{t}Bu, $^3J_{Sn\text{-}H}$= 57 Hz), 0.927 (s, 9H, CN-^{t}Bu). FTIR in hexane- ν_{CN} cm^{-1} : 2129 (s). ν_{CO} cm^{-1} : 1996 (s), 1959 (s).

Synthesis of $[Ni(Sn^tBu_3)(^tBuNC)_2(CO)]_2$. A 30 mg (0.0036 mmol) sample of compound $Ni(Sn^tBu_3)_2(^tBuNC)_2(CO)$ was loaded into a sidearm Schlenk flask. Under flow of argon, 30ml of hexane was added by cannula and the mixture was stirred to dissolve all solids. The flask was placed under slight vacuum and then irradiated with a 150W Sylvania flood lamp. The solution began to change color from light yellow to pink to deep purple over the period of one minute. The light was extinguished and the mixture was evacuated to dryness. The purple solid residue was redissolved in 2ml of diethyl ether, filtered into a glass vial, and placed in a -25 °C freezer in a drybox. Slow evaporation of solvent resulted in 6.25 mg (32 % yield) of purple blocks of $[Ni(Sn^tBu_3)(^tBuNC)_2(CO)]_2$. A sample of ^{13}CO-$[Ni(Sn^tBu_3)(^tBuNC)_2(CO)]_2$ was prepared for ^{13}C NMR by using ^{13}CO- $Ni(Sn^tBu_3)_2(^tBuNC)_2(CO)$ in the same procedure. Spectral data for $[Ni(Sn^tBu_3)(^tBuNC)_2(CO)]_2$**:** ^{13}C-CO NMR (toluene-d_8 in ppm)= 205 (s, 1C, -80°C). Single Crystal FTIR- ν_{CN} cm^{-1}: 2096 (s), 2063 (m). ν_{CO} cm^{-1}: 1906 (s).

UV-Vis= 564 nm. Elemental analysis: Found= C 50.12 %, H 8.40 %, N 4.87 %; Calculated= C 50.81 %, H 8.35 %, N 5.15 %.

Synthesis of Ni**(η^2-N,O-TEMPO)(Sn^tBu_3)(^{t}BuNC).** A 30 mg (0.0036 mmol) sample of Ni(Sn^tBu_3)$_2$(^{t}BuNC)$_2$(CO) and 17 mg (0.0108 mmol) of TEMPO were loaded into a sidearm Schlenk flask. Under flow of argon, 30ml of hexane was added by cannula and the mixture was stirred to dissolve all solids. The flask was placed under slight vacuum and then irradiated with a 150 W Sylvania flood lamp. The solution began to change color from light yellow to brownish yellow over the period of one minute. The light was extinguished and the volatiles were removed in *vacuo*. The brownish yellow solid residue was redissolved in 2ml of diethyl ether, filtered into a glass vial, and placed in a -20 °C freezer in a drybox. Slow evaporation of solvent resulted in 11.5 mg (54 % yield) of brownish yellow blocks of Ni(η^2-N,O-TEMPO)(Sn^tBu_3)(^{t}BuNC)**.** Spectral data for Ni(η^2-N,O-TEMPO)(Sn^tBu_3)(^{t}BuNC)**:** ^{1}H NMR (C_6D_6 in ppm): δ= 1.639 (s, $^3J_{Sn-H}$= 49 Hz, 27H, Sn-^{t}Bu), 0.954 (s, 9H, CN-^{t}Bu), 1.784 (s, 6H, $(CH_3)_2$-TEMPO), 1.213 (s, 6H, $(CH_3)_2$-TEMPO). FTIR in hexane- ν_{CN} cm^{-1}: 2086 (s).

Crystallographic Analysis. Single crystals of Ni(Sn^tBu_3)$_2$(^{t}BuNC)$_2$(CO)**,** Ni(Sn^tBu_3)$_2$(^{t}BuNC)(CO)$_2$, [Ni(Sn^tBu_3)(^{t}BuNC)$_2$(CO)]$_2$**,** Ni(η^2-N,O-TEMPO)(Sn^tBu_3)(^{t}BuNC), Ni(^{t}BuNC)$_4$, Ni(I)$_2$(^{t}BuNC)$_2$, $(Ph_3C)^+(PF_6^-)$, Fe(Sn^tBu_3)$_2$(CO)$_4$, and Mo(Sn^tBu_3)(CO)$_3$Cp suitable for diffraction analysis were grown by slow evaporation of concentrated diethyl ether solutions at – 20 °C. The data crystal for Ni(Sn^tBu_3)$_2$(^{t}BuNC)$_3$ was grown by slow evaporation of a concentrated benzene

solution at 5 °C. The data crystals for $[Sn(O)(^tBu)_2(CO_3Sn^tBu_3)]_2$ and $Ni(SnPh_3)_2(^tBuNC)_3$ were grown by slow evaporation of a 1:1 methylene chloride/hexane solution at – 20 °C. The data crystal for $[(^tBu_3Sn)(PF_4)]_\infty$ was grown by slow evaporation of a pure methylene chloride solution at – 20 °C. All data crystals were glued onto the end of a thin glass fiber and collected under ambient atmosphere at room temperature. The only exceptions are the data crystals for $[(^tBu_3Sn)(PF_4)]_\infty$ and $(Ph_3C)^+(PF_6)^-$ which were secured to a glass fiber with Paratone-N for data collection at 100 K under flow of N_2.

X-ray intensity data were measured with a Bruker SMART APEX2 CCD-based diffractometer using Mo KR radiation (λ=0.71073 Å).[92] The raw data frames were integrated with the SAINT+ program by using a narrow-frame integration algorithm.[93] Corrections for Lorentz and polarization effects were also applied with SAINT+. An empirical absorption correction based on the multiple measurement of equivalent reflections was applied using the program SADABS. All structures were solved by a combination of direct methods and difference Fourier syntheses, and refined by full-matrix least-squares on F^2, by using the SHELXTL software package.[93] All non-hydrogen atoms were refined with anisotropic displacement parameters. Hydrogen atoms were placed in geometrically idealized positions and included as standard riding atoms during the least-squares refinements. Crystal data, data collection parameters, and results of the analyses are listed in Appendix B Tables B.1-B.5.

The compound $Ni(Sn^tBu_3)_2(^tBuNC)_3$ crystallized in the orthorhombic crystal system. The systematic absences in the intensity data were consistent with the unique

space group *Cmca*. $Ni(Sn^tBu_3)_2(^tBuNC)_3$ crystallized with a molecule of benzene solvent in the unit cell.

The compound $Ni(Sn^tBu_3)_2(^tBuNC)_2(CO)$ crystallized in the orthorhombic crystal system. The systematic absences in the intensity data were consistent with the unique space group *Pmmn*. $Ni(Sn^tBu_3)_2(^tBuNC)_2(CO)$ crystallized with a molecule of diethyl ether in the unit cell.

The compound $Ni(SnPh_3)_2(^tBuNC)_3$ crystallized in the orthorhombic crystal system. The systematic absences in the intensity data were consistent with the unique space group *Pnma.*

The compound and $[(^tBu_3Sn)(PF_4)]_\infty$ crystallized in the orthorhombic crystal system. The systematic absences in the intensity data were consistent with the unique space group *Pnma.*

The compound $Ni(Sn^tBu_3)_2(^tBuNC)(CO)_2$ crystallized in the monoclinic crystal system. The systematic absences in the intensity data were consistent with the unique space group $P2_1/n$.

The compound $[Ni(Sn^tBu_3)(^tBuNC)_2(CO)]_2$ crystallized in the monoclinic crystal system. The systematic absences in the intensity data were consistent with the unique space group $P2_1/n$.

The compound $[Sn(O)(^tBu)_2(CO_3Sn^tBu_3)]_2$ crystallized in the monoclinic crystal system. The systematic absences in the intensity data were consistent with the unique

space group $C2/c$. $[Sn(O)(^tBu)_2(CO_3Sn^tBu_3)]_2$ crystallized with a molecule of methylene chloride solvent in the unit cell.

The compound $Ni(\eta^2\text{-N,O-TEMPO})(Sn^tBu_3)(^tBuNC)$ crystallized in the monoclinic crystal system. The systematic absences in the intensity data were consistent with the unique space group $P2_1/c$.

The compound $(Ph_3C)^+(PF_6)^-$ crystallized in the monoclinic crystal system. The systematic absences in the intensity data were consistent with the unique space group $P2_1/n$.

The compound $Fe(Sn^tBu_3)_2(CO)_4$ crystallized in the monoclinic crystal system. The systematic absences in the intensity data were consistent with the unique space group $P2_1/n$.

The compound $Mo(Sn^tBu_3)(CO)_3Cp$ crystallized in the monoclinic crystal system. The systematic absences in the intensity data were consistent with the unique space group $P2_1/m$.

The compound $Ni(^tBuNC)_4$ crystallized in the cubic crystal system. The systematic absences in the intensity data were consistent with the highly symmetrical space group $F\bar{4}3c$. The high symmetry made crystallographic analysis difficult, and slight distortion of the crystal structure exists. There are final Q peaks in the unit cell for which no atoms can be assigned, most likely belonging to either distorted solvent or purely a crystallographic trick of the very high symmetry.

Chapter 4: Synthesis, Characterization, and Reactivity Study of $Ni(\eta^2\text{-}N,O\text{-}TEMPO)_2$: The First Transition Metal Complex Bearing Exclusively TEMPO Ligands.

4.1 Background

The stable TEMPO, (2,2,6,6-tetramethylpiperidin-1-yl)oxyl, radical has received constant industrial and academic interest since its discovery in 1960 by Lebedev and Kazarnowskii.[138] This solid heterocyclic radical was prepared by oxidation of the similar starting material, 2,2,6,6-tetramethylpiperidine, shown in equation 4.1.

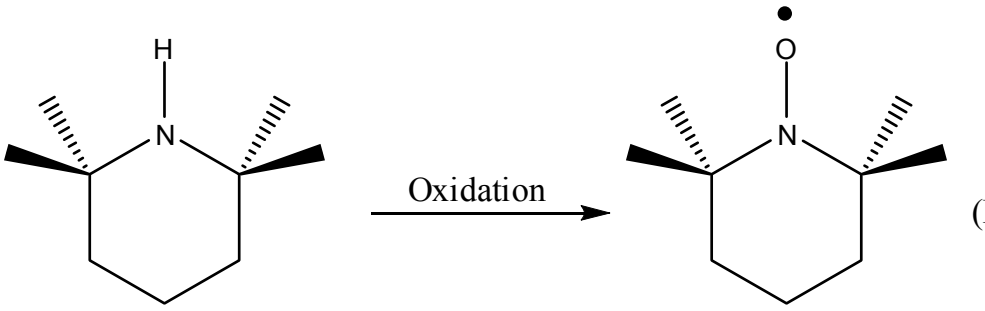

(Eqn 4.1)

2,2,6,6-tetramethylpiperidine

(2,2,6,6-tetramethylpiperin-1-yl)oxyl TEMPO

These oxygen centered radicals are unable to bond with a second equivalent to form the bridging peroxide, and thus are stable and free. The non-bonding character is attributed to the four methyl group substituents on the ring which are deceptively bulky and provide steric protection of the oxygen radical. It has proven to be an extremely powerful tool, especially in the field of controlled radical polymerization initiation reactions.[139] This free radical also plays a major role in generating paramagnetic compounds possessing extremely high spins and is used as a spin-probe/label in ESR studies to understand the environment of complex chemical and biochemical systems.[140,141]

Perhaps most interesting is the proficiency with which this stable radical can oxidize organic substrates, typically used in organic synthesis to catalytically convert primary alcohols to aldehydes.[142,143] Work has shown that most of these oxidation reactions are carried out by the N-oxoammonium salt, typically generated with sodium hypochlorite and TEMPO, shown in equation 4.2.[144]

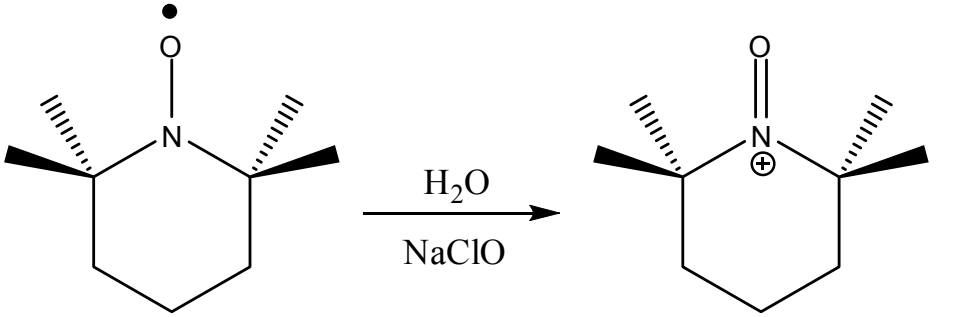

(Eqn 4.2)

These alcohol oxidation reactions were found to be quite selective, affecting only primary alcohols vs secondary and tertiary, a useful synthetic reagent.

While the field of organics and biochemistry have intensively studied TEMPO, the coordination chemistry of this radical and any subsequent organometallic complexes have been less than thoroughly investigated. Several existing metal-TEMPO complexes are known. A select few show interesting chemical abilities including primary alcohol oxidation, which is not surprising when the many mesomeric forms of metal-TEMPO binding are considered.[145] Rey et al. showed that their $Cu(Cl)_2$(TEMPO) complex was capable of quantitatively oxidizing benzyl alcohol to benzaldehyde, shown below.

$$2\ Cu(Cl)_2(TEMPO) + 2\ PhCH_2OH \longrightarrow 2\ PhCHO + CuCl + (CuCl_3)^{2-}(TEMPO\text{-}H^+)_2$$

Sheldon et al. later reported that their $Cu(Bipy)(Br)_2$ compound catalytically converted benzyl alcohol to benzaldehyde with use of co-catalytic TEMPO and KOH, assuming the active catalyst to be a free N-oxoammonium salt in solution.[145] However, it was recently shown by Wu et al. that the actual catalytic species is a Cu(Bipy)(TEMPO) complex formed in situ, shown in equation 4.3.[146] Baerends et al. also studied this reaction and their findings will be discussed later.[146]

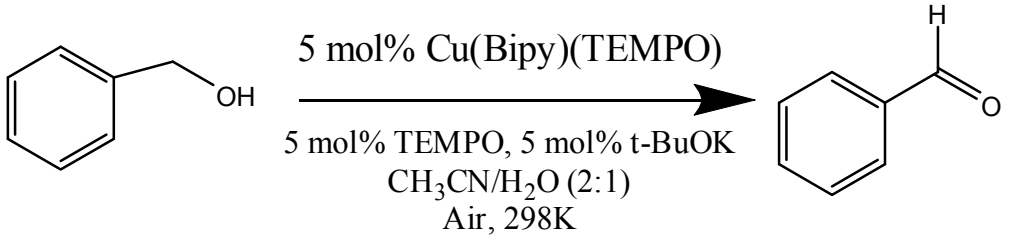

(Eqn 4.3)

Relatively few metal-TEMPO compounds have been generated and studied, some possessing η^1-O-TEMPO ligands[147], and others with η^2-N,O-TEMPO ligands[148]. There is only one literature example of an organometallic complex possessing solely TEMPO ligands, and this dinuclear lanthanide complex, $[(\eta^1\text{-}ONC_5H_6Me_4)_2Sm(\mu\text{-}\eta^1\text{: }\eta^2\text{-}ONC_5H_6Me_4)]_2$, contains η^1, η^2, and μ_2-TEMPO; it was not studied further.[149] There were previously 4 reported examples of Group 10 metal-TEMPO compounds (2 for Ni and 2 for Pd), but this short list was lengthened to 5 (3 for Ni) in the Chapter 3. There are no reported platinum-TEMPO compounds and this will be mentioned in a later conclusion.

When we attempted to trap the proposed photolytically generated monomeric radical $\bullet Ni(Sn^tBu_3)(^tBuNC)_2(CO)$ with TEMPO, we instead isolated the $16e^-$ square planar complex $Ni(\eta^2\text{-N,O-TEMPO})(Sn^tBu_3)(^tBuNC)$ shown in Figure 4.1. This

organometallic nickel compound has the extremely bulky $^{t}Bu_3Sn$ group incorporated into the ligand system, a main focus of our laboratory research.

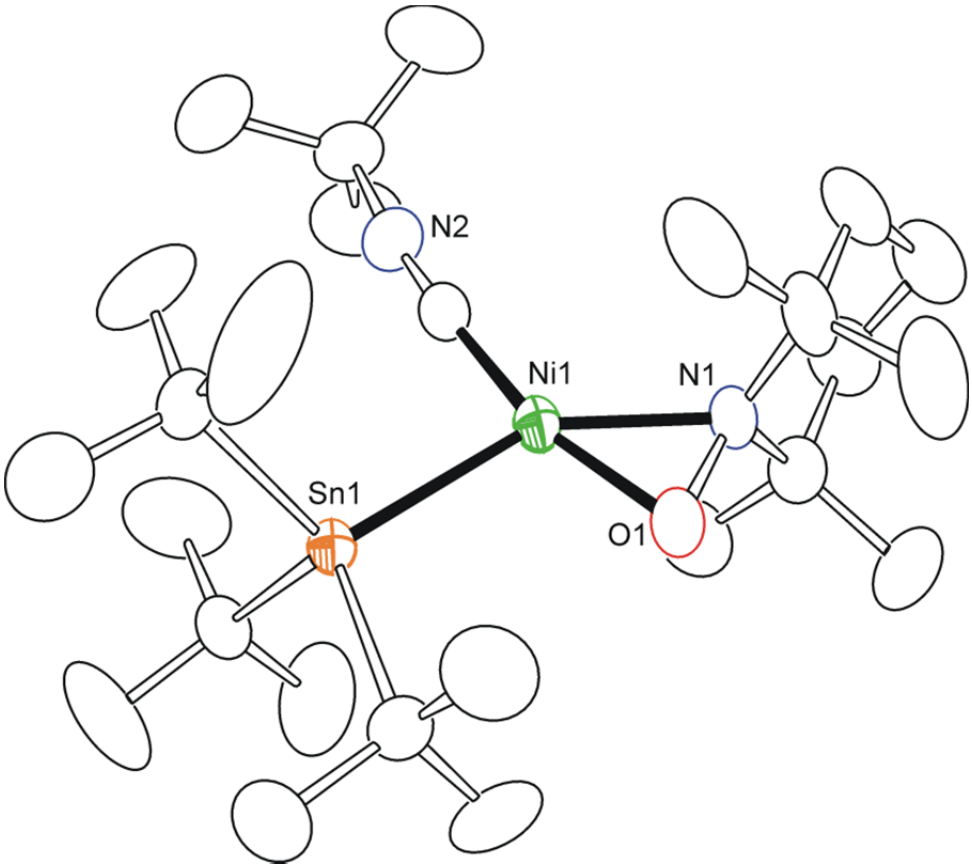

Figure 4.1 An ORTEP showing the molecular structure of Ni(η^2-N,O-TEMPO)(Sn^{t}Bu$_3$)(^{t}BuNC) at 30 % thermal ellipsoid probability.

The TEMPO ligand appears to have induced the elimination of both an isocyanide and CO ligand from tetrahedral •Ni(Sn^{t}Bu$_3$)(^{t}BuNC)$_2$(CO) to adopt a distorted square planar structure displaying an η^2-N,O-TEMPO ligand acting as a 3e$^-$ donor. This Ni-O-N metallacycle is unusually stable to subsequent reaction with *tert*-butyl isocyanide or carbon monoxide, even in great excess. The demand for 16e$^-$ square planar geometry may be due some thermodynamic preference by TEMPO radical to exist as the 3e$^-$

donating η^2-N,O-TEMPO ligand as opposed to the η^1-O-TEMPO which is well known in the literature on other metal complexes. All of the published Ni or Pd-TEMPO compounds are square planar and possess this η^2-N,O-TEMPO ligand. The interesting product seen in Figure 4.1 led us to question whether TEMPO radical would be able to activate $Ni(COD)_2$ sufficiently, like CO and ^{t}BuNC, to afford reaction with our ^{t}Bu$_3$SnH.

Unfortunately, TEMPO radical did not enable the addition of tin hydride to nickel and we have not been able to generate any new Ni-Sn-TEMPO compounds since $Ni(\eta^2$-N,O-TEMPO$)(Sn^tBu_3)(^t$BuNC). However, we discovered the surprising reaction of $Ni(COD)_2$ and TEMPO alone. Reported here in this chapter of work is the synthesis and characterization of $Ni(\eta^2$-N,O-TEMPO$)_2$, the first example of an unsaturated mononuclear transition metal complex supported exclusively by an organic TEMPO ligand system. Also contained herein is a preliminary reactivity study of $Ni(\eta^2$-N,O-TEMPO$)_2$ with a wide variety of chemical reagents.

4.2 Results and Discussion

The Reaction of $Ni(COD)_2$ with TEMPO radical. When one equivalent of (1,5-biscyclooctadiene) nickel, $Ni(COD)_2$, and two equivalents of (2,2,6,6-tetramethylpiperidin-1-yl)oxyl, TEMPO, radical were dissolved in room temperature hexane under argon, a color change from light orange to deep purple occurred over the period of approximately 10 minutes. The reaction was found to be nearly instantaneous at 68 °C reflux. Removal of volatiles in *vacuo* and crystallization of the solid residue from diethyl ether yielded purple block crystals of $Ni(\eta^2$-N,O-TEMPO$)_2$ in 78 % yield.

Single crystal X-ray diffraction analysis at 100 K gave the molecular structure of Ni(η^2-N,O-TEMPO)$_2$, shown in Figure 4.2. This complex was characterized by ^{1}H NMR, mass spectroscopy, and X-ray diffraction analysis. Further crystallographic data can be found in Appendix C Table C.1. Ni(η^2-N,O-TEMPO)$_2$ is extremely air and moisture sensitive, and crystallographic analysis required data collection at 100 K under flow of N_2 to avoid rapid crystal decomposition. The instability in ambient atmosphere made elemental analysis and mass spectroscopy very difficult, and we were fortunate to obtain the acetonitrile adduct of Ni(η^2-N,O-TEMPO)$_2$ during ESI-TOF mass spectroscopy at 412 m/z, shown in Appendix C Figure C.1. This highly unstable acetonitrile adduct will be discussed later. The parent peak of 370 m/z is obtained in many of the other mass spectrums in this chapter as does the acetonitrile adduct.

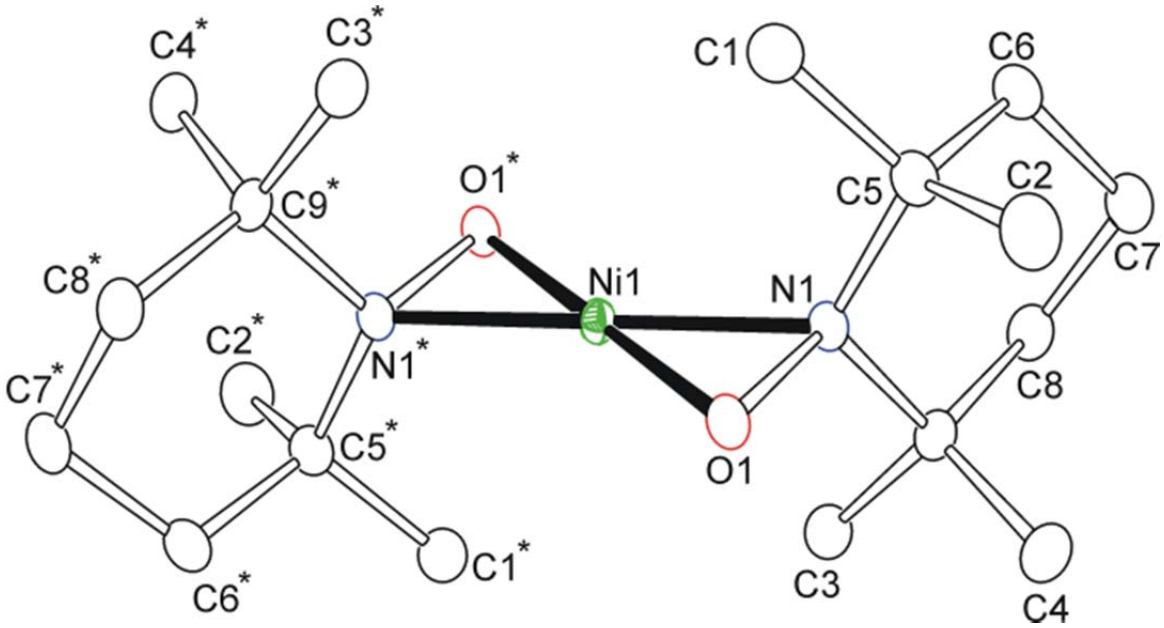

Figure 4.2 An ORTEP showing the molecular structure of Ni(η^2-N,O-TEMPO)$_2$ at 50 % thermal ellipsoid probability.

This molecule is crystallographically centrosymmetrical with point of inversion, but overall possesses C_{2h} symmetry. The N-Ni-O angle is 43.88(4) °. The nickel, nitrogen, and oxygen atoms all lie in the same plane forming a "bow-tie" type rectangular planar structure. Both of the three membered Ni-O-N metallacycles would appear to be geometrically strained and thus reactive, but this could not be assumed because it was previously shown that the similar η^2-TEMPO binding mode found in Ni(η^2-N,O-TEMPO)(Sn^{t}Bu$_3$)(^{t}BuNC) was stable to reaction with strong donor ligands like isocyanide and carbon monoxide. The N-O bond distance of 1.4136(12) Å is longer than that found in free TEMPO [1.283(9) Å]. The geometry around the nitrogen atom is pyramidal [O1-N1-C5 = 110.83(9) °, O1-N1-C9 = 110.97(9) °, C5-N1-C9 = 116.59(9) °], and the Ni-N and Ni-O bond distances are short [Ni1-N1= 1.9360(10) Å, Ni1-O1=1.8404(11) Å]. These structural parameters are consistent with the bidentate η^2-N,O-TEMPO coordination mode and formulation of a reduced TEMPO radical. These monoanionic η^2-N,O-TEMPO ligands are known to act as neutral 3e$^-$ or anionic 4e$^-$ donors. Thus the oxidation state of the Ni atom can be considered to be formally Ni^{II} having an unsaturated 16e$^-$ configuration.

^{1}H NMR study of this purple compound confirmed that the solid state η^2 binding mode persists in solution, displaying magnetically inequivalent methyl groups on the ring as two distinct sets exist on differing sides of the N-O bonds. Even at much higher and lower temperatures these Ni-O-N metallacycles appear to be stable as little change was found in the ^{1}H NMR spectrum from -80 °C to 90 °C in toluene-d_8. This was unexpected as the metallacycle angles are extremely acute and we assumed they would be easily opened and closed by varying temperatures. Unsure as to whether or not this complex

would possess FTIR active stretches, solution and solid state spectra were recorded. Neither showed any detectable peaks other than the C-H stretches of the ring CH_2 groups around 3000 cm^{-1}. Stated earlier, Ni(η^2-N,O-TEMPO)$_2$ is extremely air and moisture sensitive and exposure to either results in rapid decomposition to colorless products which are insoluble in all tested solvents.

Reaction of Ni(η^2-N,O-TEMPO)$_2$ with *Tert*-Butyl Isocyanide, ^{t}BuN≡C.

Having shown that a nearly identical Ni-O-N metallacycle in Ni(η^2-N,O-TEMPO)-(Sn^tBu_3)(^{t}BuNC) was stable to ^{t}BuNC, we were unsure if Ni(η^2-N,O-TEMPO)$_2$ would show any reaction with *tert*-butyl isocyanide. When 1eq of ^{t}BuNC was added to a room temperature hexane solution of Ni(η^2-N,O-TEMPO)$_2$ a very rapid color change from purple to dark red was observed. The reaction mixture was stirred for 10 minutes and the volatiles were removed in *vacuo.* Crystallization of the solid residue from diethyl ether gave metallic red blocks of Ni(η^2-N,O-TEMPO)(η^1-O-TEMPO)(^{t}BuNC) in 90 % yield. X-ray crystallographic analysis yielded the distorted square planar structure of Ni(η^2-N,O-TEMPO)(η^1-O-TEMPO)(^{t}BuNC) shown in Figure 4.3. Further crystallographic information is provided in Appendix C Table C.1. This complex was characterized by ^{1}H NMR, FTIR, mass spectroscopy, and X-ray crystallographic analysis. Ni(η^2-N,O-TEMPO)(η^1-O-TEMPO)(^{t}BuNC) is extremely air and moisture sensitive like Ni(η^2-N,O-TEMPO)$_2$, and crystallographic analysis required data collection at 100 K under flow of N_2 to avoid crystal decomposition.

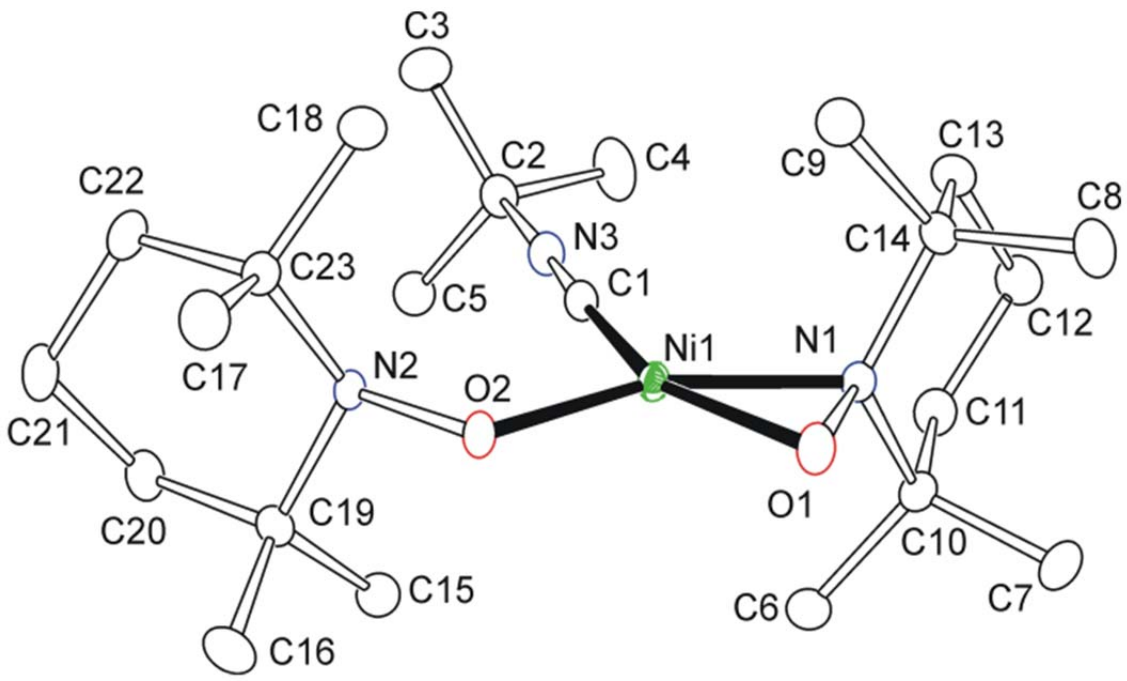

Figure 4.3 An ORTEP showing the molecular structure of Ni(η^2-N,O-TEMPO)-(η^1-O-TEMPO)(^{t}BuNC) at 50 % thermal ellipsoid probability.

It is clear from Figure 4.3 that a single metallacycle was broken and the ^{t}BuNC replaced the nitrogen atom in TEMPO as a 2e$^-$ donor. The overall molecular structure consists of the Ni atom bound to a η^2-N,O-TEMPO ligand, a η^1-O-TEMPO ligand and a ^{t}BuNC group in a distorted square-planar configuration. The N-O bond distances [N1-O1 = 1.3850(10) Å and N2-O2 = 1.4354(10) Å] and the pyramidal geometry around the nitrogen atoms [O1-N1-C10 = 112.69(7) °, O2-N2-C20 = 108.66(7) °] suggests that both TEMPO ligands in this complex have been reduced to their monoanionic TEMPO forms, with nickel formally in the +2 oxidation state possessing a 16 electron configuration.

The ^{1}H NMR spectrum of Ni(η^2-N,O-TEMPO)(η^1-O-TEMPO)(^{t}BuNC) at room temperature consists of a series of broad overlapping resonances indicative of some

dynamical processes occurring in solution. Raising the temperature incrementally to 90 °C resulted in some sharpening of the peaks. However, as shown in Appendix C Figure C.2 line broadening remained even at that high temperature. Above 90 °C the complex undergoes unselective reaction, i.e. decomposes. It is clear that some exchange occurs within this molecule, though the exact nature of the fluxional process remains unresolved presently. Similar fluxional processes will be found in NMR spectra of other products in this chapter and these appear to be due to equilibrium formation in solution, discussed later with pyridine.

Based on the structure, we would expect a single C≡N stretch to be found in FTIR spectra, and this is indeed so. The instability of this complex in air made elemental analysis and mass spectroscopy extremely difficult. After many unsuccessful attempts, we were very fortunate to finally obtain the parent peak of Ni(η^2-N,O-TEMPO)-(η^1-O-TEMPO)(^{t}BuNC) at 453 m/z in acetonitrile by direct exposure probe mass spectroscopy techniques, shown in Figure 4.4. Unexpectedly, this spectra also shows major peaks at 412, 370, and 355 m/z which are attributable to Ni(η^2-N,O-TEMPO)-(η^1-O-TEMPO)(MeCN), Ni(η^2-N,O-TEMPO)$_2$, and [Ni(η^2-N,O-TEMPO)$_2$ – CH_3], respectively. These products all show loss of ^{t}BuNC, and provides experimental evidence for the fluxionality of Ni(η^2-N,O-TEMPO)(η^1-O-TEMPO)(^{t}BuNC) in solution. All peaks show appropriate isotopic distribution for the presence of 1 nickel atom.

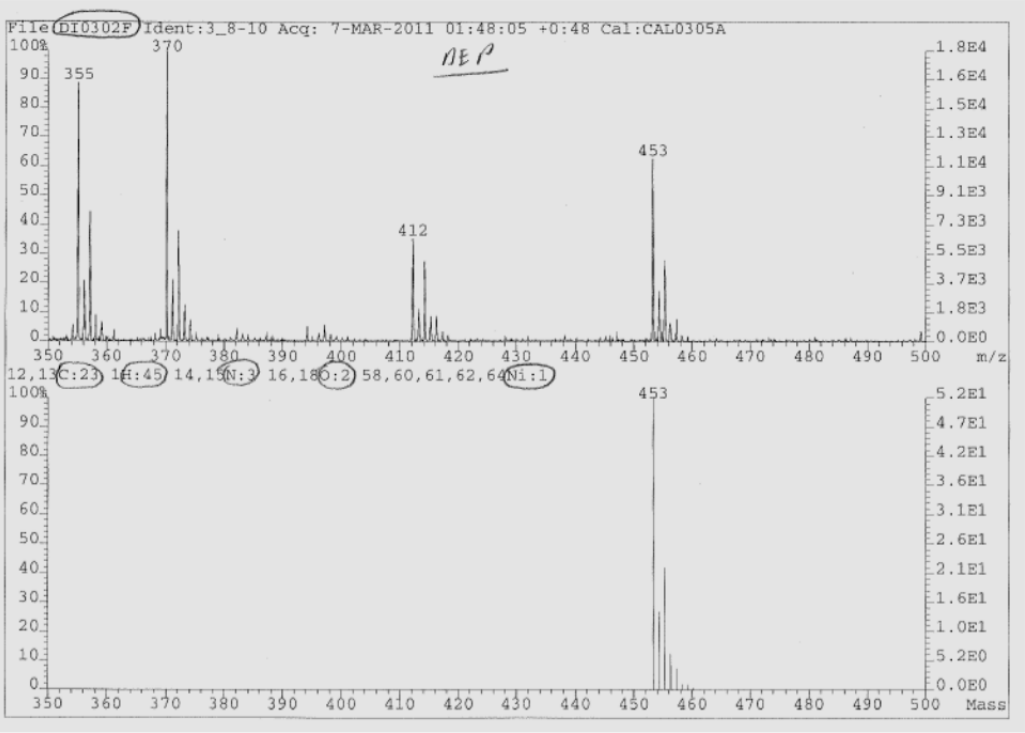

Figure 4.4 DEP mass spectroscopy report showing the parent peak of Ni(η^2-N,O-TEMPO)(η^1-O-TEMPO)(^{t}BuNC) (top) and the predicted spectrum (bottom).

We are still unsure of the mechanism for this reaction, as well as for all other reactions associated with Ni(η^2-N,O-TEMPO)$_2$. It is possible that the ring opening and isocyanide binding are concerted. This is most probable since the variable ^{1}H NMR of Ni(η^2-N,O-TEMPO)$_2$ in solution showed no appreciable flux between η^2 and η^1 ligand binding which would leave a vacant coordination site. Ni(η^2-N,O-TEMPO)(η^1-O-TEMPO)(^{t}BuNC) is unreactive towards excess ^{t}BuNC or CO gas like the Ni-Sn-TEMPO compound above. The second η^2-N,O-TEMPO metallacycle appears to be extremely stable in all further reported compounds.

Based on the structure of Ni(η^2-N,O-TEMPO)$_2$, it was fair to propose that the reaction of Ni(η^2-N,O-TEMPO)$_2$ and ^{t}BuNC should have produced the hypothetical compound Ni(η^2-N,O-TEMPO)$_2$(^{t}BuNC), shown in equation 4.4.

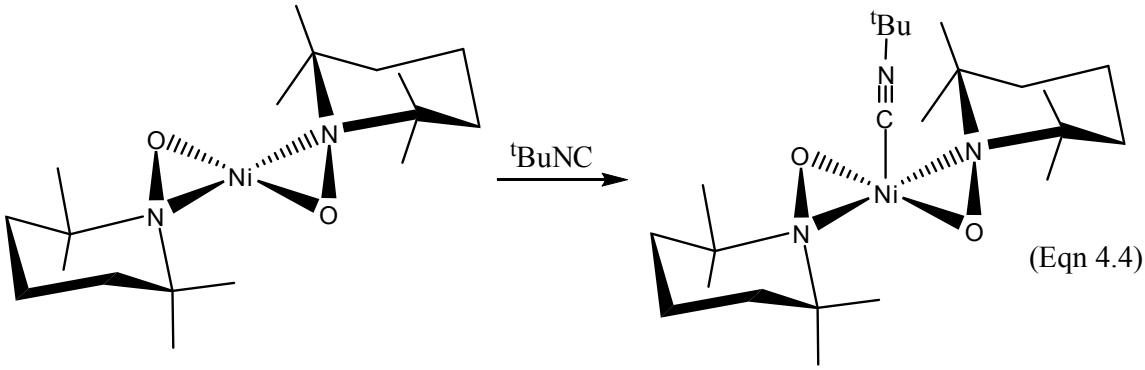

(Eqn 4.4)

This hypothetical product, Ni(η^2-N,O-TEMPO)$_2$(^{t}BuNC), is an ideal 18e$^-$ rectangular pyramidal type structure that seems far more likely than the actual ORTEP in Figure 4.3. However, recent work has shown that axial coordination to very similar Ni^{II} porphyrin complexes results in a spin transition from the singlet to triplet state, and the entropy of formation for these five coordinate Ni^{II} porphyrins is extremely large and negative.[150] These porphyrin structures are rigid planar frameworks around a Ni^{II} center, analogous to Ni(η^2-N,O-TEMPO)$_2$ which should show similar response to ligand binding at an axial site.

To better understand the factors influencing ligand binding to this nickel center, space-filling models were prepared of Ni(η^2-N,O-TEMPO)$_2$ and are shown in Figure 4.5. It is clear that the axial sites above and below the N1-O1-N*1-O*1 square plane are simply not accessible. The green color of the nickel atom above and below the plane is virtually hidden by the methyl group electron clouds of the TEMPO ligands. However,

the equatorial sites are plainly visible as large green areas, primed and available for ligand binding.

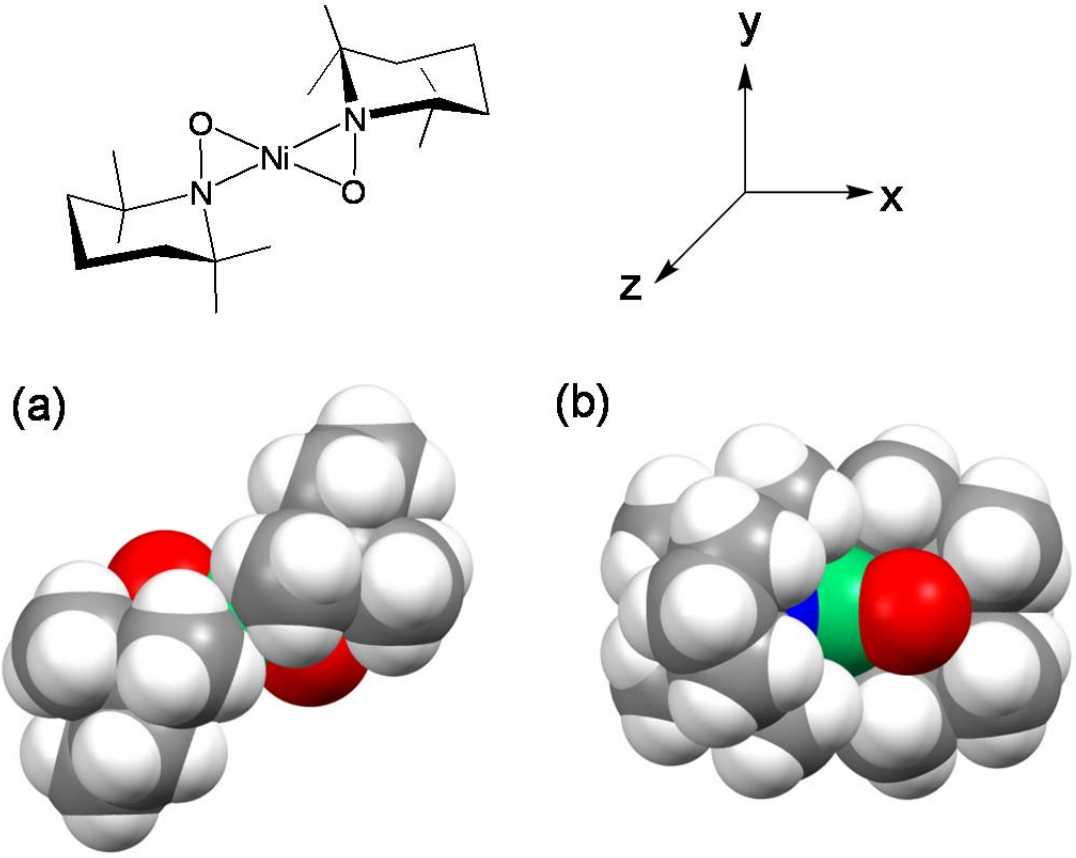

Figure 4.5 Space-filling model of Ni(η^2-N,O-TEMPO)$_2$ seen from (a) down the C_2 (z) axis above the square plane and (b) down the xy plane perpendicular to the C_2 (z) axis. Atomic dimensions are the van der Waals radii. Nickel is shown in green, oxygen in red, nitrogen in blue, carbon in gray, and hydrogen in white.

Mentioned earlier, these methyl substituents are responsible for the free and stable nature of the TEMPO radical, preventing dimerization and peroxide formation. These four CH_3 groups, though not very bulky individually, are now spatially arranged in such a manner about the nickel atom that they have become extremely sterically encumbering, preventing direct access to any axial electronic orbitals and maintaining a square planar

geometry. Thus Ni(η^2-N,O-TEMPO)$_2$ exemplifies the use of both steric bulk and rigid geometry for imparting electronic unsaturation of a transition metal center. It seems to accept 2e$^-$ ligands along the square plane edge to afford a single transition from 3e$^-$ donating η^2-N,O-TEMPO to 1e$^-$ donating η^1-O-TEMPO, preferring to maintain products with a 16e$^-$ square planar arrangement.

It is interesting to note that the once *trans* O atoms in Ni(η^2-N,O-TEMPO)$_2$ are now *cis* to each other in Ni(η^2-N,O-TEMPO)(η^1-O-TEMPO)(^{t}BuNC), seen in Figures 4.2 and 4.3 respectively. This mechanistic anomaly will be seen again later, and it is still unclear as to how the geometrical flip occurs. It is possible that this *trans* to *cis* transformation is somehow afforded by initial ligand electronic donation into oxygen or nitrogen anti-bonding orbitals since they are both clearly visible in Figure 4.5. Any discussion of mechanistic detail throughout this chapter is purely conjecture at this point in time. Continued investigation of Ni(η^2-N,O-TEMPO)(η^1-O-TEMPO)(^{t}BuNC) is underway in our lab.

Reaction of Ni(η^2-N,O-TEMPO)$_2$ with Iodine, I$_2$. To further study the reactivity of Ni(η^2-N,O-TEMPO)$_2$, we chose to explore it's reaction with a known 1e$^-$ donor as opposed to the 2e$^-$ donation of isocyanides. Iodine atoms are well known 1e$^-$ donors, and I$_2$ has been shown to react with many organometallic complexes via oxidative addition to yield a di-iodide product.[151] Based on this evidence, we assumed that addition of I$_2$ might result in the octahedral 18e$^-$ product Ni(η^2-N,O-TEMPO)$_2$(I)$_2$ shown in Figure 4.6.

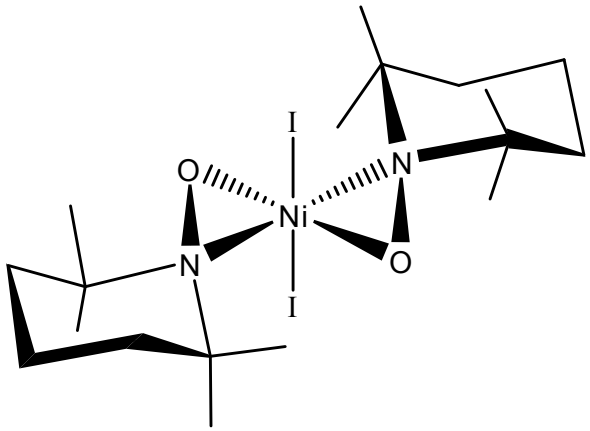

Figure 4.6 Line drawing of the proposed compound Ni(η^2-N,O-TEMPO)$_2$(I)$_2$.

When 1eq of I_2 was added to a room temperature hexane solution of Ni(η^2-N,O-TEMPO)$_2$ a rapid color change from purple to dark green occurred. Removal of volatiles in *vacuo* and crystallization of the solid residue from diethyl ether resulted in metallic green blocks of Ni(η^2-N,O-TEMPO)(2,2,6,6-Tetramethylpiperidin-1-yl)(I) in 64 % yield. X-ray crystallographic analysis yielded the distorted square planar structure of Ni(η^2-N,O-TEMPO)(2,2,6,6-Tetramethylpiperidin-1-yl)(I) shown in Figure 4.7. Further crystallographic information is provided in Appendix C Table C.2. This extensively air stable complex was characterized by ^{1}H NMR, elemental and X-ray crystallographic analyses. The parent peak for this complex was never detected with mass spectroscopy for unknown reasons.

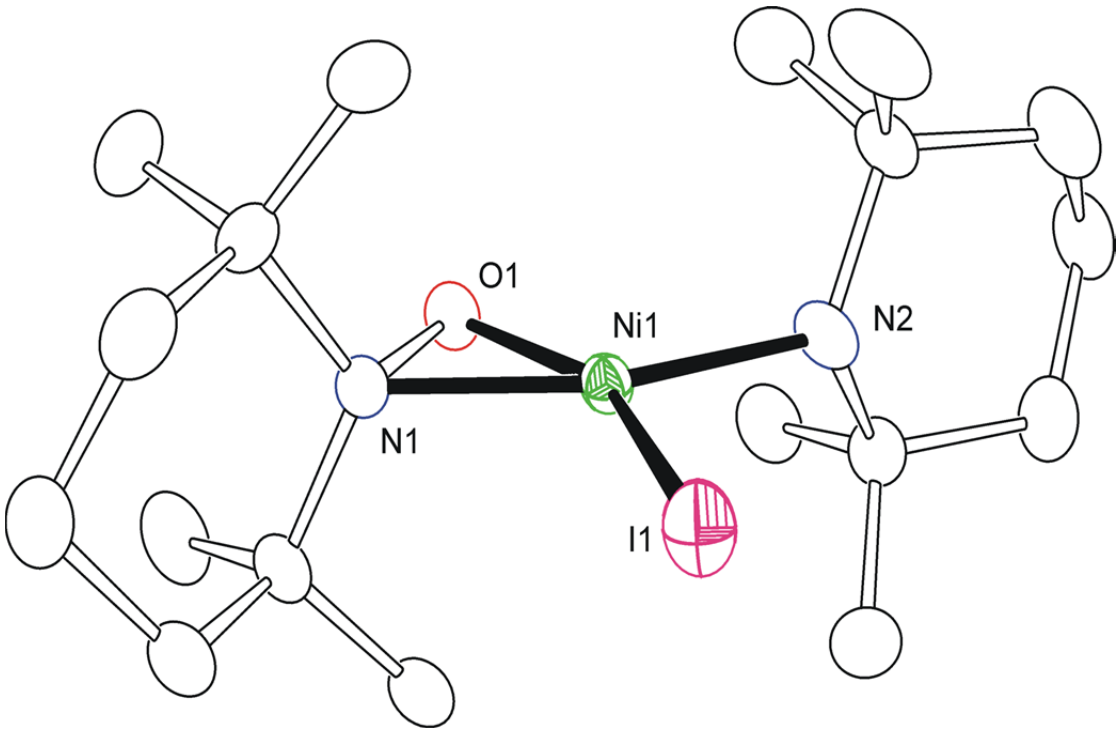

Figure 4.7 An ORTEP showing the molecular structure of Ni(η^2-N,O-TEMPO)(2,2,6,6-Tetramethylpiperidin-1-yl)(I) at 30 % thermal ellipsoid probability.

It is clear that the structure shown in Figure 4.7 is nothing like the proposed product in Figure 4.6, and once again the TEMPO methyl groups have forced equatorial reaction and maintained a 16e$^-$ distorted square planar geometry. Examination of the structure in Figure 4.7 reveals the curious loss of an oxygen atom from one of the TEMPO ligands.

Addition of iodine seems to have completely reduced the TEMPO ligand to its oxygen-free precursor 2,2,6,6-tetramethylpiperidine, but there is no N-H hydrogen like that seen in Equation 4.1. Instead, the N atom is now bound directly to Ni. In fact, the nitrogen atom is in a nearly planar 354 ° arrangement with the Ni and two C atoms it shares a bond with, no longer possessing a pyramidal geometry. Assuming the iodine

atom is providing its customary $1e^-$ donation, the N atom must be acting as a $2e^-$ donor to result in the $16e^-$ count typical for these planar Ni-TEMPO compounds. This electronic arrangement is still quite puzzling to us because the near planarity around N suggests a double bond to Ni, yet the actual bond distance is close to 1.9 Å, much longer than known Ni=N bonds. It is possible this ligand is acting as an amide, but that would result in a Ni^{III} species, thus paramagnetic. ^{1}H NMR confirms diamagnetism and now shows symmetrically appropriate equivalence of the piperidine ring methyl groups, unlike any of the other η^1-TEMPO ligands in this chapter which all display two separate resonances. An example ^{1}H NMR spectrum of Ni(η^2-N,O-TEMPO)(2,2,6,6-Tetramethylpiperidin-1-yl)(I) showing magnetic equivalence of piperidine methyls is provided in Appendix C Figure C.3.

This iodide product is now able to participate in many types of salt elimination reactions. Future work with this compound may yield cationic Ni-TEMPO species with non-coordinated anions or perhaps with alky/aryl substituents like Me or Ph groups. It is even conceivable that reaction with lithium or sodium hydrides would produce a Ni-H species. Further study of Ni(η^2-N,O-TEMPO)(2,2,6,6-Tetramethylpiperidin-1-yl)(I) is currently underway.

Reaction of Ni(η^2-N,O-TEMPO)$_2$ with Phenylacetylene, HC≡CPh. Having shown very different reactivity of Ni(η^2-N,O-TEMPO)$_2$ with known 1 and $2e^-$ donating ligands, we questioned how the complex would react towards ligands with multiple possible modes of binding. Unsaturated carbon-carbon bonds like alkynes are capable of bonding in several ways, including "side-on" η^2 portrayed earlier in Ziese's salt. To test the reactivity of Ni(η^2-N,O-TEMPO)$_2$ with unsaturated alkynes, we pursued its reaction

with the easily handled phenylacetylene, HCCPh. When 1eq of phenylacetylene was added to a hexane solution of Ni(η^2-N,O-TEMPO)$_2$, a color change from purple to light red occurred over a period of less than 1 hour. The reaction is nearly instantaneous at 68 °C reflux. Removal of volatiles in *vacuo* and crystallization from diethyl ether resulted in light red bars of Ni(η^2-N,O-TEMPO)(η^1-O-TEMPO-H)(η^1-CCPh) in 73 % yield. X-ray crystallographic analysis yielded the typically distorted square planar structure of Ni(η^2-N,O-TEMPO)(η^1-O-TEMPO-H)(η^1-CCPh) shown in Figure 4.8. Further crystallographic information is provided in Appendix C Table C.2. This complex was characterized by ^{1}H NMR, FTIR, mass spectroscopy, and X-ray crystallographic analysis. Ni(η^2-N,O-TEMPO)(η^1-O-TEMPO-H)(η^1-CCPh) is moderately air and moisture sensitive though crystallographic analysis can be satisfactorily accomplished at ambient conditions with some evident crystal decomposition. Data was later collected at 100 K under flow of N_2 for reasons stated below.

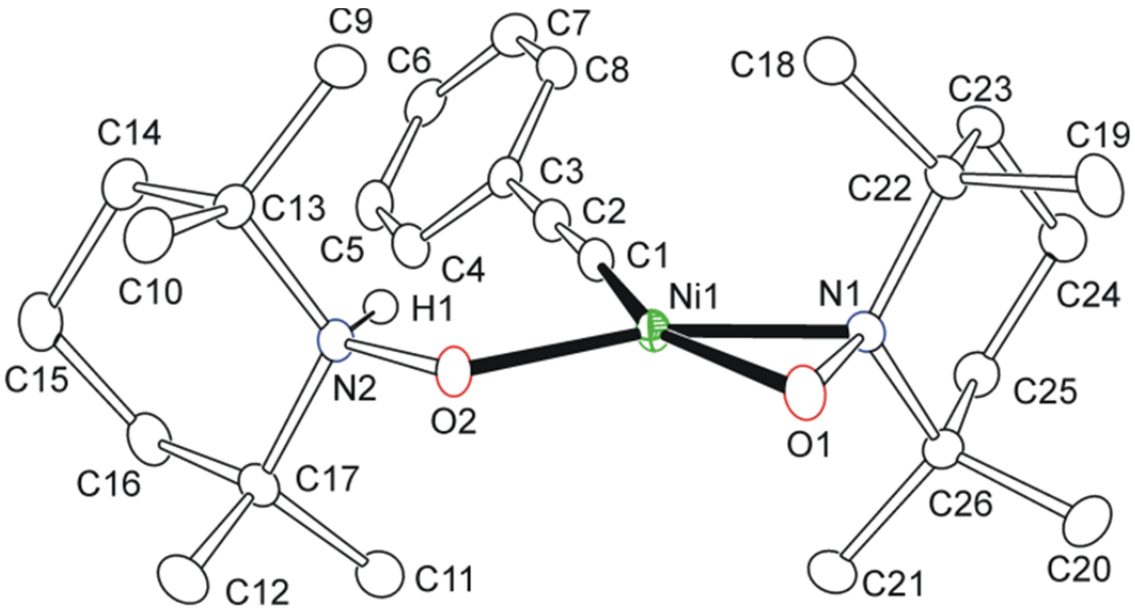

Figure 4.8 An ORTEP showing the molecular of Ni(η^2-N,O-TEMPO)-(η^1-O-TEMPO-H)(η^1-CCPh) at 50 % thermal ellipsoid probability.

Apparent from Figure 4.8, the phenylacetylene reagent did not bind side-on, but has rather been transformed into an "end-on" phenylacetylide group, η^1-CCPh. This reaction is an unusual example of sp hybridized C-H bond activation (~ 130 kcal/mol)[152] and is rather uncommon for group 10 organometallic complexes. A literature search for Ni(η^1-CCPh) yields relatively few results, and nearly all of them were synthesized using salt metathesis or other complicated procedures.[153] Even most of the published Pt and Pd phenylacetylides require several step syntheses or intense UV photolysis.[154] The facile activation of a sp hybridized C-H bond and formation of an η^1-CCPh phenylacetylide was extremely surprising, and shows unexpected chemical reactivity from the non-precious nickel metal. Notice that the oxygen atoms are once again *cis* for unknown mechanistic reasons.

A question immediately arose as to the fate of the hydrogen atom missing from the original phenylacetylene, and at first it was easy to assume elimination of $^1/_2$ H_2 gas. However, mass spectroscopy very accurately identified the presence of an extra 1 m/z, shown in Figure 4.9. The isotopic distribution is again found to be identical to predicted simulation.

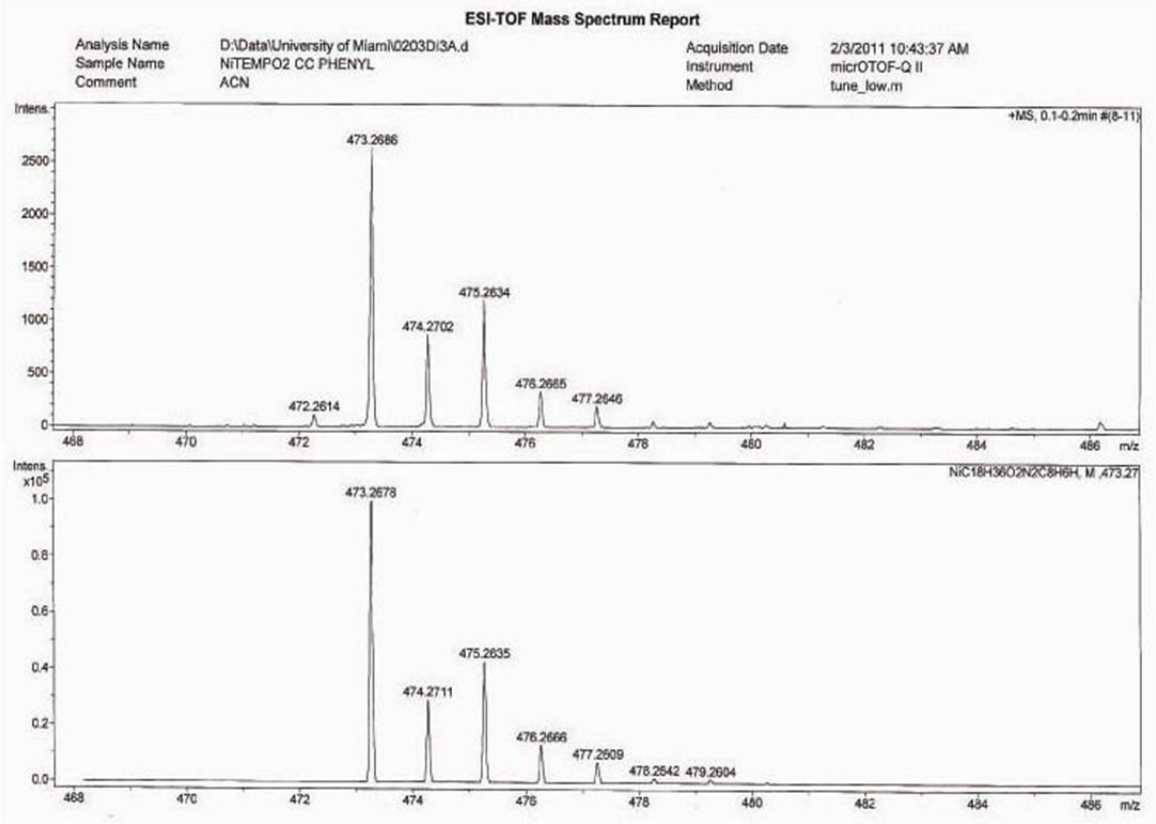

Figure 4.9 ESI-TOF mass spectra of Ni(η^2-N,O-TEMPO)(η^1-O-TEMPO-H)(η^1-CCPh) showing the experimental (top) and predicted (bottom) results.

^{1}H NMR analysis of pure crystalline Ni(η^2-N,O-TEMPO)(η^1-O-TEMPO-H)-(η^1-CCPh) in C_6D_6 was performed to check for the N-H proton resonance. The spectrum shows sharp resonances unlike the isocyanide product, indicative of some enhanced stability in solution. Integration of all non-solvent peaks gave a very accurate total of 42 H, calibrated against one of the free standing 6 H dimethyl peaks shown in Appendix C Figure C.4. A resonance at 7.62 ppm gave an integration of 1H, easily distinguishable from the 1H peak of the phenyl ring at 6.96 ppm, and we assumed this resonance to be assignable the missing phenylacetylene hydrogen.

To check this fact, phenylacetylene-d_1 was acquired from Sigma Aldrich and used to produce Ni(η^2-N,O-TEMPO)(η^1-O-TEMPO-**D**)(η^1-CCPh). ^{1}H NMR of this deuterated product very clearly confirmed the presence of all other assigned peaks, except for the one at 7.62 ppm, shown in Appendix C Figure C.5. This was taken as proof of our peak assignment as well as the presence of phenylacetylene's hydrogen, though the actual molecular position was still unclear.

Having shown the presence of phenylacetylene's hydrogen atom with mass and ^{1}H NMR spectroscopy, we sought to determine its location in the molecule. The most logical positions were on either the oxygen or nitrogen atoms of the η^1-O-TEMPO or on the Ni atom itself. Since ^{1}H NMR showed no evidence for a nickel hydride, we performed single crystal FTIR spectroscopy to check for N-H or O-H stretches. Indeed, the spectrum showed a very broad hump between 3675-3100 cm^{-1}, which could be assigned to either an N-H or O-H bond. For us to state with 100 % certainty that the hydrogen resides on either the N or O atom, neutron diffraction would need to be performed. This is clearly not available at most universities or institutes, and the use of such instruments requires long wait times and large monetary costs.

While not truly definitive, low temperature X-ray crystallographic analysis of an extremely high quality crystal can allow for the successful location and refinement of hydrogen atoms, especially with small molecules that do not contain atoms with intense X-ray absorption like platinum. In fact, low temperature X-ray diffraction analysis of Ni(η^2-N,O-TEMPO)$_2$ had easily allowed location and refinement all 36 hydrogen atoms. For this reason, the crystal structure of Ni(η^2-N,O-TEMPO)(η^1-O-TEMPO-H)(η^1-CCPh) was recollected from a visually flawless single crystal at 100 K under flow of N_2. The

non-hydrogen atoms were all located within one refinement cycle of the crystal data, and the second refinement found most of the hydrogen atoms, the first of which was the H on N2 shown in Figure 4.7. Furthermore, after successfully locating and refining all atoms in the molecule, there were no questionable "Q" peaks on either of the oxygen atoms or N1 whatsoever. This structural data, along with all previous spectroscopic information, is taken by our laboratory as acceptable proof of the hydrogen's assigned location on the η^1-O-TEMPO nitrogen atom.

Ni(η^2-N,O-TEMPO)(η^1-O-TEMPO-H)(η^1-CCPh) remains a 16e$^-$ Ni^{II} complex typical in this chapter with the η^1-O-TEMPO-H ligand acting as an apparent 2e$^-$ donating neutral ligand. The η^1-O-TEMPO-H ligand can be viewed as a fully reduced monoanionic TEMPO that has been protonated at nitrogen, as in the tautomeric form of free TEMPO-H where H is bonded to O rather than N. This type of bonding mode for η^1-O-TEMPO-H is apparently quite rare in transition metal complexes and there are only two other crystallographically characterized examples.[155] Both of these compounds gained the TEMPO-H by abstraction from other reactants such as water, and we presume ours to be the only example of organometallic TEMPO-H not formed in such a manner. This Ni-phenylacetylide complex exhibits H atom transfer from a sp hybridized C-H bond to the N atom of a coordinated TEMPO ligand, the first such reaction found in the literature. Mentioned earlier, work by Baerends et al. has shown that similar hydrogen abstraction by copper bound TEMPO is involved in catalytic oxidation of primary alcohols.[146] The reaction Ni(η^2-N,O-TEMPO)$_2$ with primary alcohols will be discussed later.

The mechanism behind this hydrogen transfer reaction is by no means clear, and many of our questions may never be answered. Our proposed pathways take one of two possible routes. In the concerted mechanism, the HCCPh is inserted upon the Ni center with the simultaneous opening of a single η^2-N,O-TEMPO to form the η^1-O-TEMPO ligand. The lone pair on the η^1-O-TEMPO nitrogen atom is then free to abstract the proton in an acid/base type reaction, shown in equation 4.5.

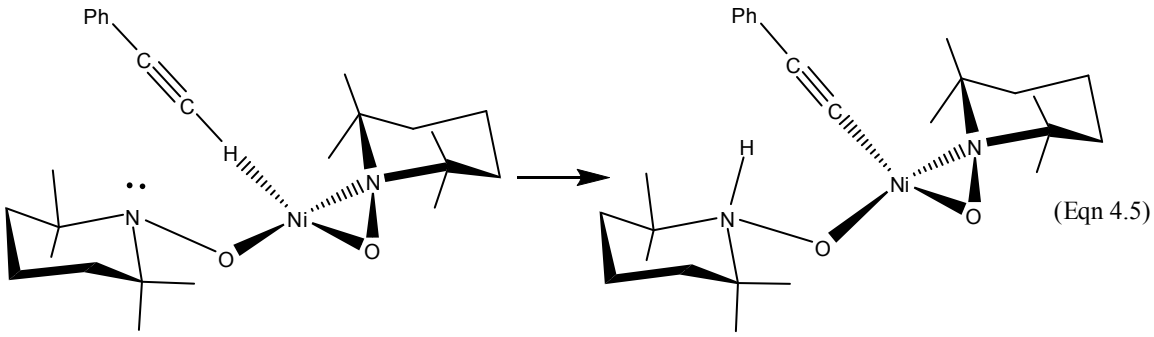

(Eqn 4.5)

The other possible mechanism relies on oxidative addition of both the hydrogen and acetylide groups to the nickel center, followed by hydrogen migration/abstraction to the nitrogen atom of TEMPO. However, this mechanism is most likely not preferred because oxidative addition would proceed through a six coordinate octahedral intermediate similar to Vaska's complex which would be highly strained due to the axial steric shielding by TEMPO methyl groups seen in Figure 4.5. Ni(η^2-N,O-TEMPO)(η^1-O-TEMPO-H)(η^1-CCPh) is stable to reaction with ^{t}BuNC, CO, and even H_2 which was added to check for possible alkyne hydrogenation. It is thermally stable in toluene reflux.

Reaction of Ni(η^2-N,O-TEMPO)$_2$ with 1,4-Diethynylbenzene, HC≡C(C_6H_4)C≡CH. Discovering how Ni(η^2-N,O-TEMPO)$_2$ reacts with phenylacetylene, we decided to extend our study and pursue other alkyne reagents. 1,4-diethynylbenzene is an interesting aromatic compound consisting of a benzene ring substituted with two *para* acetylene groups, shown in Figure 4.10.

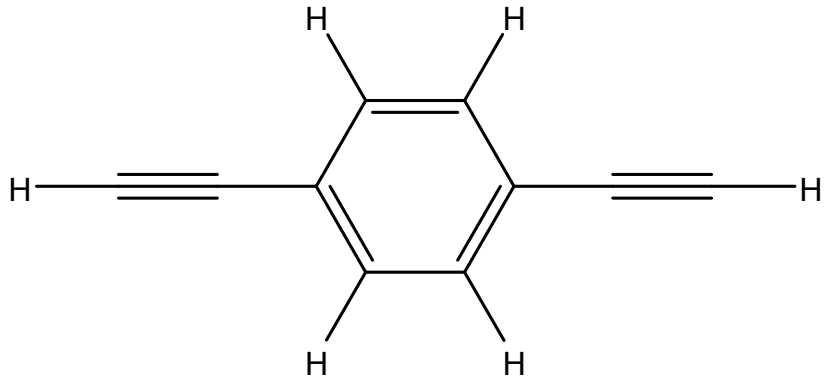

Figure 4.10 Line drawing of 1,4-diethynylbenzene.

Possessing two equivalent acetylene hydrogens, it was unknown how this ligand would react with Ni(η^2-N,O-TEMPO)$_2$. When 1eq of 1,4-diethynylbenzne was added to a hexane solution of Ni(η^2-N,O-TEMPO)$_2$, a color change from purple to auburn red occurred over a period of 1 hour. The reaction is nearly instantaneous at 68 °C though becomes slightly dark with some apparent decomposition. Removal of volatiles in *vacuo* and crystallization of solid residues from diethyl ether resulted in cherry red bars of Ni(η^2-N,O-TEMPO)(η^1-O-TEMPO-H)(η^1-CC[C_6H_4]CCH) in 71% yield. X-ray crystallographic analysis yielded the expected distorted square planar structure of Ni(η^2-N,O-TEMPO)(η^1-O-TEMPO-H)(η^1-CC[C_6H_4]CCH) shown in Figure 4.11.

Further crystallographic information is provided in Appendix C Table C.3. This complex was characterized by ^{1}H NMR, FTIR, mass spectroscopy, and X-ray crystallographic analysis. Ni(η^2-N,O-TEMPO)(η^1-O-TEMPO-H)(η^1-CC[C_6H_4]CCH) is surprisingly stable in air compared to the previous compounds, and a full sphere 20 hour X-ray crystallographic analysis was accomplished at ambient conditions with no apparent decomposition.

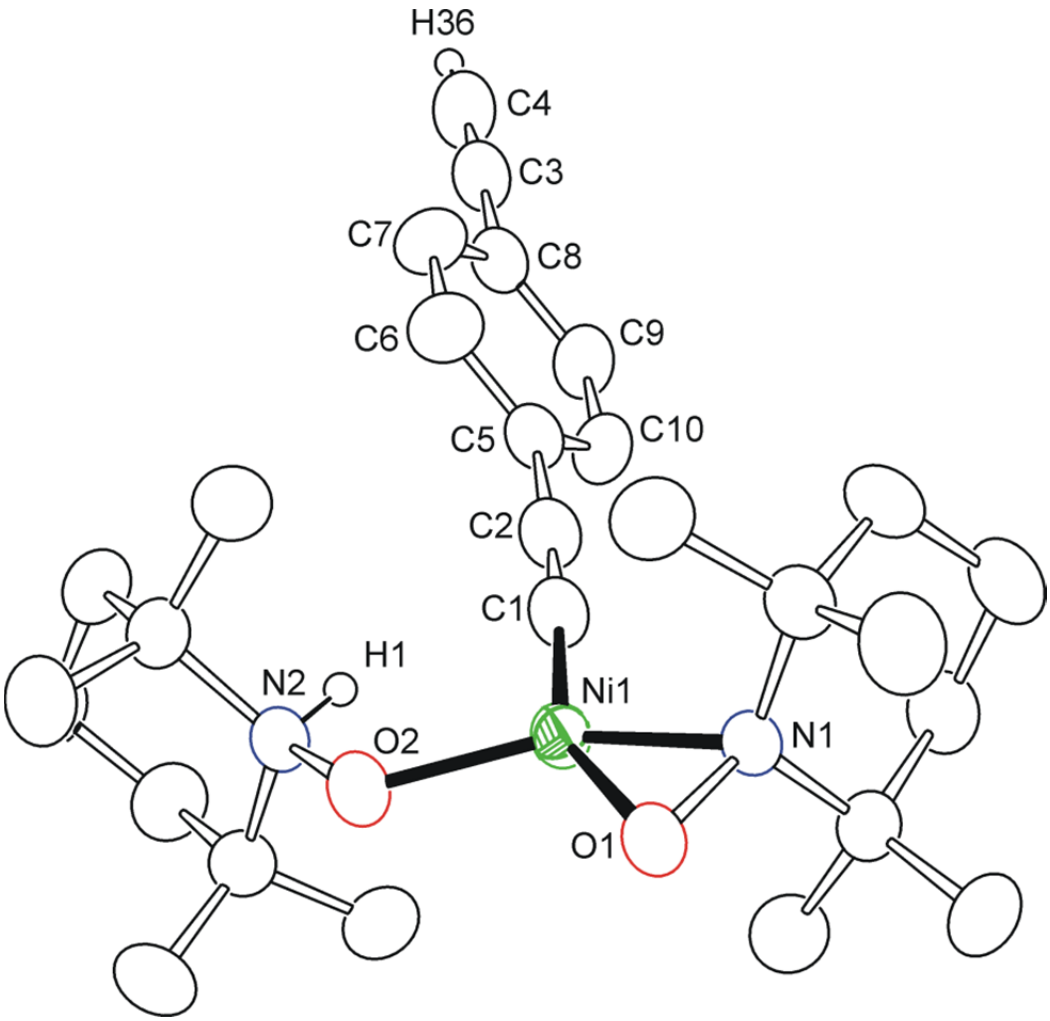

Figure 4.11. An ORTEP showing the molecular structure of Ni(η^2-N,O-TEMPO)-(η^1-O-TEMPO-H)-(η^1-CC[C_6H_4]CCH) at 30 % thermal ellipsoid probability.

Location and refinement of all atoms was again successful, and the very first hydrogen atom found was on N2. There were no final Q peaks on either oxygen atom or N1. Mass spectroscopy once again very accurately confirmed the presence of the acetylene hydrogen, shown in Figure 4.12 at 473 m/z and appropriate isotopic distribution. ^{1}H NMR spectroscopy again shows evidence for this N-H at 7.65 ppm with precise integration of 1H, as well as also showing the second acetylene hydrogen in-tact at 3.26 ppm in C_6D_6. Deuterated products were not commercially available to confirm NMR assignments. FTIR spectroscopy gives the same broad hump suggestive of a N-H stretch around 3200 cm^{-1}.

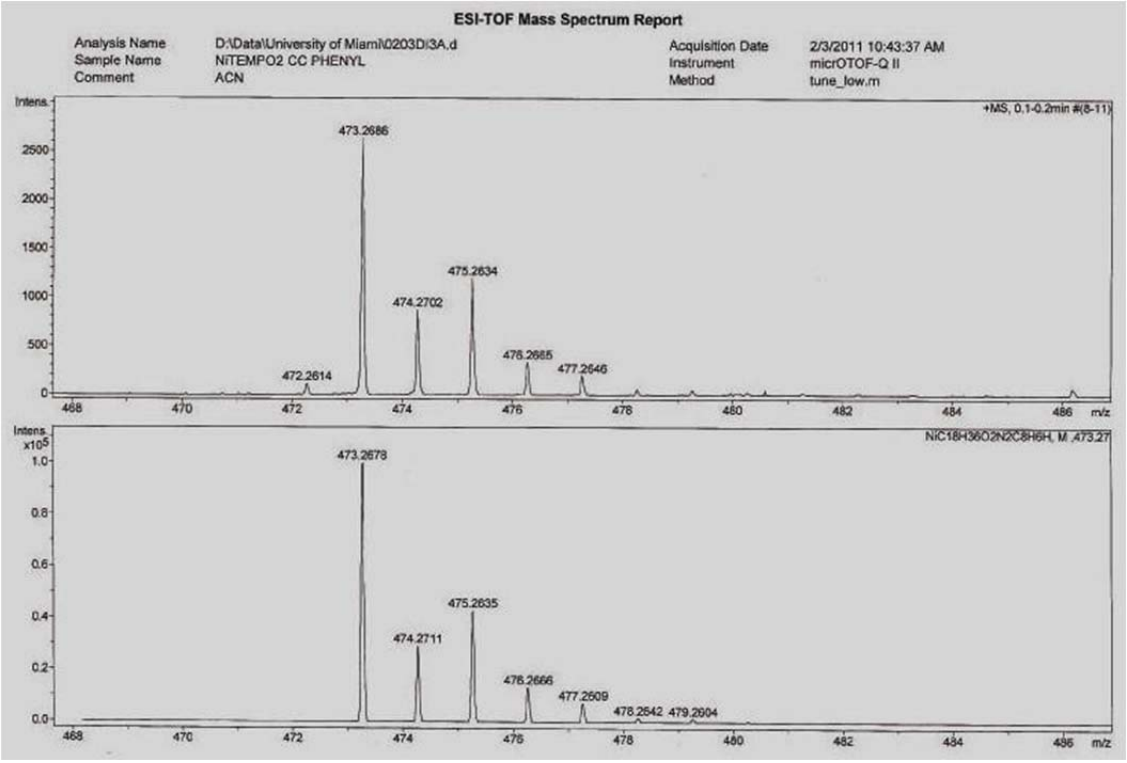

Figure 4.12. ESI-TOF mass spectrum report of Ni(η^2-N,O-TEMPO)(η^1-O-TEMPO-H)-(η^1-CC[C_6H_4]CCH) showing the experimental (top) and predicted (bottom) results.

The crystal structure of Ni(η^2-N,O-TEMPO)(η^1-O-TEMPO-H)-(η^1-CC[C_6H_4]CCH) is nearly identical to that of Ni(η^2-N,O-TEMPO)(η^1-O-TEMPO-H)(η^1-CCPh) with one major difference: there is now a free alkyne hydrogen available for further reaction. This dangling ethynyl group immediately lead us to attempt the capping reaction of Ni(η^2-N,O-TEMPO)(η^1-O-TEMPO-H)(η^1-CC[C_6H_4]CCH) with another equivalent of Ni(η^2-N,O-TEMPO)$_2$. Assuming there is enough steric space to allow approach of Ni(η^2-N,O-TEMPO)$_2$, this reaction should yield the proposed dimeric product [Ni(η^2-N,O-TEMPO)(η^1-O-TEMPO-H)]$_2$[CC(C_6H_4)CC], shown in Figure 4.13.

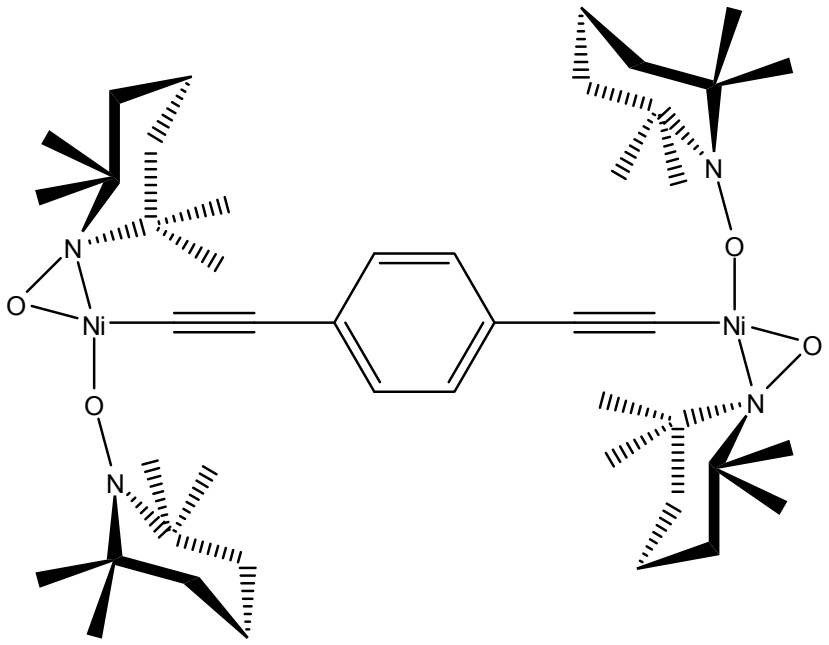

Figure 4.13 Line drawing of the proposed compound [Ni(η^2-N,O-TEMPO)(η^1-O-TEMPO-H)]$_2$[CC(C_6H_4)CC].

This hypothetical compound is bridged by an aromatic link and may show signs of charge transfer in the near IR region if able to be produced.[156] However, this proposed product has not been generated as of yet. FTIR spectroscopy shows little change in the

C≡C stretching region for this reaction even in refluxing hexane, and visual evidence of some decomposition is provided by evolution of dark insoluble material. This capping reaction is under further study and may yet be successful with time. The free acetylene group provides many intriguing chemical possibilities and accordingly this compound will be thoroughly investigated in the future.

Reaction of Ni(η^2-N,O-TEMPO)$_2$ with Trimethylsilyl and Triisopropylsilyl Acetylene, $Me_3SiC{\equiv}CH$ and $^{i}Pr_3SiC{\equiv}CH$. To further extend our reactivity study of Ni(η^2-N,O-TEMPO)$_2$ with sp hybridized C-H bonds, we purchased Me_3SiCCH and $^{i}Pr_3SiCCH$ from Sigma-Aldrich. These two silyl acetylenes are similar, yet possess vastly different alkyl substituents around Si. While the trimethylsilyl acetylene is structurally similar to ^{t}BuNC, the triisopropyl analogue is much more bulky and we were unsure if sterics would allow reaction with Ni(η^2-N,O-TEMPO)$_2$ similar to previous acetylenes.

When one equivalent of Me_3SiCCH was added to a room temperature hexane solution of Ni(η^2-N,O-TEMPO)$_2$ a color change from purple to light red occurred over the period of less than one hour. The reaction was found to be nearly instantaneous at 68 °C. The volatiles were removed in *vacuo* and the solid residues were crystallized from diethyl ether affording bright red blocks of Ni(η^2-N,O-TEMPO)(η^1-O-TEMPO-H)(η^1-$CCSiMe_3$) in 79 % yield. X-ray crystallographic analysis yielded the expected distorted square planar structure of Ni(η^2-N,O-TEMPO)(η^1-O-TEMPO-H)(η^1-$CCSiMe_3$) shown in Figure 4.14. Further crystallographic information is provided in Appendix C Table C.3. This complex was characterized by ^{1}H NMR, FTIR, mass spectroscopy, and X-ray crystallographic analysis. Ni(η^2-N,O-TEMPO)(η^1-O-TEMPO-H)(η^1-$CCSiMe_3$) is very

stable in air compared to the previous compounds, and X-ray crystallographic analysis was successfully accomplished at ambient conditions with no apparent decomposition.

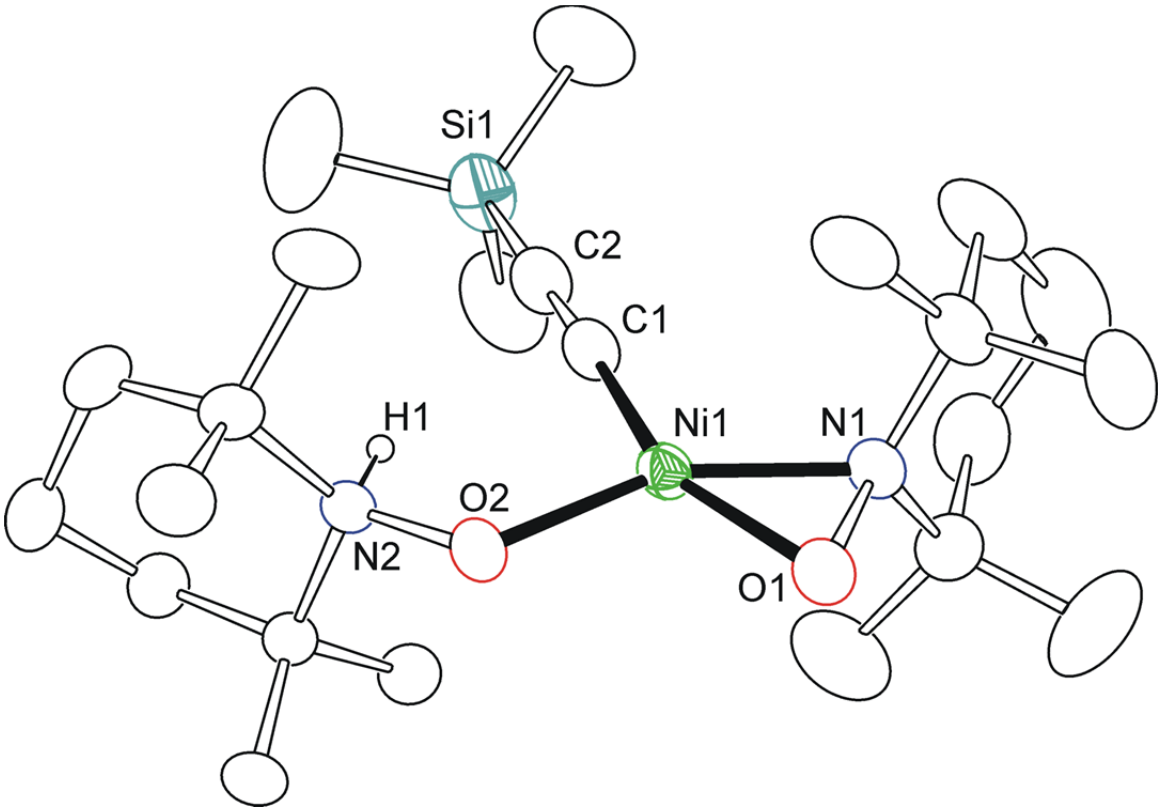

Figure 4.14 An ORTEP showing the molecular structure of Ni(η^2-N,O-TEMPO)-(η^1-O-TEMPO-H)(η^1-CCSiMe$_3$) at 30 % thermal ellipsoid probability.

The acetylene hydrogen was again found easily on N2 with no "Q" peaks on either oxygen atoms or N1. Mass spectroscopy accurately identified the presence of acetylene's hydrogen shown in Figure 4.15. The FTIR spectrum shows a single C≡C stretch now at 2009 cm^{-1} in hexane, significantly less energy than the previous Ni-TEMPO-acetylene derivatives. This is most likely due to the electropositive silicon atom donating electron density into the triple bond, weakening it. This crystal structure is

nearly identical to the one for Ni(η^2-N,O-TEMPO)(η^1-O-TEMPO)(^{t}BuNC) with *cis* oxygen atoms.

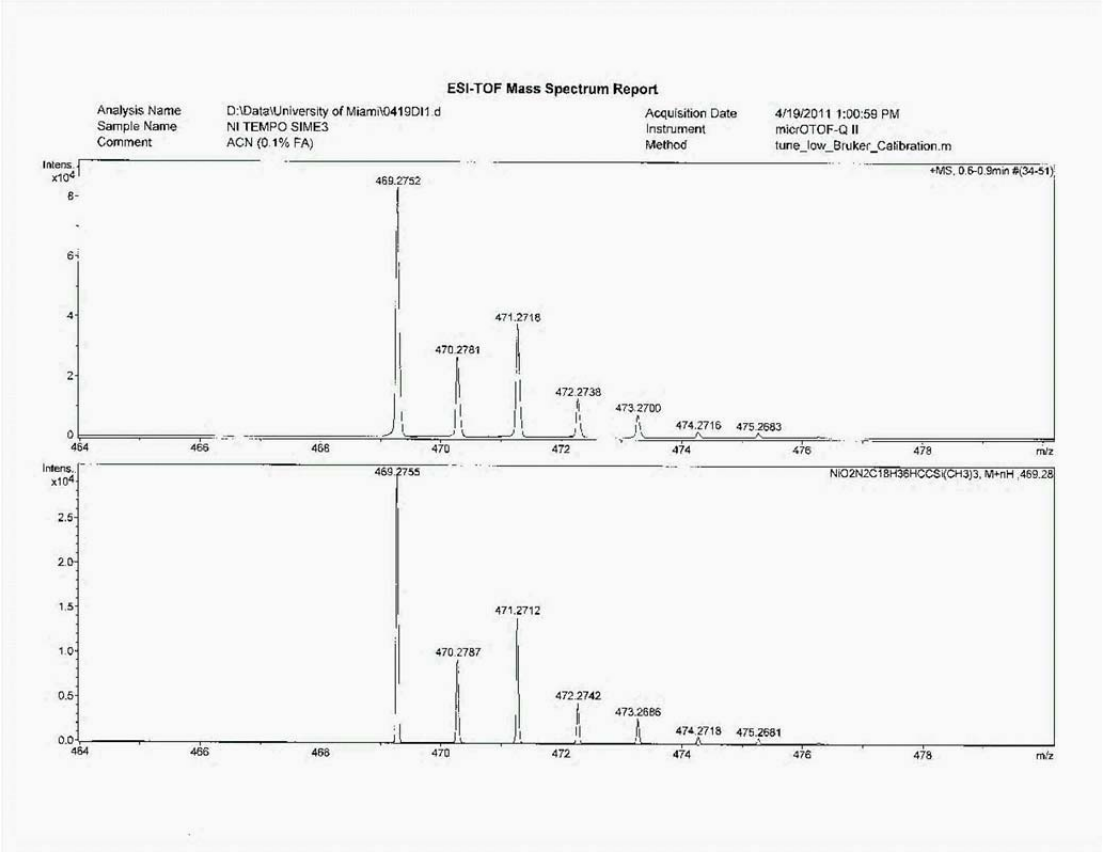

Figure 4.15. ESI-TOF mass spectrum report for Ni(η^2-N,O-TEMPO)(η^1-O-TEMPO-H)-(η^1-$CCSiMe_3$) showing the experimental (top) and predicted (bottom) results.

We expected a nearly identical reaction with $^{i}Pr_3SiCCH$ yielding the proposed product shown in Figure 4.16.

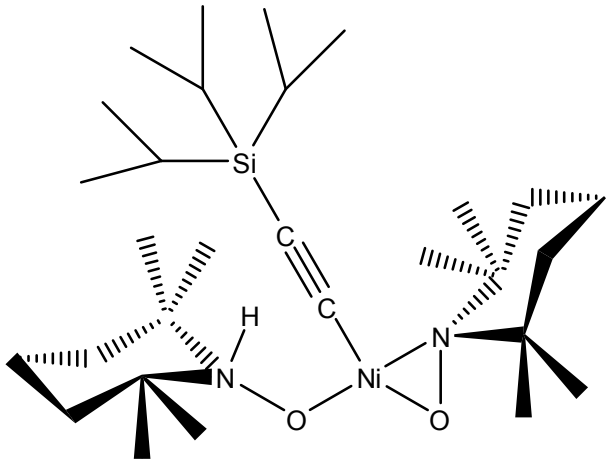

Figure 4.16 Line structure of the proposed Ni(η^2-N,O-TEMPO)(η^1-O-TEMPO-H)-(η^1-CCSi^{i}Pr$_3$).

However, addition of excess $^{i}Pr_3SiCCH$ to Ni(η^2-N,O-TEMPO)$_2$ even in refluxing hexane does not afford a new product. Since the only differing factor between these two silyl acetylenes is a change in the amount of steric bulk around Si, the larger isopropyl groups must forbid approach and addition to the Ni center. This result was semi-expected, though needed to be experimentally confirmed. This seems to imply a size limit for molecules that will react with Ni(η^2-N,O-TEMPO)$_2$.

Reaction of Ni(η^2-N,O-TEMPO)$_2$ with Acetylene Gas, HC≡CH. The reaction of Ni(η^2-N,O-TEMPO)$_2$ with substituted acetylenes was found to produce the above complexes, but we were unsure as to whether the symmetrical acetylene gas would react without any substituents. When acetylene gas was purged through a hexane solution of Ni(η^2-N,O-TEMPO)$_2$ a color change from purple to light red occurred over the period of

one hour. The reaction was found to be nearly instantaneous at 68 °C reflux. Removal of volatiles in *vacuo* followed by crystallization from diethyl ether afforded bright red blocks of Ni(η^2-N,O-TEMPO)(η^1-O-TEMPO-H)(η^1-CCH) in 74 % yield. X-ray crystallographic analysis yielded the distorted square planar structure of Ni(η^2-N,O-TEMPO)(η^1-O-TEMPO-H)(η^1-CCH) shown in Figure 4.17. Further crystallographic information is provided in Appendix C Table C.4. This complex was characterized by ^{1}H NMR, FTIR, mass spectroscopy, and X-ray crystallographic analysis. Mass spectra again identifies the acetylene H very accurately at 397 m/z and ^{1}H NMR shows the usual N-H resonance at 7.64 ppm.

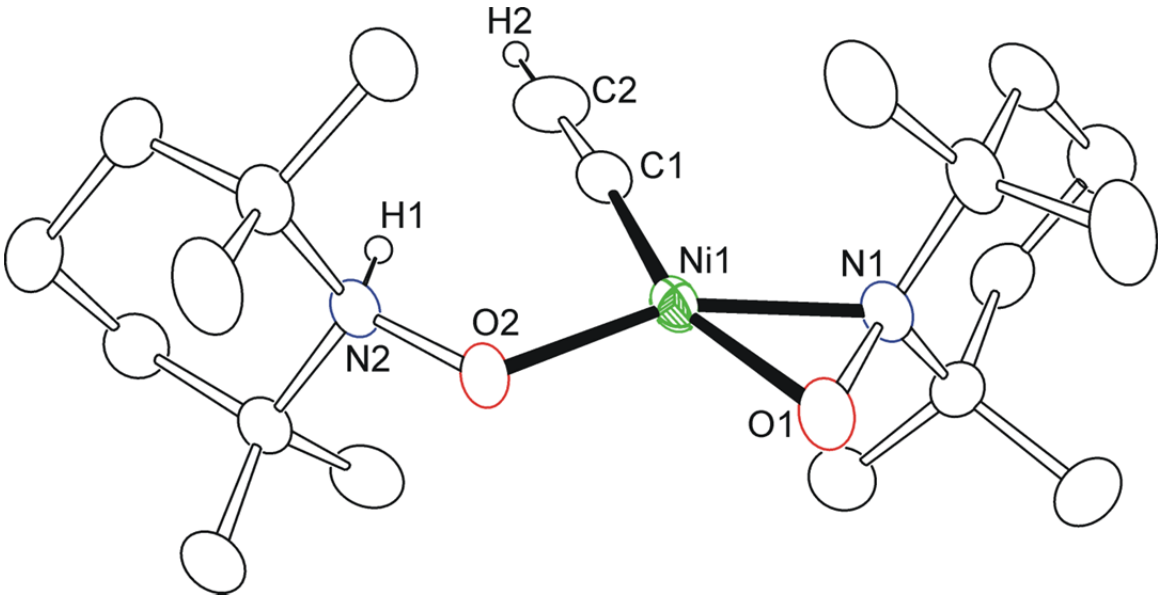

Figure 4.17 An ORTEP showing the molecular structure of Ni(η^2-N,O-TEMPO)-(η^1-O-TEMPO-H)(η^1-CCH) at 30 % thermal ellipsoid probability.

A crystallographic database search reveals six examples of "end-on" group 10 metal-CCH compounds, all of which were synthesized by salt elimination. We believe Ni(η^2-N,O-TEMPO)(η^1-O-TEMPO-H)(η^1-CCH) to be the first structurally characterized

example of acetylene C-H bond activation to yield a Ni-(η^1-CCH) compound. The FTIR stretch for the C≡C bond is now found at 1933 cm^{-1} in hexane, significantly lower in energy than any of the other Ni-acetylene compounds above. Literature values for these terminal acetylides are also around 1930 cm^{-1}.[157] This low energy should correspond to a slightly longer bond but the C≡C distance is 1.19 Å, appropriately. We are currently unsure as to why this bond is so much weaker, even than the $SiMe_3$ substituted product above, and further study of Ni(η^2-N,O-TEMPO)(η^1-O-TEMPO-H)(η^1-CCH) is currently underway.

Reaction of Ni(η^2-N,O-TEMPO)$_2$ with Pyridine and Pyrazine. The isocyanide substituted product Ni(η^2-N,O-TEMPO)(η^1-O-TEMPO)(^{t}BuNC) was discussed earlier and it was assumed that all appropriate $2e^-$ donors would react in a similar fashion. To further investigate this assumption, the nitrogen atom electron donating solvent pyridine was used. When excess pyridine was added to a room temperature hexane solution of Ni(η^2-N,O-TEMPO)$_2$ an immediate color change from purple to dark brown/yellow occurred. During removal of volatiles in *vacuo* a partial regeneration of purple color on the Schlenk flask walls was observed. Recrystallization of solid residues from diethyl ether with a drop of pyridine afforded dark brown blocks of Ni(η^2-N,O-TEMPO)-(η^1-O-TEMPO)(NC_5H_5) in 95 % yield. X-ray crystallographic analysis yielded the expected distorted square planar structure of Ni(η^2-N,O-TEMPO)(η^1-O-TEMPO)-(NC_5H_5) shown in Figure 4.18. Further crystallographic information is provided in Appendix C Table C.4. This complex was characterized by ^{1}H NMR, mass spectroscopy, and X-ray crystallographic analysis. Ni(η^2-N,O-TEMPO)(η^1-O-TEMPO)(NC_5H_5) is

highly unstable in air, and X-ray crystallographic analysis will require data collection at 100 K under flow of N_2 to avoid crystal decomposition.

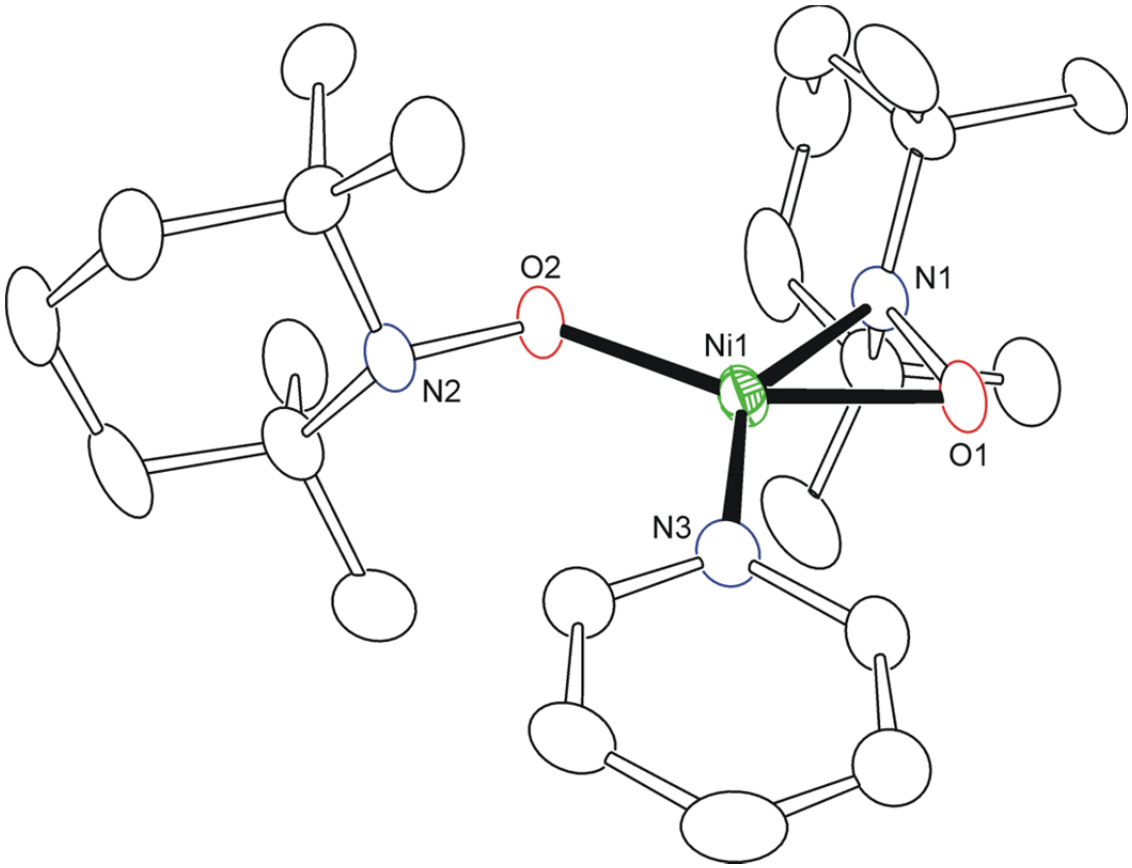

Figure 4.18 An ORTEP showing the molecular structure of Ni(η^2-N,O-TEMPO)(η^1-O-TEMPO)(NC_5H_5) at 30 % thermal ellipsoid probability.

At first glance, the structure seen in Figure 4.18 appears to be normal and expected from previous work. However, a second look reveals a very unusual anomaly: the oxygen atoms are not *cis* but rather *trans* like in Ni(η^2-N,O-TEMPO)$_2$. This structure is what we had expected from every other product, with the simple opening of one metallacycle and addition of a new ligand without somehow flipping to yield *cis* oxygen

atoms. As of yet, we are unsure as to why this particular complex acts in a differing manner, although the lability of the Ni-N bond to pyridine may be responsible.

Stated earlier, this compound appears to exist in equilibrium between starting material Ni(η^2-N,O-TEMPO)$_2$ and its pyridine adduct. Reduction of atmospheric pressure while evacuating the reaction mixture to dryness provided purple solid on the flask walls. In fact, during attempts at mass spectroscopy the brown crystals were seen to become instantly purple in acetonitrile and methanol solvents before quickly decomposing, discussed later. It was not until the spectroscopy was performed in non-coordinating acetone solvent with a drop of pyridine that we obtained a minor parent peak of Ni(η^2-N,O-TEMPO)(η^1-O-TEMPO)(NC_5H_5) at 450 m/z shown in Figure 4.19, along with a very major peak at 370 m/z for Ni(η^2-N,O-TEMPO)$_2$. The fact that the major peak belongs to starting material is also evidence of equilibrium in solution. This suggested the need for ^{1}H NMR analysis.

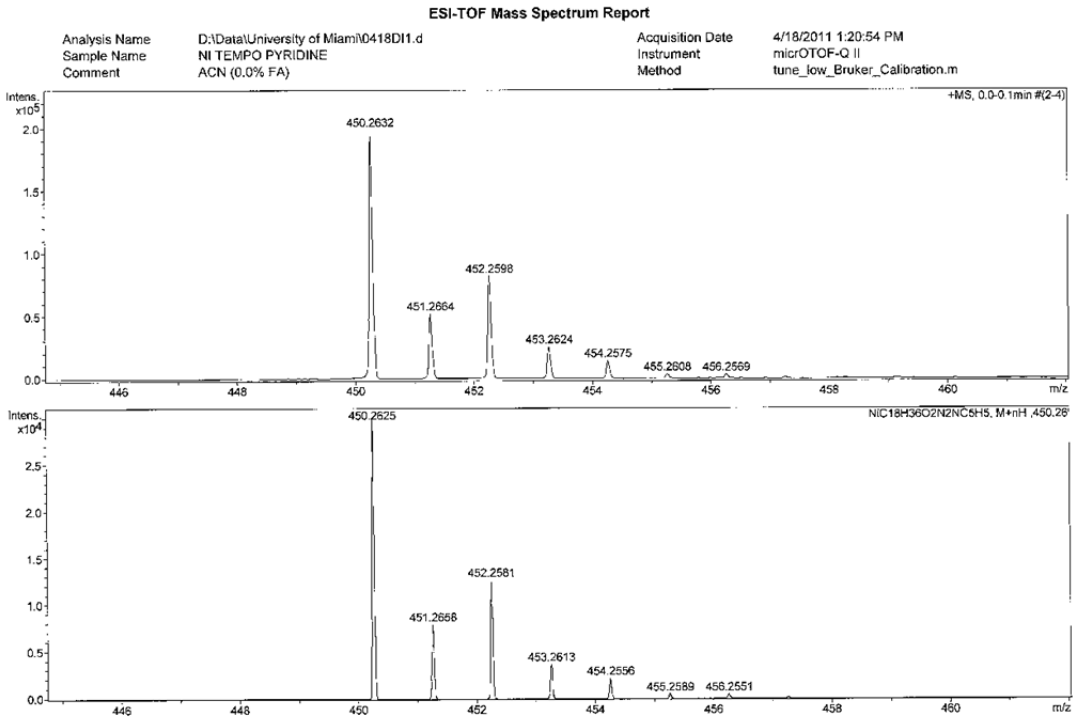

Figure 4.19 ESI-TOF mass spectrum report for Ni(η^2-N,O-TEMPO)(η^1-O-TEMPO)(NC_5H_5) showing experimental results (top) and predicted results (bottom).

^{1}H NMR analysis of Ni(η^2-N,O-TEMPO)(η^1-O-TEMPO)(NC_5H_5) is difficult for several reasons. When dissolving pure crystals in C_6D_6 an apparent equilibrium is generated instantly and the solution will become more purple than dark brown due to dilution effects. The ^{1}H NMR spectrum of this solution seems to show mostly free pyridine with other minor peaks in this region (~8-6 ppm), however the metal bound pyridine ligands appear to show more than the 3 predicted proton resonances. This suggests lack of rotation around the Ni-NC_5H_5 bond thus generating magnetically distinct hydrogen atoms on the pyridine ring due to differing environments. To better understand

why this is so, space filling models were prepared and are shown in Appendix C Figures C.6, C.7, and C.8. Examination of these space filling models shows the pyridine ligand to be inserted on the nickel atom tightly between the methyl groups of the TEMPO ligands. The pyridine ring is seemingly blocked from rotation by these methyl groups and forced into the plane of the molecule. This may explain the existence of extra ^{1}H NMR resonances in the pyridine region.

^{1}H NMR spectra for pure crystalline Ni(η^2-N,O-TEMPO)(η^1-O-TEMPO)(NC_5H_5) shows a methyl region (~3-0 ppm) that is more or less identical to Ni(η^2-N,O-TEMPO)$_2$ with other very minor broad peaks. This again suggests the existence of equilibrium in solution which seems to heavily favor free pyridine and Ni(η^2-N,O-TEMPO)$_2$. To better understand this finding, a large excess of pyridine (~100 fold) was added to the tube making the region around 7 ppm extremely intense and unable to be interpreted. The methyl region now showed significant change, and line broadening is immediately apparent in Appendix C. Figure C.9. This spectrum is very similar to the only other $2e^-$ substituted product described so far, the isocyanide complex shown in Appendix C Figure C.2. There is also a detectable amount of Ni(η^2-N,O-TEMPO)$_2$ still present, and this shows that the equilibrium favors free pyridine even when in large excess. The pyridine complex appears to undergo dynamical process in solution much like the isocyanide complex. This is still not well understood, though is under further study. ^{1}H NMR analysis in pyridine-d_5 shows nearly complete change of the methyl region, and the unknown dynamical process is easily apparent as broad hump resonances.

Pyrazine is similar to pyridine, replacing the carbon atom *para* to nitrogen in the aromatic ring with a second nitrogen atom. Adding one equivalent of NC_4H_4N to a

solution of Ni(η^2-N,O-TEMPO)$_2$ will result in an instantaneous color change to the dark brown/yellow of the pyridine complex mentioned above. During evacuation of volatiles from the reaction mixture, a similar regeneration of purple color on the flask walls was observed to an even greater extent. We expected to isolate the proposed product Ni(η^2-N,O-TEMPO)(η^1-O-TEMPO)(NC_4H_4N) from this reaction shown in Figure 4.20.

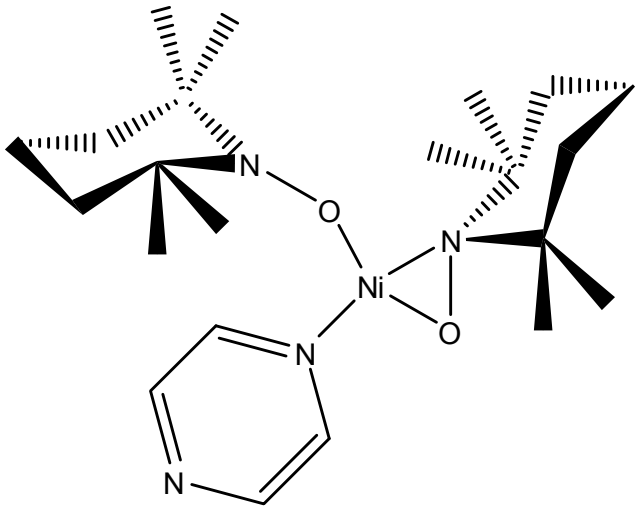

Figure 4.20 Proposed line structure of Ni(η^2-N,O-TEMPO)(η^1-O-TEMPO)(NC_4H_4N).

However, even with 4 equivalents of solid pyrazine added to the crystallization solution, only purple crystals of Ni(η^2-N,O-TEMPO)$_2$ are formed. This is quizzical, as the ligand excess should have provided at least a fractional amount of solid Ni-pyrazine product. ^{1}H NMR spectroscopy again shows equilibrium formation similar to pyridine as well as dynamical processes when pyrazine is in excess. However, an even larger excess of pyrazine is required to produce noticeable changes in the ^{1}H NMR methyl region than for pyridine. This suggests weaker binding of pyrazine which may due to the lack of dipole moment found in pyridine.

It is worth mentioning in this section that Ni(η^2-N,O-TEMPO)$_2$ reacts instantly with ammonia gas, NH_3. A color change from purple to reddish brown is observed. However, even slight reduction in atmospheric pressure results in instantaneous color change back to purple affording only purple solid residues. This suggests similar equilibrium to that described above, and it can be assumed that the product Ni(η^2-N,O-TEMPO)(η^1-O-TEMPO)(NH_3) is formed. Isolation will likely require crystallization under ammonia atmosphere and this will be attempted in the future.

Reaction of Ni(η^2-N,O-TEMPO)$_2$ with CO gas. Based on the reaction of Ni(η^2-N,O-TEMPO)$_2$ with ^{t}BuNC to afford Ni(η^2-N,O-TEMPO)(η^1-O-TEMPO)(^{t}BuNC), we postulated that reaction with the very similar ligand CO should produce the analogous complex Ni(η^2-N,O-TEMPO)(η^1-O-TEMPO)(CO), shown in Figure 4.21.

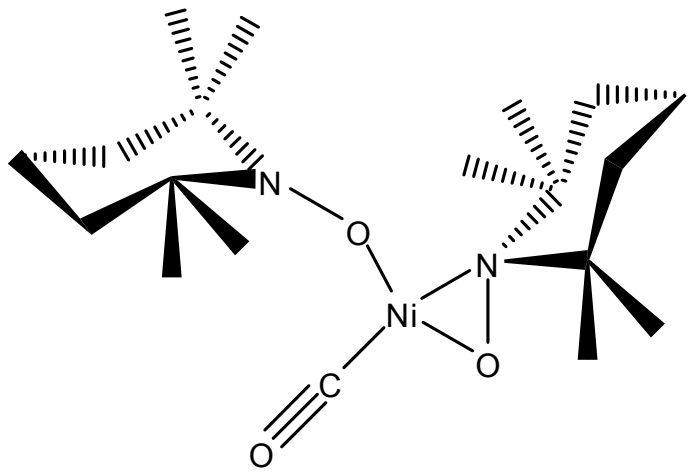

Figure 4.21 Proposed line structure of Ni(η^2-N,O-TEMPO)(η^1-O-TEMPO)(CO).

The structure of this proposed complex should be nearly identical to the isocyanide derivative shown in Figure 4.3 though may possess *trans* oxygen atoms similar to the

pyridine product. When Carbon monoxide gas was purged through a room-temperature hexane solution of Ni(η^2-N,O-TEMPO)$_2$ there was an immediate color change to a dark reddish purple. Quickly performing FTIR spectroscopy of this solution shows the appropriate appearance of one new CO stretching frequency at 2045 cm^{-1}, seen in Appendix C Figure C.10, and we assume this single peak to belong to the proposed structure shown in Figure 4.21. However, within minutes the solution became clear and showed signs of decomposition as precipitation of colorless solids. These decomposition products are not soluble in hexane, toluene, diethyl ether, THF, DMSO, methylene chloride, or water. Assuming that low temperature may stabilize this CO adduct the reaction was performed two times identical to the previous attempt, but this time the solution was maintained at either 0 or -78 °C. Even at these depressed temperatures, the reaction goes forward to decomposition with solution decolorization at some time after addition of CO, signifying decomposition of products. The lifetime of this CO product is indeed extended at lower temperature though not nearly long enough for satisfactory crystallization.

It is possible that the excess bulk of the *tert*-butyl isocyanide ligand provides stabilization to its corresponding product. The proposed CO product lacks the steric volume to prevent further access to the unsaturated nickel center by excess CO. At this time we are unsure as to why this product is so prone to decomposition, but as stated below, unstable reaction with small molecules is common for Ni(η^2-N,O-TEMPO)$_2$.

Reaction of Ni(η^2-N,O-TEMPO)$_2$ with Tetrahydrofuran and Acetonitrile Solvents. We have found that Ni(η^2-N,O-TEMPO)$_2$ is stable in non-coordinating solvents such as hexane, benzene, toluene, methylene chloride and even diethyl ether.

However, dissolving purple crystals of Ni(η^2-N,O-TEMPO)$_2$ in either tetrahydrofuran, THF, or acetonitrile, MeCN, will result in quick loss of color and evidence of decomposition in the form of colorless solid precipitation. It is proposed that an analogous reaction to that with CO is occurring, yielding the unstable products Ni(η^2-N,O-TEMPO)(η^1-O-TEMPO)(MeCN) and Ni(η^2-N,O-TEMPO)(η^1-O-TEMPO)(THF) shown in Figure 4.22.

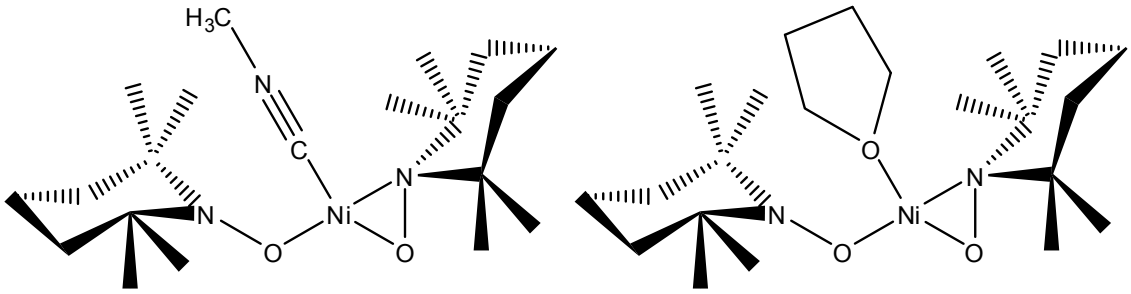

Figure 4.22 Proposed line structures of the unstable products Ni(η^2-N,O-TEMPO)(η^1-O-TEMPO)(MeCN) and Ni(η^2-N,O-TEMPO)(η^1-O-TEMPO)(THF).

Even at depressed temperatures, these products are not stable to decomposition, but this fact suggests strong reaction with coordinating solvents. Though not shown above, Ni(η^2-N,O-TEMPO)$_2$ will also react with methanol in a similar manner although it is likely that this reaction proceeds through a different mechanism, discussed later with benzyl alcohol.

Stated earlier in this chapter, the mass spectrometry of Ni(η^2-N,O-TEMPO)$_2$ in acetonitrile afforded a major peak at 412 m/z, the predicted mass for an acetonitrile adduct. The mass spectrum showed an exact isotopic distribution for the theoretical

Ni(η^2-N,O-TEMPO)(η^1-O-TEMPO)(MeCN) as predicted by computer simulation. This piece of evidence helps support the hypothetical structures shown above and below.

Reaction of Ni(η^2-N,O-TEMPO)$_2$ with H_2 and $H_2C{=}CH_2$ Gasses. After finding the complex Ni(η^2-N,O-TEMPO)$_2$ to be capable of reaction with coordinating solvents as well as the ligands discussed above, we extended our reactivity study to include the small molecule gasses H_2 and C_2H_4. We were unsure as to how these ligands would react with Ni(η^2-N,O-TEMPO)$_2$, if at all. When hydrogen or ethylene gas was purged through a hexane solution of Ni(η^2-N,O-TEMPO)$_2$, even at depressed temperatures, there was rapid decolorization with precipitation of insoluble colorless solids. Again, there was no isolation of new products. It is possible that a similar reaction to that with phenylacetylene is occurring, yielding the hypothetical hydrogen transfer products shown in Figure 4.23. The hydride and ethylene ligands would provide very little steric protection, and it is possible that excess reagent is pushing the reaction forward to an unstable final product. Our attempts at adding precisely 1eq of these gasses still results in decolorization and precipitation.

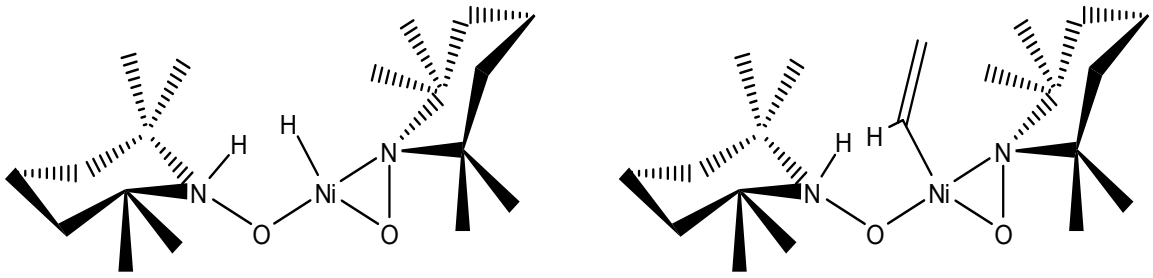

Figure 4.23 Proposed line structures of Ni(η^2-N,O-TEMPO)(η^1-O-TEMPO-H)(H) and Ni(η^2-N,O-TEMPO)(η^1-O-TEMPO-H)(C_2H_3).

As of yet, no products have been isolated from any of the unstable reactions listed above though they may be more actively pursued in the future. These decomposition reactions suggest strong reaction with and possible activation of tested substrates, and it is feasible that these reactions can be used for synthesis in the presence of other reagents.

Reaction of Ni(η^2-N,O-TEMPO)$_2$ with Benzyl Alcohol, BzOH. Having found literature evidence for organometallic TEMPO complexes capable of primary alcohol oxidation discussed earlier, we set out to investigate whether or not Ni(η^2-N,O-TEMPO)$_2$ might possess this synthetic ability. Benzyl alcohol and benzaldehyde were purchased from Sigma Aldrich and reference ^{1}H NMR spectra were recorded in C_6D_6. Even when greatly zooming in on the concentrated benzyl alcohol spectrum, there was no sign of trace benzaldehyde at 9.66 ppm.

Upon addition of 5 mg of Ni(η^2-N,O-TEMPO)$_2$ to the very concentrated BzOH/C_6D_6 solution in the reference NMR tube there was no decolorization like that in methanol. In fact, the typical purple color took on a more blueish hue. The tube was then analyzed by ^{1}H NMR again, but now there was evidence of change. Expanding the spectrum revealed new peaks above 8 ppm, including a clear resonance at 9.66 attributable to benzaldehyde. An even larger peak at 10.8 ppm is assumed to be another aldehyde, though we are unsure as to what this could be. Notably, there are also numerous peaks in the region below 0. These negative ppm resonances are suggestive of hydride species, though these have not been isolated at this time. The ^{1}H NMR spectrum exemplifying these results is shown in Figure 4.24. There was still a large excess of BzOH displayed in the NMR spectrum, and allowing the reaction to proceed with time did not afford an increase in benzaldehyde concentration. Clearly this reaction is not

catalytic. However, this data is taken to be proof of concept and is very promising. We are working to optimize this reaction which may require co-catalytic species like KOH or TEMPO.

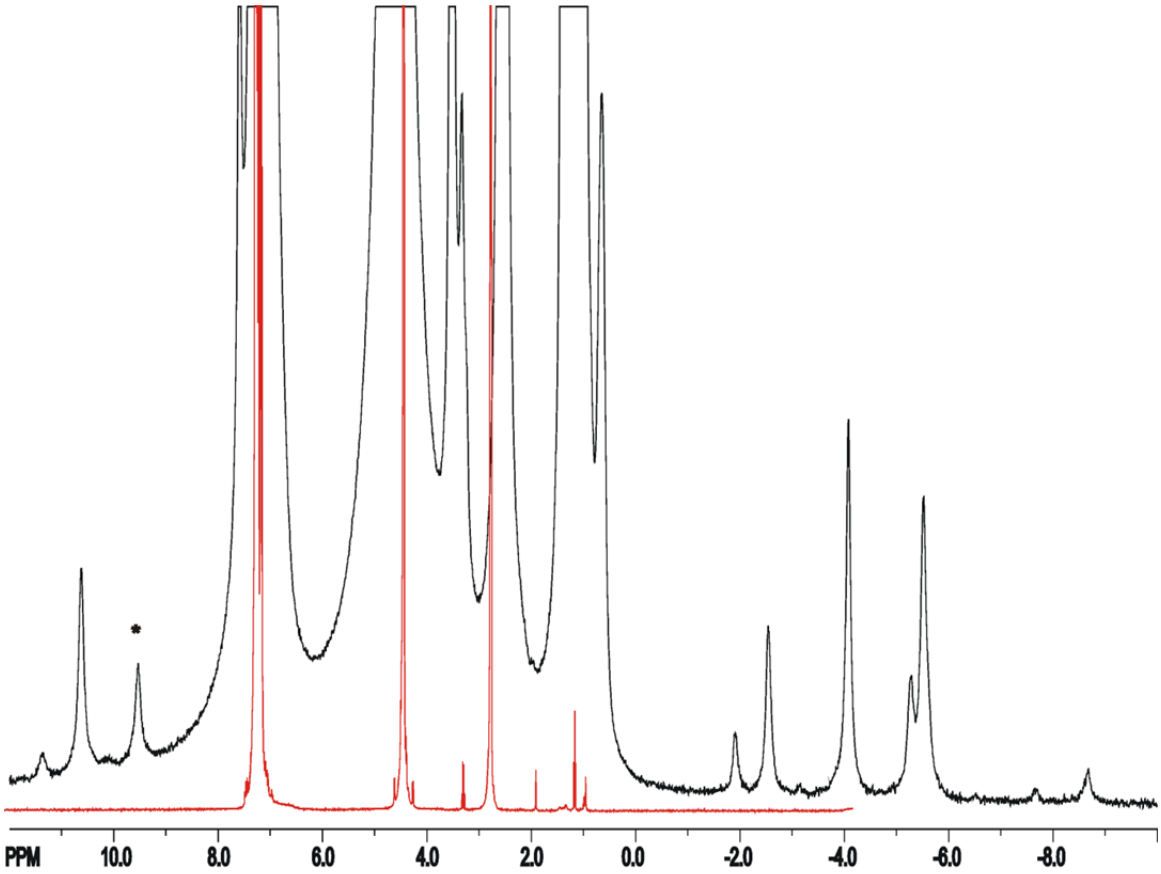

Figure 4.24 ^{1}H NMR spectra showing benzyl alcohol in C_6D_6 (red) and subsequent addition of Ni(η^2-N,O-TEMPO)$_2$. * denotes benzaldehyde H at 9.66 ppm.

6.3 Conclusions

We have reported the synthesis of Ni(η^2-N,O-TEMPO)$_2$ which is the first literature example of an unsaturated transition metal complex with a ligand system consisting solely of TEMPO radicals. This molecule is deceivingly simple, yet displays

elegantly complex reactivity. The compound was shown to react with *tert*-butyl isocyanide to afford Ni(η^2-N,O-TEMPO)(η^1-O-TEMPO)(^{t}BuNC) which exemplifies the mode of reactivity common for Ni(η^2-N,O-TEMPO)$_2$. The reaction results in a single η^2 to η^1 transition of a coordinated TEMPO ligand and yields a 16e$^-$ planar product. This compound showed broadened ^{1}H NMR resonances suggestive of dynamical processes in solution which may be due to equilibrium formation.

Ni(η^2-N,O-TEMPO)$_2$ was reacted with iodine to give Ni(η^2-N,O-TEMPO)-(2,2,6,6-tetramethylpiperidin-1-yl)(I). This product shows reduction of a TEMPO ligand to its precursor 2,2,6,6-tetramethylpiperidine with the nitrogen atom bound directly to the nickel center. Ni(η^2-N,O-TEMPO)(2,2,6,6-tetramethylpiperidin-1-yl)(I) again shows the 16e$^-$ planar structure which is typical in this chapter of work.

Addition of phenylacetylene to Ni(η^2-N,O-TEMPO)$_2$ afforded the surprising product Ni(η^2-N,O-TEMPO)(η^1-O-TEMPO-H)(η^1-CCPh). This complex was formed by apparent sp hybridized C-H bond activation with hydrogen transfer to the nitrogen atom of η^1-O-TEMPO. Substituting HCC(C_6H_4)CCH for phenylacetylene gave the similar product Ni(η^2-N,O-TEMPO)(η^1-O-TEMPO-H)(η^1-CC[C_6H_4]CCH) which now has a free ethynyl group available for further reactions. The reaction with Me_3SiCCH provides the analogous product Ni(η^2-N,O-TEMPO)(η^1-O-TEMPO-H)(η^1-CC$SiMe_3$) though the $^iPr_3Si$ analogue showed no reaction presumably due to sterics. All of these acetylene substituted products portray uncommon chemical reactivity from the central nickel metal since similar group 10 acetylides require elaborate syntheses. This ability to activate sp C-H bonds may find use in future synthetic procedures.

Addition of pyridine to Ni(η^2-N,O-TEMPO)$_2$ produces the dark brown product Ni(η^2-N,O-TEMPO)(η^1-O-TEMPO)(NC_5H_5). This is the first product which shows *trans* oxygen atoms as opposed to *cis*. This pyridine product was shown to exist in equilibrium with the starting materials. ^{1}H NMR spectroscopy displayed a dynamical process, similar to the isocyanide compound, also suggestive of a fluxional equilibrium in solution. Reaction with the very similar pyrazine appears to proceed identically to pyridine, however crystallization of products even in the presence of excess pyrazine affords only starting material Ni(η^2-N,O-TEMPO)$_2$. Reaction with ammonia, NH_3, affords a deep reddish brown solution. However, this product also seems to exist in equilibrium with starting materials and the volatility of ammonia gas makes isolation extremely difficult.

Reaction with carbon monoxide, CO, generated the proposed product Ni(η^2-N,O-TEMPO)(η^1-O-TEMPO)(CO). We have obtained FTIR spectroscopic evidence of this hypothetical complex, though it quickly decomposes even at low temperature to give insoluble colorless precipitate. Dissolving Ni(η^2-N,O-TEMPO)$_2$ in acetonitrile, tetrahydrofuran, or methanol solvents results in rapid decolorization and precipitation of insoluble solids similar to reaction with CO. Purging H_2 or C_2H_4 gas through solutions of Ni(η^2-N,O-TEMPO)$_2$ result in identical decolorization and precipitation of insoluble solids. These decompositions are not understood though suggest strong reaction with all mentioned substrates along with possible activation. Further study may yield synthetic abilities.

Adding Ni(η^2-N,O-TEMPO)$_2$ and benzyl alcohol to C_6D_6 resulted in ^{1}H NMR spectroscopic detection of benzaldehyde at 9.66 ppm. While this reaction is not catalytic

it is a very promising proof of concept, and continued fine tuning may yet result in catalytic conversion of primary alcohols to aldehydes.

Our attempts at generating platinum or palladium analogues of Ni(η^2-N,O-TEMPO)$_2$ were completely unsuccessful. Addition of TEMPO radical to solutions of Pt(COD)$_2$, Pt(COD)Cl$_2$, Pd(allyl)Cp, or Pd(dba)$_2$ yield no products even at elevated temperature. This selectivity for reaction with nickel is unusual in and of itself, and is a rare example of increased reactivity of nickel compared to platinum and palladium. Ni(η^2-N,O-TEMPO)$_2$ is clearly very reactive, but little is known about it presently. The brief survey of reactions presented above represent only a very preliminary investigation into the true chemical nature of Ni(η^2-N,O-TEMPO)$_2$. Future work will include both experimental and theoretical studies to elucidate reaction mechanisms. The complex Ni(η^2-N,O-TEMPO)$_2$ provides hope that non-precious metal catalysts will be found that are capable of useful chemistry, replacing the rare and expensive precious metal catalysts like platinum, palladium, and rhodium.

6.4 Experimental

General Data. Unless indicated otherwise, all reactions were performed under an atmosphere of Argon. Reagent grade solvents were dried by the standard procedures and were freshly distilled prior to use. Solution phase Infrared spectra were recorded on a Nicolet 380 FT-IR spectrophotometer. Single crystal FTIR spectra were obtained on a Perkin Elmer Spectrum 400 using a Perkin Elmer Universal ATR Sampling Accessory. ^{1}H NMR spectra were recorded on a Bruker 400 spectrometer operating at 399.993 MHz.

Elemental analyses were performed by Columbia Analytical Services (Tucson, AZ). Mass spectrometric measurements performed by direct–exposure probe using electron impact ionization (EI) were made on a VG 70S instrument at the University of South Carolina, Columbia, SC, and electrospray mass spectrometric measurements were obtained on a Bruker micrOTOF-Q II at the University of Miami. Bis(1,5-cyclooctadiene)nickel, $Ni(COD)_2$, was purchased from Strem Chemicals, used without further purification, and stored and handled in a drybox. TEMPO (2,2,6,6-tetramethylpiperidine-N-oxyl), *tert*-butyl isocyanide, pyrazine, and phenylacetylene were purchased from Alfa Aesar and used without further purification. 1,4-diethynylbenzene was purchased from TCI and used without further purification. Atomic absorption grade acetylene, argon, and carbon monoxide gasses were purchased from AirGas and used without further purification. Phenylacetylene-d_1 (99 %), Pyridine, Benzyl Alcohol, Benzaldehyde, Trimethylsilyl acetylene, and Triisopropylsilyl acetylene were purchased from Sigma-Aldrich and used without further purification.

Synthesis of Ni(η^2-N,O-TEMPO)$_2$. A 100 mg (0.36 mmol) amount of $Ni(COD)_2$ and 115 mg (0.72 mmol) of TEMPO were loaded into a Schlenk flask. 30 mL of hexane solvent was then added to the flask using a cannula. The stirred solution changed color from light orange to deep purple as it was heated to reflux, for approximately 5 min. The solvent was then removed in *vacuo* and the residue was dissolved in 4 mL of diethyl ether, filtered into a glass vial, and placed in a -25 °C freezer in a drybox. Evaporation of solvent afforded 105 mg (78% yield) of purple crystalline blocks of Ni(η^2-N,O-TEMPO)$_2$. Spectral data for Ni(η^2-N,O-TEMPO)$_2$: ^{1}H NMR (C_6D_6

in ppm): δ = 2.39 (s, 12 H, 4 CH_3), 1.36 (s, 12 H, 4 CH_3), 1.40 – 1.25 (m, broad,12 H, 6 CH_2). Mass Spec. ES^+/MS calcd for [M + CH_3CN], 412; found 412. The isotope distribution is consistent with the presence of one nickel atom.

Synthesis of Ni(η^2-N,O-TEMPO)(η^1-O-TEMPO)(^{t}BuNC). A 40 mg (0.108 mmol) amount of Ni(η^2-N,O-TEMPO)$_2$ was loaded into a sidearm Schlenk flask and dissolved in 20 mL of hexane after which 10 mg (0.125 mmol) of ^{t}BuNC was added, resulting in an immediate color change from purple to dark red. The reaction mixture was stirred at room temperature for 10 min. The volatiles were removed in *vacuo* and the residue was dissolved in 2 mL of diethyl ether, filtered into a glass vial, and placed in a -25 °C freezer in a dry box. Evaporation of solvent afforded 44 mg (90% yield) of red crystalline blocks of Ni(η^2-N,O-TEMPO)(η^1-O-TEMPO)(^{t}BuNC)**.** Spectral data for Ni(η^2-N,O-TEMPO)(η^1-O-TEMPO)(^{t}BuNC)**:** IR ν_{CN} (cm^{-1}, in hexane) 2169. ^{1}H NMR (toluene-d_8 in ppm): δ = 2.46 (s), 2.43-1.00 (broad), 1.55 (s), 1.50-1.20 (broad), 1.19 – 1.02 (broad multiplet), 0.95 (s). Note: The ^{1}H NMR spectrum at room temperature indicates some dynamical processes in solution, see text and supporting information. Mass Spec. EI/MS: *m/z* calcd for M^+= 453; found 453; calcd (M^+- ^{t}BuNC)= 370 (= Ni[η^2-N,O-TEMPO]$_2$); found 370. The isotope distribution is consistent with the presence of one nickel atom.

Synthesis of Ni(η^2-N,O-TEMPO)(2,2,6,6-Tetramethylpiperidin-1-yl)(I). A 40 mg (0.108mmol) amount of Ni(η^2-N,O-TEMPO)$_2$ was loaded into a Schlenk flask and dissolved in 20ml of hexane by cannula. Under flow of argon, 28 mg (0.110mmol) of I_2

was added resulting in an immediate color change from purple to dark green. The volatiles were removed in *vacuo* and the solids were dissolved in 2ml of diethyl ether, filtered into a glass vial, and placed in a -25 °C freezer. Slow evaporation of solvent afforded 29 mg (64 % yield) of green crystalline blocks of Ni(η^2-N,O-TEMPO)(2,2,6,6-tetramethylpiperidin-1-yl)(I). Spectral data for Ni(η^2-N,O-TEMPO)(2,2,6,6-Tetramethylpiperidin-1-yl)(I): ^{1}H NMR (C_6D_6 in ppm): δ= 3.30 (s, 6 H, 2 CH_3), 2.49 (s, 6 H, 2 CH_3), 1.05 (s, 12 H, 4 CH_3), 2.0-0.3 (m, 12 H, 6 CH_2). Elemental analysis: Calculated- C 44.84 %, H 7.52 %, N 5.81 %. Found- C 44.09 %, H 7.52 %, N 5.32 %.

Synthesis of Ni(η^2-N,O-TEMPO)(η^1-O-TEMPO-H)(η^1-CCPh). A 40 mg (0.108 mmol) amount of Ni(η^2-N,O-TEMPO)$_2$ was loaded into a sidearm Schlenk flask and dissolved in 20 mL of hexane. 12 mg (0.117 mmol) of phenylacetylene was added and the reaction mixture was stirred at room temperature for 1 hour, during which time the color changed from purple to light red. The volatiles were then removed in *vacuo* and the residue dissolved in 2 mL of diethyl ether, filtered into a glass vial, and placed in a -25 °C freezer in a dry box. Evaporation of solvent afforded 37 mg (73% yield) of red crystalline blocks of Ni(η^2-N,O-TEMPO)(η^1-O-TEMPO-H)(CCPh). Spectral data for Ni(η^2-N,O-TEMPO)(η^1-O-TEMPO-H)(CCPh)**:** FTIR (single crystal) $\nu_{(C\equiv C)}$: 2079(s) cm^{-1}, $\nu_{(N-H)}$: 3675-3100 (broad) cm^{-1}. FTIR $\nu_{(C\equiv C)}$ (cm^{-1} in hexane): 2074(s). ^{1}H NMR (C_6D_6 in ppm): δ= 7.62 (s, 1 H, N-H), 7.50 (d, 2 H, Ph), 7.10 (t, 2 H, Ph), 6.96 (t, 1 H, Ph), 3.10 (s, 6 H, 2 CH_3), 2.11 (s, 6 H, 2 CH_3), 1.76 (br, 2 H, CH_2), 1.29 (s, 8 H, 2 CH_3 and 1 CH_2), 1.08 (m, 6 H, 3 CH_2), 0.90 (s, 8 H, 2 CH_3 and 1 CH_2). Mass Spec. ES^+/MS calcd for

$[M + H]^+$= 473; found 473. The isotope distribution is consistent with the presence of one nickel atom.

Synthesis of Ni(η^2-N,O-TEMPO)(η^1-O-TEMPO-H)-(η^1-CC[C_6H_4]CCH). A 40 mg (0.108 mmol) amount of Ni(η^2-N,O-TEMPO)$_2$ was loaded into a sidearm Schlenk flask and dissolved in 20 mL of hexane. 15 mg (0.119 mmol) of 1,4-diethynylbenzene was added and the reaction mixture was stirred at room temperature for 1 h, during which time the color changed from purple to auburn red. The volatiles were then removed in *vacuo* and the residue dissolved in 2 mL of diethyl ether, filtered into a glass vial, and placed in a -25 °C freezer in a dry box. Evaporation of solvent afforded 38 mg (71 % yield) of red crystalline blocks of Ni(η^2-N,O-TEMPO)(η^1-O-TEMPO-H)(η^1-CC[C_6H_4]CCH). Spectral data for Ni(η^2-N,O-TEMPO)(η^1-O-TEMPO-H)(η^1-CC[C_6H_4]CCH)**:** FTIR $\nu_{(C\equiv C)}$ (cm^{-1} in hexane): 2071(s). ^{1}H NMR (C_6D_6 in ppm): δ= 7.65 (s, 1 H, N-H), 7.44-7.31 (d, 4 H, C_6H_4), 3.26 (s, 1 H, C≡CH), 3.08 (s, 6 H, 2 CH_3), 2.10 (s, 6 H, 2 CH_3), 1.76 (m, 2 H, CH_2), 1.28 (s, 6 H, 2 CH_3), 0.90 (s, 6 H, 2 CH_3), 1.5-0.8 (m, broad, 10 H, 5 CH_2) . Mass Spec. ES^+/MS calculated for $[M + H]^+$= 497; found 497. The isotope distribution is consistent with the presence of one nickel atom.

Synthesis of Ni(η^2-N,O-TEMPO)(η^1-O-TEMPO-H)-(η^1-CCSiMe_3). A 40 mg (0.108 mmol) amount of Ni(η^2-N,O-TEMPO)$_2$ was loaded into a sidearm Schlenk flask and dissolved in 20 mL of hexane. 12 mg (0.122 mmol) of trimethylsilyl acetylene was added and the reaction mixture was stirred at room temperature for 1 h, during which

time the color changed from purple to light red. The volatiles were then removed in *vacuo* and the residue dissolved in 2 mL of diethyl ether, filtered into a glass vial, and placed in a -25 °C freezer in a dry box. Evaporation of solvent afforded 40 mg (79 % yield) of red crystalline blocks of Ni(η^2-N,O-TEMPO)(η^1-O-TEMPO-H)(η^1-CCSiMe$_3$). Spectral data for Ni(η^2-N,O-TEMPO)(η^1-O-TEMPO-H)(η^1-CCSiMe$_3$)**:** FTIR $\nu_{(C\equiv C)}$ (cm^{-1} in hexane): 2009(s). ^{1}H NMR (C_6D_6 in ppm): δ= 7.69 (s, 1 H, N-H), 2.99 (s, 6 H, 2 CH_3), 2.09 (s, 6 H, 2 CH_3), 1.76 (m, 2 H, CH_2), 1.26 (s, 6 H, 2 CH_3), 0.91 (s, 6 H, 2 CH_3), 1.5-0.9 (m, broad, 10 H, 5 CH_2), 0.29 (s, 9 H, $SiMe_3$). Mass Spec. ES$^+$/MS calculated for $[M + H]^+$= 470 m/z; found 470 m/z. The isotope distribution is consistent with the presence of one nickel atom.

Synthesis of Ni(η^2-N,O-TEMPO)(η^1-O-TEMPO-H)-(η^1-CCH). A 40 mg (0.108 mmol) amount of Ni(η^2-N,O-TEMPO)$_2$ was loaded into a sidearm Schlenk flask and dissolved in 20 mL of hexane. Acetylene gas was purged through the reaction mixture and stirred at room temperature for 1 h, during which time the color changed from purple to light red. The volatiles were then removed in *vacuo* and the solid residue dissolved in 2 mL of diethyl ether, filtered into a glass vial, and placed in a -25 °C freezer in a dry box. Evaporation of solvent afforded 32 mg (74 % yield) of red crystalline blocks of Ni(η^2-N,O-TEMPO)(η^1-O-TEMPO-H)(η^1-CCH). Spectral data for Ni(η^2-N,O-TEMPO)(η^1-O-TEMPO-H)(η^1-CCH)**:** FTIR $\nu_{(C\equiv C)}$ (cm^{-1} in hexane): 1933(s). ^{1}H NMR (C_6D_6 in ppm): δ= 7.64 (s, 1 H, N-H), 3.10 (s, 6 H, 2 CH_3), 2.08 (s, 6 H, 2 CH_3), 2.06 (s, 1 H, CCH), 1.78 (m, 2 H, CH_2), 1.26 (s, 6 H, 2 CH_3), 0.90 (s, 6 H, 2 CH_3), 1.4-0.8 (m,

broad, 10 H, 5 CH_2). Mass Spec. ES^+/MS calculated for $[M + H]^+$= 397 m/z; found 397 m/z. The isotope distribution is consistent with the presence of one nickel atom.

Synthesis of Ni(η^2-N,O-TEMPO)(η^1-O-TEMPO)(NC_5H_5). A 40 mg (0.108 mmol) amount of Ni(η^2-N,O-TEMPO)$_2$ was loaded into a sidearm Schlenk flask and dissolved in 20 mL of hexane. Excess pyridine (0.1 mL) was added and the reaction mixture immediately changed color from purple to dark brown. The volatiles were then removed in *vacuo* and the residue dissolved in 2 mL of diethyl ether with a drop of pyridine, filtered into a glass vial, and placed in a -25 °C freezer in a dry box. Evaporation of solvent afforded 46 mg (95 % yield) of brown blocks of Ni(η^2-N,O-TEMPO)(η^1-O-TEMPO)(NC_5H_5). Spectral data for Ni(η^2-N,O-TEMPO)(η^1-O-TEMPO)(NC_5H_5)**:** ^{1}H NMR (C_6D_6 in ppm, pyridine peaks and integrations not listed due to dynamical processes): δ= 2.96 (s), 2.35 (s), 3.0-1.8 (broad), 1.54 (s), 1.35 (s). ^{1}H NMR (NC_5D_5 in ppm, pyridine peaks and integrations not listed due to dynamical processes): δ= 3.03 (s), 2.38 (s), 3.0-1.8 (broad), 1.55 (s), 1.36 (s), 1.19 (s). Mass Spec. ES^+/MS calculated for $[M]^+$= 450 m/z; found 450 m/z. The isotope distribution is consistent with the presence of one nickel atom. NOTE: placing solid Ni(η^2-N,O-TEMPO)(η^1-O-TEMPO)(NC_5H_5) under vacuum results in partial decomposition and regeneration of Ni(η^2-N,O-TEMPO)$_2$. Dissolving Ni(η^2-N,O-TEMPO)(η^1-O-TEMPO)(NC_5H_5) in hexane or benzene appears to create an equilibrium between starting Ni(η^2-N,O-TEMPO)$_2$ and product Ni(η^2-N,O-TEMPO)(η^1-O-TEMPO)(NC_5H_5).

Crystallographic Analysis

Single crystals of Ni(η^2-N,O-TEMPO)$_2$, Ni(η^2-N,O-TEMPO)(η^1-O-TEMPO)(^{t}BuNC), Ni(η^2-N,O-TEMPO)(2,2,6,6-Tetramethylpiperidin-1-yl)(I), Ni(η^2-N,O-TEMPO)(η^1-O-TEMPO-H)(CCPh), Ni(η^2-N,O-TEMPO)(η^1-O-TEMPO-H)-(η^1-CC[C_6H_4]CCH), Ni(η^2-N,O-TEMPO)(η^1-O-TEMPO-H)(η^1-CCSiMe$_3$), Ni(η^2-N,O-TEMPO)(η^1-O-TEMPO-H)(η^1-CCH), and Ni(η^2-N,O-TEMPO)(η^1-O-TEMPO)(NC_5H_5), and suitable for X-ray diffraction analysis were grown by slow evaporation of diethyl ether solutions at – 25 °C. Data crystals for Ni(η^2-N,O-TEMPO)(2,2,6,6-Tetramethylpiperidin-1-yl)(I), Ni(η^2-N,O-TEMPO)(η^1-O-TEMPO-H)-(η^1-CC[C_6H_4]CCH), Ni(η^2-N,O-TEMPO)(η^1-O-TEMPO-H)(η^1-CCSiMe$_3$), and Ni(η^2-N,O-TEMPO)(η^1-O-TEMPO-H)(η^1-CCH) were glued to the end of a thin glass fiber for data collection under ambient conditions. Data crystals for Ni(η^2-N,O-TEMPO)$_2$, Ni(η^2-N,O-TEMPO)(η^1-O-TEMPO)(^{t}BuNC), Ni(η^2-N,O-TEMPO)(η^1-O-TEMPO-H)(CCPh), and Ni(η^2-N,O-TEMPO)(η^1-O-TEMPO)(NC_5H_5) were mounted onto the end of a thin glass fiber using Paratone-N for data collection at 100 K under flow of N_2.

X-ray intensity data were measured by using a Bruker SMART APEX2 CCD-based diffractometer using Mo Kα radiation (λ = 0.71073 Å).[92] The raw data frames were integrated with the SAINT+ program by using a narrow-frame integration algorithm.[93] Corrections for Lorentz and polarization effects were also applied with SAINT+. An empirical absorption correction based on the multiple measurement of equivalent reflections was applied using the program SADABS. All structures were solved by a combination of direct methods and difference Fourier syntheses, and refined by full-matrix least-squares on F^2, by using the SHELXTL software package.[93] All non-

hydrogen atoms were refined with anisotropic displacement parameters. Hydrogen atoms were located from the difference map and refined with isotropic thermal parameters. Crystal data, data collection parameters, and results of the analyses are listed in Appendix C Tables C.1-C.4.

The compound Ni(η^2-N,O-TEMPO)$_2$ crystallized in the monoclinic crystal system. The systematic absences in the intensity data were consistent with the unique space group $P2_1/n$. With $Z = 2$ the molecule is crystallographically centrosymmetrical and thus contains only one-half of the formula equivalent of the molecule in the asymmetric crystal unit.

The compound Ni(η^2-N,O-TEMPO)(η^1-O-TEMPO)(^{t}BuNC) crystallized in the monoclinic crystal system. The systematic absences in the intensity data were consistent with the unique space group $P2_1/n$.

The compound Ni(η^2-N,O-TEMPO)(2,2,6,6-Tetramethylpiperidin-1-yl)(I) crystallized in the monoclinic crystal system. The systematic absences in the intensity data were consistent with the unique space group $P2_1/n$.

The compound Ni(η^2-N,O-TEMPO)(η^1-O-TEMPO-H)(η^1-CCSiMe$_3$) crystallized in the monoclinic crystal system. The systematic absences in the intensity data were consistent with the unique space group $P2_1/c$.

The compound Ni(η^2-N,O-TEMPO)(η^1-O-TEMPO-H)(η^1-CCH) crystallized in the monoclinic crystal system. The systematic absences in the intensity data were consistent with the unique space group $P2_1/c$.

The compound Ni(η^2-N,O-TEMPO)(η^1-O-TEMPO-H)(CCPh) crystallized in the triclinic crystal system. The space group $P\ \bar{1}$ was assumed and confirmed by the successful solution and refinement of the structure.

The compound Ni(η^2-N,O-TEMPO)(η^1-O-TEMPO-H)(η^1-CC[C_6H_4]CCH) crystallized in the triclinic crystal system. The space group $P\ \bar{1}$ was assumed and confirmed by the successful solution and refinement of the structure.

The compound Ni(η^2-N,O-TEMPO)(η^1-O-TEMPO)(NC_5H_5) crystallized in the orthorhombic crystal system. The systematic absences in the intensity data were consistent with the unique space group *Pbca*.

Compounds Ni(η^2-N,O-TEMPO)$_2$, Ni(η^2-N,O-TEMPO)(η^1-O-TEMPO)(^{t}BuNC), Ni(η^2-N,O-TEMPO)(η^1-O-TEMPO-H)(CCPh), and Ni(η^2-N,O-TEMPO)(η^1-O-TEMPO)(NC_5H_5) decompose rapidly in air and thus their X-ray data collections were performed at 100 K under flow of N_2.

Appendix A: Supporting Information for Chapter 2.

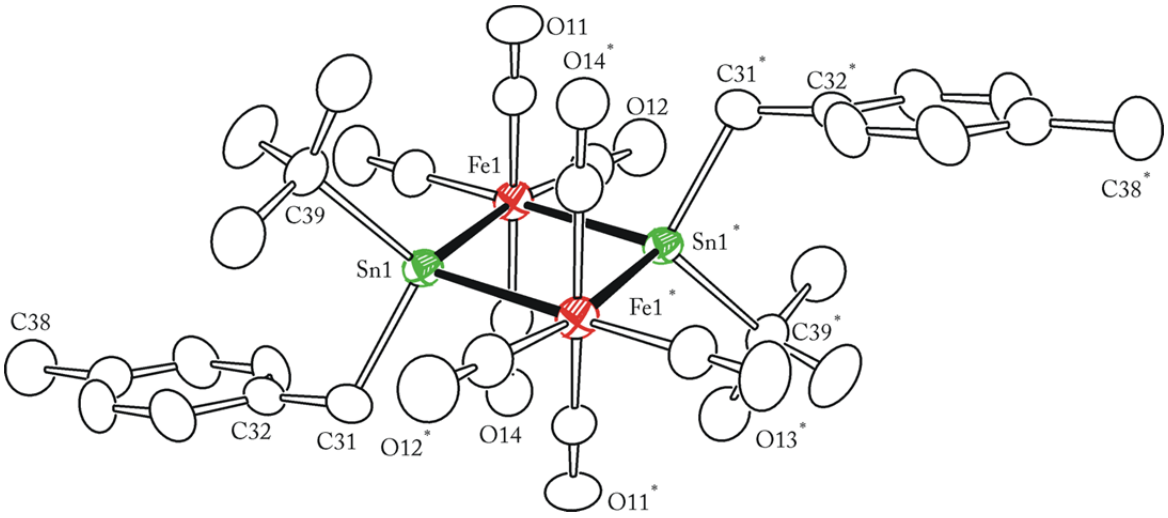

Figure A.1 An ORTEP showing the molecular structure of $Fe_2[\mu\text{-}Sn^tBu(p\text{-}CH_2PhMe)]_2(CO)_8$ at 30 % thermal ellipsoid probability.

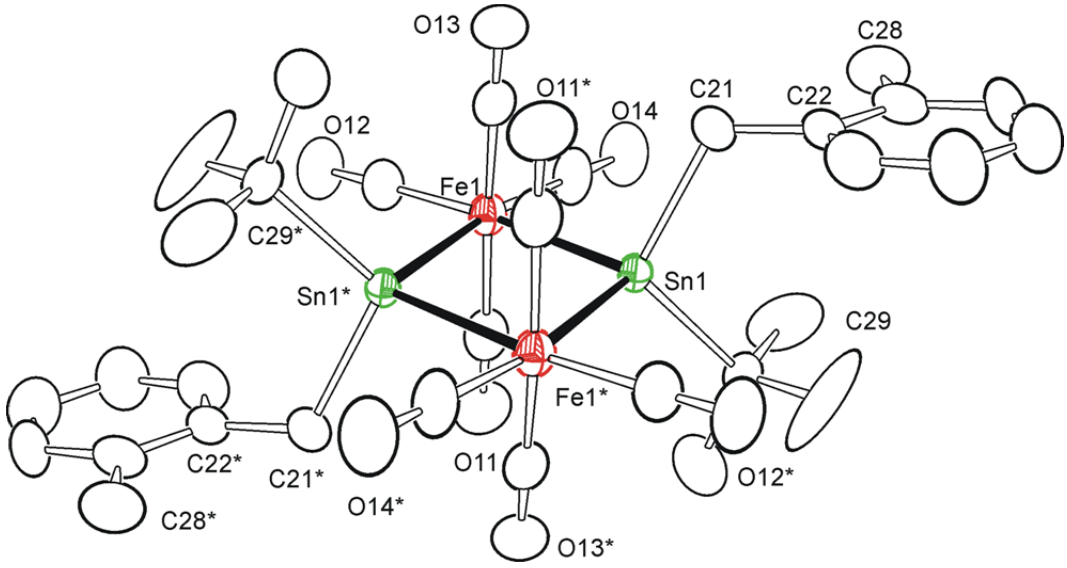

Figure A.2 An ORTEP showing the molecular structure of $Fe_2[\mu\text{-}Sn^tBu(o\text{-}CH_2PhMe)]_2(CO)_8$ at 30 % thermal ellipsoid probability.

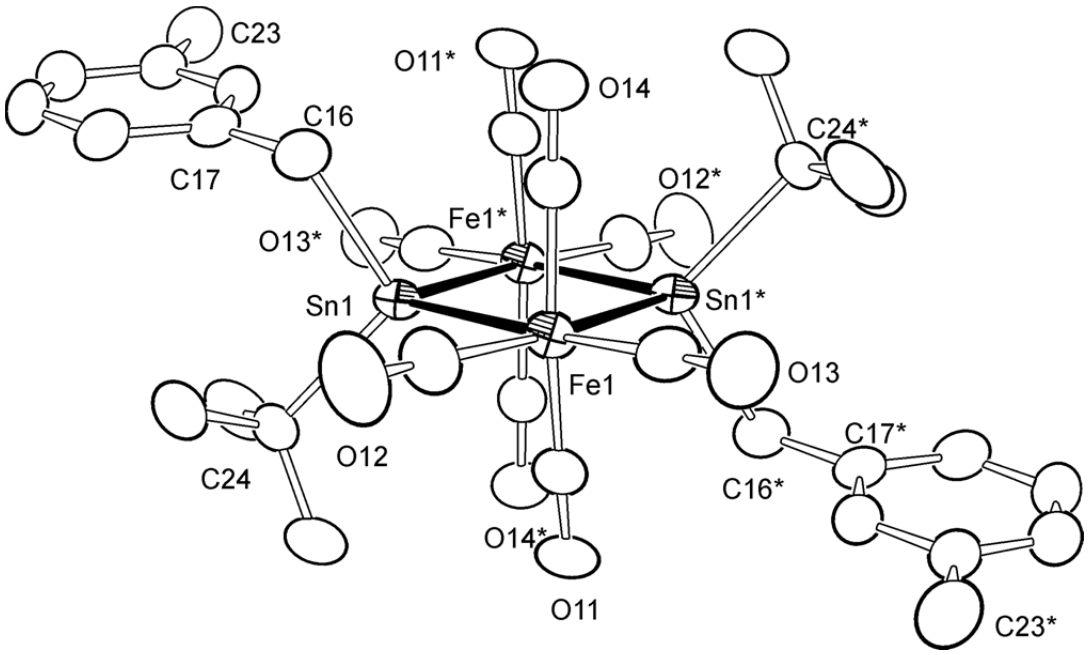

Figure A.3 An ORTEP showing the molecular structure of $Fe_2[\mu\text{-}Sn^tBu(m\text{-}CH_2PhMe)]_2(CO)_8$ at 30 % thermal ellipsoid probability.

Table A.1 Crystallographic Data for Compounds $Ni(Sn^tBu_3)_2(CO)_3$ and $Co(Sn^tBu_3)(CO)_4$.

Compound	Ni(SntBu3)2(CO)3	Co(SntBu3)(CO)4
Empirical formula	$NiSn_2O_3C_{27}H_{54}$	$CoSnO_4C_{16}H_{27}$
Formula weight	722.79	461
Crystal system	Monoclinic	Monoclinic
Lattice parameters		
a (Å)	9.0869(4)	8.3019(3)
b (Å)	14.8041(7)	27.7529(10)
c (Å)	25.2267(12)	9.2626(3)
β (°)	93.8980(10)	113.3356(5)
V (Å^3)	3385.7(3)	1959.55(12)
Space group	$P2_1/c$ (#14)	$P2_1/n$ (#14)
Z value	4	4
ρ_{calc} (g / cm^3)	1.418	1.563
μ (Mo Kα) (mm^{-1})	2.036	2.133
Temperature (K)	296	100
$2\Theta_{max}$ (°)	54.14	60.98
No. Obs. ($I > 2\sigma(I)$)	6170	5434
No. Parameters	316	208
Goodness of fit	1.021	1.055
Max. shift in cycle	0.002	0.002
Residuals*:R1; wR2	0.0232; 0.0518	0.0193;0.0459
Absorption Correction, Max/min	Multi-scan 0.7365/0.4965	Multi-scan 0.9195/0.5670
Largest peak in Final Diff. Map (e$^-$ / Å^3)	0.389	0.685

*$R = \Sigma_{hkl}(\,|\,|F_{obs}| - |F_{calc}|\,|)/\Sigma_{hkl}|F_{obs}|$; $R_w = [\Sigma_{hkl}w(|F_{obs}| - |F_{calc}|)^2/\Sigma_{hkl}wF_{obs}^2]^{1/2}$, $w = 1/\sigma^2(F_{obs})$; $GOF = [\Sigma_{hkl}w(|F_{obs}| - |F_{calc}|)^2/(n_{data} - n_{vari})]^{1/2}$.

Table A.2 Crystallographic Data for Compounds $Fe_2(\mu\text{-}Sn^tBu_2)_2(CO)_8$ and $Fe_2[\mu\text{-}Sn^tBu(CH_2Ph)]_2(CO)_8$.

Compound	$Fe_2(\mu\text{-}Sn^tBu_2)_2(CO)_8$	$Fe_2[\mu\text{-}Sn^tBu(CH_2Ph)]_2(CO)_8$
Empirical formula	$Fe_2Sn_2O_8C_{24}H_{36}$	$Fe_2Sn_2O_8C_{30}H_{32}$
Formula weight	801.61	869.64
Crystal system	Triclinic	Triclinic
Lattice parameters		
a (Å)	11.7046(6)	9.0660(7)
b (Å)	17.3507(9)	12.7084(9)
c (Å)	17.5946(9)	14.9109(9)
α (deg)	113.439(1)	89.464(1)
β (deg)	100.839(1)	86.641(1)
γ (deg)	101.634(1)	77.270(1)
V ($Å^3$)	3064.6(3)	1672.8(2)
Space group	$P\ \bar{1}$ (# 2)	$P\ \bar{1}$ (# 2)
Z value	4	2
ρ_{calc} (g / cm^3)	1.737	1.726
μ (Mo Kα) (mm^{-1})	2.579	2.370
Temperature (K)	296	296
$2\Theta_{max}$ (°)	56.0	52.0
No. Obs. ($I > 2\sigma(I)$)	11237	4237
No. Parameters	673	385
Goodness of fit	1.081	1.001
Max. shift in cycle	0.001	0.001
Residuals*:R1; wR2	0.0446, 0.0618	0.0409; 0.0749
Absorption Correction, Max/min	Multi-scan 0.7459/0.5945	Multi-scan 0.9767/0.7641
Largest peak in Final Diff. Map (e^- / $Å^3$)	2.086	0.839

*$R = \Sigma_{hkl}(\ |\ |F_{obs}| - |F_{calc}|\ |\ )/\Sigma_{hkl}|F_{obs}|$; $R_w = [\Sigma_{hkl}w(|F_{obs}| - |F_{calc}|)^2/\Sigma_{hkl}wF_{obs}^2]^{1/2}$, $w = 1/\sigma^2(F_{obs})$; $GOF = [\Sigma_{hkl}w(|F_{obs}| - |F_{calc}|)^2/(n_{data} - n_{vari})]^{1/2}$.

Table A.3 Crystallographic Data for Compounds $Fe_4(\mu_4\text{-}Sn)(\mu\text{-}Sn^tBu_2)_2(CO)_{16}$ and $Fe_2[\mu\text{-}Sn(m\text{-}CH_2PhMe)_2]_2(CO)_8$.

Compound	$Fe_4(\mu_4\text{-}Sn)(\mu\text{-}Sn^tBu_2)_2(CO)_{16}$	$Fe_2[\mu\text{-}Sn(m\text{-}CH_2PhMe)_2]_2(CO)_8$
Empirical formula	$Fe_4Sn_3O_{16}C_{32}H_{36}$	$Fe_2Sn_2O_8C_{40}H_{36}$
Formula weight	1256.08	993.77
Crystal system	Triclinic	Triclinic
Lattice parameters		
a (Å)	8.8258(12)	9.8250(5)
b (Å)	14.868(2)	10.9039(5)
c (Å)	17.417(2)	11.3067(6)
α (deg)	105.102(2)	81.535(1)
β (deg)	90.980(2)	67.180(1)
γ (deg)	101.626(2)	63.534(1)
V ($Å^3$)	2155.4(5)	998.99(9)
Space group	$P\ \bar{1}$ (# 2)	$P\ \bar{1}$ (# 2)
Z value	2	1
ρ_{calc} (g / cm^3)	1.935	1.652
μ (Mo Kα) (mm^{-1})	3.081	1.996
Temperature (K)	296(2)	296
$2\Theta_{max}$ (°)	63.0	59.0
No. Obs. ($I > 2\sigma(I)$)	6054	4651
No. Parameters	508	237
Goodness of fit	0.838	1.018
Max. shift in cycle	0.002	0.003
Residuals*:R1; wR2	0.0445; 0.0894	0.0276; 0.0597
Absorption Correction, Max/min	Multi-scan 0.9133/0.3080	Multi-scan 0.9612/0.7539
Largest peak in Final Diff. Map ($e^- / Å^3$)	0.954	0.678

*$R = \Sigma_{hkl}(\ |\ |F_{obs}| - |F_{calc}|\ |\ )/\Sigma_{hkl}|F_{obs}|$; $R_w = [\Sigma_{hkl}w(|F_{obs}| - |F_{calc}|)^2/\Sigma_{hkl}wF_{obs}^2]^{1/2}$, $w = 1/\sigma^2(F_{obs})$; $GOF = [\Sigma_{hkl}w(|F_{obs}| - |F_{calc}|)^2/(n_{data} - n_{vari})]^{1/2}$.

Table A.4 Crystallographic Data for Compounds $Pt_2Ru_2(Sn^tBu_3)_2(CO)_9(\mu\text{-}H)_2$ and $Pt(Sn^tBu_3)_2(CO)_2$.

Compound	Pt2Ru2(SntBu3)2(CO)9(μ-H)2	Pt(SntBu3)2(CO)2
Empirical formula	$Pt_2Ru_2Sn_2O_9C_{33}H_{56}$	$PtSn_2C_{26}H_{54}O_2$
Formula weight	1426.48	831.16
Crystal system	Triclinic	Monoclinic
Lattice parameters		
a (Å)	9.6022(4)	15.3248(2)
b (Å)	12.0461(5)	9.19810(10)
c (Å)	21.2192(8)	24.1611(3)
α (deg)	89.733(1)	90.00
β (deg)	80.605(1)	98.2477(6)
γ (deg)	73.446(1)	90.00
V (Å^3)	2318.84(16)	3370.50(7)
Space group	$P\ \bar{1}$ (# 2)	*C*2/*c* (# 15)
Z value	2	4
ρ_{calc} (g / cm^3)	2.043	1.638
μ (Mo Kα) (mm^{-1})	7.746	5.627
Temperature (K)	296	296(2)
$2\Theta_{max}$ (°)	61.02	60.00
No. Obs. (I > 2σ(I))	11134	152
No. Parameters	459	4301
Goodness of fit	1.046	1.199
Max. shift in cycle	0.002	0.001
Residuals*:R1; wR2	0.0269, 0.0637	0.0455; 0.1165
Absorption Correction, Max/min	Multi-Scan 1.0000/0.582	Multi-Scan 0.7468/0.4928
Largest peak in Final Diff. Map (e$^-$ / Å^3)	1.451	1.064

*$R = \Sigma_{hkl}(\,|\,|F_{obs}|-|F_{calc}|\,|)/\Sigma_{hkl}|F_{obs}|$; $R_w = [\Sigma_{hkl}w(|F_{obs}|-|F_{calc}|)^2/\Sigma_{hkl}wF_{obs}^2]^{1/2}$, $w = 1/\sigma^2(F_{obs})$; $GOF = [\Sigma_{hkl}w(|F_{obs}|-|F_{calc}|)^2/(n_{data} - n_{vari})]^{1/2}$.

Appendix B: Supporting Information for Chapter 3.

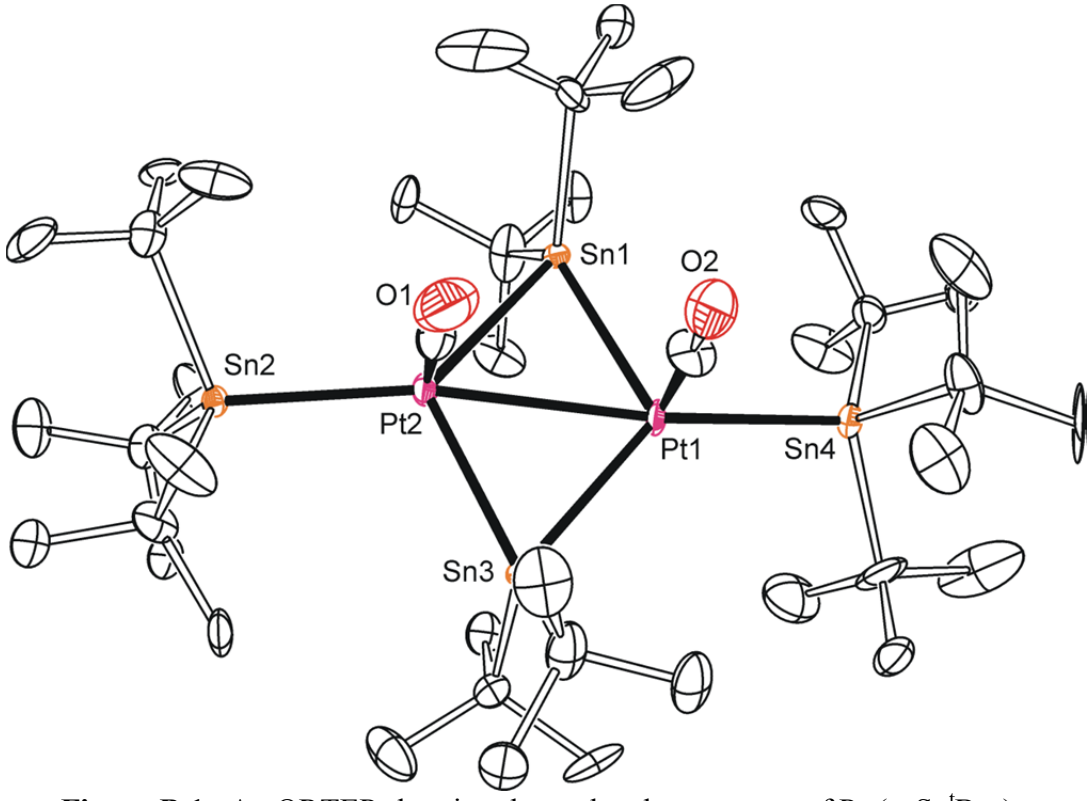

Figure B.1 An ORTEP showing the molecular structure of $Pt_2(\mu\text{-}Sn^tBu_2)_2\text{-}(Sn^tBu_3)_2(CO)_2$ at 30 % thermal ellipsoid probability.

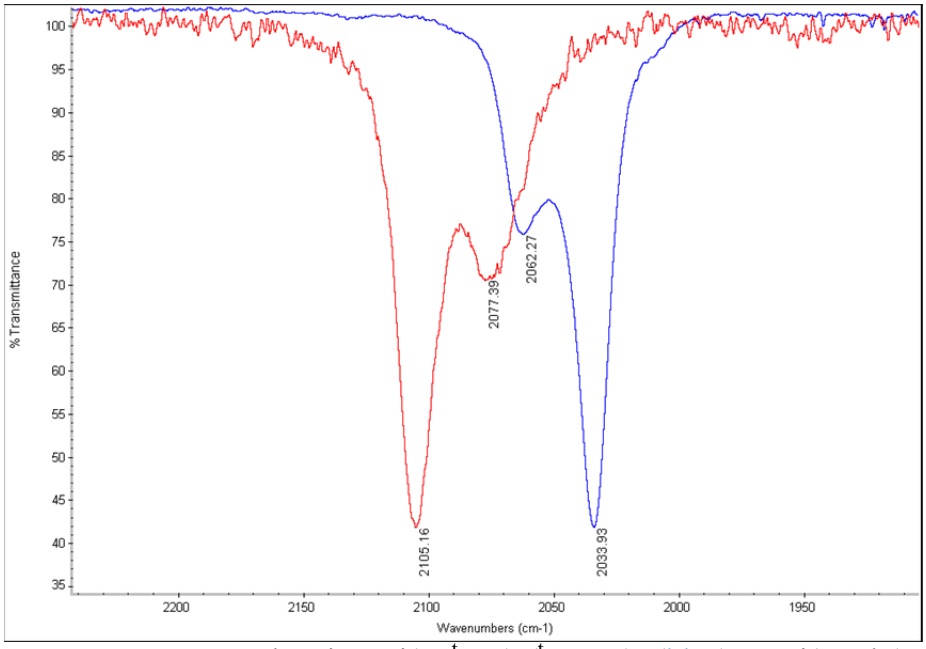

Figure B.2 FTIR spectrum showing $Ni(Sn^tBu_3)_2(^tBuNC)_3$ (blue) vs $Ni(SnPh_3)_2(^tBuNC)_3$ (red) in hexane solvent.

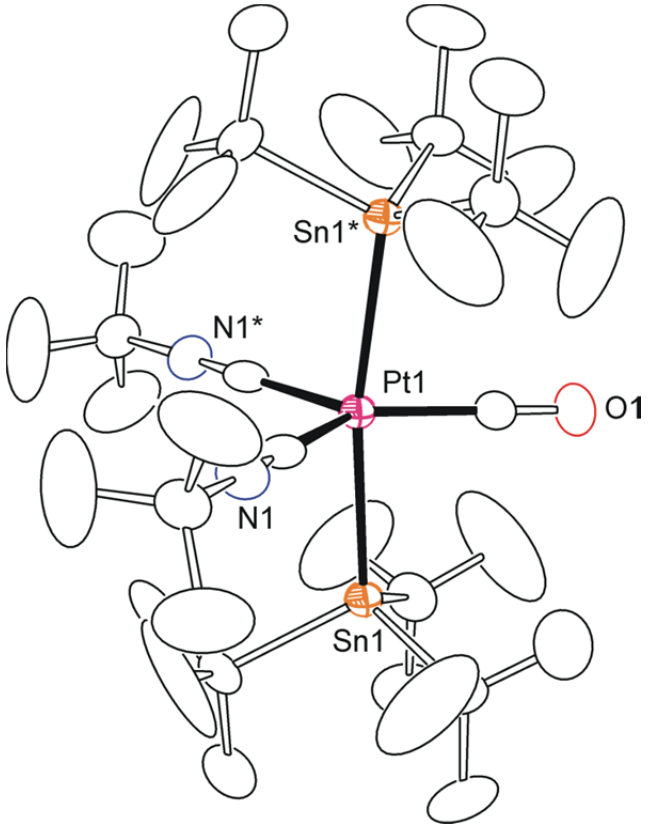

Figure B.3 An ORTEP showing the molecular structure of $Pt(Sn^tBu_3)_2(^tBuNC)_2(CO)$ at 30 % thermal ellipsoid probability.

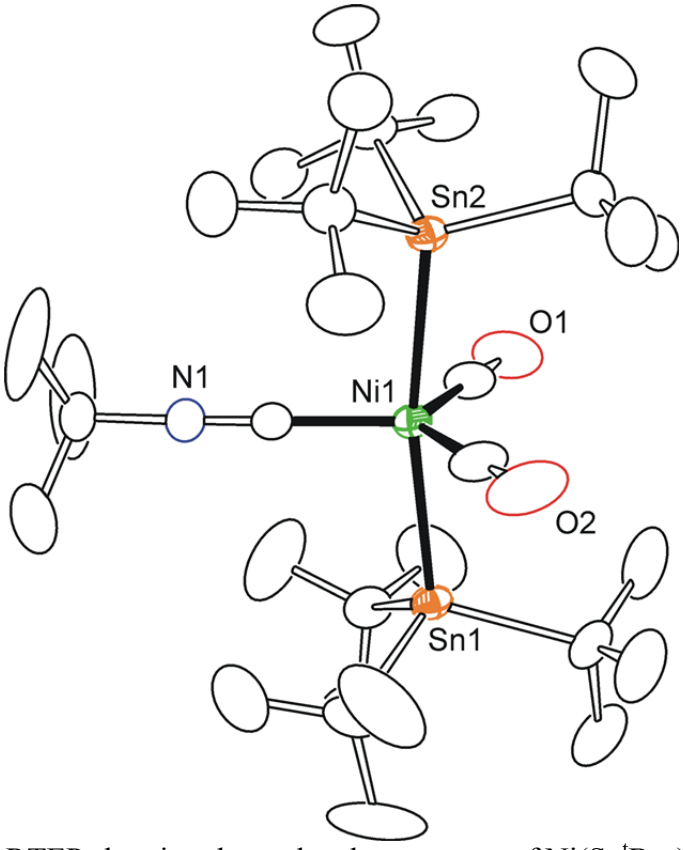

Figure B.4 An ORTEP showing the molecular structure of $Ni(Sn^tBu_3)_2(^tBuNC)(CO)_2$ at 30 % thermal ellipsoid probability.

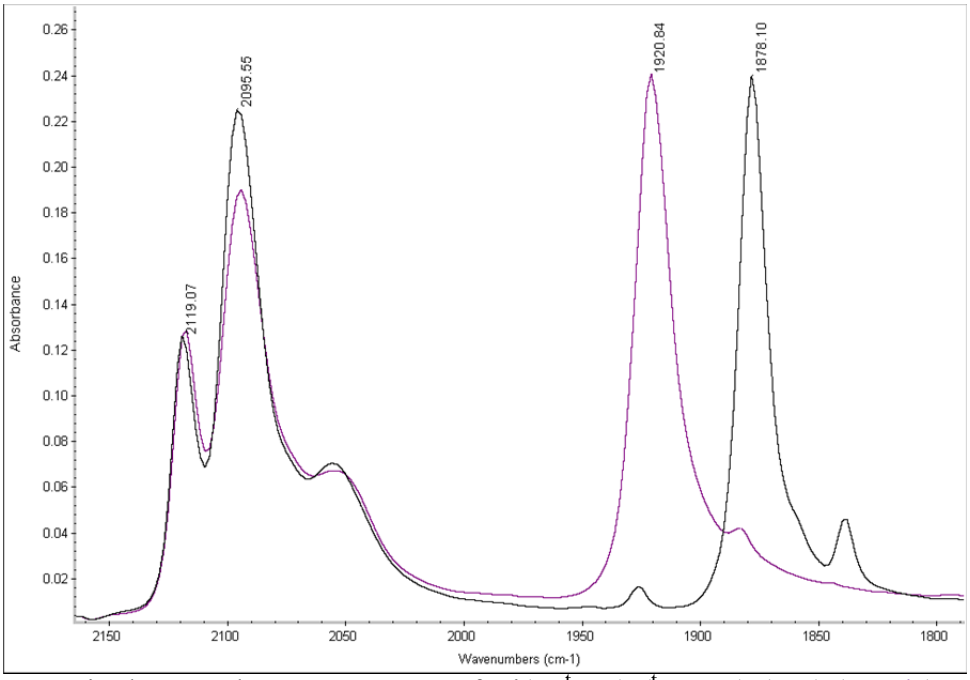

Figure B.5 Single crystal FTIR spectrum of $Ni(Sn^tBu_3)_2(^tBuNC)_2(CO)$ (purple) vs ^{13}CO- $Ni(Sn^tBu_3)_2(^tBuNC)_2(CO)$ (black).

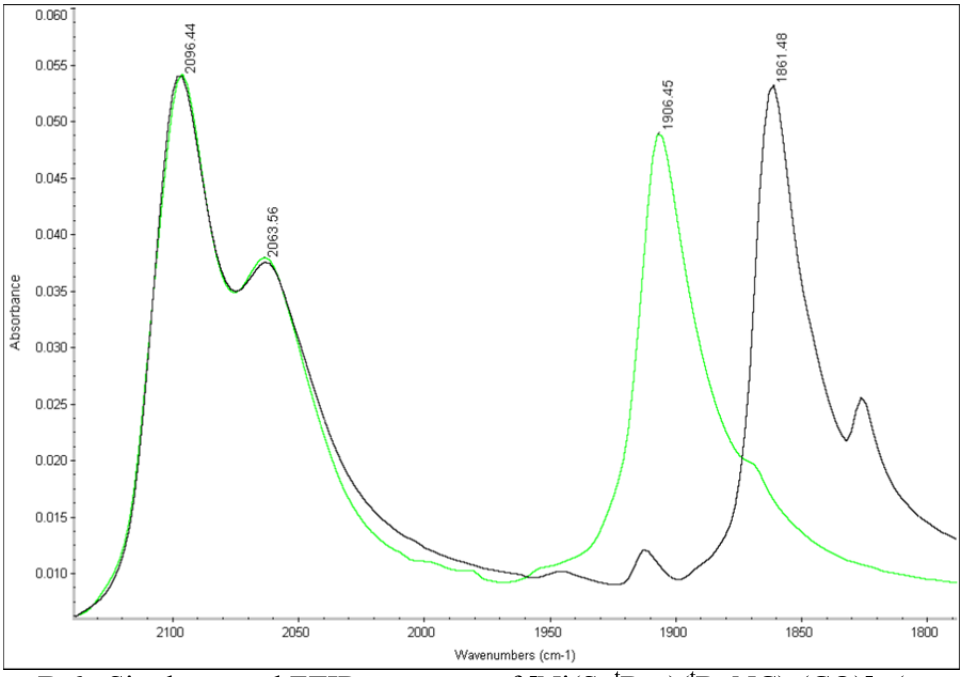

Figure B.6 Single crystal FTIR spectrum of $[Ni(Sn^tBu_3)(^tBuNC)_2(CO)]_2$ (green) vs ^{13}CO-$[Ni(Sn^tBu_3)(^tBuNC)_2(CO)]_2$ (black).

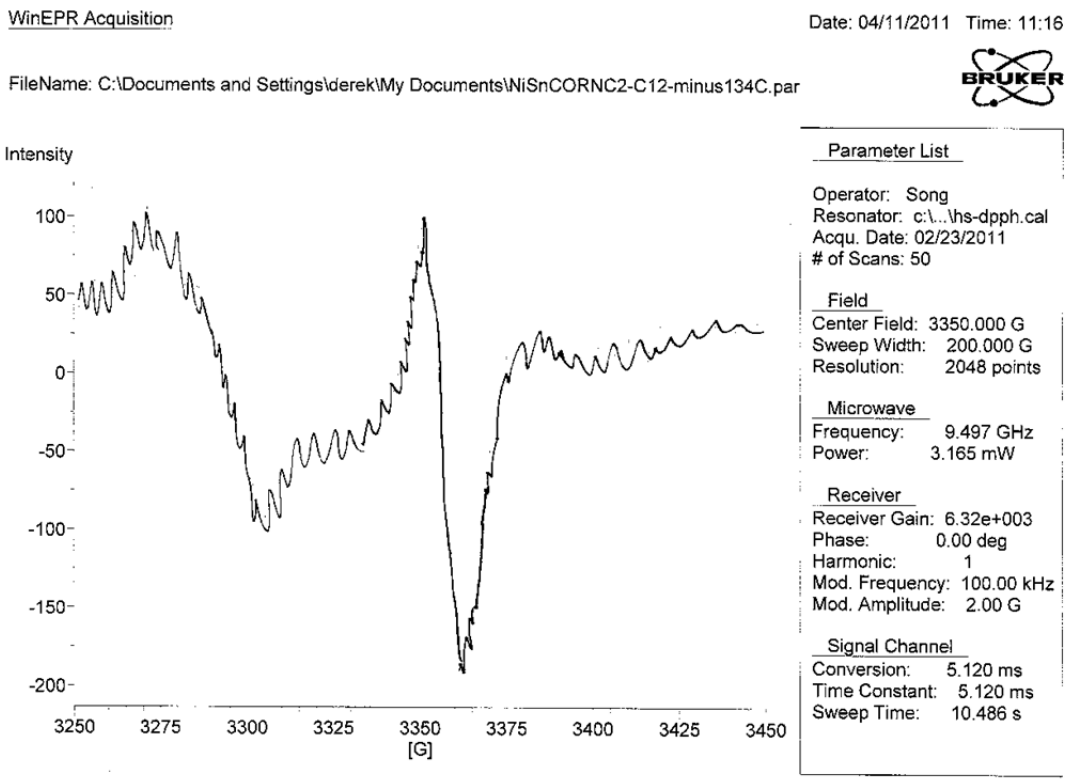

Figure B.7 ESR spectrum of ^{12}CO-$[Ni(Sn^tBu_3)(^tBuNC)_2(CO)]_2$ in toluene at 134 K.

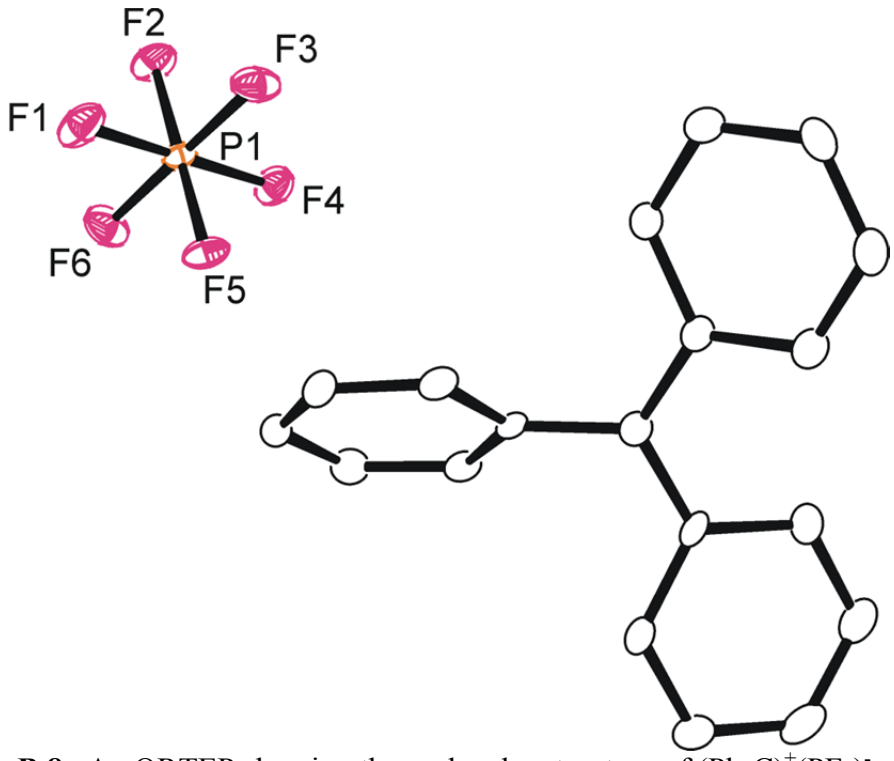

Figure B.8 An ORTEP showing the molecular structure of $(Ph_3C)^+(PF_6)^-$ at 30 % thermal ellipsoid probability.

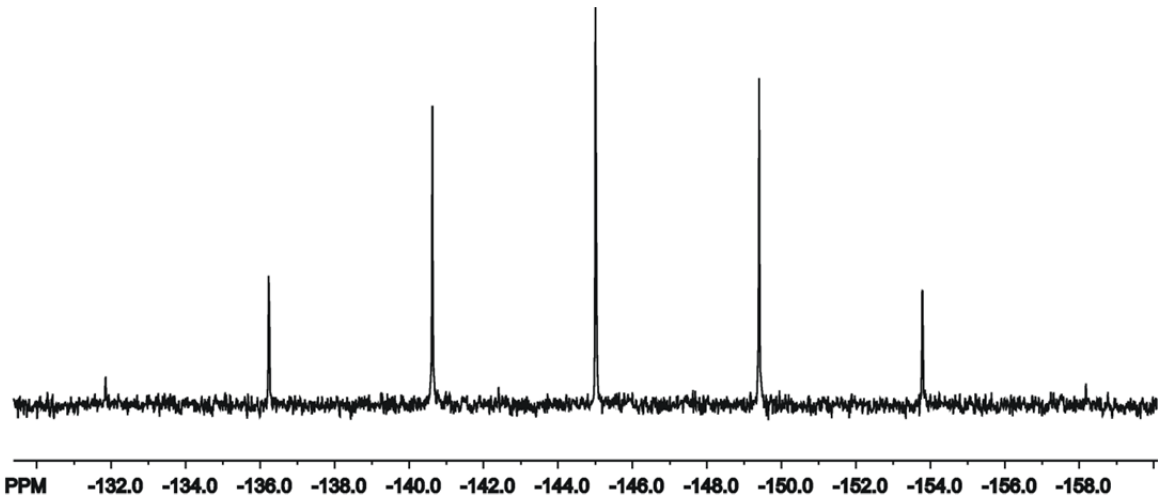

Figure B.9 ^{31}P NMR of $(Ph_3C)^+(PF_6)^-$.

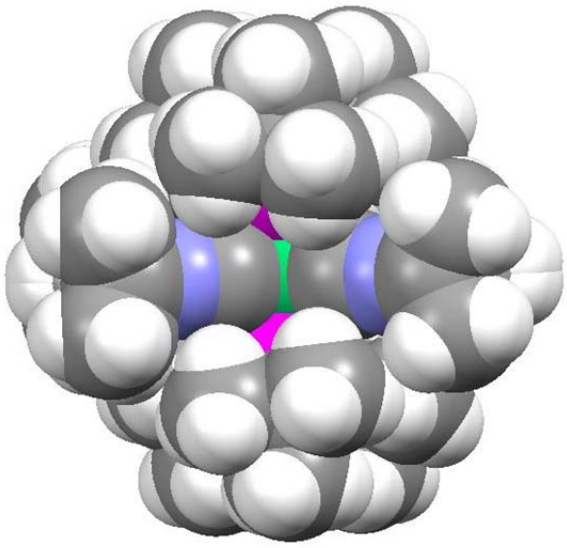

Figure B.10 A spacefilling model of $Ni(Sn^tBu_3)_2(^tBuNC)_3$. Atomic dimensions are the atomic van der Waals radii. The Ni atom is shown in green, Sn in pink, N in blue, C in gray, and H in white.

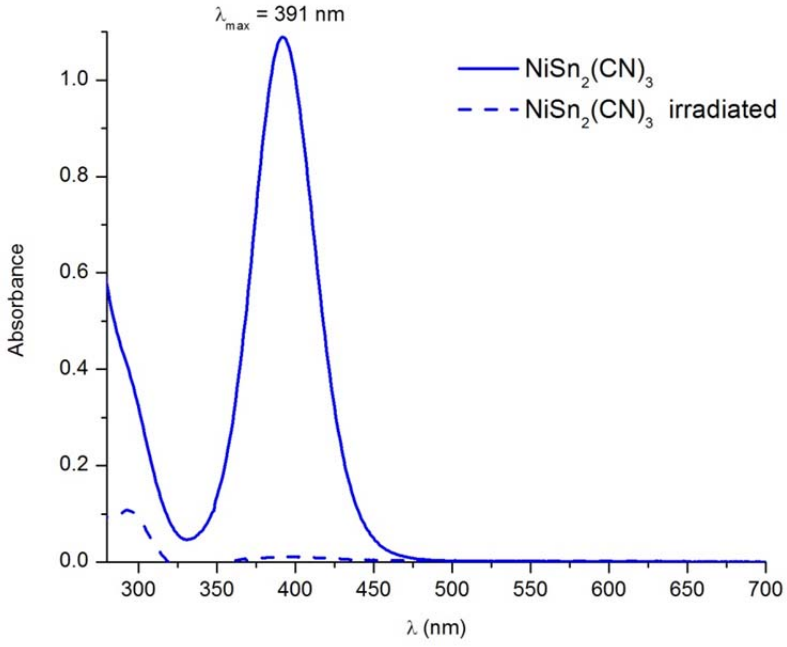

Figure B.11 UV-Vis spectra showing $Ni(Sn^tBu_3)_2(^tBuNC)_3$ (solid line) and subsequent room temperature photolysis to $Ni(^tBuNC)_4$ (dashed line).

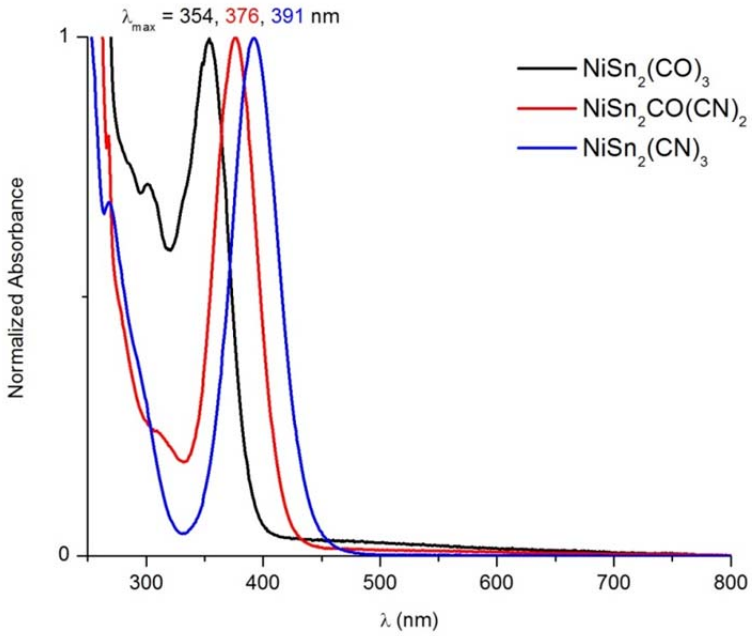

Figure B.12 UV-Vis spectra showing $Ni(Sn^tBu_3)_2(^tBuNC)_3$ (blue), $Ni(Sn^tBu_3)_2(^tBuNC)_2(CO)$ (red), and $Ni(Sn^tBu_3)_2(CO)_3$ (black).

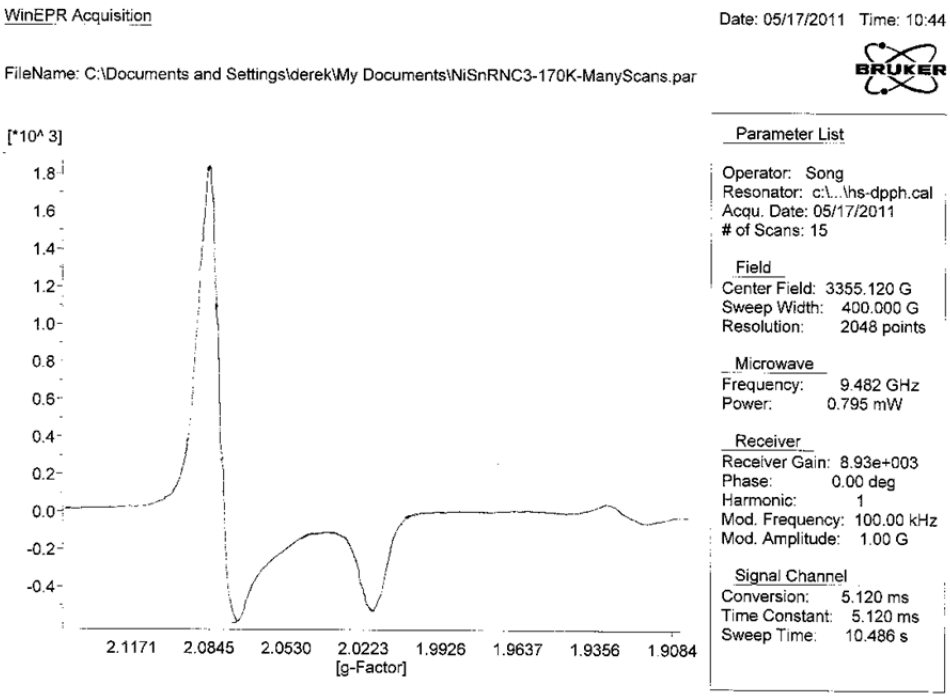

Figure B.13 ESR spectrum of proposed $Ni(Sn^tBu_3)(^tBuNC)_3$ in toluene at 170 K

Table B.1 Crystallographic Data for Compounds $Ni(Sn^tBu_3)_2(^tBuNC)_3$, $Ni(Sn^tBu_3)_2(^tBuNC)_2(CO)$, and $Ni(Sn^tBu_3)_2(^tBuNC)(CO)_2$.

Compound	$Ni(Sn^tBu_3)_2(^tBuNC)_3 \cdot C_6H_6$	$Ni(Sn^tBu_3)_2(^tBuNC)_2(CO) \cdot Et_2O$	$Ni(Sn^tBu_3)_2(^tBuNC)(CO)_2$
Empirical formula	$NiSn_2N_3C_{45}H_{87}$	$NiSn_2N_2O_2C_{39}H_{82}$	$NiSn_2NO_2C_{31}H_{63}$
Formula weight	966.27	907.19	777.91
Crystal system	Orthorhombic	Orthorhombic	Monoclinic
Lattice parameters			
a (Å)	13.6127(5)	13.3434(6)	9.1651(4)
b (Å)	19.6978(8)	19.3749(9)	23.2951(10)
c (Å)	39.0026(15)	9.2939(4)	18.5204(8)
α (deg)	90.00	90.00	90.00
β (deg)	90.00	90.00	99.8580(7)
γ (deg)	90.00	90.00	90.00
V ($Å^3$)	10458.1(7)	2402.72(19)	3895.8(3)
Space group	*Cmca* (# 64)	*Pmmn* (# 59)	$P2_1/n$ (# 14)
Z value	8	4	4
ρ_{calc} (g / cm^3)	1.227	2.344	1.326
μ (Mo Kα) (mm^{-1})	1.333	2.470	1.773
Temperature (K)	296	296	296
$2\Theta_{max}$ (°)	56.00	56.00	56.00
No. Obs. ($I > 2\sigma(I)$)	4627	2706	6776
No. Parameters	254	133	355
Goodness of fit	1.098	1.006	1.001
Max. shift in cycle	0.001	0.045	0.175
Residuals*:R1; wR2	0.0529; 0.1344	0.0303; 0.0759	0.0384; 0.0838
Absorption Correction, Max/min	Multi-scan 0.7465; 0.5501	Multi-scan 0.7465, 0.5695	Multi-scan 0.7465, 0.5877
Largest peak in Final Diff. Map ($e^- / Å^3$)	2.098	0.569	0.752

*$R = \Sigma_{hkl}(\,|\,|F_{obs}| - |F_{calc}|\,|)/\Sigma_{hkl}|F_{obs}|$; $R_w = [\Sigma_{hkl}w(|F_{obs}| - |F_{calc}|)^2/\Sigma_{hkl}wF_{obs}^2]^{1/2}$, $w = 1/\sigma^2(F_{obs})$; $GOF = [\Sigma_{hkl}w(|F_{obs}| - |F_{calc}|)^2/(n_{data} - n_{vari})]^{1/2}$.

Table B.2 Crystallographic Data for Compounds $[Ni(Sn^tBu_3)(^tBuNC)_2(CO)]_2$, $[Sn(O)(^tBu)_2(CO_3Sn^tBu_3)]_2$, and $Ni(^tBuNC)_4$.

Compound	$[Ni(Sn^tBu_3)(^tBuNC)_2$-$(CO)]_2$	$[Sn(O)(^tBu)_2(CO_3Sn^tBu_3)]_2$ ·CH_2Cl_2	$Ni(^tBuNC)_4$
Empirical formula	$Ni_2Sn_2N_4O_2C_{46}H_{90}$	$Sn_4Cl_4O_8C_{44}H_{94}$	$NiN_4C_{20}H_{36}$
Formula weight	1086.02	1367.75	391.24
Crystal system	Monoclinic	Monoclinic	Cubic
Lattice parameters			
a (Å)	10.2875(5)	36.056(2)	26.04910(10)
b (Å)	15.7767(7)	9.4611(6)	26.04910(10)
c (Å)	17.8035(8)	21.8430(13)	26.04910(10)
α (deg)	90.00	90.00	90.00
β (deg)	94.1568(8)	120.9200(9)	90.00
γ (deg)	90.00	90.00	90.00
V ($Å^3$)	2882.0(2)	6392.3(7)	17675.8(9)
Space group	$P2_1/n$ (# 14)	$C2/c$ (# 15)	F-43c (# 219)
Z value	2	4	24
ρ_{calc} (g / cm^3)	1.251	1.421	0.882
μ (Mo Kα) (mm^{-1})	1.533	1.751	0.665
Temperature (K)	296	296	296
$2\Theta_{max}$ (°)	56.00	56.00	54.00
No. Obs. (I > 2σ(I))	4826	4983	1191
No. Parameters	268	286	61
Goodness of fit	1.012	1.007	1.215
Max. shift in cycle	0.059	0.001	0.906
Residuals*:R1; wR2	0.0317; 0.0782	0.0429; 0.0859	0.0552; 0.1467
Absorption Correction, Max/min	Multi-scan 0.7465, 0.6127	Multi-scan 0.7465, 0.5224	Multi-scan 0.7464; 0.5279
Largest peak in Final Diff. Map (e^- / $Å^3$)	0.438	0.727	1.162

*$R = \Sigma_{hkl}(||F_{obs}| - |F_{calc}||)/\Sigma_{hkl}|F_{obs}|$; $R_w = [\Sigma_{hkl}w(|F_{obs}| - |F_{calc}|)^2/\Sigma_{hkl}wF_{obs}^2]^{1/2}$, $w = 1/\sigma^2(F_{obs})$; $GOF = [\Sigma_{hkl}w(|F_{obs}| - |F_{calc}|)^2/(n_{data} - n_{vari})]^{1/2}$.

Table B.3 Crystallographic Data for Compounds Ni(η^2-N,O-TEMPO)(Sn^{t}Bu$_3$)(^{t}BuNC), [Sn(O)(^{t}Bu)$_2$(CO$_3$Sn^{t}Bu$_3$)]$_2$, and $(Ph_3C)^+(PF_6)^-$.

Compound	Ni(η^2-N,O-TEMPO)-(Sn^{t}Bu$_3$)(^{t}BuNC)	[(^{t}Bu$_3$Sn)(PF$_4$)]$_\infty$	$(Ph_3C)^+(PF_6)^-$
Empirical formula	$NiSnON_2C_{26}H_{54}$	$SnPF_4C_{12}H_{27}$	$PF_6C_{19}H_{15}$
Formula weight	588.11	397.00	388.28
Crystal system	Monoclinic	Orthorhombic	Monoclinic
Lattice parameters			
a (Å)	17.2516(7)	13.1792(6)	9.8236(5)
b (Å)	11.3442(4)	14.2988(6)	8.6626(5)
c (Å)	17.5158(7)	8.8652(4)	19.2827(11)
α (deg)	90.00	90.00	90.00
β (deg)	109.8390(6)	90.00	90.6450(9)
γ (deg)	90.00	90.00	90.00
V (Å^3)	3224.5(2)	1670.62(13)	1640.81(16)
Space group	$P2_1/c$ (# 14)	*Pnma* (# 62)	$P2_1/n$ (# 14)
Z value	4	4	2
ρ_{calc} (g / cm^3)	1.211	1.578	1.572
μ (Mo Kα) (mm^{-1})	1.375	1.647	0.231
Temperature (K)	296	100	100
$2\Theta_{max}$ (°)	56.00	56.00	56.00
No. Obs. (I > 2σ(I))	6236	1977	3283
No. Parameters	296	95	235
Goodness of fit	1.015	1.232	1.074
Max. shift in cycle	0.004	0.001	0.026
Residuals*:R1; wR2	0.0292; 0.0750	0.0420; 0.0958	0.0501; 0.1610
Absorption Correction, Max/min	Multi-scan 0.7457; 0.5671	Multi-scan 0.7459, 0.5816	Multi-scan 0.7465, 0.6489
Largest peak in Final Diff. Map (e$^-$ / Å^3)	0.857	1.067	0.411

*$R = \Sigma_{hkl}(||F_{obs}| - |F_{calc}||)/\Sigma_{hkl}|F_{obs}|$; $R_w = [\Sigma_{hkl}w(|F_{obs}| - |F_{calc}|)^2/\Sigma_{hkl}wF_{obs}^2]^{1/2}$, $w = 1/\sigma^2(F_{obs})$; $GOF = [\Sigma_{hkl}w(|F_{obs}| - |F_{calc}|)^2/(n_{data} - n_{vari})]^{1/2}$.

Table B.4 Crystallographic Data for Compounds $Ni(I)_2(^tBuNC)_2$ and $Ni(SnPh_3)_2(^tBuNC)_3$.

Compound	Ni(η^2-N,O-TEMPO)(Sn^tBu_3)(^{t}BuNC)	$Ni(SnPh_3)_2(^tBuNC)_3$
Empirical formula	$NiSnON_2C_{26}H_{54}$	$SnPF_4C_{12}H_{27}$
Formula weight	588.11	397.00
Crystal system	Monoclinic	Orthorhombic
Lattice parameters		
a (Å)	17.2516(7)	13.1792(6)
b (Å)	11.3442(4)	14.2988(6)
c (Å)	17.5158(7)	8.8652(4)
α (deg)	90.00	90.00
β (deg)	109.8390(6)	90.00
γ (deg)	90.00	90.00
V ($Å^3$)	3224.5(2)	1670.62(13)
Space group	$P2_1/c$ (# 14)	*Pnma* (# 62)
Z value	4	4
ρ_{calc} (g / cm^3)	1.211	1.578
μ (Mo Kα) (mm^{-1})	1.375	1.647
Temperature (K)	296	296
$2\Theta_{max}$ (°)	56.00	56.00
No. Obs. ($I > 2\sigma(I)$)	6236	1977
No. Parameters	296	95
Goodness of fit	1.015	1.232
Max. shift in cycle	0.004	0.001
Residuals*:R1; wR2	0.0292; 0.0750	0.0420; 0.0958
Absorption Correction, Max/min	Multi-scan 0.7457; 0.5671	Multi-scan 0.7459, 0.5816
Largest peak in Final Diff. Map (e^- / $Å^3$)	0.857	1.067

*$R = \Sigma_{hkl}(||F_{obs}| - |F_{calc}||)/\Sigma_{hkl}|F_{obs}|$; $R_w = [\Sigma_{hkl}w(|F_{obs}| - |F_{calc}|)^2/\Sigma_{hkl}wF_{obs}^2]^{1/2}$, $w = 1/\sigma^2(F_{obs})$; $GOF = [\Sigma_{hkl}w(|F_{obs}| - |F_{calc}|)^2/(n_{data} - n_{vari})]^{1/2}$.

Table B.5 Crystallographic Data for Compounds $Fe(Sn^tBu_3)_2(CO)_4$ and $Mo(Sn^tBu_3)(CO)_3Cp$.

Compound	$Fe(Sn^tBu_3)_2(CO)_4$	$Mo(Sn^tBu_3)(CO)_3(C_5H_5)$
Empirical formula	$FeSn_2C28H54O4$	$MoSnO_3C_{20}H_{32}$
Formula weight	747.94	535.09
Crystal system	Monoclinic	Monoclinic
Lattice parameters		
a (Å)	9.0445(5)	8.5304(5)
b (Å)	14.3038(7)	13.5088(8)
c (Å)	13.2353(7)	10.5802(7)
α (deg)	90.00	90.00
β (deg)	91.9563(8)	112.2640(8)
γ (deg)	90.00	90.00
V ($Å^3$)	1711.26(16)	1128.32(12)
Space group	$P2_1/n$ (# 14)	$P2_1/m$ (# 11)
Z value	2	2
ρ_{calc} (g / cm^3)	1.452	1.575
μ (Mo Kα) (mm^{-1})	1.893	1.676
Temperature (K)	296	296
$2\Theta_{max}$ (°)	60.00	56.00
No. Obs. ($I > 2\sigma(I)$)	3822	1644
No. Parameters	169	129
Goodness of fit	1.207	1.052
Max. shift in cycle	0.002	2.075
Residuals*:R1; wR2	0.0317; 0.0733	0.0425; 0.0908
Absorption Correction, Max/min	Multi-scan 0.7465, 0.6227	Multi-scan 0.7464, 0.4828
Largest peak in Final Diff. Map (e^- / $Å^3$)	0.827	0.677

*$R = \Sigma_{hkl}(||F_{obs}| - |F_{calc}||)/\Sigma_{hkl}|F_{obs}|$; $R_w = [\Sigma_{hkl}w(|F_{obs}| - |F_{calc}|)^2/\Sigma_{hkl}wF_{obs}^2]^{1/2}$, $w = 1/\sigma^2(F_{obs})$; $GOF = [\Sigma_{hkl}w(|F_{obs}| - |F_{calc}|)^2/(n_{data} - n_{vari})]^{1/2}$.

Appendix C: Supporting Information for Chapter 6.

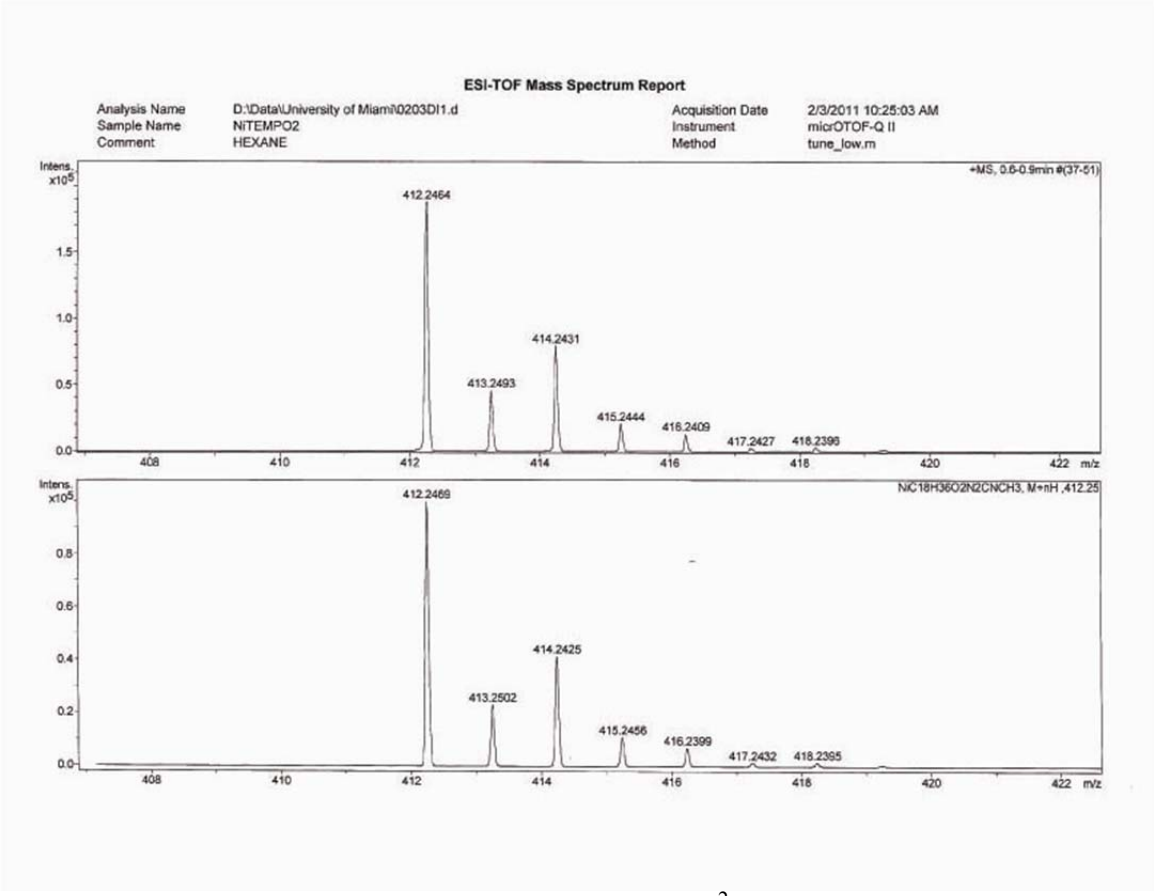

Figure C.1 ESI-TOF mass spectrum report for Ni(η^2-N,O-TEMPO)$_2$ in acetonitrile solvent showing found M + MeCN = 412 (top) and calculated M + MeCN (bottom).

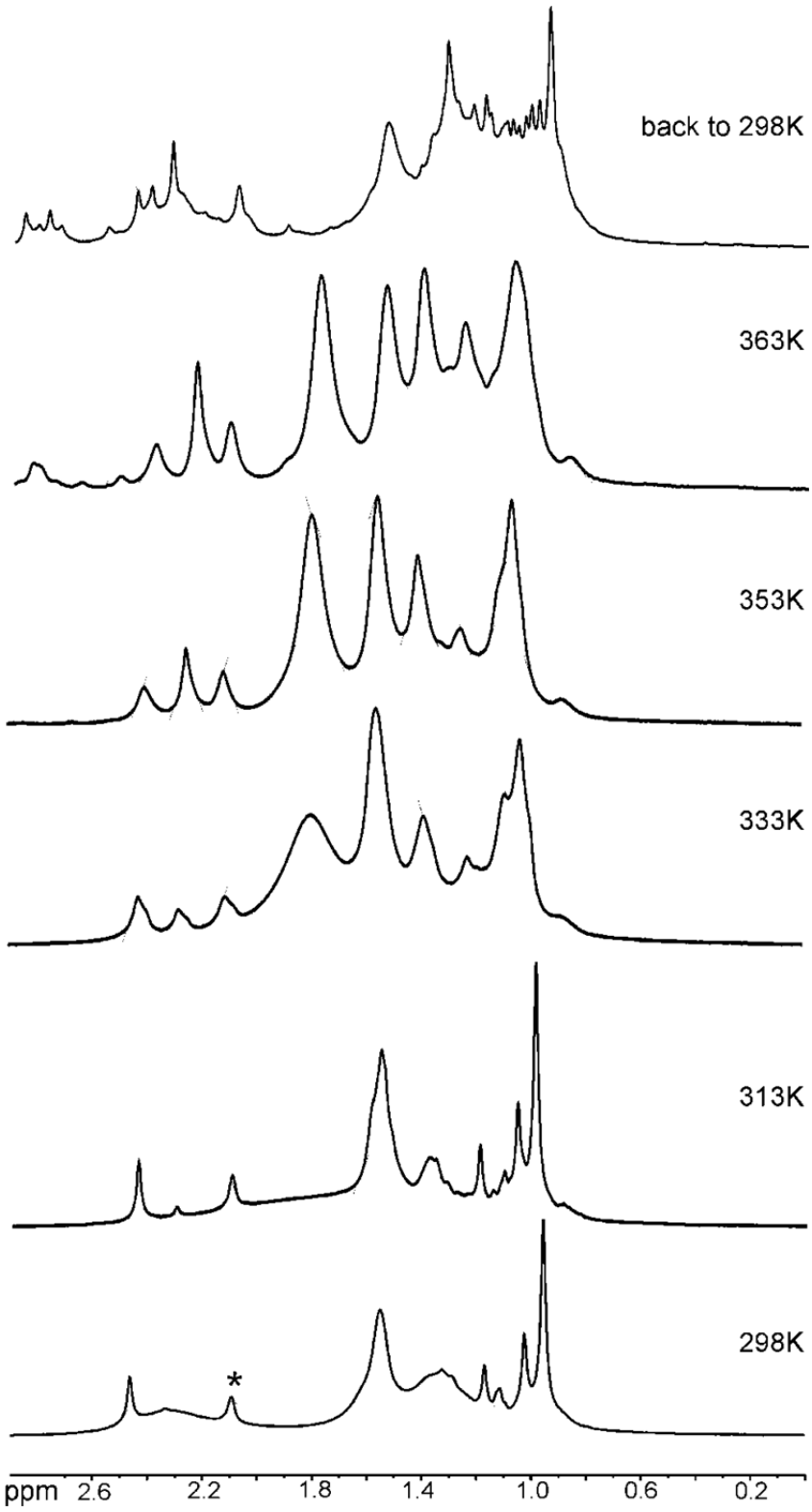

Figure C.2 ^{1}H NMR spectra at 400 MHz of Ni(η^2-N,O-TEMPO)(η^1-O-TEMPO)(^{t}BuNC) at various temperatures in toluene-d_8 solvent. * denotes the methyl peak from toluene-d_8 solvent.

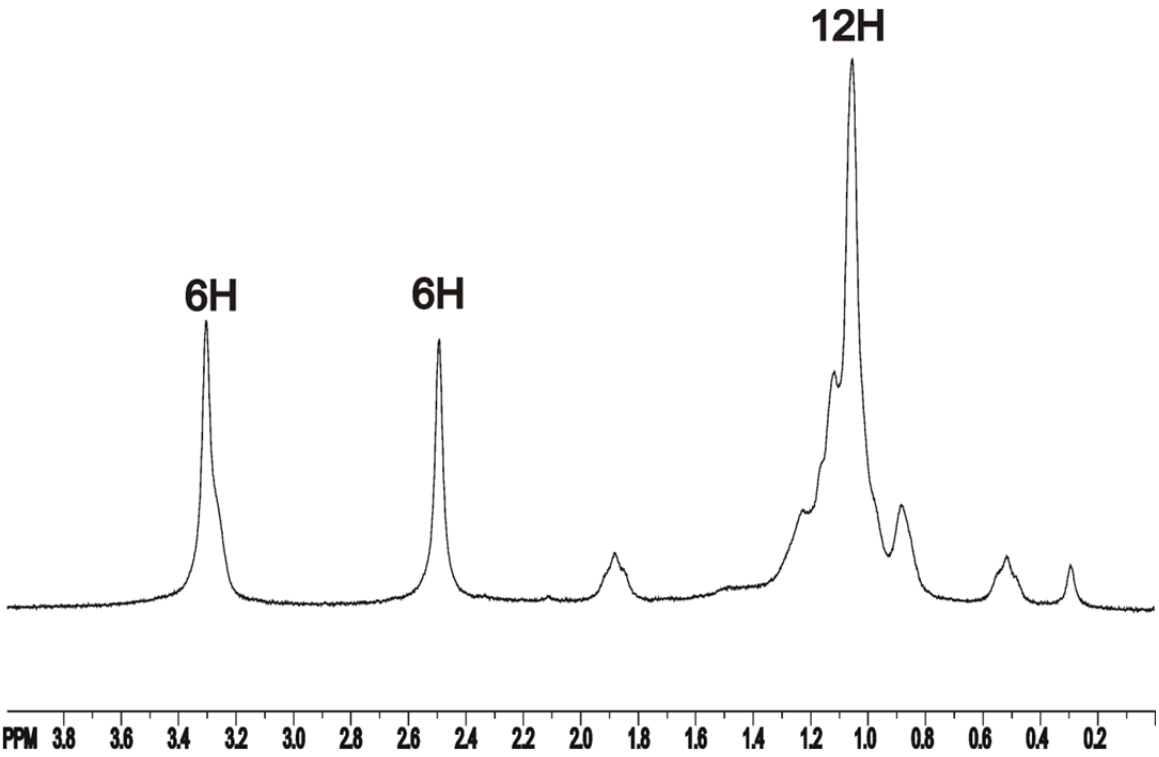

Figure C.3 ^{1}H NMR spectrum of Ni(η^2-N,O-TEMPO)(2,2,6,6-Tetramethylpiperidin-1-yl)(I) showing magnetic equivalence of piperidine ring methyl groups marked 12H.

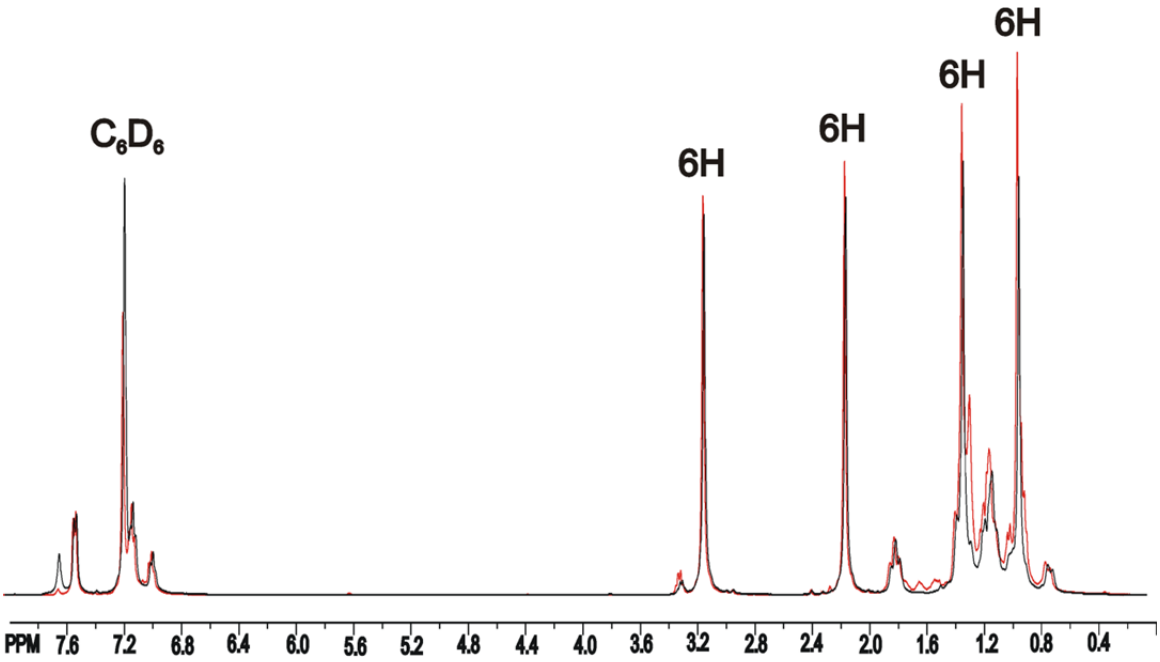

Figure C.4 ^{1}H NMR spectrum of Ni(η^2-N,O-TEMPO)(η^1-O-TEMPO-H)(η^1-CCPh) (black) and Ni(η^2-N,O-TEMPO)(η^1-O-TEMPO-**D**)(η^1-CCPh) (red).

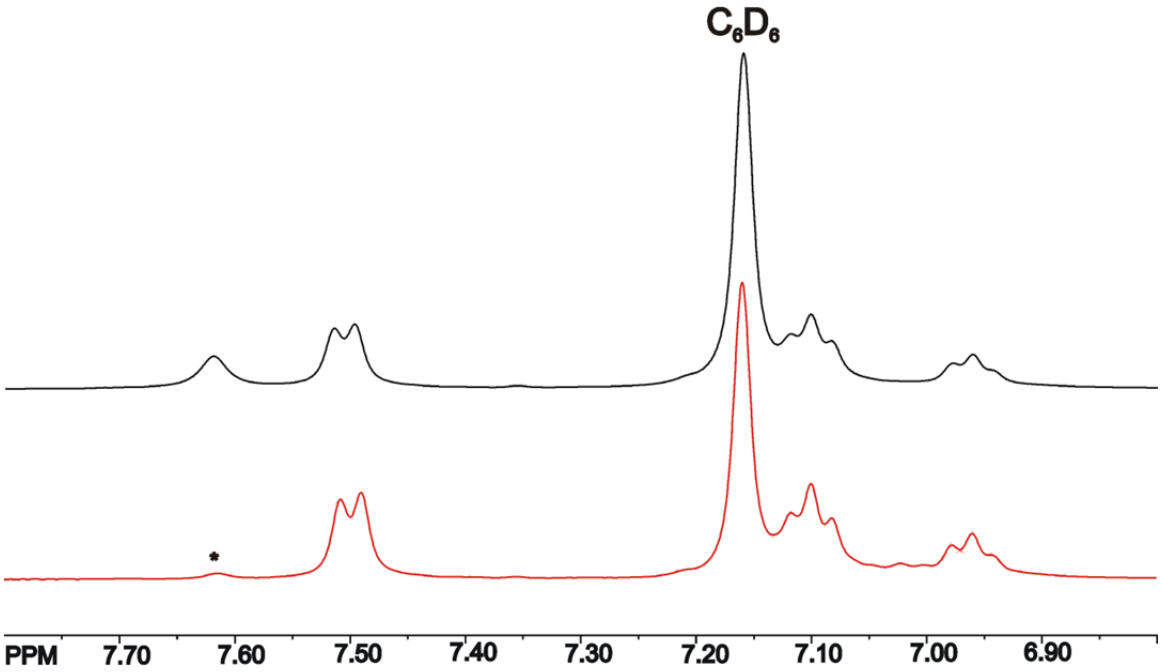

Figure C.5 ^{1}H NMR spectrum of Ni(η^2-N,O-TEMPO)(η^1-O-TEMPO-H)(η^1-CCPh) (black) and Ni(η^2-N,O-TEMPO)(η^1-O-TEMPO-**D**)(η^1-CCPh) (red). * denotes acetylene hydrogen now on TEMPO nitrogen N2.

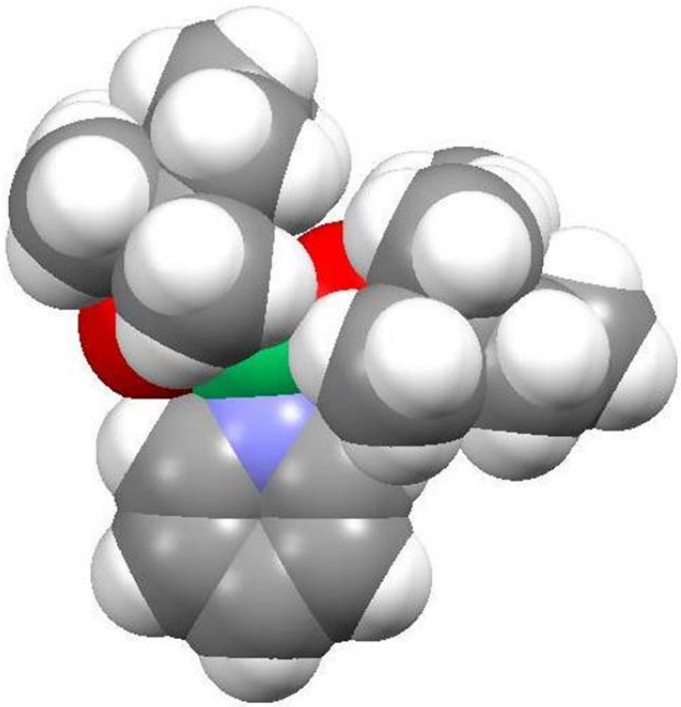

Figure C.6 Space-filling model of Ni(η^2-N,O-TEMPO)(η^1-O-TEMPO)(NC_5H_5) seen from above the square plan. Atomic dimensions are the van der Waals radii. Nickel is shown in green, oxygen in red, nitrogen in blue, carbon in gray, and hydrogen in white.

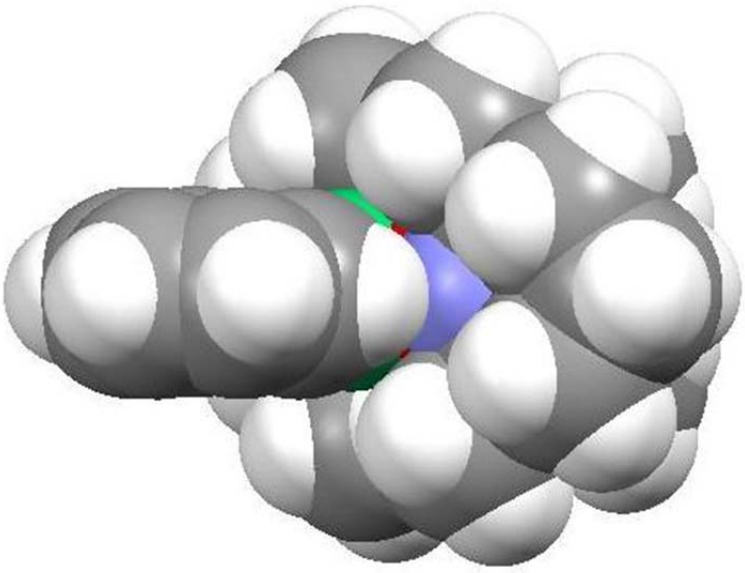

Figure C.7 Space-filling model of Ni(η^2-N,O-TEMPO)(η^1-O-TEMPO)(NC_5H_5) seen down the square plane of the molecule. Atomic dimensions are the van der Waals radii. Nickel is shown in green, oxygen in red, nitrogen in blue, carbon in gray, and hydrogen in white.

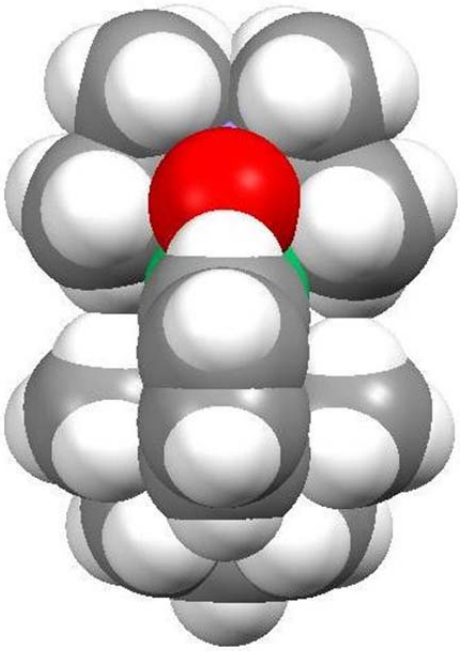

Figure C.8 Space-filling model of Ni(η^2-N,O-TEMPO)(η^1-O-TEMPO)(NC_5H_5) seen down the square plane of the molecule through the pyridine ring. Atomic dimensions are the van der Waals radii. Nickel is shown in green, oxygen in red, nitrogen in blue, carbon in gray, and hydrogen in white.

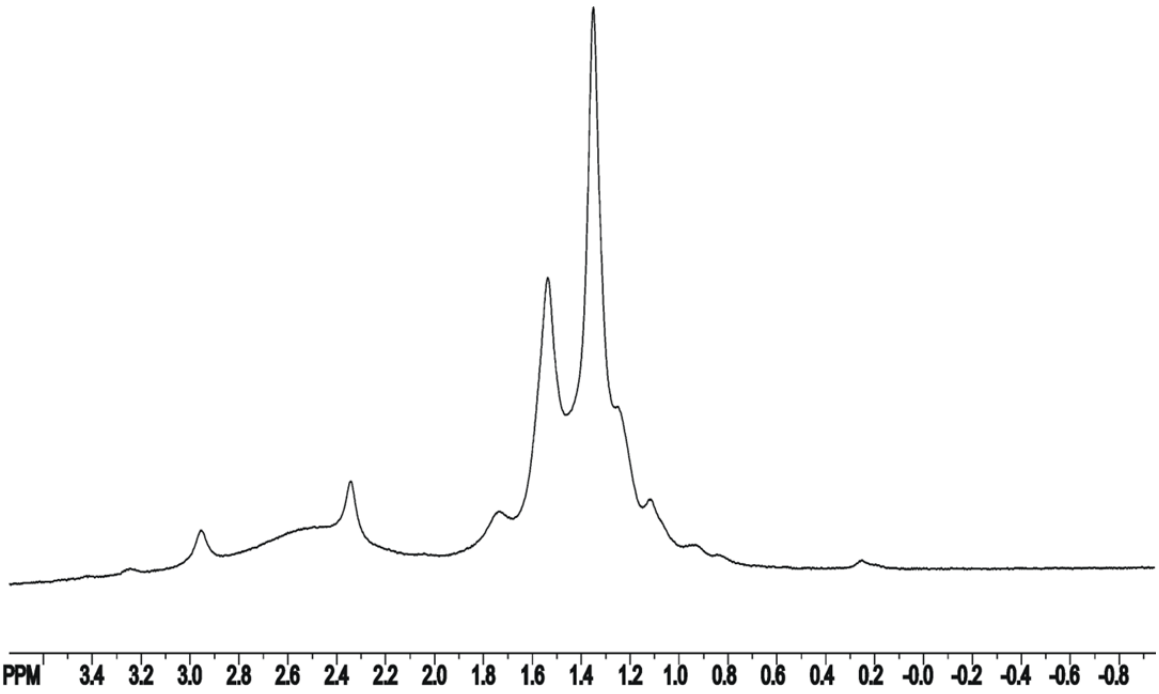

Figure C.9 ^{1}H NMR spectrum of Ni(η^2-N,O-TEMPO)(η^1-O-TEMPO)(NC_5H_5) with excess pyridine showing dynamical processes in solution.

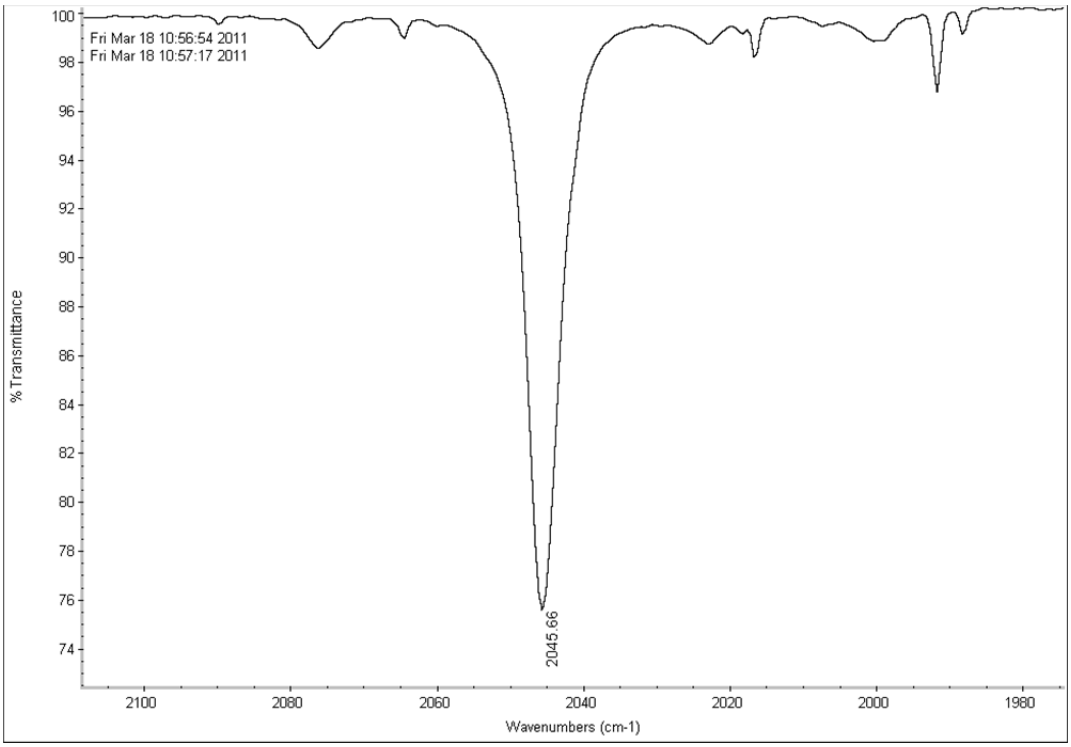

Figure C.10 FTIR spectrum of the proposed compound Ni(η^2-N,O-TEMPO)-(η^1-O-TEMPO)(CO) taken quickly after addition of CO before decomposition.

Table C.1 Crystallographic Data for Compounds Ni(η^2-N,O-TEMPO)$_2$ and Ni(η^2-N,O-TEMPO)(η^1-O-TEMPO)(^{t}BuNC).

Compound	Ni(η^2-N,O-TEMPO)$_2$	Ni(η^2-N,O-TEMPO)(η^1-O-TEMPO)(^{t}BuNC)
Empirical formula	$NiO_2N_2C_{18}H_{36}$	$NiO_2N_3C_{23}H_{45}$
Formula weight	371.20	454.33
Crystal system	Monoclinic	Monoclinic
Lattice parameters		
a (Å)	8.1165(4)	7.7242(3)
b (Å)	10.6126(5)	21.8142(8)
c (Å)	11.6382(6)	15.2535(6)
α (deg)	90.00	90.00
β (deg)	107.224(3)	92.041(7)
γ (deg)	90.00	90.00
V (Å^3)	957.52(8)	2568.54(17)
Space group	$P2_1/n$ (# 14)	$P2_1/n$ (# 14)
Z value	2	4
ρ_{calc} (g / cm^3)	1.287	1.175
μ (Mo Kα) (mm^{-1})	1.024	0.777
Temperature (K)	100	100
$2\Theta_{max}$ (°)	57.00	58.00
No. Obs. (I > 2σ(I))	2139	6360
No. Parameters	178	442
Goodness of fit	1.057	1.075
Max. shift in cycle	0.001	0.003
Residuals*:R1; wR2	0.0315; 0.0830	0.0234; 0.0581
Absorption Correction, Max/min	Multi-scan 0.7465; 0.4399	Multi-scan 0.7465, 0.5552
Largest peak in Final Diff. Map (e$^-$ / Å^3)	0.966	0.423

*$R = \Sigma_{hkl}(||F_{obs}| - |F_{calc}||)/\Sigma_{hkl}|F_{obs}|$; $R_w = [\Sigma_{hkl}w(|F_{obs}| - |F_{calc}|)^2/\Sigma_{hkl}wF_{obs}^2]^{1/2}$, $w = 1/\sigma^2(F_{obs})$; $GOF = [\Sigma_{hkl}w(|F_{obs}| - |F_{calc}|)^2/(n_{data} - n_{vari})]^{1/2}$.

Table C.2 Crystallographic Data for Compounds Ni(η^2-N,O-TEMPO) (2,2,6,6-Tetramethylpiperidin-1-yl)(I) and Ni(η^2-N,O-TEMPO)(η^1-O-TEMPO-H)(CCPh).

Compound	Ni(η^2-N,O-TEMPO) (2,2,6,6-Tetramethylpiperidin-1-yl)(I)	Ni(η^2-N,O-TEMPO)(η^1-O-TEMPO-H)(CCPh)
Empirical formula	$NiON_2IC_{18}H_{36}$	$NiO_2N_2C_{26}H_{42}$
Formula weight	482.10	473.33
Crystal system	Monoclinic	Triclinic
Lattice parameters		
a (Å)	12.4835(5)	8.3519(3)
b (Å)	12.4200(5)	12.3164(4)
c (Å)	14.4214(6)	14.5401(5)
α (deg)	90.00	111.5580(5)
β (deg)	107.2986(6)	95.8880(5)
γ (deg)	90.00	107.7300(4)
V (Å^3)	2134.83(15)	1285.55
Space group	$P2_1/n$ (# 14)	$P\bar{1}$ (# 2)
Z value	4	2
ρ_{calc} (g / cm^3)	1.500	1.223
μ (Mo Kα) (mm^{-1})	2.361	0.778
Temperature (K)	296	100
$2\Theta_{max}$ (°)	56.34	56.00
No. Obs. (I > 2σ(I))	4386	5974
No. Parameters	216	448
Goodness of fit	1.030	1.043
Max. shift in cycle	0.001	0.002
Residuals*:R1; wR2	0.0289; 0.0750	0.0217; 0.0569
Absorption Correction, Max/min	Multi-scan 0.7457, 0.5526	Multi-scan 0.7465, 0.6322
Largest peak in Final Diff. Map (e$^-$ / Å^3)	0.910	0.346

*$R = \Sigma_{hkl}(\,|\,|F_{obs}|-|F_{calc}|\,|)/\Sigma_{hkl}|F_{obs}|$; $R_w = [\Sigma_{hkl}w(|F_{obs}|-|F_{calc}|)^2/\Sigma_{hkl}wF_{obs}^2]^{1/2}$, $w = 1/\sigma^2(F_{obs})$; $GOF = [\Sigma_{hkl}w(|F_{obs}|-|F_{calc}|)^2/(n_{data} - n_{vari})]^{1/2}$.

Table C.3 Crystallographic Data for Compounds Ni(η^2-N,O-TEMPO)(η^1-O-TEMPO-H)(η^1-CC[C_6H_4]CCH) and Ni(η^2-N,O-TEMPO)(η^1-O-TEMPO-H)(CCSiMe_3).

Compound	Ni(η^2-N,O-TEMPO)(η^1-O-TEMPO-H)(η^1-CC[C_6H_4]CCH)	Ni(η^2-N,O-TEMPO)(η^1-O-TEMPO-H)(CCSiMe_3)
Empirical formula	$NiO_2N_2C_{28}H_{42}$	$NiSiN_2O_2C_{23}H_{46}$
Formula weight	497.345	469.42
Crystal system	Triclinic	Monoclinic
Lattice parameters		
a (Å)	7.7421(3)	7.8725(3)
b (Å)	12.3093(5)	10.8105(4)
c (Å)	15.1659(6)	33.0125(13)
α (deg)	74.2830(5)	90.00
β (deg)	77.7570(5)	93.2530(6)
γ (deg)	84.2730(6)	90.00
V (Å^3)	1358.25(9)	2805.02(19)
Space group	$P\ \bar{1}$ (# 2)	$P2_1/c$ (# 14)
Z value	1	4
ρ_{calc} (g / cm^3)	1.216	1.112
μ (Mo Kα) (mm^{-1})	0.740	0.753
Temperature (K)	296	296
$2\Theta_{max}$ (°)	56.00	56.00
No. Obs. (I > 2σ(I))	6003	5803
No. Parameters	466	277
Goodness of fit	1.043	1.009
Max. shift in cycle	0.009	0.451
Residuals*:R1; wR2	0.0274; 0.0744	0.0440; 0.1133
Absorption Correction, Max/min	Multi-scan 0.7465; 0.4399	Multi-scan 0.7465; 0.6085
Largest peak in Final Diff. Map (e$^-$ / Å^3)	0.371	1.098

*$R = \Sigma_{hkl}(\,|\,|F_{obs}|-|F_{calc}|\,|)/\Sigma_{hkl}|F_{obs}|$; $R_w = [\Sigma_{hkl}w(|F_{obs}|-|F_{calc}|)^2/\Sigma_{hkl}wF_{obs}^2]^{1/2}$, $w = 1/\sigma^2(F_{obs})$; GOF = $[\Sigma_{hkl}w(|F_{obs}|-|F_{calc}|)^2/(n_{data}-n_{vari})]^{1/2}$.

Table C.4 Crystallographic Data for Compounds Ni(η^2-N,O-TEMPO)(η^1-O-TEMPO-H)(CCH) and Ni(η^2-N,O-TEMPO)(η^1-O-TEMPO)(NC_5H_5).

Compound	Ni(η^2-N,O-TEMPO)(η^1-O-TEMPO-H)(CCH)	Ni(η^2-N,O-TEMPO)(η^1-O-TEMPO)(NC_5H_5)
Empirical formula	$NiN_2O_2C_{20}H_{38}$	$NiN_3O_2C_{23}H_{41}$
Formula weight	397.23	450.30
Crystal system	Monoclinic	Orthorhombic
Lattice parameters		
a (Å)	13.6684(6)	14.906(2)
b (Å)	11.5267(5)	14.965(2)
c (Å)	14.3518(6)	22.487(3)
α (deg)	90.00	90.00
β (deg)	92.6580(6)	90.00
γ (deg)	90.00	90.00
V ($Å^3$)	2258.72(17)	5016.2(12)
Space group	*$P2_1/c$* (# 14)	*Pbca* (#61)
Z value	4	8
ρ_{calc} (g / cm^3)	1.168	1.193
μ (Mo Kα) (mm^{-1})	0.873	0.795
Temperature (K)	296	296
$2\Theta_{max}$ (°)	56.00	50.00
No. Obs. ($I > 2\sigma(I)$)	4597	2240
No. Parameters	242	270
Goodness of fit	1.018	0.998
Max. shift in cycle	0.001	0.006
Residuals*:R1; wR2	0.0307; 0.0813	0.0443; 0.0889
Absorption Correction, Max/min	Multi-scan 0.7465; 0.6023	Multi-scan 0.7461;0.5510
Largest peak in Final Diff. Map (e^- / $Å^3$)	0.260	0.391

*$R = \Sigma_{hkl}(\,|\,|F_{obs}|-|F_{calc}|\,|)/\Sigma_{hkl}|F_{obs}|$; $R_w = [\Sigma_{hkl}w(|F_{obs}|-|F_{calc}|)^2/\Sigma_{hkl}wF_{obs}^2]^{1/2}$, $w = 1/\sigma^2(F_{obs})$; $GOF = [\Sigma_{hkl}w(|F_{obs}|-|F_{calc}|)^2/(n_{data} - n_{vari})]^{1/2}$.

References

(1) Zeise, W. C. *Annalen der Physik und Chemie* **1831**, *97*, 497

(2) Black, M.; Mais, H. B.; Owston, P. G. *Acta Crystallographica Section B* **1969**, *B25*, 1753-1759

(3) Grisham, C. M.; Garrett, R. H. *Biochemistry* **1999**, 426-427

(4) Bozso, F.; Ertl, G.; Grunze, M.; Weiss, M. *Journal of Catalysis* **1977**, *49* (1), 18-41

(5) Imbihl, R.; Behm, R. J.; Ertl, G.; Moritz, W. *Surface Science* **1982**, *123* (1), 129-140

(6) Magistrato, A.; Robertazzi, A.; Carloni, P. *J. Chem. Theory Comput.* **2007**, *3* (5), 1708-1720

(7) "Recognizing the Best in Innovation: Breakthrough Catalyst". *R&D Magazine*, September **2005**, 20

(8) http://www.climatetechnology.gov/library/2005/tech-options/tor2005-143.pdf

(9) The Royal Society of Chemistry. *Organometallic Chemistry,* Volumes 1-36

(10) DiLuzio, J. W.; Vaska, L. *J. Am. Chem. Soc.* **1961**, *83*, 2784-2785

(11) (a) Langmuir, I. *Science* **1921**, *54* (1386), 59-67. (b) Mitchell, P. R.; Parish, J. *J. Chem. Educ.* **1969**, *46* (12), 811-814

(12) (a) Gosser, L. W.; Seidel, W. C.; Tolman, C. *J. Am. Chem. Soc.* **1974**, *96* (1), 53-60. (b) Tolman, C. A. *J. Am. Chem. Soc.* **1970**, *92* (10), 2956-2965

(13) Rothermund, P. *J. Am. Chem. Soc.* **1936***, 58* (4), 625-627

(14) Anderson, S.; Anderson, H. L.; Bashall, A.; McPartlin, M.; Sanders, J. K. M. *Angew. Chem., Int. Ed. Engl.* **1995**, *34*, 1096-1099

(15) Ostrowski, A. D.; Absalonson, R. O.; De Leo, M. A.; Wu, G.; Pavlovich, J. G.; Adamson, J.; Azhar, B.; Iretskii, A. V.; Megson, I. L.; Ford, P. C. *Inorg. Chem.* **2001**, doi: 10.1021/ic200094x

(16) Osborn, J. A.; Jardine, F. H.; Young, J. F.; Wilkinson, G. *J. Chem. Soc. A* **1966**, 1711-1732

(17) Clark, T. J.; Jaska, C. A.; Turak, A.; Lough, A. J.; Lu, Z-H.; Manners, I. *Inorg. Chem.* **2007**, *46*, 7394-7402

(18) Millard, C. B.; Kryger, G.; Ordentlich, A. *Biochemistry* **1999**, *38* (22), 7032-7039

(19) Denk, M. K.; Thadani, A.; Hatano, K.; Lough, A. J. *Angew. Chem., Int. Ed. Engl.* **1997**, *36*, 2607

(20) Herrmann, W. A.; Elison, M.; Fischer, J.; Kocher, C.; Artus, G. R. J. *Angew. Chem., Int. Ed. Engl.* **1995**, *34* (21), 2731-2734

(21) Wanzlick, H. W.; Schikora, E. *Angew. Chem.* **1960**, *72* (14), 494

(22) Wanzlick, H. W.; Schikora, E. *Chemische Berichte* **1960**, *94* (9), 2389-2393

(23) Kline, M.; Harlow, R. L.; Arduengo, A. J. *J. Am. Chem. Soc.* **1991**, *113* (1), 361-363

(24) Nolan, S. P. *N-Heterocyclic Carbenes in Synthesis* **2006**, ISBN: 3527314008

(25) (a) Vougioukalakis, G. C.; Grubbs, R. H. *Chem. Rev.* **2010**, *110* (3), 1746-1787. (b) Schwab, P.; Ziller, J. W.; Grubbs, R. H. *J. Am. Chem. Soc.* **1996**, *118* (1), 100-110

(26) Scholl, M.; Ding, S.; Lee, C. W.; Grubbs, R. H. *Organic Letters* **1999**, *1* (6), 953-956

(27) (a) Arduengo, A. J.; Gamper, S. F.; Calabrese, J. C.; Davidson, F. *J. Am. Chem. Soc.* **1994**, *116* (10), 4391-4394. (b) Nolan, S. P.; Fortman, G. C.; Scott, N. M.; Linden, A.; Stevens, E. D.; Dorta, R. *Chem. Commun.* **2010**, *46*, 1050-1052

(28) Driess, M.; Yao, S.; Brym, M.; van Wullen, C.; Lentz, D. *J. Am. Chem. Soc.* **2006**, *128* (30), 9628-9629

(29) Bundhun, A.; Ramasami, P.; Schaefer, H. F. *J. Phys. Chem. A* **2009**, *113* (28), 8080-8090

(30) Al-Rafia, S. M. I.; Lummis, P. A.; Ferguson, M. J.; McDonald, R.; Rivard, E. *Inorg. Chem.* **2010**, *49* (20), 9709-9717

(31) Shih, K-Y.; Kempe, R.; Schrock, R. R. *J. Am. Chem. Soc.* **1994**, *116*, 8804-8805

(32) Laplaza, C. E.; Odom, A. L.; Davis, W. M.; Protasiewicz, J. D.; Cummins, C. C. *J. Am. Chem. Soc.* **1995**, *117* (17), 4999-5000

(33) Laplaza, C. E.; Johnson, A. R.; Cummins, C. C. *J. Am. Chem. Soc.* **1996**, *118* (3), 709-710

(34) Bellamy, F. D.; Ou, K. *Tetrahedron Letters* **1984**, *25* (8), 839-842

(35) Singh, A. K.; Prakash, R.; Pandey, D. *J. Phys. Chem. B* **2011**, *115* (7), 1601-1607

(36) Llorca, J.; Homs, N.; Fierro, J-L. G.; Sales, J.; de la Piscina, P. R. *Journal of Catalysis* **1997**, *166*, 44-52

(37) Coq, B.; Figueras, F. *Journal of Catalysis* **1984**, *85*, 197

(38) Martincova, J.; Dostal, L.; Ruzicka, A.; Taraba, J.; Jambor, R. *Organometallics* **2007**, *26* (17), 4102-4104

(39) Sekiguchi, A.; Fukawa, T.; Lee, V. Y.; Nakamoto, M. *J. Am. Chem. Soc.* **2003**, *125* (31), 9250-9251

(40) Vedejs, E.; Duncan, M.; Haight, R. *J. Org. Chem.* **1993**, *58* (11), 3046-3050

(41) Tanaka, H.; Ogawa, H.; Suga, H.; Torii, S.; Jutand, A.; Aziz, S.; Suarez, A. G.; Atamore, C. *J. Org. Chem.* **1996**, *61* (26), 9402-9408

(42) Clayden, J.; Greeves, N.; Warren, S.; Wothers, P. *Organic Chemistry* **2000**, Ch. 39, 1040-1041

(43) Baillargeon, V. P.; Stille, J. K. *J. Am. Chem. Soc.* **1983**, *105* (24), 7175-7176

(44) (a) Holt, M. S.; Wilson, W. L.; Nelson, J. H. *Chem. Rev.* **1989**, *89*, 11-49. (b) Captain, B.; Adams, R. D. *Turning Points in Solid-State Materials and Surface Chemistry*, Royal Society of Chemistry, UK, **2007**, Chapter 31, 534-539

(45) Schneider, B.; Wilhelm, W. P. *Justus Liebigs Annalen der Chemie* **1967**, *707*, 7-14

(46) Krause, E.; Weinberg, K. *Ber.* **1930**, *63,* 381

(47) Farrar, W. V.; Skinner, H. A. *J. Organometallic Chem.* **1964**, *1*, 434

(48) Krause, E. *Berichte der Deutschen Chemischen Gesellschaft* **1918**, *51*, 912-914

(49) Jones, W. J.; Davies, W. C.; Bowden, S. T.; Edwards, C.; Davis, V. E.; Thomas, L. H. *J. Chem. Soc.* **1947**, 1446-1450

(50) Kandil, S. A.; Allred, A. L. *J. Chem. Soc. A* **1970**, 2987-2992

(51) Dodero, V. I.; Mitchell, T. N.; Podesta, J. C. *Organometallics* **2003**, *22* (4), 856-860

(52) www.VWR.com, CAS #19429-30-2

(53) Cemal, P. *International Journal of Nautical Archeology* **1998**, *27* (3), 188-224

(54) Kennedy, D. G.; Young, P. B.; Kennedy, S.; Scott, J. M.; Molloy, A. M.; Weir, D. G.; Price, J. *Int. J. Vitam. Nutr. Res.* **1995**, *65* (4), 241-247

(55) Sweany, R. L.; Brown, T. L. *Inorg. Chem.* **1977**, *16*, 415-421

(56) Pauson, P. L.; Khand, U. *Ann. N.Y. Acad. Sci.* **1977**, *295*, 2

(57) Geller, J. M.; Wosnick, J. H.; Butler, I. S.; Gilson, D. F. R.; Morin, F. G.; Belenger-Geriepy, F. *Can. J. Chem.* **2001**, *80*, 813-820

(58) Adams, R. D.; Trufan, E. *Inorg. Chem.* **2010**, *49* (6), 3029-3034

(59) Jackson, S. A.; Eisenstein, O.; Martin, J. D.; Albeniz, A. C.; Crabtree, R. H. *Organometallics* **1991**, *10*, 3062-3069

(60) Douglas, B. E.; McDaniel, D. H.; Alexander, J. J. *Concepts and Models in Inorganic Chemistry;* 3rd Edition. Wiley: New York **1994,** Chapter 12

(61) Heiber, W.; Brue, R. *Chem. Ber.* **1957**, *90*, 1270-1274

(62) (a) Harrod, J. F.; Chalk, A. J. *J. Am. Chem. Soc.* **1965**, *87,* 1133-1135. (b) Harrod, J. F.; Chalk, A. J. *J. Am. Chem. Soc.* **1967**, *89*, 1640-1647

(63) Onda, A.; Komatsu, T.; Yashima, T. *Chem. Commun.* **1998**, 1507-1508

(64) Rossi, A. R.; Hoffman, R. *Inorg. Chem.* **1975**, *14*, 365-374

(65) Captain, B.; Zhu, L.; Isrow, D.; Yempally, V. *J. Cluster Sci.* **2010**, *21* (3), 417-426

(66) (a) Groshens, T. J.; Klabunde, K. J. *J. Organometallic Chem.* **1983**, *259,* 337-343. (b) Janikowski, S. T.; Radonovich, L. J.; Groshens, T. J.; Klabunde, K. J. *Organometallics* **1985**, *4,* 396-398

(67) (a) Chen, M. S.; White, M. C. *Science* **2007**, *318*, 783. (b) Lersch, M.; Tilset, M. *Chem. Rev.* **2005**, *105*, 2471. (c) Crabtree, R. H. *J. Organometallic Chem.* **2004**, *689*, 4083. (d) Labinger, J. A.; Bercaw, J. E. *Nature* **2002**, *417,* 507. (e) Shilov, A. E.; Shul'pin, G. B. *Chem. Rev.* **1997**, *97*, 2879

(68) Ohki, Y.; Hatanaka, T.; Tatsumi, K. *J. Am. Chem. Soc.* **2008**, *130*, 17174-17186

(69) Jana, A.; Roesky, H. W.; Schulzke, C.; Samuel, P. P. *Organometallics* **2010**, *29* (21), 4837-4841

(70) Marks, T. J.; Newman, A. R. *J. Am. Chem. Soc.* **1973**, *95*, 769

(71) Gilmore, C. J.; Woodward, P. J. *Chem. Soc. Dalton Trans.* **1972**, 1387

(72) Captain, B.; Adams, R. D.; Zhu, L. *Inorg. Chem.* **2007**, *46* (11), 4605-4611

(73) (a) Zhang, F.; Kirby, C. W.; Hairsine, D. W.; Jennings, M. C.; Puddephatt, R. J. *J. Am. Chem. Soc.* **2005**, *127*, 14196. (b) Burger, P.; Bergman, R. G. *J. Am. Chem. Soc.* **1993**, *115*, 10462. (c) Vedernikov, A. N.; Borisoglebski, A. B.; Solomonov, B. N. *Mendeleev Commun.* **2000**, *10*, 20

(74) Pyror, W. A.; Tang, F. Y.; Tang, R. H.; Church, D. F. *J. Am. Chem. Soc.* **1982**, *104*, 2885

(75) Captain, B.; Adams, R. D.; Zhu, L. *Organometallics* **2006**, *25*, 4183-4187

(76) Captain, B.; Adams, R. D.; Hollandsworth, C. B.; Johansson, M.; Smith, J. L. *Organometallics* **2006**, *25*, 3848-3855

(77) Captain, B.; Adams, R. D.; Johansson, M.; Smith, J. L. *J. Am. Chem. Soc.* **2005**, *127*, 488-489

(78) Captain, B.; Adams, R. D.; Hall, M. B.; Trufan, E.; Yang, X. *J. Am. Chem. Soc.* **2007**, *129*, 12328-12340

(79) (a) Farrugia, L. J. *Adv. Organomet. Chem.* **1990**, *31*, 301. (b) Biswas, J.; Bickle, G. M.; Gray, P. G.; Do, D. D.; Barbier, J. *Catal. Rev-Sci. Eng.* **1988**, *30*, 161. (c) Sinfelt, J. H. *Bimetallic Catalysts. Discoveries, Concepts and Applications* (John Wiley & Sons, New York, **1983**). (d) Sinfelt, J. H. *Sci. Am.* **1985**, *253*, 90

(80) (a) Adams, R. D.; Cheng, G.; Lii, J.-C.; Wu, W. *Inorg. Chem.* **1991**, *30*, 1007. (b) Adams, R. D.; Li, Z.; Lii, J.-C.; Wu, W. *Inorg. Chem.* **1992**, *31*, 3445. (c) Adams, R. D.; Chen, G.; Wu, W.; Yin, J. *Inorg. Chem.* **1990**, *29,* 4208. (d) Adams, R. D.; Pompeo, M. P.; Wu, W. *Inorg. Chem.* **1991**, *30*, 2425. (e) Adams, R. D.; Pompeo, M. P.; Wu, W. *Inorg. Chem.* **1991**, *30*, 2899. (f) Adams, R. D.; Li, Z.; Sweptson, P.; Wu, W.; Yamamoto, J. *J. Am. Chem. Soc.* **1992**, *114*, 10657. (g) Adams, R. D.; Wu, W. *Inorg. Chem.* **1991**, *30*, 3605. (h) Adams, R. D.; Li, Z.; Lii, J.-C.; Wu, W. *Organometallics* **1992**, *11*, 4001

(81) Adams, R. D.; Chen, G.; Wu, W. *J. Cluster Sci.* **1993**, *4* (2), 119-132

(82) Adams, R. D.; Chen, G.; Wang, J.-G.; Wu, W. *Organometallics* **1990**, *9*, 1339

(83) Captain, B.; Adams, R. D.; Trufan, E.; Zhu, L. *J. Am. Chem. Soc.* **2007**, *129*, 7545

(84) Captain, B.; Adams, R. D.; Boswell, E. M.; Hungria, A. B.; Midgley, P. A.; Raja, R.; Thomas, J. M. *Angew. Chem. Int. Ed.* **2007**, *46*, 8182-8185

(85) Captain, B.; Adams, R. D.; Thomas, J. M.; Siani, A.; Alexeev, O. S.; Stafyla, E.; Hungria, A. B.; Midgley, P. A.; Amiridis, M. D. *Langmuir* **2006**, *22*, 5160-5167

(86) Captain, B.; Isrow, D.; Zhu, L.; Yempally, V.; Manzoli, M.; Shetti, V. N.; Blaine, J. A. L.; Coluccia, S.; Raja, R.; Gianotti, E. *Journal of Catalysis*, **2011**, Manuscript Submitted

(87) Travis, A. S. *in The Chemistry of Functional Groups: The Chemistry of Anilines, ed. Z.* Rappoport, Wiley-VCH, Winheim, **2007**, 715-782

(88) Lei, Y. J. *Appl. Catalysis* **1991**, *72,* 33

(89) Spencer, J. L. *Inorg. Synth.* **1979**, *19*, 213

(90) Captain, B.; Zhu, L.; Isrow, D.; Yempally, V. *J. Organometallic Chem.* **2010**, *695* (1), 1-5

(91) Captain, B.; Zhu, L.; Isrow, D.; Yempally, V. **2011,** Manuscript Submitted

(92) Apex2 Version 2.2-0 and SAINT+ Version 7.46A; Bruker Analytical X-Ray Systems, Inc., Madison, Wisconsin, USA, **2007**.

(93) (a) Sheldrick, G. M. SHELXTL Version 6.1; Bruker Analytical X-Ray Systems, Inc., Madison, Wisconsin, USA, **2000.** (b) Sheldrick, G. M. *Acta Cryst.* **2008**, *A64*, 112-122

(94) Wilburn, D. R.; Bleiwas, D. I. *U.S. Geological Survey Open-File Report* **2004**, 1224

(95) Randolph, N. G. *Pure & Appl. Chem.* **1993**, *65* (12), 2411-2416

(96) Captain, B.; Adams, R. D.; Thomas, J. M.; Blom, D. A.; Raja, R.; Trufan, E. *Langmuir* **2008**, *24*, 9223-9226

(97) Ruiz, A. G.; Escribano, A. S.; Ramos, I. R. *Applied Catalysis A: General* **1992**, *81* (1), 101-112

(98) Poinern, G. E.; Ng, Y. J.; Fawcett, D. *J. Colloid Interface Sci.* **2010**, *352* (2), 259-264

(99) Burge, H. D.; Collins, D. J.; Davis, B. H. *Ind. Eng. Chem. Prod. Res. Dev.* **1980**, *19* (3), 389-391

(100) Raney, M. "*Method of Producing Finely Divided Nickel*" **1927**, U.S. Patent 1,628,190

(101) Carruthers, W. *Some Modern Methods of Organic Synthesis* **1986**, Cambridge University Press, 413-414

(102) Sigel, A.; Sigel, H. *Nickel and Its Surprising Impact in Nature* **2007**, John Wiley & Sons, Ltd.: Chichester, UK. Metal Ions in Life Science, Vol. 2.

(103) Arana, J.; de la Piscina, P. R.; Llorca, J.; Sales, J.; Homs, N.; Fierro, J. L. G. *Chem. Mater.* **1998**, *10*, 1333-1342

(104) Onda, A.; Komatsu, T.; Yashima, T. *Chem. Commun.* **1998**, 1507-1508

(105) Morgenstern, D. A.; Wittrig, R. E.; Franwick, P. E.; Kubiak, C. P. *J. Am. Chem. Soc.* **1993**, *115*, 6470-6471

(106) Captain, B.; Yempally, V.; Zhu, L. *Inorg. Chem.* **2010**, *49*, 7238-7240

(107) Fox, B. J.; Millard, M. D.; DiPasquale, A. G.; Rheingold, A. L.; Figueroa, J. S. *Angew. Chem. Int. Ed.* **2009**, *48*, 3473-3477

(108) Day, V. W.; Kristoff, J. S.; Hirsekorn, F. J.; Muetterties, E. L. *J. Am. Chem. Soc.* **1975**, *97* (9), 2571-2573

(109) Mindiola, D. J.; Waterman, R.; Jenkings, D. M.; Hillhouse, G. L. *Inorganica Chimica Acta* **2003**, *345*, 299-308

(110) Buschhaus, H. U.; Neumann, W. P.; Apoussidis, T. *Liebigs Annalen der Chemie* **1981**, *7*, 1190-1197

(111) Puff, H.; Breuer, B.; Gehrke-Brinkmann, G.; Kind, P.; Reuter, H.; Schuh, W.; Wald, W.; Weidenbruck, G. *J. Organometallic Chem.* **1989**, *363*, 265

(112) Kerschl, S.; Wrackmeyer, B.; Mannig, D.; Noth, H.; Staudigl, R. *Z. Naturforsch, B: Chem. Sci.* **1987**, *42*, 387

(113) Choi, J.-C.; Sakakura, T.; Sako, T. *J. Am. Chem. Soc.* **1999**, *121* (15), 3793-3794

(114) Ballivet-Tkatchenko, D.; Chermette, H.; Plasseraud, L.; Walter, O. *Dalton Trans.* **2006**, *43*, 5167-5175

(115) Kummerlen, J.; Sebald, A.; Reuter, H. *J. Organometallic Chem.* **1992**, *427*, 309

(116) Tiekink, E. R. T. *J. Organometallic Chem.* **1986**, *302*, C1

(117) Darensbourg, D. J. *Inorg. Chem.* **2010**, *49* (23), 10765-10780

(118) Bauch, C. G.; Ovalles, C.; Darensbourg, D. J. *Catalytic Activation of Carbon Dioxide*, Chapter 4, **1988**, 26-41

(119) Blanchard, S.; Neese, F.; Bothe, E.; Bill, E.; Weyhermuller, T.; Wieghardt, K. *Inorg. Chem.* **2005**, *44*, 3636-3656

(120) Lebedev, O. L.; Kazarnovskii, S. N. *Zhur. Obshch. Khim.* **1960**, *30* (5), 1631-1635

(121) Barriga, S. *Synlett.* **2001**, *4*, 563

(122) Mahanthappa, M. K.; Huang, K.-W.; Cole, A. P.; Waymouth, R. M. *Chem. Commun.* **2002**, 502-503

(123) Laugier, J.; Latour, J.-M.; Caneshi, A.; Rey, P. *Inorg. Chem.* **1991**, *30*, 4474-4477

(124) Zhu, Z.; Fettinger, J. C.; Olmstead, M. M.; Power, P. P. *Organometallics* **2009**, *28*, 2091-2095

(125) Mindiola, D. J.; Waterman, R.; Jenkins, D. M.; Hillhouse, G. L. *Inorg. Chim. Acta.* **2003**, *345*, 299

(126) Matsumoto, T.; Ito, M.; Tatsumi, K. *Inorg. Chem.* **2009**, *48*, 2215-2223

(127) Christe, K. O.; Dixon, D. A.; Mercier, H. P. A.; Sander, J. C. P.; Schrobilgen, G. J.; Wilson, W. W.; *J. Am. Chem. Soc.* **1994**, *116*, 2850-2858

(128) de Fremont, P.; Marion, N.; Nolan, S. P. *J. Organometallic Chem.* **2009**, *694*, 551-560

(129) (a) Tarascon, J. M.; Hull, G. W.; Di Salvo, F. J. *Mater. Res. Bull.* **1984**, *19*, 915. (b) Perrin, C.; Sergent, M. *J. Chem. Res.* **1983**, *5*, 38-39

(130) Iitaka, Y.; Oohama, T.; Shiina, M.; Takizawa, T.; Yamamoto, Y.; Yamazaki, H. *J. Chem. Soc., Dalton Trans.: Inorganic Chemistry* **1987**, *4*, 853-857

(131) Emerich, B. M.; Moore, C. E.; Fox, B. J.; Rheingold, A. L.; Figeuroa, J. S. *Organometallics* **2011**, doi/10.1021/om200209w

(132) Smith, A. L. *Oxford Dictionary of Biochemistry and Molecular Biology* **1997**, Oxford: Oxford University Press, 508

(133) Cabeza, J. A.; del Rio, I.; Fernandez-Colinas, J. M.; Sanchez-Vega, M. G. *Organometallics* **2009**, *28*, 1243-1247

(134) Pomeroy, R. K.; Vancea, L.; Calhoun, H. P.; Graham, W. A. G. *Inorg. Chem.* **1977**, *16* (6), 1508-1514

(135) Burchell, R. P. L.; Sirsch, P.; Decken, A.; McGrady, G. S. *Dalton Trans.* **2009**, 5851-5857

(136) Fischer, P. J.; Krohn, K. M.; Mwenda, E. T.; Young, V. G. *Organometallics* **2005**, *24* (7), 1776-1779. (b) Neto, J. L.; de Lima, G. M.; Porto, A. O.; Ardisson, J. D.; Doriguetto, A. C.; Elena, J. *J. Molecular Structure* **2006**, *782* (2-3), 110-115

(137) Hermans, S.; Raja, R.; Thomas, J. M.; Johnson, B. F. G.; Sankar, G.; Gleeson, D. *Angew. Chem. Int. Ed.* **2001**, *40*, 1211-1215

(138) Ciriminna, R.; Pagliaro, M. *Org. Process Res. Dev.* **2010**, *14*, 245-251

(139) (a) Georges, M. K.; Lukkarila, J. L.; Szkurhan, A.R. *Macromolecules* **2004,** *37*, 1297-1303. (b) Maehata, H.; Buragina, C.; Cunningham, M.; Keoshkerian, B. *Macromolecules* **2007**, *40*, 7126-7131. (c) Hawker, C. J. *Acc. Chem. Res.* **1997**, *30*, 373-382. (d) Benoit, D.; Chaplinski, V.; Braslau, R.; Hawker, C. J. *J. Am. Chem. Soc.* **1999**, *121*, 3904-3920.

(140) Dane, E. L.; Maly, T.; Debelouchina, G. T.; Griffin, R. G.; Swagger, T. M. *Org. Lett.,* **2009**, *11*, 1871-1874.

(141) (a) Keana, J. F. W. *Chem. Rev.* **1978**, *78*, 37-64. (b) Borbat, P. P.; Costa-Filho, A. J.; Earle, K. A.; Moscicki, J. K.; Freed, J. H. *Science* **2001**, *291*, 266-269. (c) Chen, J. Y.-C.; Jayaraj, N.; Jockusch, S.; Ottaviani, M. F.; Ramamurthy, V.; Turro, N. J. *J. Am. Chem. Soc.* **2008**, *130*, 7206–7207. (d) Jayaraj, N.; Porel, M.; Ottaviani, M. F.; Maddipatla, M. V. S. N.; Modelli, A.; Da Silva, J. P.; Bhogala, B. R.; Captain, B.; Jockusch, S.; Turro, N. J.; Ramamurthy, V. *Langmuir* **2009**, *25*, 13820–13832. (e) Yi, S.; Captain, B.; Ottaviani, M. F.; Kaifer. A. E. *Langmuir* **2011**, *in press*.

(142) (a) Hu, S.; Gao, W.; Kumar, R.; Gross, R. A.; Gu, Q.-M.; Cheng, H. N. *Biocatalysis in Polymer Science,* Chapter 21, **2002**, 253-264. (b) Michaud, A.; Gingras, G.; Morin, M.; Beland, F.; Cirimimna, R.; Avnir, D.; Pagliaro, M. *Org. Process Res. Dev.* **2007**, *11*, 766-768. (c) Bordenave, N.; Grelier, S.; Coma, V. *Biomacromolecules* **2008,** *9*, 2377-2382.

(143) (a) deNooy, A. E. J.; Besemer, A. C.; vanBekkum, H. *Synthesis (Stuttgart)*, **1996**, 1153-1174. (b) Sheldon, R. A.; Arends, I. W. C. E. *Adv. Synth. Catal.* **2004**, *346*, 1051-1071. (c) Recupero, F.; Punta, C. *Chem. Rev.* **2007**, *107*, 3800-3842.

(144) (a) Anelli, P. L.; Montanari, F.; Quici, S. *Org. Synth.* **1993**, *8,* 367. (b) Zhao, M. M.; Li, J.; Mano, E.; Song, Z. J.; Tschaen, D. M. *Org. Synth. Vol.* **2005,** *81,* 195

(145) (a) Semmelhack, M. F.; Schmid, C. R.; Cortes, D. A. *Tetrahedron Lett.* **1986**, *27*, 1119-1122. (b) Laugier, J.; Latour, J.-M.; Caneshi, A.; Rey, P. *Inorg. Chem.* **1991,** *30*, 4474-4477. (c) Gamez, P.; Arends, I.; Reedijk, J.; Sheldon, R. *Chem. Commun.* **2003**, 2414-2415. (d) Cheng, L.; Wang, J.; Wang, M.; Wu, Z. *Inorg. Chem.* **2010**, *49*, 9392-9399.

(146) (a) Cheng, L.; Wang, J.; Wang, M.; Wu, Z. *Inorg. Chem.* **2010**, *49*, 9392-9399. (b) Michel, C.; Belanzoni, P.; Gamez, P.; Reedijk, J.; Baerends, E. J. *Inorg. Chem.* **2009**, *48*, 11909-11920. (c) Dijksman, A.; Arends, I. W. C. E.; Sheldon, R. *Org. Biomol. Chem.* **2003**, *1*, 3232

(147) (a) Pervukhina, N. V.; Romanenko, G. V.; Podberezskaya, N. V. *J. Struct. Chem.* **1994**, *35*, 367-390. (b) Dong, T.-Y.; Hendrickson, D. N.; Felthouse, T. R.; Shieh, H.-S. *J. Am. Chem. Soc.* **1984**, *106*, 5373-5375. (c) Felthouse, T.; Dong, T.-Y.; Hendrickson, D.; Shieh, H.-S.; Thompson, M. R. *J. Am. Chem. Soc.* **1986**, *108*, 8201-8214. (d) Dickman, M. H.; Porter, L. C.; Doedens, R. J. *Inorg. Chem.* **1986**, *25*, 2595-2599.

(148) (a) Caneschi, A.; Grand, A.; Laugier, J.; Rey, P.; Subra, R. *J. Am. Chem. Soc.* **1988**, *110*, 2307-2309. (b) Jaitner, P.; Huber, W. *J. Organomet. Chem.* **1983**, *259*, C1-5. (c) Jaitner, P.; Huber, W. *J. Organomet. Chem.* **1986**, *311,* 379-385. (d) Jaitner, P.; Huber, W. *Z. Anorg. Allg. Chem.* **1986**, *538*, 53-60. (e) Dickman, M.; Doedens, R. *Inorg. Chem.* **1982**, *21*, 682-684. (f) Mindiola, D. J.; Waterman, R.; Jenkins, D. M.; Hillhouse, G. L. *Inorg. Chim. Acta* **2003**, *345*, 299-308. (g) Ito, M.; Matsumoto, T.; Tatsumi, K. *Inorg. Chem.* **2009**, *48*, 2215-2223. (h) Zhu, Z.; Fettinger, J. C.; Olmstead, M. M.; Powers, P. P. *Organometallics* **2009**, *28*, 2091-2095.

(149) Evans, W. J.; Perotti, J. M.; Doedens, R. J.; Ziller, J. W. *Chem. Commun.* **2001**, 2326-2327

(150) Thies, S.; Bornholdt, C.; Köhler, F.; Sönnichsen, F. D.; Näther, C.; Tuczek, F.; Herges, R. *Chem. Eur. J.* **2010**, *16*, 10074-10083.

(151) Detty, M. R.; Friedman, A. E.; McMillan, M. *Organometallics* **1995**, *14* (3), 1442-1449

(152) (a) Ervin, K. M.; Gronert, S.; Barlow, S. E.; Gilles, M. K.; Harrison, A. G.; Bierbaum, V. M.; DePuy, C. H.; Lineberger, W. C.; Ellison, G. B. *J. Am. Chem. Soc.* **1990**, *112*, 5750-5759. (b) Segall, J.; Lavi, R.; Wen, Y.; Wittig, C. *J. Phys. Chem.* **1989**, *93* (21), 7287-7289

(153) (a) Groux, L. F.; Zargarian, D. *Organometallics* **2003**, *22*, 4759-4769. (b) Khairul, W. M.; Fox, M. A.; Zaitseva, N. N.; Gaudio, M.; Yufit, D. S.; Skelton, B. W.; Low, P. J. *Dalton Trans.* **2009**, 610-620. (c) Burling, S.; Elliot, P. I. P.; Jasim, N. A.; Lindup, R. J.; Whitwood, A. C. *Dalton Trans.* **2005**, 3686-3695. (d) Goicoechea, J. M.; Sevov, S. C. *J. Am. Chem. Soc.* **2006**, *128*, 4155-4161. (e) Walther, D.; Stollenz, M.; Gorls, H. *Organometallics* **2001**, *20* (20), 4221-4229.

(154) (a) Yam, V. W. W.; Tao, C.-H.; Zhang, L.; Wong, K. M.-C.; Cheung, K.-K. *Organometallics* **2001**, 453-459. (b) Yam, V. W. W.; Tao, C.-H.; Zhang, L.; Wong, K. M.-C.; Cheung, K.-K. *J. Chem. Soc. Dalton Trans.* **2001**, 1111. (c) Walther, D.; Lamm, K.; Gorls, H. *Z. Anorg. Allg. Chem.* **2009**, *635*, 1187-1195. (d) Kim, Y.-J.; Lee, S.-H.; Jeon, S. I.; Lim, M. S.; Lee, S. W. *Inorg. Chimica Acta* **2005**, *358*, 650-658. (e) Muller, C.; Iverson, C. N.; Lachicotte, R. J.; Jones, W. D. *J. Am. Chem. Soc.* **2001**, *123*, 9718-9719. (f) West, N. M.; White, P. S.; Templeton, J. L. *Organometallics* **2008**, *27*, 5252-5262. (g) Banditelli, G.; Bandini, A. L. *Organometallics* **2006**, *25*, 1578-1582. (h) Cao, D. H.; Stang, P. J.; Arif, A. M. *Organometallics* **1995**, *14*, 2733-2740.

(155) (a) Hetterscheid, D. G. H.; Kaiser, J.; Reijerese, E.; Peters, T. P. J.; Thewissen, S.; Blok, A. N. J.; Smits, J. M. M.; de Gelder, R.; de Bruin, B. *J. Am. Chem. Soc.* **2005**, *127*, 1895–1905. (b) Ahlers, C.; Dickman, M. H. *Inorg. Chem.* **1998**, *37*, 6337-6340.

(156) Cardolaccia, T.; Li, Y.; Schanze, K. S. *J. Am. Chem. Soc.* **2008**, *130*, 2535-2545

(157) Bruce, M. I.; Ellis, B. G.; Low, P. J.; Skelton, B. W.; White, A. H. *Organometallics* **2003**, *22*, 3184-3198